Optimization Studies for Aircraft Considering Propeller-Wing Interaction

by

Shamsheer S. Chauhan

A dissertation submitted in partial fulfillment
of the requirements for the degree of
Doctor of Philosophy
(Aerospace Engineering)
in The University of Michigan
2020

Doctoral Committee:

Professor Joaquim R. R. A. Martins, Chair
Professor Carlos E. S. Cesnik
Professor Peretz P. Friedmann
Associate Professor Kevin J. Maki

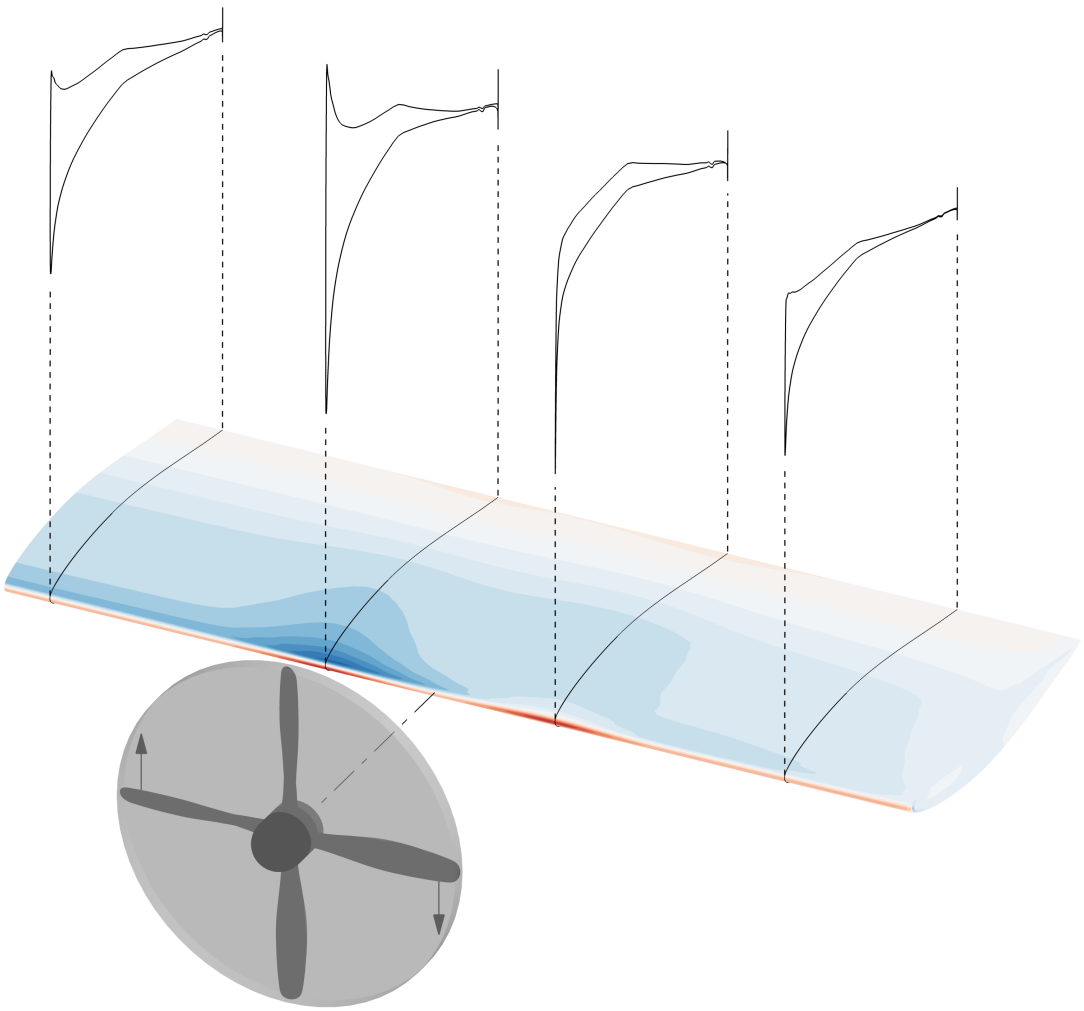

Shamsheer S. Chauhan

sschau@umich.edu

ORCID iD: 0000-0001-5768-646X

To my family

ACKNOWLEDGEMENTS

General

This would not have been possible without the following people. I thank:

- My family for all they have given me.
- Professor J. R. R. A. Martins for giving me the opportunity to study at this university full of wonders, in this incredible city, and more (3X AE481 GSI, 4X international travel, etc.).
- All my current and past office- and lab-mates* at UM for the education, wealth of support (both technical and non-technical), and laughter.
- The Bar-End Drifters Bicycle Club for helping me maintain my health and sanity.
- Professor L. L. M. Veldhuis for writing a comprehensive dissertation, which I used as a textbook.
- Dr. T. C. A. Stokkermans, Prof. T. Sinnige, N. van Arnhem, and R. de Vries (TU Delft Flight Performance and Propulsion) for their willingness to answer my questions and for their publications which set high standards.

*Alasdair Gray, Alessandro Fiumara, Alessandro Sgueglia, Alexander Coppeans, André Marta, Andrew Lamkin, Anil Yildirim, Anjali Balani, Benjamin Brelje, Bernardo Pacini, Charles Mader, Chris Wentland, David Burdette, Eirikur Jonsson, Eytan Adler, Gaetan Kenway, Galen Ng, Giovanni Pesare, Gustavo Halila, Hannah Hajdik, Jichao Li, Joan Colmer, John Hegseth, John Hwang, John Jasa, Joshua Anibal, Justin Gray, Mads Madsen, Marco Mangano, Mohamed Bouhlel, Neil Wu, Ney Secco, Nicolas Bons, Nitin Garg, Ping He, Puneet Singh, Raphael Gross, Ryan Patterson, Sabet Seraj, Saja Kaiyoom, Shugo Kaneko, Sicheng He, Timothy Brooks, Xiaolong He, Xiaosong Du, Yayun Shi, and Yingqian Liao.

- My doctoral committee (Professors P. P. Friedmann, C. E. S. Cesnik, and K. J. Maki) for their time and inspiration, both in and outside the classroom.

- The Hyundai Motor Company[†] for funding this research and giving me the opportunity to visit South Korea.

- The countless others whose shoulders we stand upon.

Technical

I also acknowledge:

- Dr. John Jasa and Benjamin Brelje for their valuable suggestions related to the eVTOL takeoff trajectory optimization studies presented here.

- Dr. Charles Mader, Dr. Nicolas Bons, Anil Yildirim, Yingqian Liao, Dr. Eirikur Jonsson, Neil Wu, and Prof. Ping He for their helpful suggestions and invaluable support with the various computational tools (ICEM and MACH-Aero) used for the RANS-based aerodynamic shape optimization studies presented here.

- The anonymous reviewers of my journal papers, on the eVTOL takeoff trajectory optimization studies and the RANS-based aerodynamic shape optimization studies, for improving the quality of the work presented here through their valuable suggestions and constructive criticism.

- Dr. John Jasa and Dr. Justin Gray for their support with OpenAeroStruct and OpenMDAO, which were used for the aerostructural optimization work presented here.

- Dr. Justin Gray, Dr. Mads Madsen, and Yingqian Liao for reviewing drafts of this dissertation and suggesting improvements.

[†]Braden Kim, Hyun-Su Cho, and Hansol Yoon, in particular.

- Advanced Research Computing - Technology Services (ARC-TS), a division of Information and Technology Services (ITS) at the University of Michigan, Ann Arbor, for partially supporting the work presented here through computational resources and services.

TABLE OF CONTENTS

LIST OF TABLES

Table

LIST OF FIGURES

Figure

Nomenclature

General Introduction and Background

α	wing angle of attack
α_{prop}	propeller inclination angle
Γ	circulation
Γ_{tr}	trailing-vortex circulation
$\theta_{0.75R}$	blade pitch angle at $0.75R$
ν	number of rotations per unit time
ρ	freestream fluid density
ω	angular speed
A_{disk}	propeller disk area, πR^2
b	wing span
c	chord length
c_{d}	sectional drag coefficient
C_D	drag coefficient
$\Delta C_{D\text{prop}\rightarrow\text{wing}}$	drag coefficient change due to propeller-wash effect
$C_{D\text{w}}$	isolated-wing drag coefficient
$C_D^{'}$	drag coefficient reduction
$c_{\text{l}}, C_{\text{l}}$	sectional lift coefficient
C_L	lift coefficient
$\Delta C_{L\text{prop}\rightarrow\text{wing}}$	lift coefficient change due to propeller-wash effect
$C_{L\text{w}}$	isolated-wing lift coefficient
C_{n}	normal-force coefficient
C_p	pressure coefficient
$C_{p_{\text{t}}}$	total-pressure coefficient
C_T	thrust coefficient
$D_{\varnothing}$	propeller diameter
J	advance ratio (propeller definition), $\frac{V_\infty}{\nu D_{\varnothing}}$
J_{R}	advance ratio (rotor definition), $\frac{V_\infty}{\omega R}$
l_{eff}	sectional lift due to the effective freestream velocity
p_{s}	static pressure
p_{t}	total pressure
P	ideal power
q_∞	freestream dynamic pressure
r	radial coordinate
r_{s}	slipstream radius
R, R_{p}	propeller radius
s_s	wing semispan
T	thrust
T_{C}	thrust coefficient
u_∞, V_∞	freestream velocity[‡]

[‡]Note: In this dissertation, the terms *velocity* and *speed* are used interchangeably, as is common in propeller and aircraft-design literature.

v	propeller-induced velocity
$v_\mathrm{a}, V_\mathrm{a}$	axial velocity
v_i	propeller-induced velocity at the disk
$v_\mathrm{t}, V_\mathrm{t}$	tangential velocity
V_eff	effective freestream velocity
$V_\mathrm{i,a}$	propeller-induced axial velocity component
$V_\mathrm{i,t}$	propeller-induced tangential velocity component
x, X	axial coordinate
x_p	propeller streamwise position
y, Y	spanwise coordinate
y_p	propeller spanwise position
z, Z	vertical coordinate
z_p	propeller vertical position

Part I

α	wing angle of attack
α_∞	wing angle of attack relative to the freestream
α_EFS	wing effective-freestream angle of attack due to the propellers
α_in	propeller incidence angle
α_s	wing stall angle of attack
β	blade pitch angle at $0.75R$
η_prop	propulsive efficiency, $\frac{TV_{\infty\perp}}{P_\mathrm{electrical}}$
η_total	total efficiency, $\frac{mgy+0.5m(V_x^2+V_y^2)}{\int P_\mathrm{electrical}\,\mathrm{d}t}$
θ	wing angle relative to the vertical
θ_RCmax	wing angle (relative to the vertical) for best rate of climb
κ	propeller induced-power correction factor
μ	rotor forward-flight advance ratio, $\frac{V_{\infty\parallel}}{\Omega R}$
ρ	air density
σ	propeller solidity
σ_biplane	biplane interference factor
σ_e	effective solidity, $\frac{2Bc_\mathrm{b}}{3\pi R}$
Ω	propeller angular speed
a_airfoil	airfoil lift-curve slope
a_wing	finite-wing lift-curve slope
A_disk	propeller disk area, πR^2
AR	wing aspect ratio
b	wing span
B	number of blades per propeller
c_b	average chord length of the blades
c_d	sectional drag coefficient
c_l	sectional lift coefficient
$C_{\mathrm{d}_{0\mathrm{p}}}$	representative propeller-blade profile-drag coefficient
C_D	wing drag coefficient
C_{D_i}	wing induced drag coefficient
C_{D_s}	wing drag coefficient at stall
C_L	wing lift coefficient
C_{L_s}	wing lift coefficient at stall
C_{P_p}	propeller profile-power coefficient, $\frac{P_\mathrm{p}}{\rho A_\mathrm{disk} R^3 \Omega^3}$
D_fuse	fuselage drag force
D_i	wing induced drag force
D_wings	total drag force of the wings
e	span efficiency factor
f	thrust factor, $1 + \frac{\sqrt{1+T_\mathrm{c}}-1}{2} + \frac{T_\mathrm{c}}{4(2+T_\mathrm{c})}$
g	acceleration due to gravity

k_{w}	propeller-induced velocity factor
L_{wing}	wing lift force
L_{wings}	total lift force of the wings
m	aircraft mass
N	propeller force component normal to the propeller axis
P_{disk}	power supplied to the propeller disk excluding profile power
$P_{\mathrm{electrical}}$	electrical power from the batteries
P_{max}	maximum electrical power available for the baseline aircraft
P_{p}	propeller profile power
q	freestream dynamic pressure
$q_\perp$	dynamic pressure calculated using $V_{\infty\perp}$
R	propeller radius
Re	Reynolds number
S_{ref}	total planform area of the wings of the baseline aircraft
t	time
Δt	time-step length
t/c	airfoil thickness-to-chord ratio
T	thrust
T_{c}	thrust coefficient, $\frac{T}{q_\perp A_{\mathrm{disk}}}$
v_{i}	propeller-induced velocity at the disk
$V_{\infty\parallel}$	component of the freestream velocity parallel to the propeller disk
$V_{\infty\perp}$	component of the freestream velocity normal to the propeller disk
V_{x_i}	aircraft horizontal velocity component for time step i
V_{y_i}	aircraft vertical velocity component for time step i
x, y	Cartesian coordinates (horizontal and vertical displacements of the aircraft CG)

Part II

γ	specific-heat ratio
ν	number of rotations per unit time
ρ	fluid density
τ	FFD section twist angle
ϕ_x, ϕ_y, ϕ_z	body-force Cartesian components (force per unit volume)
a, m, n	propeller-loading model shape parameters
A	propeller disk area, πR^2
ΔA	face area of a small control volume
A_{ann}	face area of an annular region
C_D	wing drag coefficient
C_L	wing lift coefficient
C_p	pressure coefficient
C_T	propeller thrust coefficient, $\frac{T}{\rho \nu^2 D_{\varnothing}^4}$
$D_{\varnothing}$	propeller diameter
f_θ	tangential force per unit radius
$f_{\mathrm{vol},\theta}$	tangential force per unit volume, $\frac{f_\theta}{2\pi r t}$
f_x	axial force per unit radius
$\mathbf{F}_x, \mathbf{F}_y, \mathbf{F}_z, \mathbf{B}$	vectors used to write the Euler equations in a compact form
$\tilde{F}$	a reference value used to obtain the required total force for the propeller-loading model
J	propeller advance ratio, $\frac{V_\infty}{\nu D_{\varnothing}}$
k_1,k_2	constant fractions
k_3	a constant, $\left(\int_0^1 \tilde{r}^m (1-\tilde{r})^n \mathrm{d}\tilde{r}\right)^{-1}$
M	Mach number
n_x, n_y, n_z	surface-normal unit-vector Cartesian components

N	total number of computation cells
p	pressure
$P/D_{\varnothing}$	propeller pitch-to-diameter ratio
r	radial distance from the propeller axis
Δr	a small radial width, $k_2 R$
r_{in}	propeller inner radius (usually hub or spinner radius)
$\hat{r}$	normalized radius, $\frac{r-r_{\text{in}}}{R-r_{\text{in}}}$
$\tilde{r}$	normalized radius, r/R
R	propeller outer radius
S	control surface
t	actuator disk thickness
t_{a}	airfoil thickness
$t_{\text{a,initial}}$	initial airfoil thickness
T	propeller thrust
T_{ann}	thrust of an annular region
T/A	disk loading
u, v, w	flow-velocity Cartesian components
V	control volume
V_∞	freestream speed
$V_{\text{i},\theta}$	tangential induced-velocity component
$V_{\text{i,x}}$	axial induced-velocity component
x, y, z	Cartesian coordinates
Δy	FFD-control-point vertical displacement
$\Delta y_{\text{LE,upper}}$	upper-leading-edge FFD-control-point vertical displacement
$\Delta y_{\text{LE,lower}}$	lower-leading-edge FFD-control-point vertical displacement
$\Delta y_{\text{TE,upper}}$	upper-trailing-edge FFD-control-point vertical displacement
$\Delta y_{\text{TE,lower}}$	lower-trailing-edge FFD-control-point vertical displacement
y^+	law-of-the-wall nondimensional off-wall distance

Chapter 12

κ	airfoil technology factor
Λ	wing sweep angle
$\sigma_{\text{von Mises}}$	von Mises stresses aggregated using the KS function
A_{e}	enclosed area defined by the wall midlines of a cross-section
C_D	aircraft drag coefficient
$C_{D,\text{wave}}$	wave-drag coefficient
C_L	aircraft lift coefficient
$C_{L,\text{cruise}}$	aircraft lift coefficient for the cruise flight point
I_{p}	area moment of inertia of a parallelogram about an axis passing through its centroid and parallel to the z-axis
J	torsion constant
$\text{lift}_{2.5\,\text{g}}$	aircraft lift force for the 2.5 g maneuver flight point
M	Mach number
M_{crit}	critical Mach number
s	length along wall midlines
t	wall thickness
t_{skin}	thickness of upper and lower skins
t_{spar}	thickness of forward and rear spars
t/c	streamwise airfoil thickness-to-chord ratio
$\text{weight}_{2.5\,\text{g}}$	aircraft weight for the 2.5 g maneuver flight point
x, y, z	Cartesian coordinates
z_i, y_i	i^{th} user-specified wingbox coordinates

ABSTRACT

Environmental concerns and advances in battery technology are currently fueling a widespread growth of interest in electric aircraft. Additionally, the fundamentally different nature of electric motors, compared to combustion engines, allows designers to experiment with unconventional aircraft configurations that would otherwise be impractical. Because of the relatively low specific energy available through current battery technology, and the high efficiency of propellers at low subsonic speeds, this interest has led to a renewed focus on the design and optimization of short-range propeller aircraft. Along with providing benefits related to emissions, procurement cost, and maintenance, electric motors allow distributing propulsion on an aircraft with greater ease compared to combustion engines, which further allows taking advantage of performance benefits through propulsion integration. To design aircraft that effectively take advantage of this increased design freedom requires the ability to answer some questions that have not been addressed in previous literature. Two such questions that this dissertation focuses on, with the common theme of propeller-wing interaction, are: What does the optimal takeoff trajectory for a tilt-wing electric vertical-takeoff-and-landing aircraft look like and how do various design and performance considerations, including those related to propeller-wing interaction and wing stall, affect it? Does optimizing a wing while considering propeller effects using computational fluid dynamics provide significant aerodynamic performance benefits? The first part of this dissertation explores the design space with takeoff in mind, and

the second part explores the design space with cruise in mind.

For the first part, simplified models for the aerodynamics, propulsion, propeller-wing flow interaction, and flight mechanics are used to carry out gradient-based optimization studies for the takeoff-to-cruise trajectory of a tandem tilt-wing eVTOL aircraft. Results for optimizations with and without stall and acceleration constraints, with varying levels of flow augmentation from propellers, are presented and show that the optimal takeoffs involve stalling the wings or flying near the stall angle of attack. However, the results also show that the energy penalty for avoiding stall is practically negligible. Additionally, without acceleration constraints, the optimized trajectories involve rapidly transitioning to forward flight and accelerating, followed by climbing at roughly constant speed, and then accelerating to the required cruise speed. With an acceleration constraint for passenger comfort, the transition, climb, and acceleration phases are more gradual and less distinct. Results showing the impact of wing size and available power on the optimized trajectories are also presented.

For the second part, the cruise drag of a wing with a tractor propeller is minimized using aerodynamic shape optimization. Reynolds-averaged Navier–Stokes computational fluid dynamics with an actuator-disk approach is used for the simulations, and a gradient-based algorithm is used for the optimization. Changing the rotation direction of the propeller, changing the spanwise location of the propeller, and optimizing the twist and airfoil shapes of the wing impact the aerodynamic performance significantly. However, optimizing the wing while considering the propeller slipstream provides little additional benefit compared to optimizing it without considering the propeller slipstream (the difference is less than one drag count). The wings optimized without considering the propeller slipstream are naturally able to

recover swirl almost as effectively as the wings optimized while considering the propeller slipstream, and the propeller-induced velocities for the cruise condition are not high enough to lead to significant airfoil-shape design changes. These conclusions are reached for both inboard-mounted and tip-mounted propellers. Additionally, a simple first-principles-based analytic expression for estimating propeller-induced tangential velocities is derived.

The overarching conclusion and recommendation is that, for eVTOL aircraft, the design focus should be on sound, simple, and safe aircraft. From a takeoff point of view, the aircraft design should prioritize factors such as mechanical simplicity, noise, and safety because factors such as wing and fuselage drag are not significant during the takeoff-to-cruise phase (the induced losses from the propellers dominate). From a cruise point of view, strategically selecting the locations and rotation directions of wing-mounted propellers should be the primary focus (this will require aeroelastic considerations).

CHAPTER 1

General Introduction

> Study hard what interests you the most in the most undisciplined, irreverent and original manner possible.
>
> *R. P. Feynman*

> It's better to be a warrior in a garden than a gardener in a war.
>
> Ancient proverb

Environmental concerns and advances in battery technology are currently fueling a widespread growth of interest in the development of hybrid and fully electric aircraft. Additionally, the fundamentally different nature of electric motors, compared to combustion engines, is allowing aircraft designers to experiment with unconventional aircraft configurations that would otherwise be impractical. These factors, combined with advances in autonomous control and ride-hailing services, make a future with electric aircraft providing urban and regional transportation seem more feasible than ever.

The potential for transporting people by air within urban areas, urban air mobility (UAM), is especially receiving significant interest, and a large number* of different electric vertical takeoff and landing (eVTOL) aircraft are currently under development. Some examples of the companies that tested full-scale UAM eVTOL proto-

*The Vertical Flight Society's eVTOL News website lists almost 300 concepts as of May 2020 (`https://evtol.news/aircraft/`)

types in 2019 are Airbus[†], Aurora Flight Sciences[‡] (a Boeing subsidiary), EHang[§], Joby Aviation, Kitty Hawk[¶], Lilium[‖], and Volocopter[**]. Most of the concepts under development can be categorized into a few major categories of aircraft type. Four major categories are multicopter (e.g., Volocopter 2X), lift+cruise (e.g., Kitty Hawk Cora), tilt rotor (e.g., Joby S4), and tilt wing (e.g., Airbus A^3 Vahana) [11].

Because of the relatively low specific energy available through current battery technology [11–13], and the high efficiency of propellers at low subsonic speeds, this recent growth of interest has led to a renewed focus on the design and optimization of short-range propeller aircraft [12–28]. Along with providing benefits related to emissions, procurement cost, and maintenance, electric motors allow distributing propulsion on an aircraft with greater ease compared to combustion engines, which further allows taking advantage of performance benefits through propulsion integration [12]. For example, distributing propellers across a wing can allow smaller wings for conventional and short takeoff and landing (C/STOL) aircraft or help avoid stall for vertical takeoff and landing (VTOL) aircraft [12, 14, 29, 30]. As another example, strategically selecting the placement and rotation directions of wing-mounted propellers can provide span-efficiency or propulsive-efficiency improvements [7, 12, 31–33].

To design aircraft that effectively take advantage of the aforementioned increased design freedom and propulsion-integration benefits requires the ability to answer some questions that have not been addressed in previous literature. Two such questions that this dissertation focuses on, which satisfy the four criteria in Fig. 1.0.1,

[†]Airbus A^3 Vahana flight-test footage: `https://youtu.be/n8yfDTiZH4Q` [Accessed: 5 June 2020]

[‡]Aurora/Boeing Passenger Air Vehicle flight-test footage: `https://youtu.be/FpaYoF12Rnk` [Accessed: 5 June 2020]

[§]EHang Autonomous Aerial Vehicle passengered flight-demonstration footage: `https://youtu.be/6tIBFaxGYoc` [Accessed: 5 June 2020]

[¶]Kitty Hawk Cora flight-test footage: `https://youtu.be/kJNACCPqFRQ` [Accessed: 5 June 2020]

[‖]Lilium Jet flight-test footage: `https://youtu.be/5ukmS9ZJm40` [Accessed: 5 June 2020]

[**]Volocopter 2X flight-test footage: `https://youtu.be/NxBTzAbPSeY` [Accessed: 5 June 2020]

are:

1. What does the optimal takeoff trajectory for a tilt-wing eVTOL aircraft look like and how do various design and performance considerations, including those related to propeller-wing interaction and wing stall, affect it?

2. Does optimizing a wing while considering propeller effects using computational fluid dynamics (CFD) provide significant aerodynamic performance benefits?

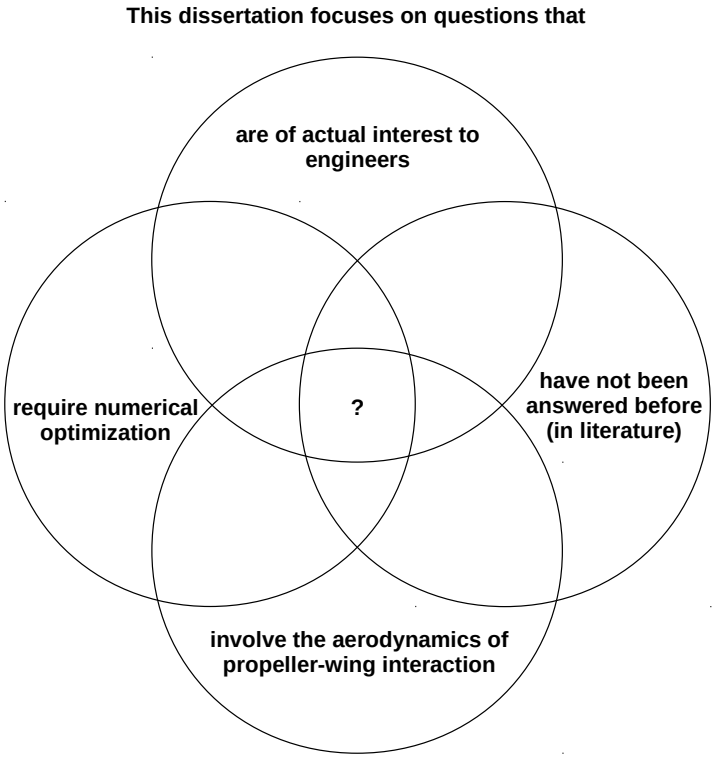

Figure 1.0.1: The questions selected for this dissertation satisfy these four criteria.

This dissertation has two main parts (Parts I and II), and as the title indicates, the common theme is optimization considering propeller-wing interaction. These two parts correspond to the two aforementioned questions. Part I presents takeoff trajectory optimization studies for a tandem tilt-wing eVTOL aircraft, and Part II presents CFD-based aerodynamic shape optimization studies for wings considering

propeller-wing interaction for both inboard- and tip-mounted tractor-propeller configurations. Part I explores the design space with takeoff in mind, and Part II explores the design space with cruise in mind. Additionally, Chapter 12 contains a third part that presents a wingbox model, implemented in an open-source tool [34], and presents low-to-mid-fidelity aerostructural optimization studies for a transport-aircraft wing (without propeller-wing flow interaction). This open-source model has been used for optimization studies for a VTOL commuter aircraft [35, 36]. Before the main parts begin, Chapter 2 provides a general review of propeller slipstream characteristics and the various propeller-wing interaction effects relevant to tractor configurations (i.e., configurations in which the propeller is in front of the wing). After the main parts conclude, Chapter 11 lists the novel contributions, conclusions, and recommendations for future work.

CHAPTER 2

General Background: Propeller Slipstream Characteristics and Propeller-Wing Interaction

> The aerodynamics phenomena that play a role in the characteristics of propeller-driven aircraft constitute a formidable problem that needs to be carefully analyzed [and] understood to arrive at optimized designs.
>
> *L. L. M. Veldhuis* [4]
> Professor, TU Delft, 2005

When a propeller is placed near a wing, the flow it induces affects the lift of the wing as well as the profile and induced drag of the wing [4, 6, 7, 31–33, 37]. The details of the flow around the wing, and consequently its performance, change with the location, settings, and rotation direction of the propeller [4, 6–8, 30–33, 37]. For example, when a propeller is placed directly in front of a wing, the propeller-induced axial and tangential (also referred to as swirl) velocity components result in spanwise variations of both the effective flow speeds and local angles of attack of the wing sections. Not only does this affect the lift and drag of the sections immediately behind the propeller, but also the lift and drag distributions across the entire wing [4, 7]. On the other hand, when the propeller is placed directly behind the wing, the spanwise variations are less pronounced because the flow speed is lower and the swirl is negligible in front of a propeller [3, 4].

At the same time, the flow induced by the wing, as well as other changes to the

flow field caused by drag or blockage effects, affect the performance of the propeller [4, 32, 33, 37]. This is primarily due to the altered inflow to the propeller and can result in a gain or loss in performance depending on the location and rotation direction of the propeller [4, 12, 32, 33, 37]. Generally, the impact on the performance of the propeller is greater when it is placed behind a wing.

Several researchers have studied these propeller-wing flow interactions, and interest in it has cycled in and out of fashion over the last century. Around 1920, Prandtl [37] was among the first to systematically study this mutual interaction and show that propellers and wings should not be looked at in isolation. The early research was a natural consequence of the achievement of powered human flight in the first decade of the 20^{th} century and its growing military and civil applications in the subsequent decades. Later, in the 1950s and 1960s, the interest in developing V/STOL aircraft [38–46] led to many studies on the effects of propeller-wing interaction on flight performance (low-speed high-lift performance in particular) [29–31, 41, 47, 48]. Then in the 1980s and 1990s, the interest in advanced propellers (also known as propfans), combined with the improvements in computing technology, led to advancements in the computational modeling of propeller-wing interaction [4, 6, 32, 33, 49–51]. And now, in the second decade of the 21^{st} century, the growth of interest in the development of electric aircraft has brought with it another renewal of interest in studying and modelling these interactions and their effects on performance [12, 14–22].

The rest of this chapter provides a brief review of the characteristics of the flow induced by a typical propeller and of the various propeller-wing interaction effects. A more comprehensive overview of propeller slipstream characteristics and propeller-wing interaction (both modeling and effects) is provided by Veldhuis [4]*. Also,

*For those new to the field and interested in learning about propeller-wing interaction, I recommend beginning with this chapter for a quick overview of the various effects and for references to more recent literature, and then exploring the more comprehensive dissertation of Veldhuis [4].

Veldhuis [4], Carlton [52], and Smith [53] together provide a broad overview of propeller modeling techniques.

2.1 Propeller Slipstream Characteristics

Although a propeller's slipstream is altered by the presence of a trailing wing, it is useful to first review the flow characteristics of an isolated propeller before studying its interaction with a wing. In this section, the axial and radial variation of axial velocity, pressure, and tangential velocity in an isolated propeller's slipstream are briefly reviewed. For future convenience, Table 2.1.1 lists the figures that can be referred to for a quick review of these characteristics.

Table 2.1.1: Figures that provide an overview of propeller slipstream characteristics

	Axial velocity	Pressure	Tangential velocity
Axial variation	Figs. 2.1.1 and 2.1.2	Fig. 2.1.1	Figs. 2.1.4 and 2.1.5
Radial variation	Fig. 2.1.7	Figs. 2.1.6 and 2.1.7	Figs. 2.1.6 and 2.1.7

2.1.1 Axial Variation of Axial Velocity, Pressure, and Tangential Velocity

Momentum theory (also known as Rankine–Froude momentum theory, classical momentum theory, and actuator-disk[†] theory) is a useful starting point for gaining insight on the flow induced by a propeller [41]. It models the propeller as a uniform actuator disk that provides a static-pressure jump, and it is derived analytically by applying the principles of mass, momentum, and energy conservation to a simplified control volume with an idealized flow (inviscid, incompressible, irrotational, radially uniform, and azimuthally uniform). Based on it, the axial velocity in the propeller streamtube increases continuously from the freestream value far upstream to a finite value far downstream. More specifically, for a given thrust T and disk area A, the

[†]This theory differs from and should not be confused with the actuator-disk approach used to model propellers in CFD simulations.

flow velocity[‡] at the disk according to momentum theory is

$$V_\infty + v_\mathrm{i} = V_\infty + \frac{\sqrt{{V_\infty}^2 + \frac{2T}{\rho A}} - V_\infty}{2}, \tag{2.1.1}$$

and the slipstream velocity far downstream is $V_\infty + 2v_\mathrm{i}$, where V_∞ and ρ are the freestream velocity and density, respectively, and v_i is the induced velocity at the disk. This and the corresponding pressure changes are illustrated in Fig. 2.1.1. The detailed-CFD results of Stokkermans et al. [3] (unsteady RANS simulations with sliding meshes for the 3-D propeller geometry) plotted in Fig. 2.1.2 show an example of this behavior.

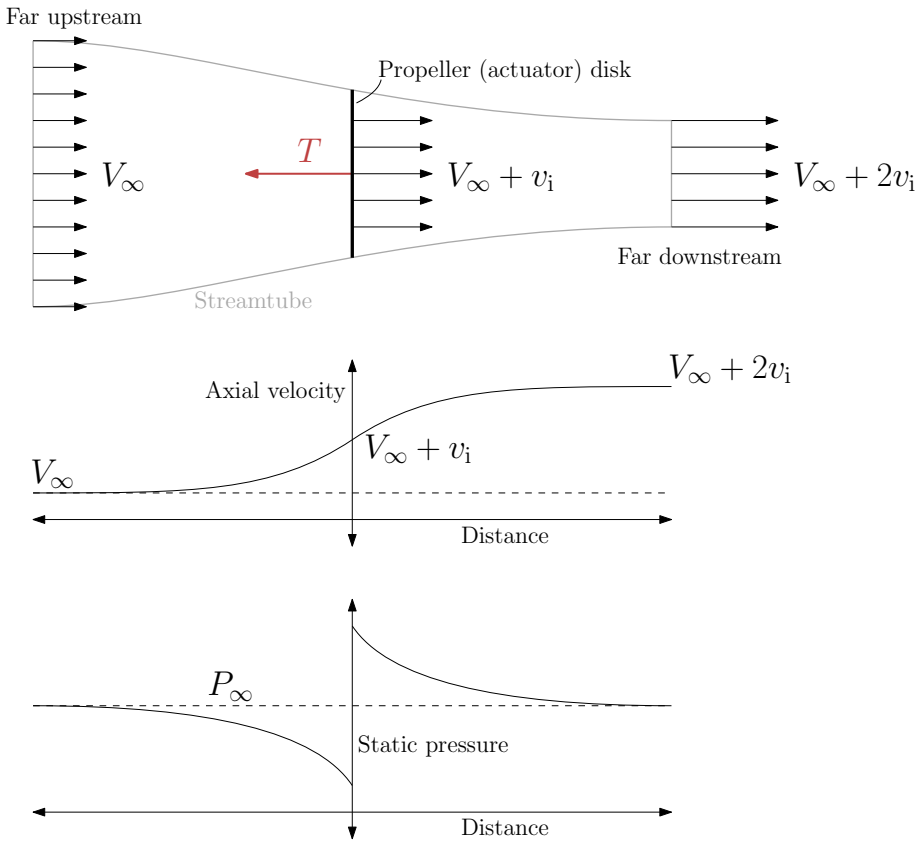

Figure 2.1.1: Illustrations of velocity and pressure variations with axial distance based on momentum theory

Although momentum theory does not capture any radial variation, viscous effects,

[‡]In this dissertation, the terms *velocity* and *speed* are used interchangeably, as is common in propeller and aircraft-design literature.

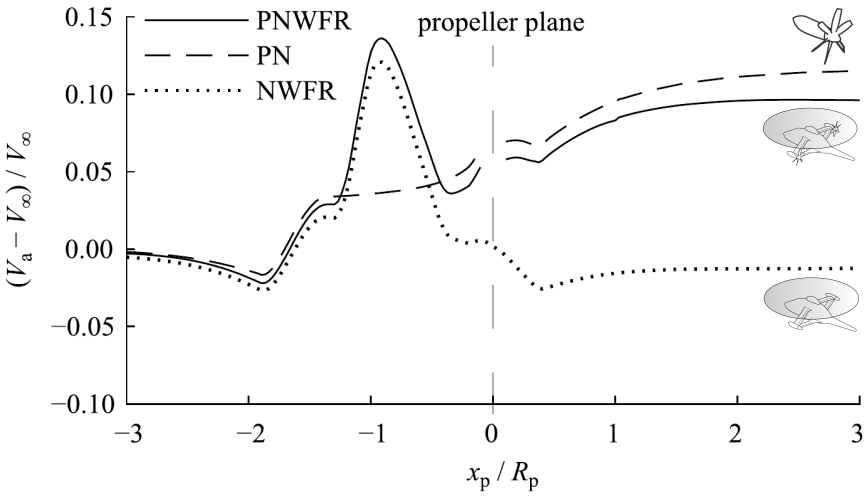

Figure 2.1.2: Radially and circumferentially averaged axial velocity (V_a) distributions for a pusher propeller are shown by the dashed curve (unsteady RANS CFD simulations for the P cases; P=propeller; N=nacelle; W=wing; F=fuselage; R=rotor; x_p is the axial distance; R_p is the propeller radius; results for a cruise condition; $J_R > 0.5$; figures from Stokkermans et al. [3])

or swirl, it provides a qualitative idea of the axial flow behavior in a propeller's slipstream and also provides quantitative estimates for the axial velocities. Momentum theory can also relate the thrust T to the ideal power P using

$$P = T\left(\frac{V_\infty}{2} + \frac{\sqrt{V_\infty^2 + \frac{2T}{\rho A}}}{2}\right). \tag{2.1.2}$$

This is simply the thrust multiplied by the flow velocity at the disk, and it provides considerable insight into the performance of a propeller. For example, it shows that, with thrust held constant, increasing the disk area decreases the power required, or as another example, with power held constant, increasing the flight speed decreases the thrust. This equation is known to underpredict power by around 15–20% [41].

A propeller blade can also be viewed as an advancing and rotating wing that produces a helical vortex system, as illustrated in Fig. 2.1.3 [4, 32, 52]. This is the rotating-wing analogue of the lifting-line representation for fixed wings. Using this representation, the tangential velocity induced by a propeller can be shown to be zero in front of the propeller and axially constant, but non-zero, behind [4]. The

contributions from the bound and trailing vortices are illustrated in Fig. 2.1.4 [4].

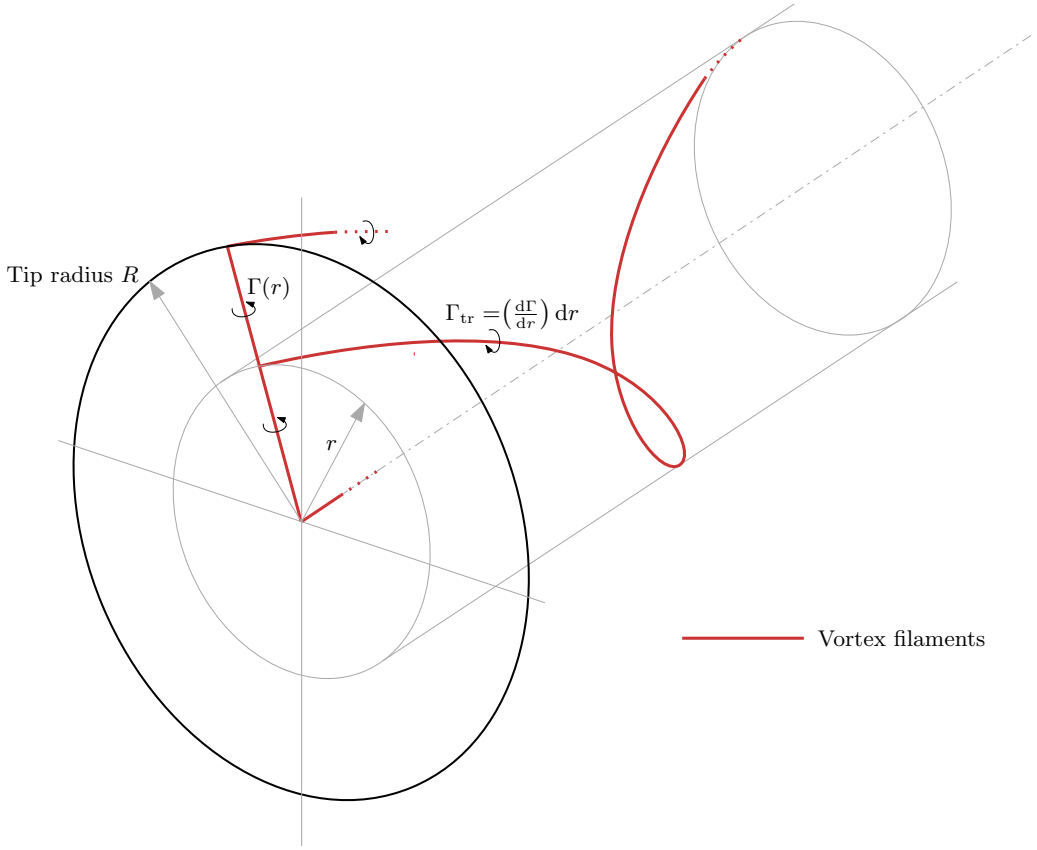

Figure 2.1.3: An illustration of bound and trailing vortex filaments of a helical vortex system representing a propeller

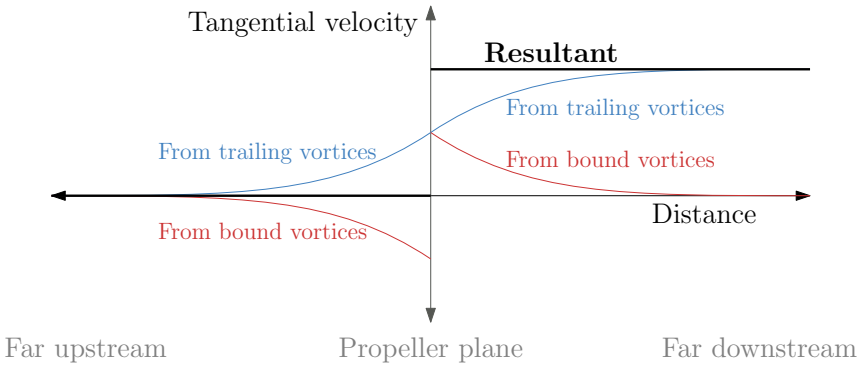

Figure 2.1.4: An illustration of the bound and trailing vortex-system contributions to the tangential velocity in a propeller's streamtube (adapted from Veldhuis [4])

The detailed-CFD results of Stokkermans et al. [3] plotted in Fig. 2.1.5 (unsteady RANS simulations with sliding meshes for the 3-D propeller geometry), for example,

also show this step-shaped tangential velocity distribution (see Fig. 2.1.2 for the corresponding axial velocity distribution). Since the axial velocities change with axial distance behind a propeller (e.g., Fig. 2.1.2), but the tangential velocities do not change as significantly (e.g., Fig. 2.1.5), the swirl angles also vary with axial distance behind a propeller. Figures 2.1.2 and 2.1.5 also show results for a case in which a propeller is mounted behind the wingtip of a compound helicopter's box-wing (note the tangential velocity reduction due to the propeller's counter-wingtip-vortex rotation direction).

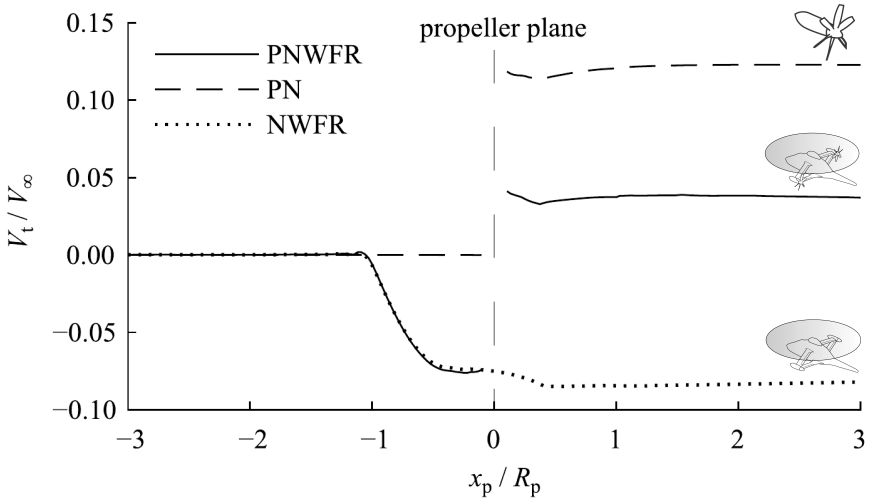

Figure 2.1.5: Radially and circumferentially averaged tangential velocity (V_t) distributions for a pusher propeller are shown by the dashed curve (unsteady RANS CFD simulations for the propeller cases; P=propeller; N=nacelle; W=wing; F=fuselage; R=rotor; x_p is the axial distance; R_p is the propeller radius; results for a cruise condition; $J_R > 0.5$; figure from Stokkermans et al. [3])

Additionally, as expected from the mass conservation principle, a propeller's streamtube contracts as the flow in it accelerates. The following equation, derived using a semi-infinite helical vortex filament [41], provides an estimate for the axial induced velocity v as a function of the axial distance x (measured from the propeller plane):

$$\frac{v}{v_i} = 1 + \frac{x/R}{\sqrt{1 + (x/R)^2}}, \tag{2.1.3}$$

where v_i is the induced velocity at the propeller disk, and R is the propeller radius. Assuming uniform axial flow, the slipstream radius r_s, as a function of the axial distance x, can then be estimated using

$$\frac{r_\mathrm{s}}{R} = \sqrt{\frac{V_\infty + v_\mathrm{i}}{V_\infty + v_\mathrm{i}\left(1 + \frac{x/R}{\sqrt{1+(x/R)^2}}\right)}}. \tag{2.1.4}$$

Momentum theory and this slipstream-contraction model are often used for low-order propeller-wing interaction modeling [54–57].

2.1.2 Radial Variation of Axial Velocity, Pressure, and Tangential Velocity

Contrary to the assumptions made for momentum theory, the flow induced by a propeller is not radially uniform, as shown by the experimental and CFD results in Fig. 2.1.6 (time-averaged results for a four-bladed propeller) [5] and by the blade-element-momentum-theory (BEMT) results in Fig. 2.1.7 [4]. BEMT, which combines blade-element theory with momentum theory for annular control volumes, is a popular low-cost approach that can predict radial variations. The relative magnitudes of the axial and tangential velocity profiles depend on the advance ratio and pitch setting of the propeller. For varying propeller loading, the form of the tangential velocity profile tends to change more noticeably than the form of the axial velocity profile [4].

So far, several methods of varying complexity and fidelity, for predicting the performance of a propeller and the behavior of the flow induced by it, have been mentioned in this section (momentum theory, helical vortex models, BEMT, full-blade unsteady CFD, actuator-line unsteady CFD, and actuator-disk steady CFD). However, several more methods exist for modeling propellers and rotors, and Veldhuis [4], Carlton [52], Smith [53], and Singh and Friedmann [58] together provide a broad overview of them.

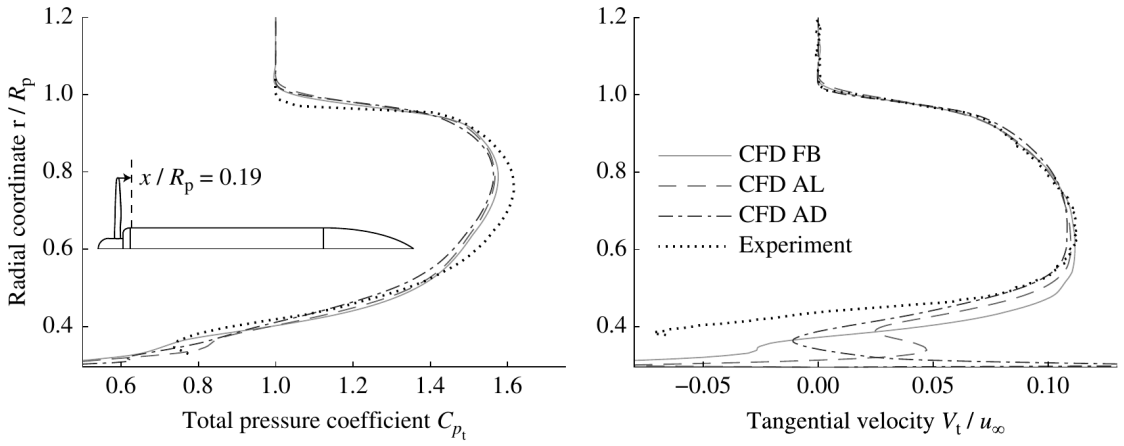

Figure 2.1.6: Time-averaged radial distributions of pressure and tangential velocity behind a propeller (FB=full blade; AL=actuator line; AD=actuator disk; $J = 0.8$; $u_\infty = 40\,\mathrm{m/s}$; $\theta_{0.75R} = 24\,\mathrm{deg}$; $R_p = 0.12\,\mathrm{m}$; figure from Stokkermans et al. [5])

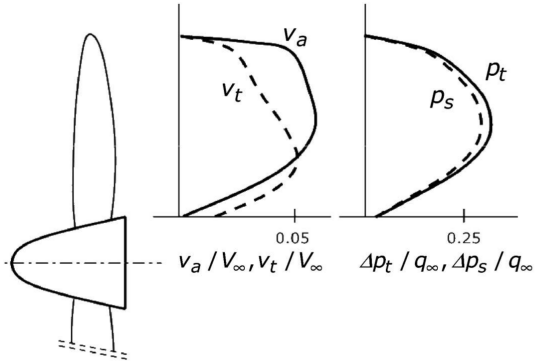

Figure 2.1.7: Radial distributions of axial velocity (v_a), tangential velocity (v_t), total pressure (p_t), and static pressure (p_s) directly behind a lightly loaded propeller (BEMT analysis; figure from Veldhuis [4])

2.2 Propeller-Wing Interaction Effects

In this section, propeller-wing interaction effects are reviewed, with a focus on tractor configurations and the effects on the wing. By a *tractor* configuration, we mean a configuration in which the propeller is in front of the wing (i.e., the propeller pulls the wing), and by a *pusher* configuration, we mean a configuration in which the propeller is behind the wing (i.e., it pushes the wing). For future convenience, Table 2.2.1 lists the figures that can be referred to for a quick overview of the effects.

Table 2.2.1: Figures that provide an overview of propeller-wing interaction effects

	Lift	Drag	Maximum lift
Streamwise location	Figs. 2.2.1 and 2.2.2	Figs. 2.2.1 and 2.2.2	–
Vertical location	Fig. 2.2.3	Fig. 2.2.3	–
Rotation direction	Figs. 2.2.7, 2.2.8a, 2.2.9a, and 2.2.10	Figs. 2.2.7, 2.2.8b, 2.2.9b, and 2.2.10	Fig. 2.2.10
Spanwise location	Fig. 2.2.11	Fig. 2.2.11	–
Thrust setting	Figs. 2.2.13, 2.2.14, and 2.2.15	Fig. 2.2.16	Fig. 2.2.15

2.2.1 Streamwise Location

As described in Sec. 2.1.1, the axial flow induced by a propeller is faster behind it than in front, and the swirl is negligible in front. Therefore, the impact on the performance of a wing is greater when it is placed directly behind a propeller than when it is placed directly in front.

On the other hand, the impact on the performance of a propeller is more significant when a wing is placed directly in front of the propeller than directly behind. This is because viscous effects, blockage effects, and the flow induced by the wing, which impact the performance of the propeller by altering the inflow to it, are more significant behind the wing. More on this can be found in the works by Prandtl [37], Kroo [32], Miranda and Brennan [33], and Veldhuis [4]. This dissertation focuses on propeller-wing interaction when a wing is located directly behind a propeller, and therefore we do not focus on the effects on a propeller's performance here.

Since the axial induced velocity and static pressure evolve with axial distance (Figs. 2.1.1 and 2.1.2), the axial distance between a propeller and a wing influences the interaction. Typically, however, for high-speed (cruise) cases, in which the propeller is lightly loaded, most of the slipstream contraction takes place within one to two propeller diameters [3, 4, 59] (e.g., Fig. 2.1.2), and the sensitivity to axial distance is low after about one propeller diameter.

The nature of the interactions changes when a wing is near a vertically offset pro-

peller but not directly in the propeller's slipstream. For an over-the-wing propeller, experimental results from Veldhuis [4], plotted in Fig. 2.2.1, show lift-to-drag ratio improvements when the propeller is directly above the wing. Despite not being in the propeller's slipstream, the performance of the wing is still affected. Prandtl [37] and Veldhuis [4] attribute this to the upwash effects (or the downwash effects with a below-the-wing propeller) due to streamtube contraction, as illustrated in Fig. 2.2.2.

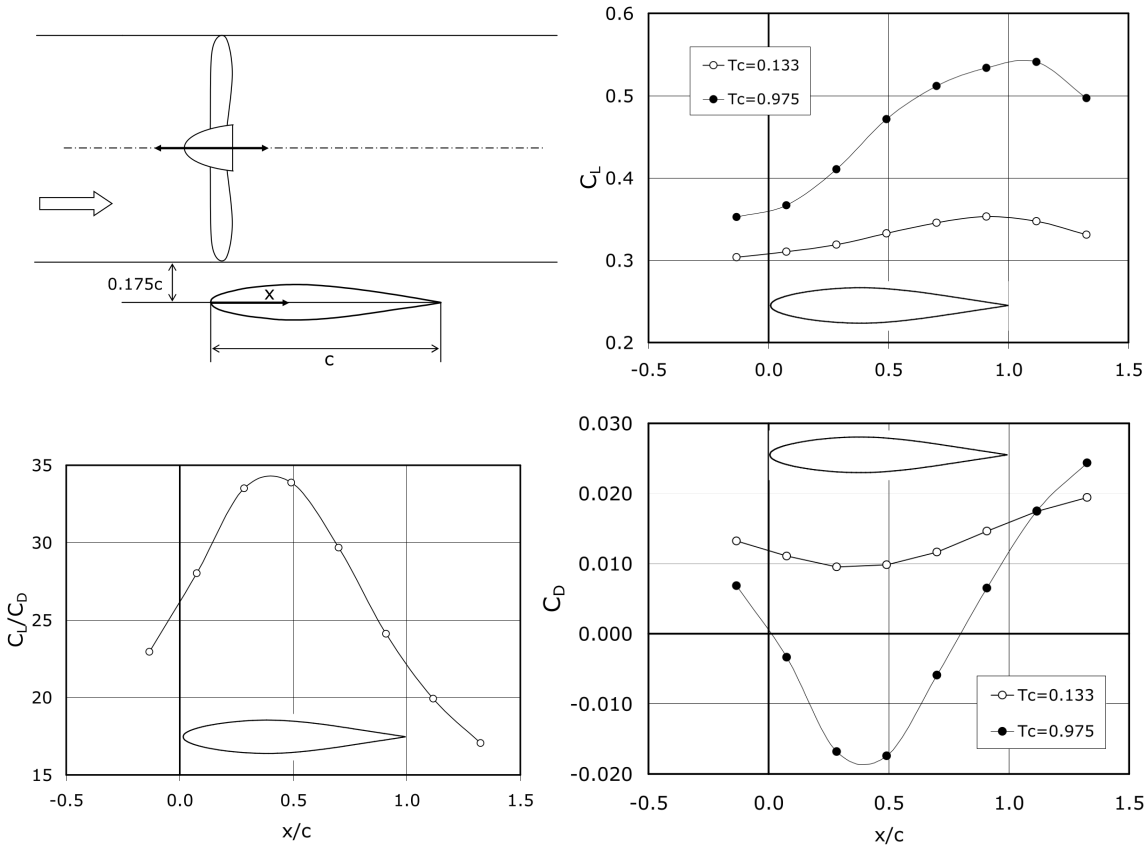

Figure 2.2.1: Experimental results showing the effect of propeller streamwise location on wing lift and drag for an over-the-wing configuration (low-thrust case: $J = 0.9$ and $T_C = 0.133$; high-thrust case: $J = 0.43$ and $T_C = 0.975$; figures from Veldhuis [4])

2.2.2 Vertical Location

As suggested by Fig. 2.2.2, the vertical offset of a propeller relative to a wing also affects the performance of the wing. Experimental results from Veldhuis [4], plotted in Fig. 2.2.3, show that the vertical location of a tractor propeller affects both wing

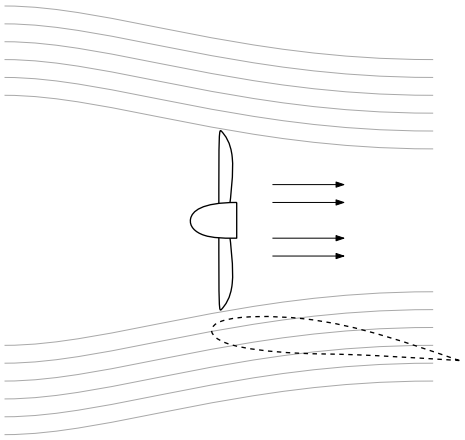

Figure 2.2.2: Illustration of the effective flow seen by a wing with an over-the-wing propeller

lift and drag, and the changes are thrust dependent.

When the propeller is moved upwards, starting from zero vertical offset, the wing's lift increases because the mass flow rate over the upper surface increases and because of the upwash effect of the slipstream contraction [4, 37]. Similarly, when the propeller is moved downwards instead, the lift decreases because the mass flow rate increases below the lower surface and because of the downwash effect of the slipstream contraction [4, 37]. Both upwards and downwards, the influence diminishes after a certain offset (between $0.5R$ and $1R$).

The drag shows different trends. The drag is lowest either when the vertical offset is around zero or when the wing is outside the propeller slipstream. These are the local minima for the dynamic pressure impinging on the wing [4]. However, the asymmetry of the drag curves about the vertical axes in Fig. 2.2.3, for the 4 deg cases in particular, indicates that the interaction effects are caused by more than just the dynamic pressure changes. This supports the claim that the upwash and downwash due to slipstream contraction also plays a role.

Figure 2.2.4 shows that the lift-to-drag ratio is greatest when the propeller axis has a positive vertical offset of about one propeller radius to the wing. Later, Sec. 2.2.4

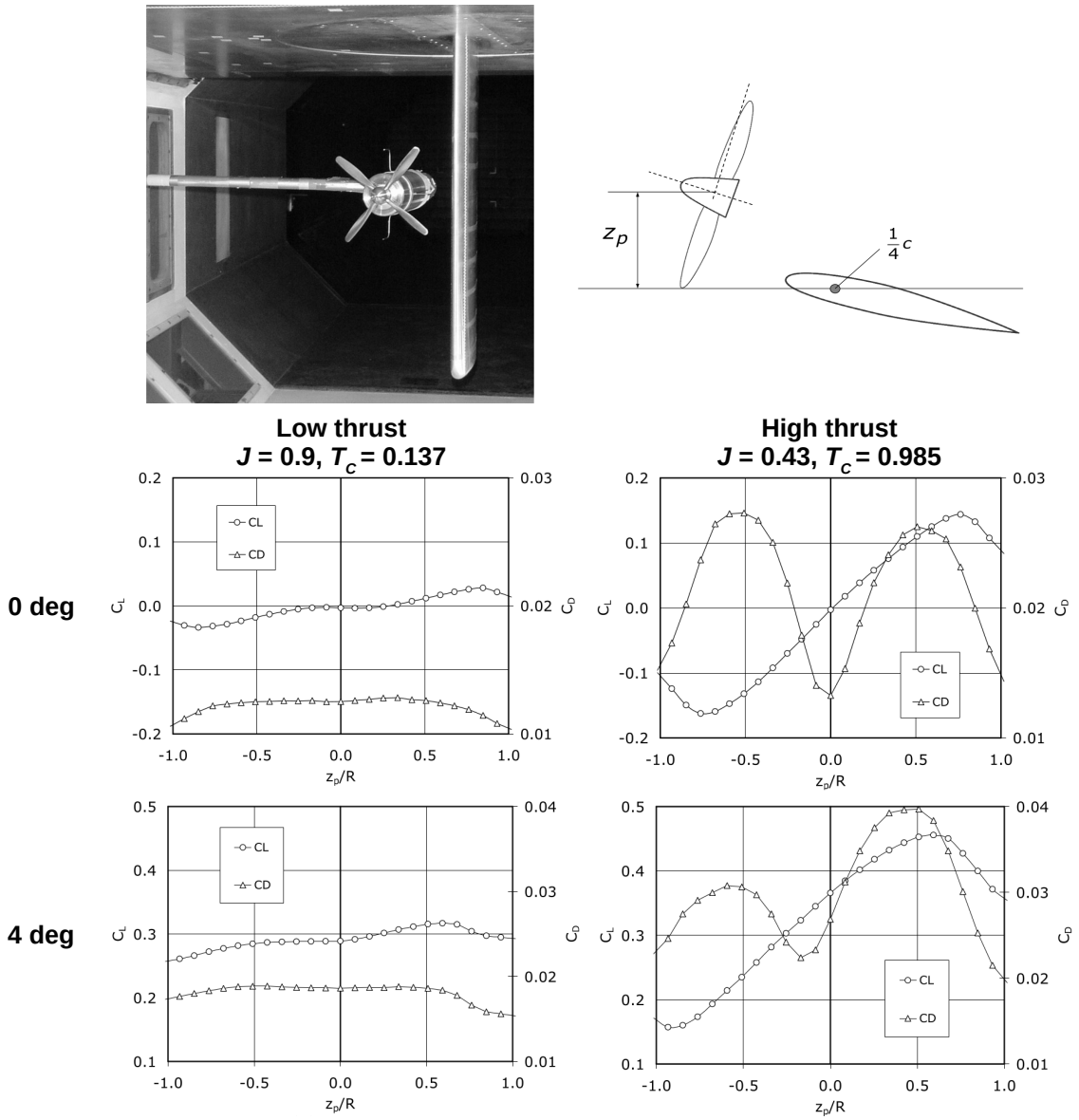

Figure 2.2.3: Experimental results showing the effect of propeller vertical location on wing lift and drag ($y_p/b/2 = 0.28$; figures from Veldhuis [4])

will show that this is not the case for a tip propeller and that the trends with respect to vertical location also depend on the spanwise location of the propeller. Additionally, because the lift and drag trends change with the thrust setting (Fig. 2.2.3), the lift-to-drag ratio trends also change with the thrust setting.

Figure 2.2.3 indicates that the dynamic pressure impinging on the wing is greatest when the propeller is offset by about half a propeller radius [4], and Fig. 2.2.4

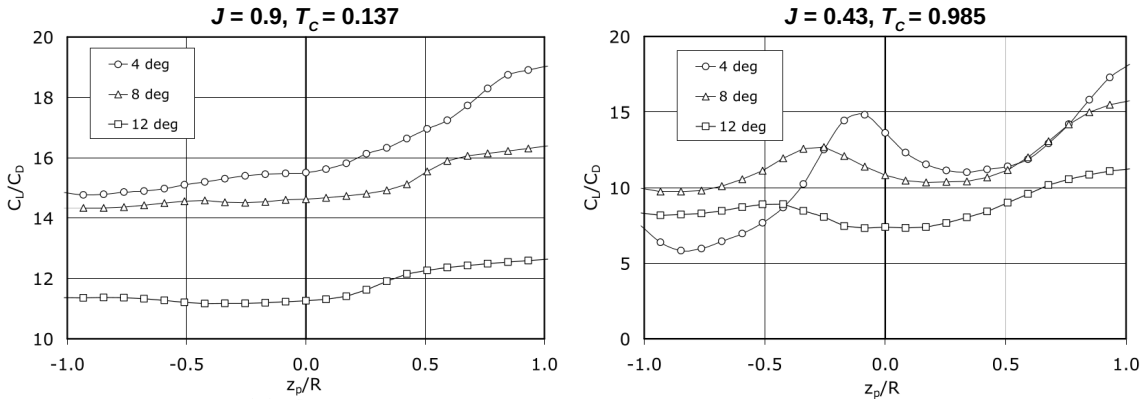

Figure 2.2.4: Experimental results showing the effect of propeller vertical location on wing lift-to-drag ratio ($y_p/b/2 = 0.28$; figures from Veldhuis [4])

shows that the lift-to-drag ratio is greatest when the propeller is offset by about one propeller radius. This suggests that selecting the vertical placement of propellers and simultaneously sizing the wings for STOL aircraft provides an interesting MDO problem because of the tradeoff between low-speed and cruise benefits[§].

2.2.3 Rotation Direction

Propeller-induced velocity components result in spanwise variations of both the effective flow speeds and local angles of attack of the wing sections directly behind the propeller, which further result in the tilting and magnitude change of the local lift vectors. For example, the experimental results from Veldhuis [4] plotted in Fig. 2.2.5 show the time-averaged lift distribution of a wing with an inboard-mounted tractor propeller with inboard-up rotation.

There is a lift peak behind the up-going-blade portion and a trough behind the down-going-blade portion. The corresponding pressure distributions of two wing sections behind the up-going and down-going portions of the propeller are compared in Fig. 2.2.6. For outboard-up rotation, the locations of the peak and trough switch (Fig. 2.2.9a).

[§]This is a suggestion for future work.

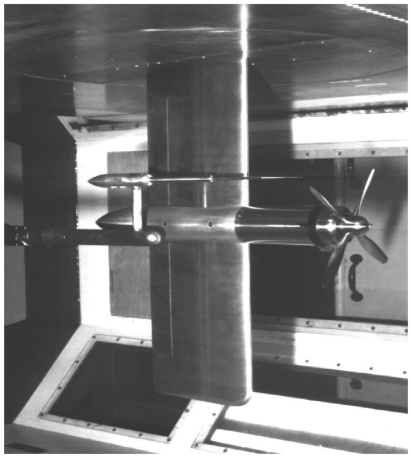

(a) Experimental setup

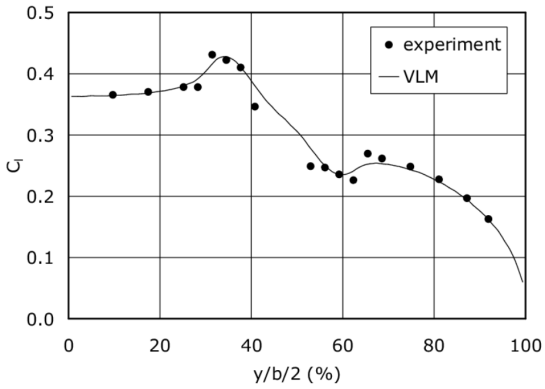

(b) Lift distribution for 4 deg angle of attack

Figure 2.2.5: Experimental lift distribution and VLM results for a wing with a tractor propeller ($J = 0.85$; $T_C = 0.168$; inboard-up rotation; figures from Veldhuis [4])

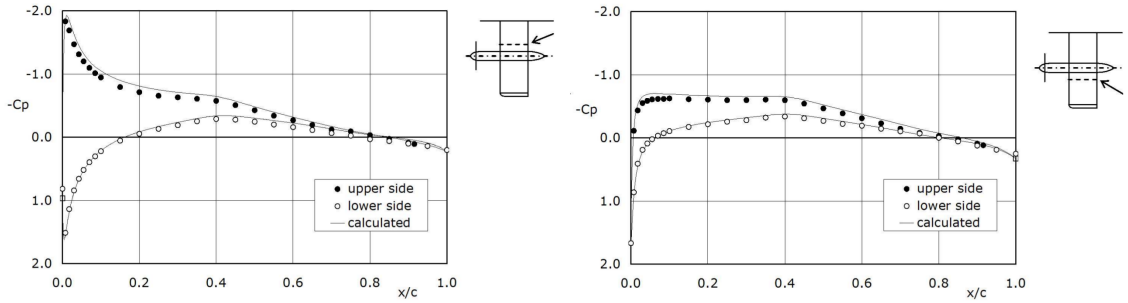

(a) Behind up-going portion

(b) Behind down-going portion

Figure 2.2.6: Experimental pressure distributions and actuator-disk CFD results for a wing with a tractor propeller (these correspond to the case in Fig. 2.2.5; inboard-up rotation; figures from Veldhuis [4])

The influence of propeller-induced axial and tangential velocity components on the lift of wing sections directly behind a propeller is illustrated in Fig. 2.2.7. The upwash behind the up-going-blade portion of the propeller increases the effective local angles of attack and tilts the local lift vectors forwards (i.e., resulting in induced thrust). The downwash behind the down-going-blade portion decreases the effective local angles of attack and tilts the local lift vectors backwards (i.e., resulting in induced drag). The drag distributions computed by Witkowski et al. [6] using a VLM analysis, plotted in Fig. 2.2.8, show an example of this.

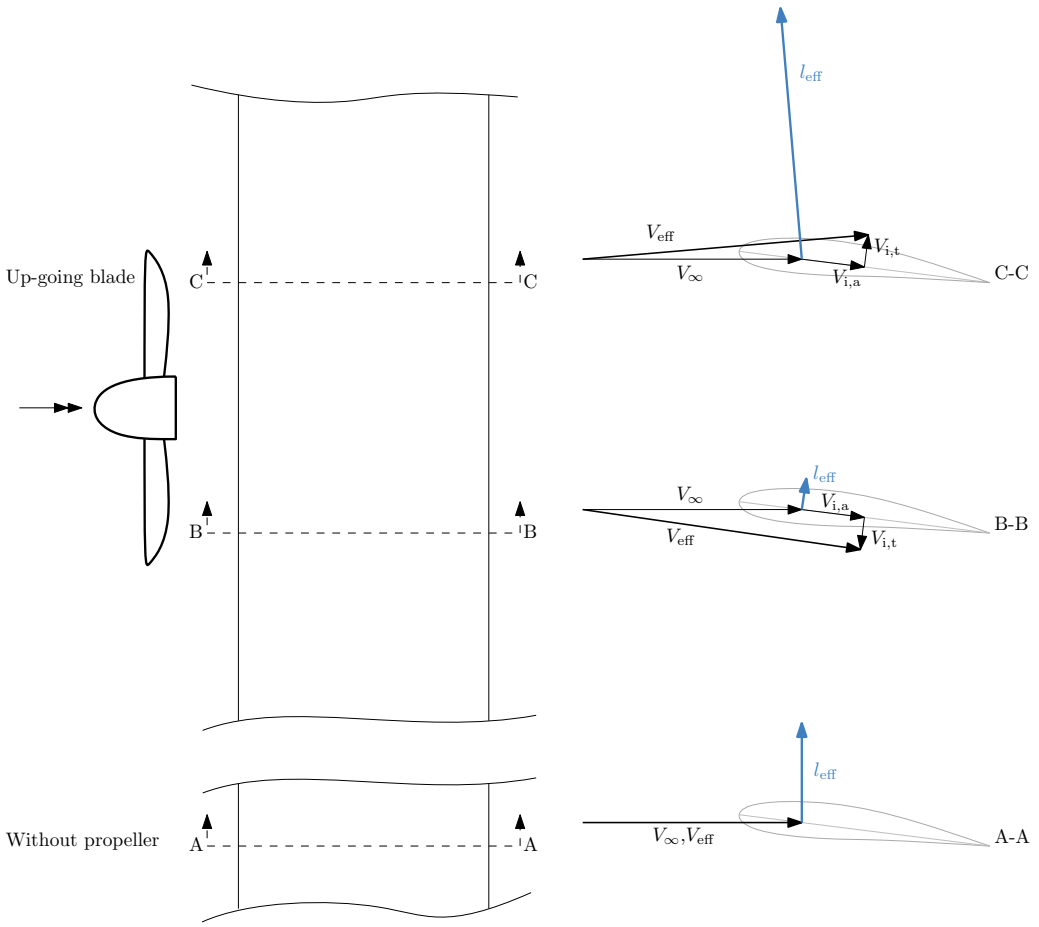

Figure 2.2.7: An illustration of the tilting of local lift vectors due to propeller-induced axial velocity components $V_{\text{i,a}}$ and tangential velocity components $V_{\text{i,t}}$ for an infinite wing. The length of the lift vector l_{eff} for each section is based on the length of the effective velocity vector V_{eff} and the effective angle of attack.

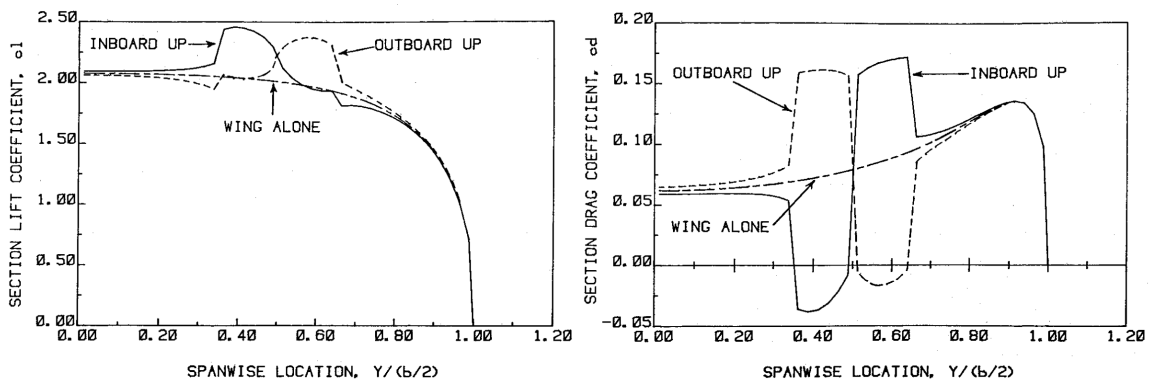

(a) Lift distributions

(b) Drag distributions

Figure 2.2.8: VLM results showing the effect of a tractor propeller's rotation direction on a trailing wing's lift and drag distributions (figures from Witkowski et al. [6])

For a finite wing, whether a net drag reduction (i.e., swirl recovery) is obtained will depend on the wing's lift distribution and on the propeller's rotation direction. Experimental drag coefficients from Veldhuis [4], plotted in Fig. 2.2.9b, show that the net drag is lower with inboard-up rotation. This is a general observation that is consistently found in literature [4, 7, 31, 32]. Wings are generally designed to have greater lift inboard than outboard, and therefore it is advantageous to have upwash where the lift is greater (from a lifting-line point of view, the induced drag is the span integral of the product of the circulation and downwash; in other words, it is more efficient to push down more-upward-moving air).

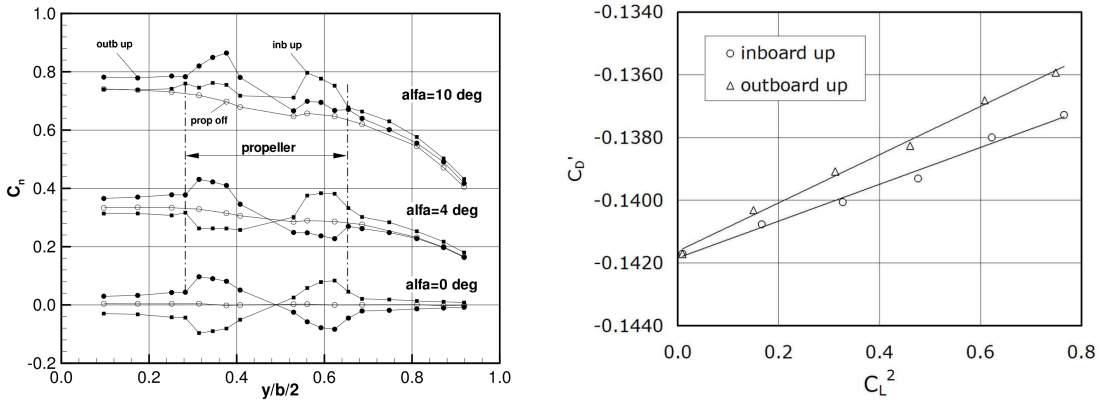

(a) Normal-force coefficient

(b) Drag coefficient reduction ($C_D' = C_{D_{\text{prop on}}} - C_{D_{\text{prop off}}}$)

Figure 2.2.9: Experimental results showing the effect of propeller rotation direction (these correspond to the experimental configuration shown in Fig. 2.2.5a; $J = 0.85$; $T_C \sim 0.17$; figures from Veldhuis [4])

The rotation direction also affects the effective maximum lift coefficient [7, 31]. The experimental results of Sinnige et al. [7] for a wing with a tip-mounted propeller, plotted in Fig. 2.2.10, show this. Not only does inboard-up rotation provide drag reductions, but it also increases the maximum lift that can be obtained.

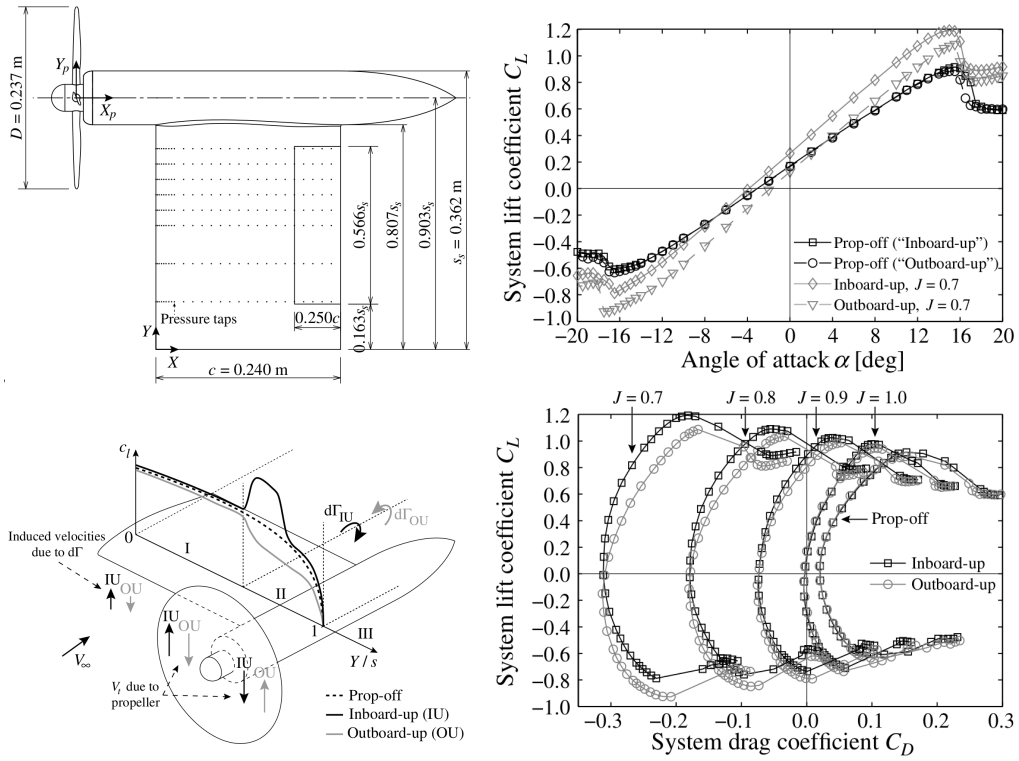

Figure 2.2.10: Experimental results showing the drag and maximum-lift-coefficient benefits of inboard-up rotation (at 0 deg angle of attack, the C_T values that correspond to the J values of 0.7, 0.8, 0.9, and 1.0 are 0.123, 0.095, 0.053, and 0.014, respectively; figures from Sinnige et al. [7])

2.2.4 Spanwise Location

Experimental results from Veldhuis [4], plotted in Fig. 2.2.11, show that moving a tractor propeller (that does not have a vertical offset) inboard starting from the wingtip decreases the trailing wing's lift and increases the wing's drag. The sensitivity to the spanwise location is greater when the propeller is outboard than when the propeller is inboard.

Furthermore, the additional experimental results plotted in Fig. 2.2.12 show that a positive vertical offset may provide the best lift-to-drag ratio for an inboard-mounted tractor propeller, but zero vertical offset may be best for a tip-mounted tractor propeller.

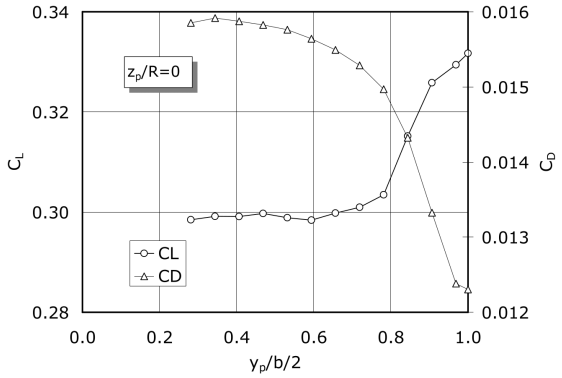

Figure 2.2.11: Experimental results showing the effect of a zero-vertical-offset tractor propeller's spanwise location on a trailing wing's lift and drag ($\alpha = 4.2\,\text{deg}$; $\alpha_{\text{prop}} = 0\,\text{deg}$; $J = 0.92$; $T_{\text{C}} = 0.025$; see Fig. 2.2.3 for the definition of z_{p}; figures from Veldhuis [4])

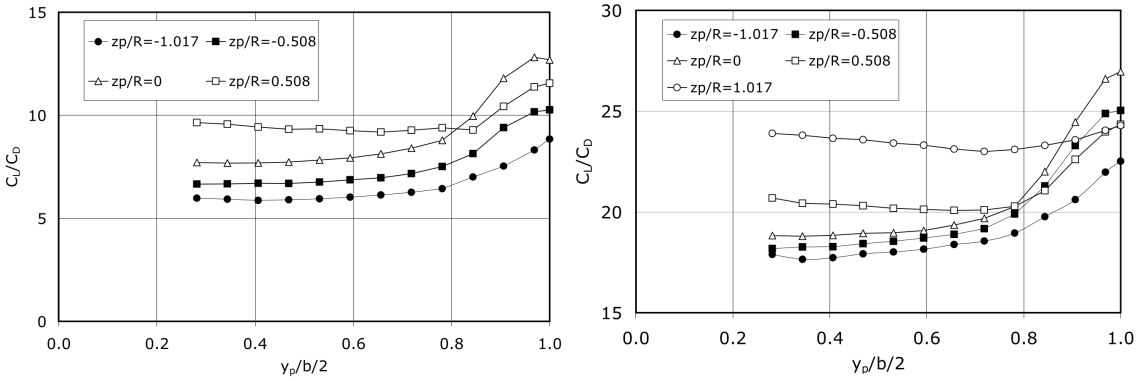

(a) $\alpha = 1.1\,\text{deg}$ (b) $\alpha = 4.2\,\text{deg}$

Figure 2.2.12: These experimental results show that a vertical offset can improve or worsen the performance of a trailing wing depending on the spanwise location of the propeller ($J = 0.92$; $T_{\text{C}} = 0.025$; $\alpha_{\text{prop}} = 0\,\text{deg}$; see Fig. 2.2.3 for the definition of z_{p}; figures from Veldhuis [4])

2.2.5 Thrust Settings

The advance ratio and pitch setting of a propeller affect the thrust generated and its induced velocities, which further affect the performance of a leading or trailing wing [4, 7, 8, 30]. The experimental results of Veldhuis [4], plotted in Fig. 2.2.13a, show that the total lift coefficient (and consequently the lift-curve slope) of a wing with a tractor propeller increases as the thrust is increased. However, these lift coefficients include contributions from the propeller normal force and the vertical component of the propeller thrust, along with the wing-lift augmentation due to the

propeller-induced velocities. Figure 2.2.13b includes a breakdown of these contributions for a 10 deg angle-of-attack case that shows that the lift-increase is not only due to the vertical component of the propeller thrust, but also due to the interaction of the propeller-induced flow with the wing.

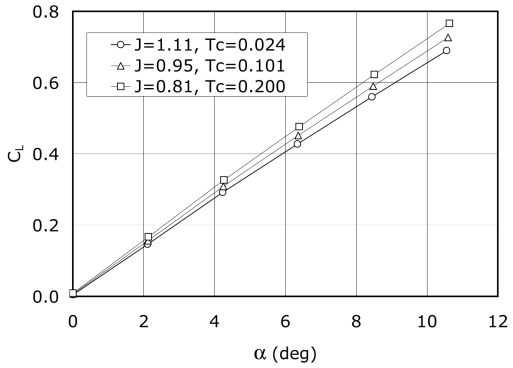

(a) Varying thrust settings

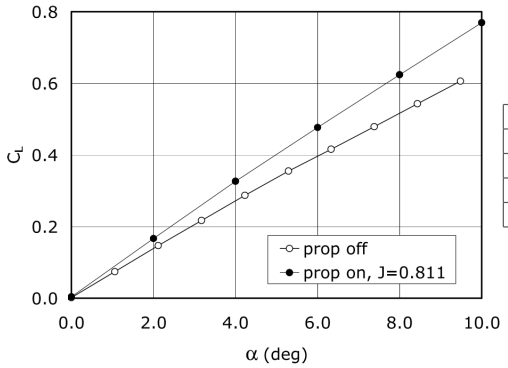

Contributor	ΔC_L	**Rel. contribution**
Propeller normal force	0.012	8.6 %
Vertical thrust component	0.035	25.1 %
Dynamic pressure and loading distr.	0.0924	66.3 %
Total propeller and slipstr. effect	**0.1394**	

(b) Breakdown of the lift increase at 10 deg

Figure 2.2.13: These experimental results show that the lift coefficient and lift-curve slope of a wing in a tractor configuration increase as the thrust setting is increased (zero vertical offset; inboard-up rotation; see Fig 2.2.5a for the experimental configuration; figures from Veldhuis [4])

The experimental results of Sinnige et al. [7], plotted in Fig. 2.2.14, show how the lift distribution of a flapped wing with a tip-mounted tractor propeller changes as the thrust increases. The lift distribution across the entire wing is affected, and, with outboard-up rotation, the lift decreases as the thrust is increased.

The experimental results of Chinwicharnam and Thipyopas [8], plotted in Fig. 2.2.15, show that the maximum lift coefficient of a wing (corrected for the propeller forces)

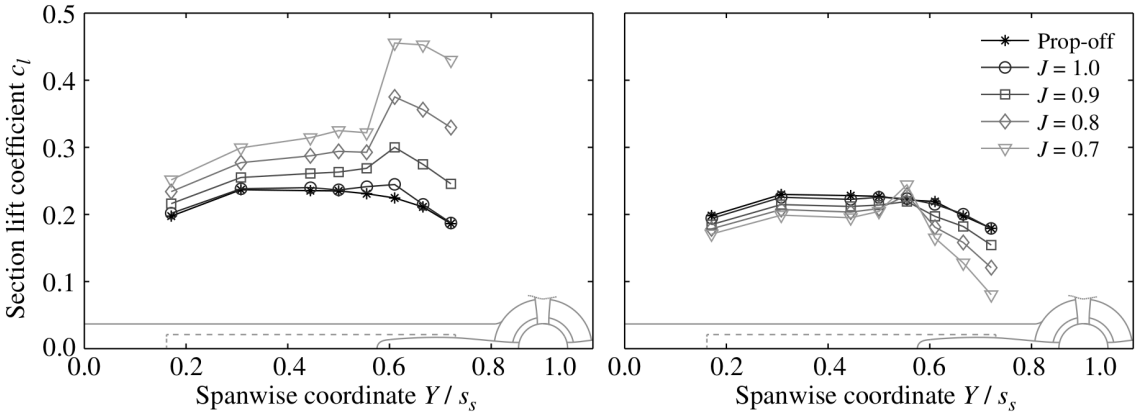

a) Inboard-up **b) Outboard-up**

Figure 2.2.14: Experimental results showing how the lift distribution of a wing with a tip-mounted tractor propeller changes as the thrust is increased (the C_T values that correspond to the J values of 0.7, 0.8, 0.9, and 1.0 are 0.123, 0.095, 0.053, and 0.014, respectively; figure from Sinnige et al. [7])

changes with the thrust setting (a lower advance ratio corresponds to a higher thrust for these cases) for both tractor and pusher configurations. As expected, because the propeller-induced velocities are greater behind a propeller than in front (see Sec. 2.1.1), the maximum lift coefficient is higher for the tractor configuration. Additionally, Fig. 2.2.16 shows how the drag coefficient is affected for these cases. For the high-thrust (low advance ratio) cases, the drag of the tractor configuration is greater than that of the pusher configuration for all angles of attack (as would be expected because of the higher dynamic pressure for the tractor case). However, for the low-thrust cases, the drag of the tractor configuration is not greater for some angles of attack. This suggests that the swirl is also playing a role. Note that these results are for a NACA 0012 flying wing with a single midspan-mounted propeller, and therefore there is no distinction between inboard- and outboard-up propeller rotation as far as the lift and drag are concerned.

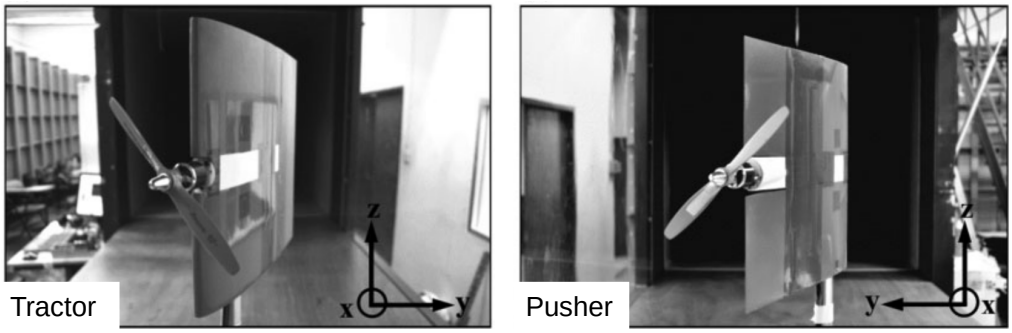

(a) Experimental configuration

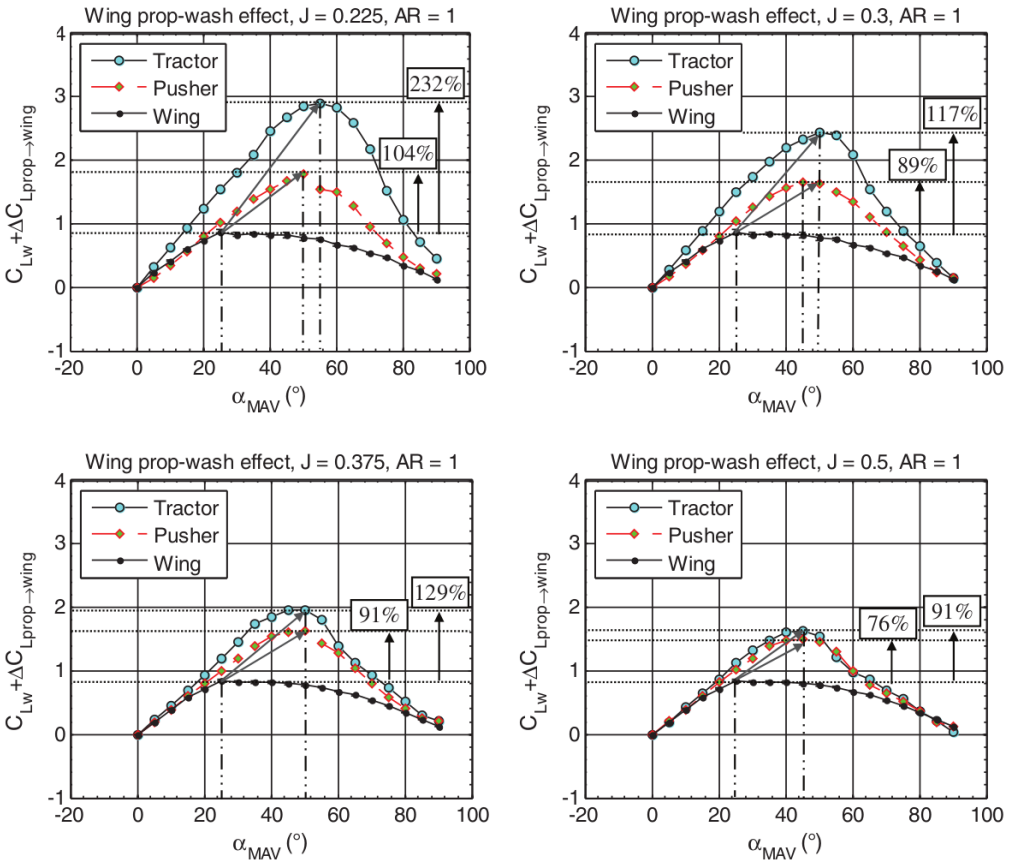

(b) Lift curves

Figure 2.2.15: Experimental results that show how the maximum lift coefficient of a wing (corrected for the propeller forces) changes with the thrust setting (a lower advance ratio corresponds to a higher thrust for these cases) for both tractor and pusher configurations (figures from Chinwicharnam and Thipyopas [8])

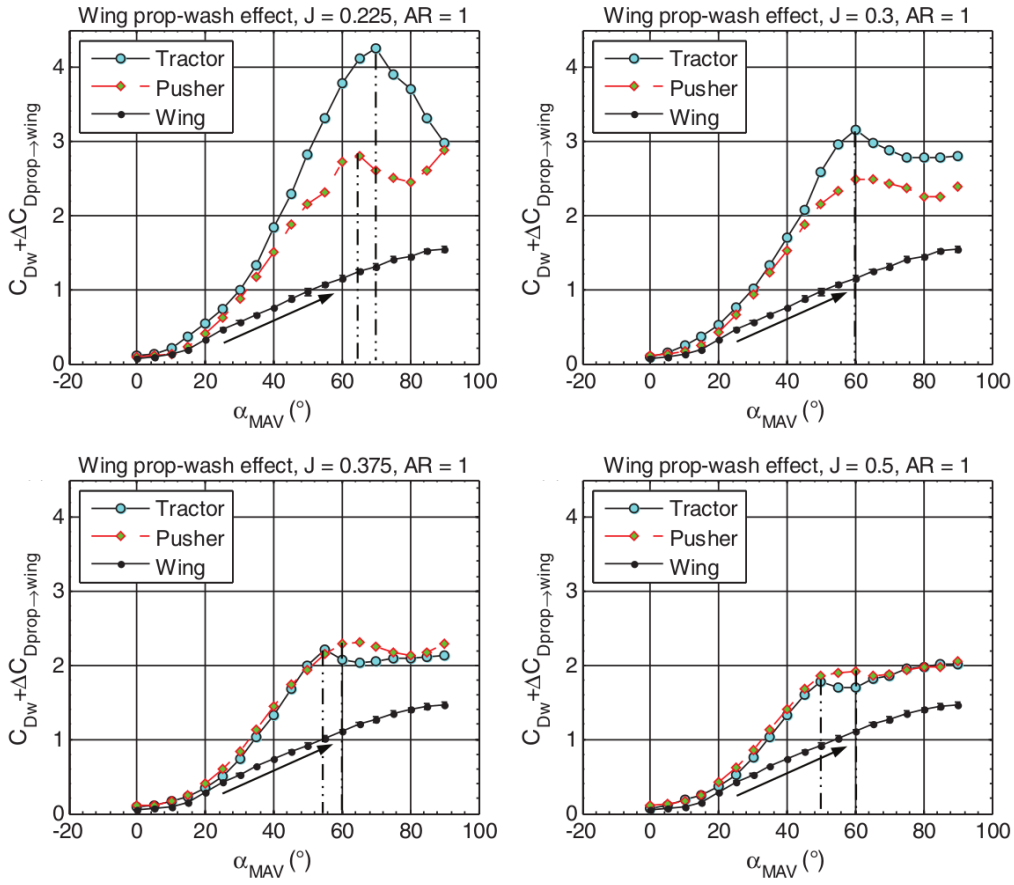

Figure 2.2.16: Experimental results that show how the drag of a wing (corrected for the propeller forces) changes with the thrust setting (a lower advance ratio corresponds to a higher thrust for these cases) for both tractor and pusher configurations (figures from Chinwicharnam and Thipyopas [8])

2.2.6 Complicating Factors

The factors discussed here that affect propeller-wing interaction are not independent (e.g., lift and drag trends with respect to propeller vertical location also depend on the spanwise location, streamwise location, and rotation direction of the propeller). Therefore, this chapter is not a complete review of every trend and effect resulting from every combination, and caution must be exercised when reaching conclusions. However, this chapter does provide a brief, but broad, overview of most of the factors and trends to keep in mind for a tractor configuration.

Additionally, when analyzing changes in the net thrust or drag of an integrated propeller-wing configuration, it is often difficult to identify and separate the contribution from changes in the propeller's thrust and the contribution from changes in the wing's drag. This can complicate the interpretation of experimental data, simulation results, and performance analyses. Therefore, caution must also be exercised with this in mind.

Part I

Tilt-Wing eVTOL Takeoff Trajectory Optimization

CHAPTER 3

Introduction

> I think it is now accepted that the criteria for VTOL transport acceptability is not how much better the aircraft is than a helicopter but how closely its transport effectiveness approaches the airplane's. It was well recognized that the technical challenges for this type [of] aircraft were not at the higher speeds but in the transitional speed regime.
>
> *J. B. Nichols* [43]
> Principal Engineer, Boeing, 1990
> (Formerly with Hiller Aircraft during the development of the tilt-wing Hiller X-18)

Tilt-wing aircraft first received serious attention in the 1950s and 1960s when a few companies including Boeing, Ling–Temco–Vought (LTV), Hiller, and Canadair developed flying prototype aircraft [38–40, 42–45]. Several successful flight tests including transitions between vertical and horizontal flight were carried out [38–40, 42, 44]. Flight-test summaries for the Boeing–Vertol VZ-2 [38] and Canadair CL-84 [42] report that flow separation and wing stall provided piloting and operational challenges. Over 300 hours of flight testing was carried out for the LTV/Hiller/Ryan XC-142 to prove its suitability for operation [40]. Despite the extensive testing, several factors including control and stability challenges and mechanical complexity led to the cancellation of these programs. However, with modern control technology and the advantages of electric propulsion, modern tilt-wing concepts may become viable.

A significant amount of literature also exists from that early period related to the design, performance, and control of tilt-wing aircraft [30, 41, 47, 48, 60, 61]. More recent work has focused on the design and control of smaller tilt-wing unmanned aerial vehicles (UAVs) [18, 62–65].

Transitioning from vertical to horizontal flight for a tilt-wing aircraft is a balancing act in which the propellers have to provide sufficient thrust to support the weight of the aircraft while also tilting with the wings to accelerate the aircraft to a speed and configuration in which sufficient lift can be provided by the wings. This transition is an important consideration for the design of these types of aircraft. Separated flow over the wing, which is undesirable and avoided in conventional aircraft design, is an important concern during the transition for tilt-wing aircraft and may even be beneficial or unavoidable. Johnson et al. [11] briefly mentioned in their conference paper that their analysis for a tilt-wing eVTOL concept suggests that the wing is operating near or just beyond stall during transition. Based on testing for the NASA Greased Lightning GL-10 prototypes, it also seems possible that spending some time with the wing stalled may provide the most energy-efficient transition for a tilt-wing aircraft [18].

Stalling the wing during the transition allows prioritizing acceleration and transitioning to the more efficient airplane configuration more quickly at the cost of some inefficient lift during early stages. However, it is not obvious whether this provides an overall benefit. One of our goals is to examine this for a tandem tilt-wing passenger eVTOL configuration based on the Airbus A^3 Vahana.

There is a lack of studies on the optimal takeoff trajectory for passenger tilt-wing eVTOL aircraft. However, some related research has been carried out on transition optimization for tail-sitter and flying-wing UAVs that take off vertically. Stone and

Clarke [66] carried out numerical optimization studies for the takeoff maneuver of a 23–32 kg tail-sitter twin-propeller wing-canard UAV with the objective of minimizing the time required to transition to forward flight and reach a specified altitude and speed. They limited the angles of attack in their optimization problem to prevent stalling the wing and concluded that it is possible for their UAV to transition without stalling the wing. They also noted that as aircraft mass increases, the optimal takeoff maneuvers have increased angles of attack for greater portions of the maneuver. Another interesting observation from their results is that for larger aircraft masses, the optimal takeoff trajectory involves overshooting the target altitude and then descending to achieve it. In a later paper, Stone et al. [67] also discussed flight-test results for their UAV and noted that, during the vertical to forward-flight transition, the UAV lost altitude instead of gaining altitude as predicted by their simulations.

Kubo and Suzuki [55] numerically optimized the transitions between hover and forward flight for a 2 kg tail-sitter UAV with a twin-propeller twin-boom wing-tail configuration. With the objective of minimizing transition time, and with stall constraints, they obtained an optimized transition from hover to forward flight without noticeable altitude change. They also noted that high throttle settings during the transition help delay stall.

Maqsood and Go [68] numerically optimized transitions between hover and cruise for a small tail-sitter tilt-wing UAV (tractor configuration without distributed propulsion) with the objective of minimizing the altitude variation during transition. They compared optimization results for the hover to forward-flight transition for a configuration with tilting wings and the same configuration with fixed wings. They noted that the optimal transition with a tilting wing avoids stalling the wing, which reduces thrust requirements compared to a fixed-wing configuration.

Oosedo et al. [69] numerically optimized the hover to forward-flight transition for a 3.6 kg quadrotor tail-sitter flying-wing UAV with the objective of minimizing the time required to transition. They compared optimization cases with and without constraints for maintaining altitude. They also compared their simulations to experimental flight tests. All four of the UAVs [55, 66, 68, 69] mentioned here are significantly different from the type of aircraft in which we are interested, due to their configurations and sizes.

Two other related research efforts focused on the landing phase instead. Pradeep and Wei [70] optimized the speed profile and time spent in the cruise, deceleration-to-hover, hover, and descent phases given a fixed arrival time requirement for the Airbus A^3 Vahana configuration. However, they did not model or study the details of the transition from cruise to hover. Verling et al. [57] optimized the transition from cruise to hover for a 3 kg tail-sitter flying-wing UAV.

In the aforementioned optimization studies, relatively low-order models were used for the multiple disciplines involved, because of the complexity of the physics and the high computational cost of higher-order methods. For the aerodynamics, the approaches used for these studies include using a database with aerodynamic coefficients and derivatives from a panel method [66], using airfoil data with corrections [55], and interpolating wind-tunnel data [57, 68, 69]. For propulsion, these studies either used momentum theory and variations of blade-element models [55, 66] or experimental data [69]. For the propeller-wing interaction, all of the above studies that considered it augmented the flow over the wing using induced-velocity estimates based on momentum theory [55, 57, 68], except for Stone and Clarke [66] who connected a blade-element model to a panel-method model and accounted for both axial and tangential induced velocities [54]. For the flight dynamics, representing the air-

craft using a three degrees-of-freedom (DOF) longitudinal model is the common approach [55, 57, 66, 68, 69].

To address the lack of literature on the optimal takeoff trajectory for passenger tilt-wing eVTOL aircraft, we present numerical optimization results for the takeoff-to-cruise phase of a tandem tilt-wing eVTOL configuration based on the Airbus A^3 Vahana. The optimization objective is to minimize the electrical energy required to reach a specified cruise altitude and speed. We aim to answer the following questions:

1. What does the optimal takeoff trajectory including transition and climb (to a cruise altitude and speed appropriate for air-taxi operations) look like?
2. Does the optimal trajectory involve stalling the wings, and, if yes, how much of a benefit does it provide?
3. How does the augmented flow over the wings due to propellers affect the energy consumption and optimal trajectory?
4. How much electrical energy is required?
5. How does the wing size affect the optimal trajectory and energy consumption?
6. How does the maximum available power affect the optimal trajectory and energy consumption?

We use simplified models, gradient-based optimization, and NASA's OpenMDAO framework [71, 72] (a Python-based open-source optimization framework) for the optimizations.

By *simplified models* we mean computationally inexpensive first-principles-based low-order models that capture the primary trends. To model the aerodynamics of the wings, we use a combination of airfoil data, well-known relations from lifting-line theory, and the poststall model developed by Tangler and Ostowari [1]. For the

propulsion and propeller-wing interaction, we use relations from momentum theory and blade-element theory. For the flight mechanics, we use a simplified 2-DOF representation of the aircraft and the forward Euler method for time integration.

The remainder of Part I of this dissertation is organized as follows. In Chapter 4, we describe the mathematical models used for this work. In Chapter 5, we describe the optimization problems (Sec. 5.1), and we present and discuss the optimization results (Sec. 5.2).

CHAPTER 4

Mathematical Models

> Many schemes for VTOL and STOL aircraft employ wings or propellers operating in an angle of attack range of zero to 90°. A prediction of their behavior under these conditions requires a blending of analytical considerations and experimental results. Not only is each problem separately difficult, but the difficulty is compounded when the wing and propeller are interacting with one another.
>
> *B. W. McCormick* [41]
> Professor, Pennsylvania State University, 1967

We use the simplified models described in this chapter for the aerodynamics, propulsion, propeller-wing interaction, and flight-mechanics disciplines. As mentioned earlier, by *simplified models* we mean computationally inexpensive first-principles-based low-order models that capture the primary trends.

4.1 Aerodynamics

Figure 4.1.1 shows the side view of the aircraft configuration that we use for this work. It is a tandem tilt-wing configuration based on the Airbus A^3 Vahana. The configuration has two rectangular tilting wings, each with four propellers in front. The total wing planform area is $9\,m^2$, an estimate based on online images of an Airbus A^3 Vahana full-scale flight-test prototype. For the configuration we model, we assume that the forward and rear wings are identical and have the same reference

area for simplicity. However, note that the actual Airbus A^3 Vahana prototype has a smaller forward wing (approximately 20% smaller than the rear wing based on flight-test prototype images).

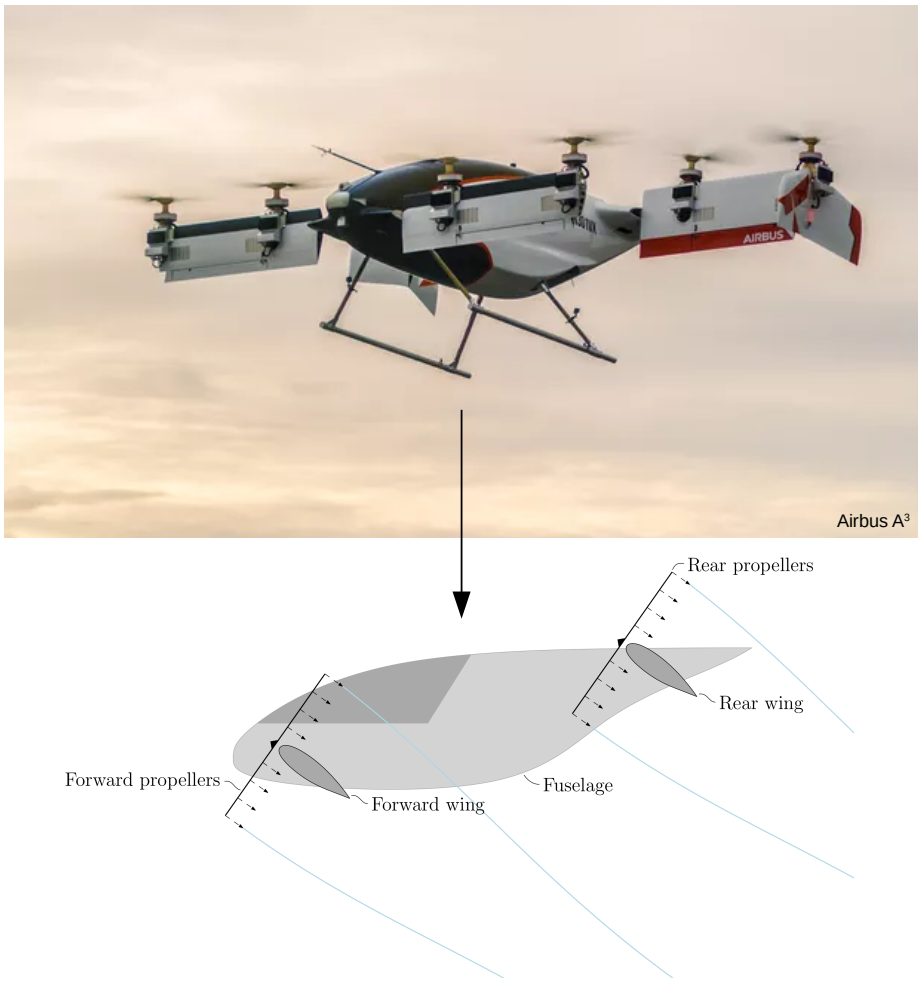

Figure 4.1.1: The VTOL configuration studied is based on the Airbus A^3 Vahana (Vahana image from `https://www.airbus.com` [Accessed: 1 Nov 2020]).

Since separated-flow conditions need to be considered for the transition from vertical to horizontal flight, we require a model for the aerodynamics of the wings that is capable of predicting the lift and drag beyond the linear-lift region. We use a model developed by Tangler and Ostowari [1] for non-rotating finite-length rectangular wings based on experimental data and the model of Viterna and Corrigan [73].

The poststall lift coefficient is given by

$$C_L = A_1 \sin 2\alpha + A_2 \frac{\cos^2 \alpha}{\sin \alpha}, \tag{4.1.1}$$

where

$$A_1 = \frac{C_1}{2}, \tag{4.1.2}$$

$$A_2 = \left(C_{L_\mathrm{s}} - C_1 \sin \alpha_\mathrm{s} \cos \alpha_\mathrm{s}\right) \frac{\sin \alpha_\mathrm{s}}{\cos^2 \alpha_\mathrm{s}}, \tag{4.1.3}$$

and

$$C_1 = 1.1 + 0.018AR. \tag{4.1.4}$$

Here, α is the wing angle of attack, α_s is the angle of attack at stall, C_{L_s} is the lift coefficient at stall, and AR is the wing aspect ratio. Before stall, the airfoil lift and drag are modified using the well-known finite-wing corrections from lifting-line theory for unswept wings in incompressible flow (Eq. (4.1.9)).

Between 27.5 deg and 90 deg, the drag coefficient is given by

$$C_D = B_1 \sin \alpha + B_2 \cos \alpha, \tag{4.1.5}$$

where

$$B_1 = C_{D_\mathrm{max}}, \tag{4.1.6}$$

$$B_2 = \frac{C_{D_\mathrm{s}} - C_{D_\mathrm{max}} \sin \alpha_\mathrm{s}}{\cos \alpha_\mathrm{s}}, \tag{4.1.7}$$

and

$$C_{D_\mathrm{max}} = \frac{1.0 + 0.065AR}{0.9 + t/c}. \tag{4.1.8}$$

Here, C_{D_s} is the drag coefficient at stall, and t/c is the airfoil thickness-to-chord ratio. For the poststall drag coefficient below 27.5 deg, the data points listed in Table 4.1.1 are used.

Viterna and Corrigan [73] and Tangler and Ostowari [1] noted that poststall characteristics are relatively independent of airfoil geometry, which is why we do not see

Table 4.1.1: Poststall drag coefficient data points below 27.5 deg from Tangler and Ostowari [1]

α [deg]	C_D
16	0.100
20	0.175
25	0.275
27.5	0.363

any input directly related to camber in the above equations. Tangler and Ostowari [1] also noted that poststall characteristics are relatively independent of the Reynolds number in the high-Reynolds range. Tangler and Ostowari [1] based their modifications to the Viterna and Corrigan [73] model on finite-length fixed-wing experimental data from Ostowari and Naik [9], who conducted tests at Reynolds numbers ranging from $0.25 \cdot 10^6$ to $1 \cdot 10^6$. This also happens to be a reasonable Reynolds number range for the takeoff phase of the configuration we are looking at ($\sim 0.7 \cdot 10^6$ at hover to $\sim 3.5 \cdot 10^6$ at cruise). The advantage of this model is that it provides reasonable predictions that can be evaluated at very little computational cost.

Figures 4.1.2 and 4.1.3 show comparisons of the Tangler–Ostowari model with experimental data from Ostowari and Naik [9] for rectangular NACA 4415 and NACA 4412 wings. Experimental data for two aspect ratios, 6 and 9, and two Reynolds numbers, $0.25 \cdot 10^6$ and $1 \cdot 10^6$, are included for comparison. The Tangler–Ostowari model provides a reasonable model for the poststall behavior, and one of the limitations is that the poststall drop in lift is not as sharp as in the experimental data.

For the airfoil used by the configuration of interest, we assume the NACA 0012 symmetric airfoil for simplicity. For the prestall aerodynamics, we refer to NACA 0012 experimental data from Critzos et al. [74] and Abbott and Von Doenhoff [75]. We estimated the lift-curve slope from the experimental data collected by Critzos et al. [74] (smooth airfoil at $Re = 1.8 \cdot 10^6$) as $5.9\,\mathrm{rad}^{-1}$ and correct it using the following

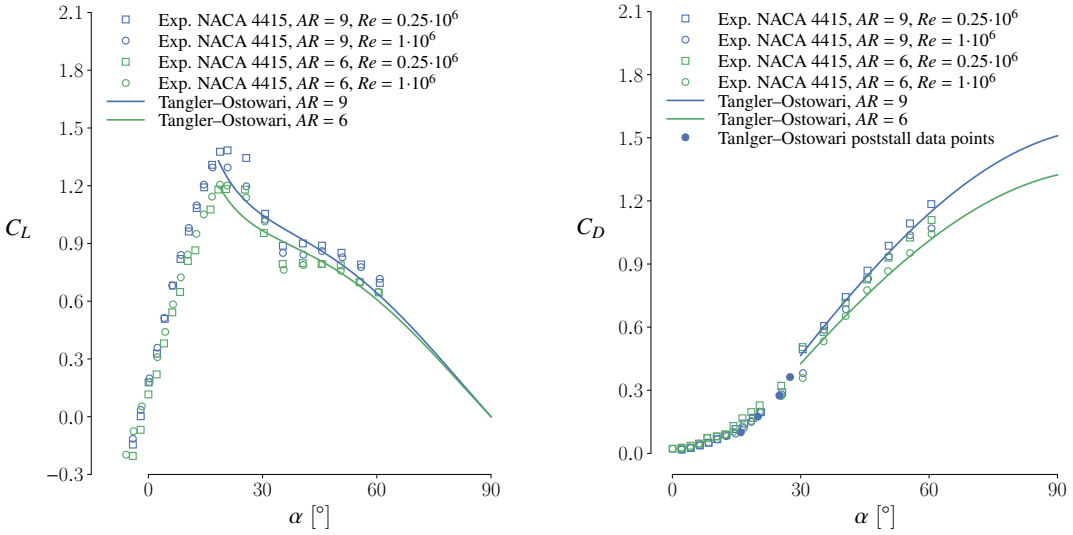

(a) Lift coefficient

(b) Drag coefficient

Figure 4.1.2: Poststall coefficients of lift and drag from the Tangler–Ostowari model compared with experimental data from Ostowari and Naik [9] for rectangular NACA 4415 wings

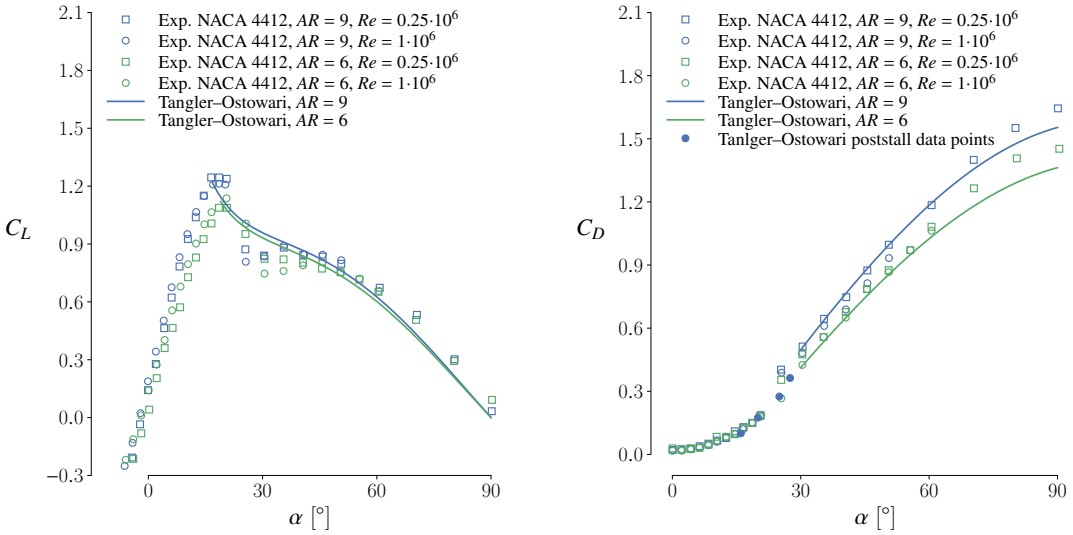

(a) Lift coefficient

(b) Drag coefficient

Figure 4.1.3: Poststall coefficients of lift and drag from the Tangler–Ostowari model compared with experimental data from Ostowari and Naik [9] for rectangular NACA 4412 wings

correction for finite wings based on lifting-line theory:

$$a_{\text{wing}} = \frac{a_{\text{airfoil}}}{1 + \frac{a_{\text{airfoil}}}{\pi ARe}}, \tag{4.1.9}$$

where a_{wing} is the finite-wing lift-curve slope, a_{airfoil} is the airfoil lift-curve slope, and

e is the span efficiency factor. We assume that the prestall lift curve is linear and that the stall angle of attack of the wing is 15 deg.

For each wing's parasite drag before stall, we use airfoil drag coefficient values from the NACA 0012 drag polar provided by Abbott and Von Doenhoff [75] (smooth airfoil at $Re = 3 \cdot 10^6$). The data points we use are listed in Table 4.1.2 under c_{d}. To obtain these c_{d} values from the drag polar, we first related α to the sectional lift coefficient, c_{l}. This was done using $c_{\mathrm{l}} = \alpha \cdot a_{\mathrm{airfoil}}$. Using this relation is not strictly correct because the sectional lift coefficient will vary along the span. However, it gives a reasonable and conservative estimate. To these prestall parasite drag coefficients, we add induced drag using the formula based on lifting-line theory,

$$C_{D_{\mathrm{i}}} = \frac{C_L^2}{\pi A R e}, \tag{4.1.10}$$

to obtain the total drag of the wing before stall. Here $C_{D_{\mathrm{i}}}$ is the induced drag coefficient, C_L is the wing's lift coefficient, and for our configuration $AR = 8$ for each wing.

Table 4.1.2: Prestall drag coefficient data points used for the quartic curve-fit ($AR = 8$)

α [deg]	c_{d} [75]	$C_{D_{\mathrm{i}}}$	$C_D = c_{\mathrm{d}} + C_{D_{\mathrm{i}}}$
0	0.006	0.0	0.006
2	0.0062	0.00137	0.00757
4	0.007	0.00549	0.01249
6	0.008	0.01234	0.02034
8	0.0095	0.02194	0.03144
10	0.012	0.03429	0.04629
12	0.015	0.04937	0.06437

We compute the lift and drag of each wing in the tandem configuration as if they are independent and isolated wings. However, since we have a tandem configuration, we consider some interaction to determine the equivalent span efficiency, e, for each wing to avoid underpredicting drag. Based on the classical work of Munk and Prandtl

[76], the induced drag of a biplane configuration with two identical wings generating the same amount of lift, L_{wing}, is

$$D_{\text{i}} = \frac{1}{\pi q}\left(2\frac{L_{\text{wing}}^2}{b^2} + 2\sigma_{\text{biplane}}\frac{L_{\text{wing}}^2}{b^2}\right), \tag{4.1.11}$$

where q is the freestream dynamic pressure, b is the span, and σ_{biplane} is a factor for the interference between the wings. This assumes that the two wings have elliptical lift distributions. For an equal-span tandem configuration with an effective gap-to-span ratio of 0.25, σ_{biplane} is approximately 0.4 [77].

For our configuration, we assume that with the effects of having a propeller at the wingtip, we can obtain a high span efficiency of approximately 0.95 for each wing in isolation. Assuming an effective gap-to-span ratio of 0.25 (i.e., $\sigma_{\text{biplane}} = 0.4$), and assuming that Eq. (4.1.11) is valid for the assumed high span efficiency of 0.95, the induced drag for the configuration is

$$D_{\text{i}} = 2\left(1.4\frac{L_{\text{wing}}^2}{\pi q b^2 \cdot 0.95}\right) = 2\left(\frac{L_{\text{wing}}^2}{\pi q b^2 \cdot 0.68}\right). \tag{4.1.12}$$

This means that when modeling the biplane as two isolated wings, the effective span efficiency, e, for each wing is approximately 0.68 (i.e., 0.95/1.4). We use this value of e in Eq. (4.1.10) for our computations (computing the lift and drag of each wing as if they were isolated).

Since the Tangler–Ostowari model only provides an analytic equation for the drag coefficient beyond 27.5 deg, we also desire an equation for the drag coefficient below this angle. To obtain an equation for the drag coefficient below 27.5 deg, we fit a quartic polynomial to the C_D values in Tables 4.1.1 and 4.1.2 to obtain

$$C_D = 0.008 + 1.107\alpha^2 + 1.792\alpha^4, \tag{4.1.13}$$

which is a least-squares fit where α is in radians. This curve and the data points are plotted in Fig. 4.1.4.

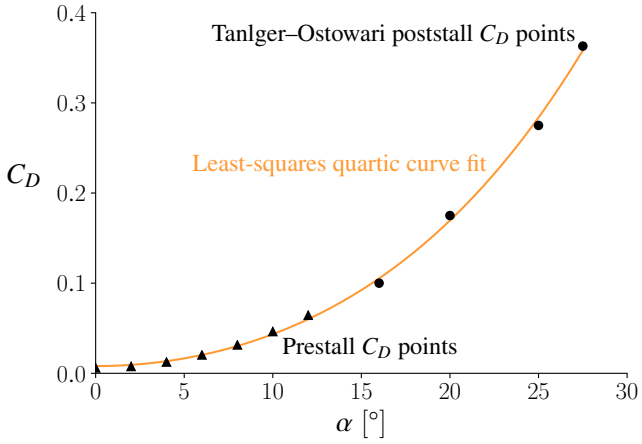

Figure 4.1.4: Least-squares quartic curve-fit for the wing drag coefficient for angles of attack below 27.5 deg

The resulting lift and drag curves for each rectangular wing with $AR = 8$ using the Tangler–Ostowari [1] model are shown in Fig. 4.1.5. Since the curves shown in Fig. 4.1.5 have points at which the slopes are discontinuous, we use Kreisselmeier–Steinhauser (KS) functions [78] to make them C^1 continuous for gradient-based optimization. Figure 4.1.6 shows the regions of the lift and drag curves that are C^1 discontinuous and compares them with the curves from the KS functions that are used to smooth them.

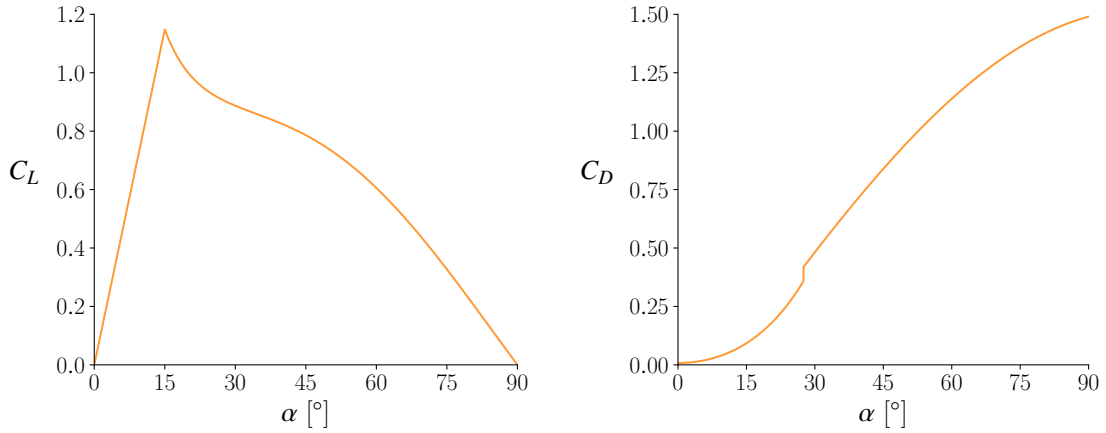

(a) Lift coefficient

(b) Drag coefficient

Figure 4.1.5: Finite-wing ($AR = 8$) coefficients of lift and drag using the Tangler–Ostowari model

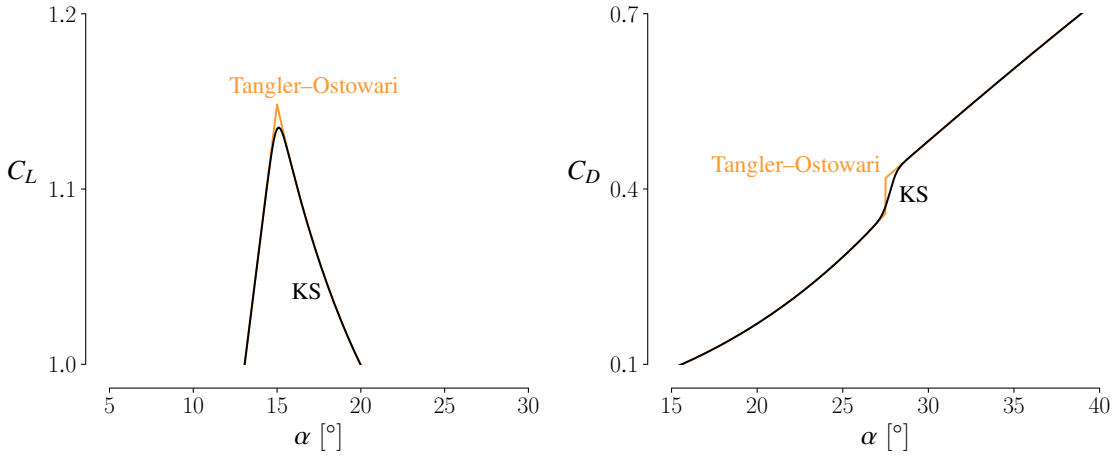

(a) Comparing the C^1-discontinuous part of the lift coefficient curve and the smooth KS curve

(b) Comparing the C^1-discontinuous part of the drag coefficient curve and the smooth KS curve

Figure 4.1.6: C^1-discontinuous lift and drag coefficient curves compared with smooth curves obtained using KS functions

Note that for low flight speeds at the beginning of takeoff, especially for the cases in which there is no flow over the wings from the propellers, the errors of this model may be significant due to the different behavior of flow at low Reynolds numbers [79].

This approach for modeling the aerodynamics of the wings is similar in nature to the approach used by Kubo and Suzuki [55], which uses airfoil data that includes poststall angles (-180 deg to 180 deg). However, it is not clear how they corrected the airfoil data for finite-wing effects. As mentioned in Chapter 3, the other approaches used in studies similar to this work include using a database with aerodynamic coefficients and derivatives from a panel method [66] and interpolating wind-tunnel data [57, 68, 69].

We have not come across the use of the Tangler–Ostowari [1] model in prior research related to airplane performance and design. However, this is not surprising because these relations are for the poststall behavior of rectangular wings. Airplane performance and design usually does not require modeling poststall behavior, and for the cases that do, the wings are usually not rectangular or in uniform freestream

flow. The advantage of using the approach described here, over methods such as panel methods and Reynolds-averaged Navier–Stokes (RANS) based computational fluid dynamics (CFD), is that it provides reasonable predictions at very low cost due to the use of analytic equations. Additionally, obtaining accurate stall and poststall predictions with higher-order methods such as panel methods and RANS-based CFD is a major challenge [80–85].

To the drag computed for the wings using the equations described so far, we further add drag based on an assumed drag area of $0.35\,\mathrm{m}^2$ for the fuselage and fixed landing gear, which is the value used in the open-source trade-studies code* shared by the Airbus A^3 Vahana team. We also assume that this coefficient for the fuselage and landing gear is independent of the freestream angle of attack and that the fuselage does not contribute any additional lift except the lift computed for the portions of the wing planforms that overlap with the fuselage.

As discussed earlier, we assume that both of the wings in our tandem configuration are identical. Apart from the interaction considered when computing the effective span efficiency for each wing, we assume that there is no interaction of flow between the two wings. We also assume that the two wings rotate identically, so this means that the angles of attack experienced by the two wings are assumed to be identical, and so are the lift and drag that they generate. Additionally, we assume that the wings are located forward and aft of the center of gravity (CG) such that their moments are always balanced and ignore any fine-tuning required for trim and stability. In reality, even with symmetric airfoils and identical, vertically offset wings located with their quarter-chords equidistant from the CG, the forces and moments on the wings will not be identical, and the aircraft will not stay perfectly balanced

*`https://github.com/VahanaOpenSource/vahanaTradeStudy`[Accessed: Dec 2018]

due to several factors including upwash and downwash, propeller interactions, CG movement, and fuselage moments. However, we assume their effects to be small and also neglect the effects of any rotation caused by them on the forces on the aircraft.

4.2 Propulsion

To compute thrust from the propellers as a function of power, we use the following relation based on momentum theory:

$$P_{\text{disk}} = TV_{\infty\perp} + \kappa T \left(-\frac{V_{\infty\perp}}{2} + \sqrt{\frac{V_{\infty\perp}^2}{4} + \frac{T}{2\rho A_{\text{disk}}}} \right), \tag{4.2.1}$$

where P_{disk} is the power supplied to the propeller disk excluding profile power, T is the thrust, $V_{\infty\perp}$ is the component of the freestream velocity normal to the propeller disk, ρ is the air density, A_{disk} is the disk area of the propeller, and κ is a correction factor to account for induced-power losses related to non-uniform inflow, tip effects, and other simplifications made in momentum theory ($\kappa = 1$ for ideal power). We use power as a design variable in the optimization problems studied in this work and use the Newton–Raphson method to solve this nonlinear equation for thrust, with power as an input. The propeller radius assumed for our configuration is 0.75 m, an estimate based on online images of an Airbus A^3 Vahana full-scale flight-test prototype, which translates to a total disk area of 14.1 m^2 for eight propellers. For κ, we assume a value of 1.2.

The equations of momentum theory are typically derived and used for propellers with purely axial inflow [41], which is not the case in general for a tilt-wing aircraft. Using the freestream velocity component normal to the propeller disk, as done here, satisfies the simplified control-volume analysis used to derive the equations (see Appendix A.1 for the derivation). However, the sources of error in the predictions increase. Momentum theory requires several assumptions including assuming that

the inflow and the propeller loading are radially and azimuthally uniform. For a propeller with purely axial inflow, the flow and loading are not radially uniform in reality, and when there is an angle of incidence to the freestream flow, they are not azimuthally uniform either. Still, Eq. (4.2.1) provides idealized estimates for the power required for a given amount of thrust, which we roughly correct using the κ factor and profile-power estimates described later.

Glauert [86] derived another modified version of momentum theory for cases in which the freestream flow is not normal to the disk. Glauert's modified derivation is based on the observation that the induced velocity of a rotor in forward flight, when the freestream velocity component parallel to the rotor axis is small, corresponds more closely to the induced velocity of a wing than that of a typical propeller [86]. We do not use Glauert's modified version of momentum theory because we consider it to be more appropriate for edgewise flight although it gives similar, but slightly higher (0 to 10%; see Appendix A.2 for plots), thrust predictions for the combinations of incidence angle, speed, and power in which we are interested.

To estimate the thrust and power of a propeller at moderate and high incidence as a function of advance ratio and blade pitch setting, de Young [87] provides semi-empirical relations for the ratios of thrust and power for a propeller at incidence to the thrust and power with zero incidence for an advance ratio corresponding to the freestream velocity component normal to the propeller. These relations, and the experimental data that they are informed by, show that as the incidence angle increases, the thrust and power both generally increase for a given advance ratio and blade pitch setting. For the range of incidence angles and advance ratios that we expect, and with a rough range of blade pitch settings that we can expect, our estimates using the equations from de Young [87] show that the thrust-to-power ratio

for the propellers at incidence to the thrust-to-power ratio with zero incidence for an advance ratio corresponding to the freestream velocity component normal to the propellers remains close to 1 ($\sim$ 1.0 to 1.05). This gives us further confidence that the approach we use to estimate thrust as a function of power, which is based on the freestream velocity component normal to the propeller, provides reasonable trends.

For an estimate of profile power, we use

$$C_{P_\mathrm{p}} = \frac{\sigma C_{\mathrm{d}_{0\mathrm{p}}}}{8}(1 + 4.6\mu^2), \tag{4.2.2}$$

which is a formula based on blade-element theory for a rotor in non-axial forward flight [41, 46]. Here, C_{P_p} is the coefficient of profile power defined as $C_{P_\mathrm{p}} = P_\mathrm{p}/(\rho A_\mathrm{disk} R^3 \Omega^3)$, where P_p is the profile power, R is the radius of the propeller, and Ω is the angular speed. Additionally, σ is the solidity, $C_{\mathrm{d}_{0\mathrm{p}}}$ is a representative constant profile-drag coefficient, and μ is defined as $V_{\infty\parallel}/(\Omega R)$ where $V_{\infty\parallel}$ is the component of the freestream velocity parallel to the disk. This provides a rough estimate for profile power that also has a dependence on the incidence angle of the propeller. For Ω, we assume that the propellers are variable-pitch propellers that operate at a constant angular speed corresponding to a tip speed of Mach 0.4 at hover for relatively low-noise operation, this gives a value of Ω =181 rad/s for $R = 0.75\,\mathrm{m}$. For the representative blade chord, we use an estimate of 0.1 m based on Airbus A^3 Vahana flight-test prototype images, which translates to a solidity of 0.13 for each three-bladed propeller. For $C_{\mathrm{d}_{0\mathrm{p}}}$, we assume a value of 0.012. The approach of using momentum theory and a profile-power formula to model the performance of a tilting propeller is described by McCormick [41] and compared with experimental data to show good agreement.

With electrical power as an input, we compute P_{disk} as

$$P_{\text{disk}} = 0.9P_{\text{electrical}} - P_{\text{p}}, \tag{4.2.3}$$

where $P_{\text{electrical}}$ is the power from the batteries. We use the 0.9 factor to account for electrical and mechanical losses related to the batteries, electrical systems, and the motors. For the optimization problems, we limit the maximum available electrical power to 311 kW. This is the electrical power, calculated using Eqs. (4.2.3) and (4.2.1), required to achieve a total thrust equal to 1.7 times the weight at hover (the 1.7 factor is taken from the Airbus A^3 Vahana design process blog[†]). We also assume that the axes of rotation of the propellers line up with the chord lines of the wings.

When the freestream flow is not normal to the propeller disks, the propellers will also generate forces normal to their axes. We estimate these normal forces using empirical formulas from de Young [87]. The normal force is calculated as

$$N = \frac{4.25\sigma_{\text{e}} \sin(\beta + 8^\circ) f q_\perp A_{\text{disk}}}{1 + 2\sigma_{\text{e}}} \tan \alpha_{\text{in}}, \tag{4.2.4}$$

where β is the blade pitch angle at $0.75R$, $q_\perp$ is the dynamic pressure based on the freestream velocity component normal to the propeller disk, A_{disk} is the propeller disk area, and α_{in} is the propeller incidence angle. The other terms are computed as follows. The effective solidity σ_{e} is defined as

$$\sigma_{\text{e}} = \frac{2Bc_{\text{b}}}{3\pi R}, \tag{4.2.5}$$

where B is the number of blades per propeller, c_{b} is the average chord length of the blades, and R is the propeller radius. The thrust factor f is defined as

$$f = 1 + \frac{\sqrt{1 + T_{\text{c}}} - 1}{2} + \frac{T_{\text{c}}}{4(2 + T_{\text{c}})}, \tag{4.2.6}$$

[†]`https://vahana.aero/vahana-design-process-part-ii-preparing-for-lift-off-a75b7ef6d583`[Accessed: Dec 2018]

where T_c is a thrust coefficient defined as $T_c = T/(q_\perp A_{\text{disk}})$, and T is the thrust. For rough values of β to use in Eq. (4.2.4), we assume that the blade pitch angle changes linearly from 10 deg at a flight speed of 0 m/s to 35 deg at the cruise speed of 67 m/s (i.e., linearly with advance ratio with a fixed rotation speed). For most propeller aircraft, the incidence angles of the propellers during normal operation are small, and the resulting normal forces are also small and can be neglected, especially during early performance studies. For some of our cases, the incidence angles will be relatively large during transition (up to ~ 30 deg). However, since the flight speeds will be relatively low during transition, the normal forces generated will still be small in comparison to the thrust forces and weight of the aircraft.

As mentioned in Chapter 3, blade-element methods are commonly used to model the performance of propellers [55, 59, 66]. We use momentum theory instead of blade-element methods because it provides reasonable predictions and captures the primary trends (e.g., the decrease in thrust with increase in flight speed) at very low computational cost. If we desired higher accuracy and wanted to take the geometry and pitch settings of specific blades and propellers into consideration, blade-element methods would be an option.

4.3 Propeller-Wing Interaction

Accurately modeling the interaction between the flow induced by propellers and a wing is complicated and an area of active research due to its complexity [5, 17, 20, 22, 88–91]. In order to account for this interaction in a simple manner, we once again turn to momentum theory. According to momentum theory, a propeller increases the axial component of the flow velocity in its streamtube to $V_{\infty\perp} + v_i$ at the propeller disk and to $V_{\infty\perp} + 2v_i$ at a distance far downstream of the disk. The induced speed

at the disk, v_i, is given by

$$v_\mathrm{i} = -\frac{V_{\infty\perp}}{2} + \sqrt{\frac{V_{\infty\perp}^2}{4} + \frac{T}{2\rho A_\mathrm{disk}}}. \tag{4.3.1}$$

The induced speed far downstream of the propeller, $2v_\mathrm{i}$, gives us an upper bound for the effective increase in flow speed downstream of a propeller. In reality, since this model is based on many simplifications, including neglecting viscous effects and assuming uniform flow, it is practically impossible for the effective flow speed experienced by a wing behind a propeller to increase by this value. However, this provides a range within which the increased effective speed experienced by a wing will be. To account for the propeller-wing flow interaction in our simulations, we increase the chordwise component of the freestream velocity for the entire wing by a range of factors k_w, between 0 and 200%, multiplied by the induced speed at the disk v_i.

According to Selig [59], when the aircraft speed is low and the propellers are highly loaded, the wake of the propeller is similar to a free jet and the wake speed within a few propeller diameters can be assumed to be the same as the speed at the disk (i.e., $k_\mathrm{w} \approx 100\%$). For higher speeds when the propellers are lightly loaded, the contraction of the streamtube occurs within a few disk diameters [59] and the additional speed of the wake will be between v_i and $2v_\mathrm{i}$ (i.e., $100\% < k_\mathrm{w} < 200\%$) within a few disk diameters.

For the wings of configurations like the Airbus A^3 Vahana, since the wakes of the propellers do not completely and uniformly envelop the entire wing, and due to other simplifications made in the momentum theory, the effective k_w for the wing, especially at low speeds, is likely to be less than but close to 1. However, since this is difficult to predict accurately, especially for the range of incidence angles and freestream speeds expected, we look at a wide range of k_w values (0 to 200%) to study its impact on the optimization results.

We neglect any interaction between the forward and rear propellers, any interaction between the wakes of the forward propellers and the rear wing, and any interaction between the forward wing and the streamtubes of the rear propellers. Because of the vertical separation of the wings, and because the wing angles for the takeoff phase will primarily lie between 0 and 90 deg to the horizontal, no significant flow interaction is expected.

This approach of augmenting the flow over the wings using the induced-velocity estimate from momentum theory with adjustment factors is common practice [55–57, 59, 68, 69]. However, one difference in our approach is that we consider a range of induced-velocity factors instead of assuming a particular value or using a particular value from a formula, such as the one for streamtube contraction provided by McCormick [41]. This allows us to study how the flow augmentation impacts the optimization results.

4.4 Dynamics

To simulate the trajectory of the aircraft, we use a 2-DOF representation and the forward Euler method. The angles and forces are illustrated in Fig. 4.4.1. We solve for the aircraft's horizontal and vertical velocity components as a function of time given the control variables, which are the wing-tilt angle and electrical power. The horizontal velocity component at each time step is computed as

$$V_{x_{i+1}} = V_{x_i} + \frac{T\sin\theta - D_{\text{fuse}}\sin(\theta+\alpha_\infty) - D_{\text{wings}}\sin(\theta+\alpha_{\text{EFS}}) - L_{\text{wings}}\cos(\theta+\alpha_{\text{EFS}}) - N\cos\theta}{m}\Delta t, \tag{4.4.1}$$

where i is the index of the time step, Δt is the length of each time step, θ is the wing angle relative to the vertical, α_∞ is the freestream angle of attack, α_{EFS} is the effective freestream angle of attack experienced by the wings due to the propellers,

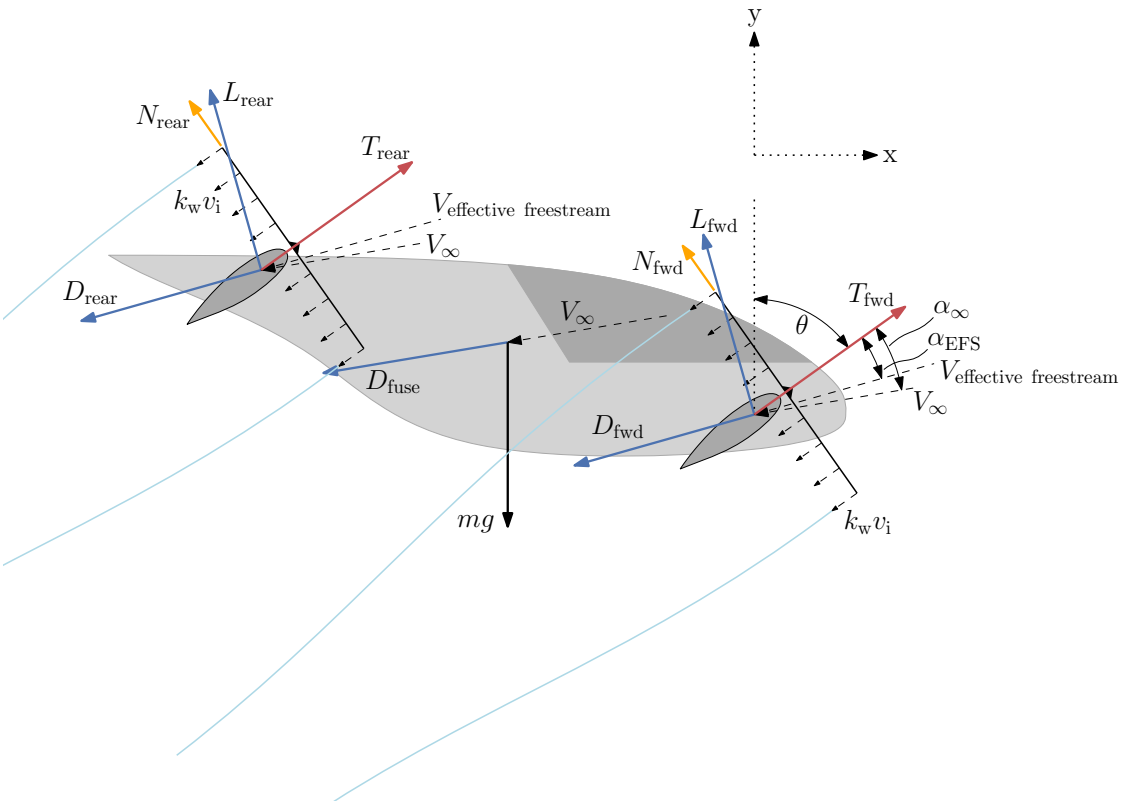

Figure 4.4.1: Angle definitions and forces on the aircraft

m is the mass of the aircraft, T is the total thrust, D_{fuse} is the drag of the fuselage, D_{wings} is the total drag of the two wings, L_{wings} is the total lift of the two wings, and N is the total normal force from the propellers. As mentioned earlier, we assume that the two wings are identical and rotate and behave identically. Similarly, the vertical velocity component at each time step is computed as

$$V_{y_{i+1}} = V_{y_i} + \frac{T\cos\theta - D_{\text{fuse}}\cos(\theta+\alpha_\infty) - D_{\text{wings}}\cos(\theta+\alpha_{\text{EFS}}) + L_{\text{wings}}\sin(\theta+\alpha_{\text{EFS}}) + N\sin\theta - mg}{m}\Delta t, \tag{4.4.2}$$

where g is the acceleration due to gravity.

The time-step length Δt is computed as the flight time (which is a design variable in our optimization problem formulation) divided by 500. As we will see later, the flight times for the optimized takeoffs are less than 50 s, this translates to time steps less than 0.1 s. Based on step-size convergence studies, we found that this is a

sufficiently small time-step range.

The common approach used in the related optimization studies cited in Chapter 3 is to represent the aircraft using a 3-DOF model (two displacements in the longitudinal plane and one pitch angle) [55, 57, 66, 68, 69]. However, we take advantage of our tandem configuration and reduce the number of DOF to two. As discussed earlier in Sec. 4.1, we assume that the wings are located forward and aft of the CG and rotate identically, such that their moments are always balanced (or at least that the effects of any imbalanced moments are negligible). We also ignore any fine-tuning that would be required in reality for trim and stability. Additionally, we assume that the pitching moments generated by the fuselage and propellers, and the reaction moments generated when the actuators rotate the wings are negligible, and neglect the effects of any rotation caused by these on the forces on the aircraft. This gives the simplified 2-DOF model (vertical and horizontal displacements only) described here.

CHAPTER 5

Optimization Problem Formulations and Results

> In general, first order effects establish the soundness of a design, second order effects define the elegance of a design, and third order effects produce PhD papers.
>
> *J. B. Nichols* [43]
> Principal Engineer, Boeing, 1990
> (Formerly with Hiller Aircraft during the development of the tilt-wing Hiller X-18)

5.1 Optimization Problem Formulations

Table 5.1.1 summarizes the baseline optimization problem formulation that we use. Table 5.1.2 lists additional constraints that are added for some of the cases.

Table 5.1.1: Baseline optimization problem formulation

	Function/variable	Note	Quantity
minimize	electrical energy consumed		
with respect to	wing angle to vertical	B-spline parameterized using 20 control points	20
	electrical power	B-spline parameterized using 20 control points	20
	flight time		1
		Total design variables	**41**
subject to	final altitude $\geq 305\,\mathrm{m}$	Uber-specified cruise altitude	1
	final horizontal speed $= 67\,\mathrm{m/s}$	Uber-specified cruise speed	1
	altitude ≥ 0		1
		Total constraint functions	**3**

The objective is to minimize the electrical energy consumed to reach an altitude of 305 m and a cruise speed of 67 m/s. These altitude and cruise-speed specifica-

Table 5.1.2: Additional constraints used for some of the optimization cases

Function/variable	Note	Quantity
angle of attack $\leq 15\,\text{deg}$	Positive stall-angle constraint	1
angle of attack $\geq -15\,\text{deg}$	Negative stall-angle constraint	1
acceleration magnitude $\leq 0.3\,g$	Acceleration constraint	1
final horizontal displacement $= 900\,\text{m}$	Horizontal-displacement requirement	1

tions are taken from the mission requirements shared by Uber Elevate in 2018*†. We also use an altitude constraint to ensure that the aircraft does not fall below an altitude of 0 m. The additional constraints are stall constraints to keep the effective freestream angle of attack of the wings between -15 and 15 deg (our assumed stall angles of attack), an acceleration constraint for passenger comfort, and a horizontal-displacement requirement for consistent energy comparisons. The acceleration and horizontal-displacement constraint values will be explained further in later sections. To avoid defining constraint functions for altitude, wing angle of attack, and acceleration at each time step, we use KS functions to aggregate [92, 93] the constraints. Therefore, instead of 501 constraint functions each (recall that 500 is the number of time steps) for the altitude, positive stall, and negative stall constraints, we have one function for each. Note that the KS functions provide conservative values for the quantities being constrained. This means that the constrained values will not lie exactly on the constraint limits when it is optimal to do so. However, we select parameters for the KS functions that keep the level of conservativeness low, allowing the constrained values to approach the constraint limits closely which will be visible in the optimization results.

The design variables are the angle of the wings (same for both wings), the total electrical power (all propellers are identical and receive the same power), and the

*https://www.uber.com/info/elevate/ecrm/[Accessed: Dec 2018]

†https://s3.amazonaws.com/uber-static/elevate/Summary+Mission+and+Requirements.pdf[Accessed: Dec 2018]

flight time. Since the wing angle and electrical power are continuous functions of time, we parameterize them using 4^{th}-order B-splines with 20 evenly spaced control points each (comparisons of optimization results using 5 to 40 control points are included in Sec. 5.2). These B-splines span the input flight time, which is why the flight time is also a design variable. This simple but unconventional approach to trajectory optimization is inspired by wing design optimization [34, 94] (see Table 12.7.1 for an example of a similar optimization problem formulation used for wing design optimization; instead of flight time, the B-splines span the wing span). The bounds for the wing-angle control points are 0 and 135 deg to the vertical, the bounds for the electrical-power control points are 1 and 311 kW, and the bounds for the flight time are 5 and 60 s. The initial velocity is 0 m/s in the horizontal direction and 0.01 m/s in the vertical direction (a small initial speed so that the angle of attack is defined at the initial condition). The initial altitude is 0.01 m (a small positive value so that the altitude constraint is not violated by the initial condition). These initial values can be interpreted either as starting from rest on the ground or starting from rest in a hover state at some baseline altitude.

We use the OpenMDAO optimization framework [71, 72] (version 2.6.0) and the SNOPT [95] gradient-based optimizer (version 7.2-5) to solve the optimization problems discussed in this chapter. We set the major optimality and major feasibility tolerances of SNOPT to 10^{-8}. Because of the low computational cost of the models and the relatively small number of design variables, we compute the gradients using the complex-step method [96]. The complex-step method provides the implementation ease and flexibility of finite-difference methods, but without the concerns related to step size and accuracy. However, as is the case for finite-difference methods, the computational cost of using the complex-step method scales poorly with the number

of design variables. If we were using a large number of design variables or computationally expensive models, this method for computing gradients would be very limiting. Since we are using computationally inexpensive models for this study, that is not an issue. Table 5.1.3 contains the aircraft specifications used for these optimization problems. The scripts used to run the optimization problems are publicly available[‡]. Each optimization problem takes on the order of minutes to solve on a desktop computer.

Table 5.1.3: Parameters and specifications for the aircraft under consideration. These values are estimates based on the Airbus A^3 Vahana.

Specification	Value	Note
Takeoff mass, m	725 kg	
Total wing planform area, S_{ref}	9.0 m^2	4.5 m^2 for each wing
Wing span, b	6 m	Same for both wings
Propeller radius, R	0.75 m	Same for all propellers
Total number of propellers	8	
Number of blades per propeller, B	3	Same for all propellers
Representative blade chord, c_{b}	0.1 m	Same for all propellers
Maximum electrical power, P_{max}	311.0 kW	Power for $T = 1.7\,mg$ at hover

5.2 Optimization Results

Section 5.2.1 presents optimization results without acceleration constraints or horizontal-displacement requirements, to show what the optimized trajectories are when the optimizer is given the most freedom. After that, Sec. 5.2.2 presents optimization results with an acceleration constraint and a horizontal-displacement requirement. Finally, Secs. 5.2.3 and 5.2.4 present optimization results with varying wing sizes and levels of maximum available power.

[‡]`https://bitbucket.org/shamsheersc19/tilt_wing_evtol_takeoff`

5.2.1 Results Without Acceleration Constraints or Horizontal-Displacement Requirements

Without Stall Constraints

Figure 5.2.1 shows optimization results without stall constraints for the first set of optimization problems, which does not have acceleration constraints or horizontal-displacement requirements. The first row of subplots in Fig. 5.2.1 shows the wing-angle and electrical-power design variables (our control variables). The rest of the subplots in Fig. 5.2.1 show the state variables (vertical and horizontal displacements, wing angle of attack, speed, wing lift and drag, total thrust, and acceleration magnitude). The same optimization problem is solved for six different values of the propeller-induced velocity factor ($k_{\mathrm{w}} = 0\%$, 25%, 50%, 75%, 100%, and 200%). A value of 0% corresponds to no flow augmentation from the propellers, and 200% is a conservative upper limit for the effective flow augmentation. As discussed in Sec. 4.3, we expect the effective k_{w} to be less than 100% for the type of configuration we are studying.

In Fig. 5.2.1, from the subplot showing the wing angle of attack as a function of time, we see that for $k_{\mathrm{w}} \leq 25\%$, the optimal trajectory involves transitioning to forward flight with the wings stalled during the first few seconds. For higher k_{w}, the optimizer does not choose to stall the wings. From the subplot showing the wing angle relative to the vertical, we see that the wing angle first increases during the initial transition phase and then decreases to around 37–40 deg during the climb phase, and finally increases again for level flight. The wing-angle range of 37–40 deg allows the aircraft to climb at vertical speeds near the best rate of climb for this aircraft (31 m/s). It is also interesting to note that the entire takeoff is carried out at or almost at maximum power for all k_{w} values.

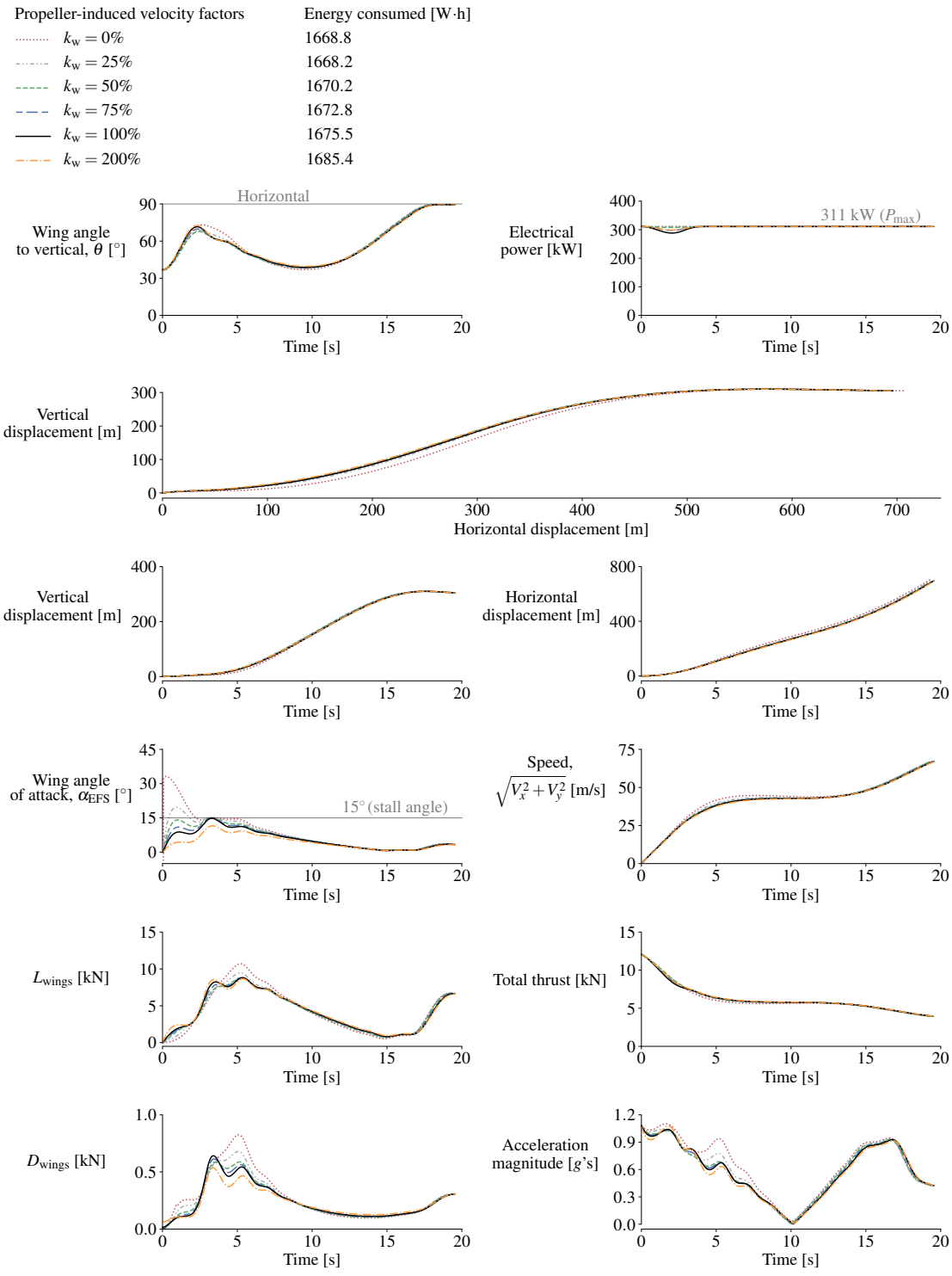

Figure 5.2.1: Results without stall constraints for the optimization problem set that does not have acceleration constraints or horizontal-displacement requirements

From the displacement and speed subplots, we see that the optimized trajectories involve first transitioning rapidly to forward flight and accelerating, followed by climbing at roughly constant speed, and then finally accelerating to the required cruise speed. The optimized trajectories also involve overshooting the required cruise altitude by a small margin and then descending while accelerating to the required cruise speed. These climb and acceleration features have been seen before in trajectory-optimization literature [97, 98].

The electrical energy-consumption values listed in Fig. 5.2.1 show that the differences in energy consumed with or without the flow augmentation from the propellers are negligible. Note that the horizontal distances covered in these results are different for the different k_{w} values, and the differences would have to be made up during cruise. However, the maximum difference is 15 m which also corresponds to a negligible energy difference.

With Stall Constraints

Fig. 5.2.2 shows optimization results with stall constraints ($-15\,\mathrm{deg} \leq \alpha_{\mathrm{EFS}} \leq 15\,\mathrm{deg}$) for the first set of optimization problems, which does not have acceleration constraints or horizontal-displacement requirements. The optimized trajectories are very similar to the optimized trajectories for the cases without stall constraints. The main difference is smaller wing angles relative to the vertical, for the cases with low flow augmentation from the propellers ($k_{\mathrm{w}} \leq 25\%$), during the initial transition phase to keep the flow attached.

Figure 5.2.3 provides a closer view of the initial transition phase of the trajectories shown in Figs. 5.2.1 and 5.2.2. With low flow augmentation and with stall constraints, the optimal trajectories involve gaining more altitude and transitioning more gradually to avoid stalling the wings.

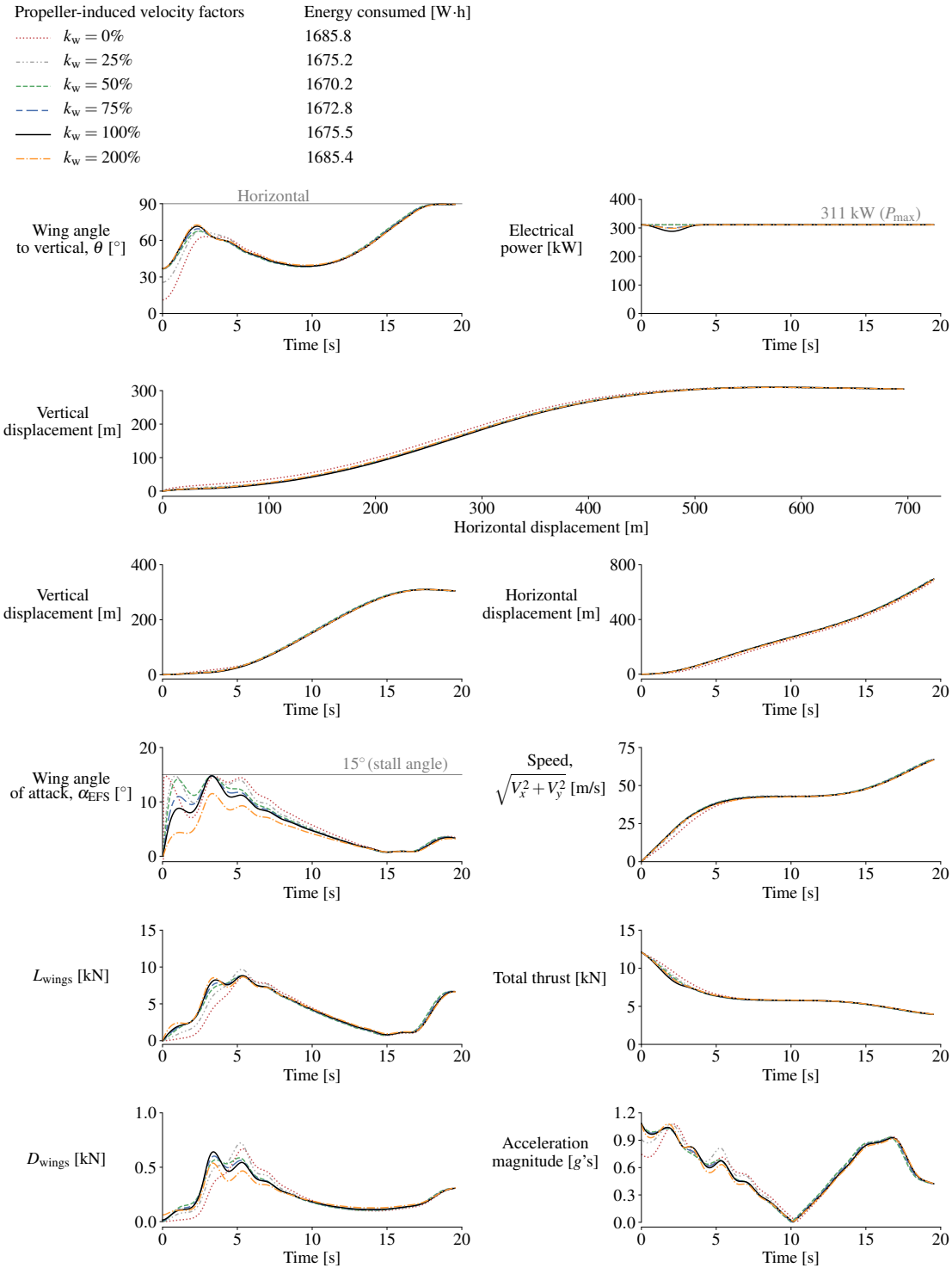

Figure 5.2.2: Results with stall constraints for the optimization problem set that does not have acceleration constraints or horizontal-displacement requirements

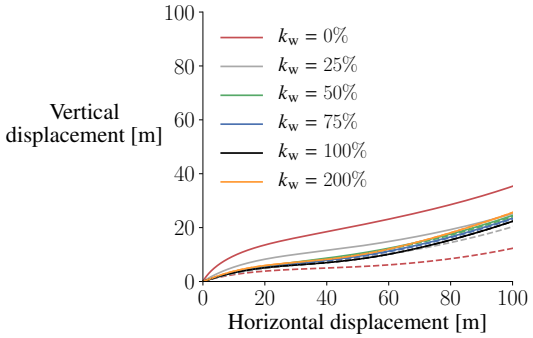

Figure 5.2.3: Enlarged view of the transition phase of the trajectories shown in Figs. 5.2.1 and 5.2.2. The dashed curves correspond to the results without stall constraints.

Figure 5.2.2 also shows that the energy-consumption differences with or without the flow augmentation from the propellers are negligible. Additionally, by comparing the energy values listed in Figs. 5.2.1 and 5.2.2, we see that the energy penalty to avoid stalling the wings is also negligible. Note again that for these cases the horizontal distances covered are slightly different, by a maximum of 27 m, which also corresponds to a negligible cruise energy difference. We add horizontal-displacement requirements for more consistent energy comparisons to the optimization problems discussed in the following sections.

The acceleration subplots in Figs. 5.2.1 and 5.2.2 show that the accelerations reach $1\,g$ in magnitude. These may be acceptable for applications such as package transportation or autonomous relocation of the aircraft, but would be uncomfortable for passengers. For the sets of optimization problems discussed in the following sections, we also add an acceleration constraint.

Figures 5.2.1 and 5.2.2 also show oscillations in the angle-of-attack, lift, and drag subplots as well as some less obvious fluctuations in the wing-angle and thrust subplots, especially during the first ten seconds. The wing angle affects all the disciplines we model, and therefore the exact tradeoffs being made here are not obvious. Chang-

ing the wing angle changes the component of the freestream velocity normal to the propeller disks, which for a given power changes the thrust, the induced velocities, and the propulsive efficiency. Changing the wing angle also changes the direction of the thrust vector which, along with the change in thrust magnitude, changes the acceleration and velocity of the aircraft, and also changes how much work is being done against gravity and to increase kinetic energy, and how much is being done against drag. Additionally, changing the wing angle, along with the resulting changes to the freestream velocity and induced velocities, also changes the angle of attack of the wings and the resulting forces, which impact the aerodynamic performance. The magnitudes and relative sensitivities of these quantities to the wing angle are all different and also change with the evolving flight conditions, making it challenging to isolate benefits and explain the fluctuations and oscillations. However, since we are minimizing energy consumption, the problem boils down to maximizing total efficiency while satisfying the mission requirements. In Fig. 5.2.4, we plot propulsive efficiency and total efficiency as a function of time for the optimization results corresponding to Fig. 5.2.2.

We define the propulsive efficiency as

$$\eta_{\text{prop}} = \frac{TV_{\infty\perp}}{P_{\text{electrical}}}, \tag{5.2.1}$$

and we define the total efficiency as

$$\eta_{\text{total}} = \frac{mgy + 0.5m(V_x^2 + V_y^2)}{\int P_{\text{electrical}}\,\mathrm{d}t}, \tag{5.2.2}$$

where y is the vertical displacement. The total efficiency is the ratio of the potential and kinetic energy to the electrical energy consumed. We do not see any significant fluctuations in the propulsive efficiency and the total efficiency curves.

Additionally, the comparison of optimization results with different numbers of

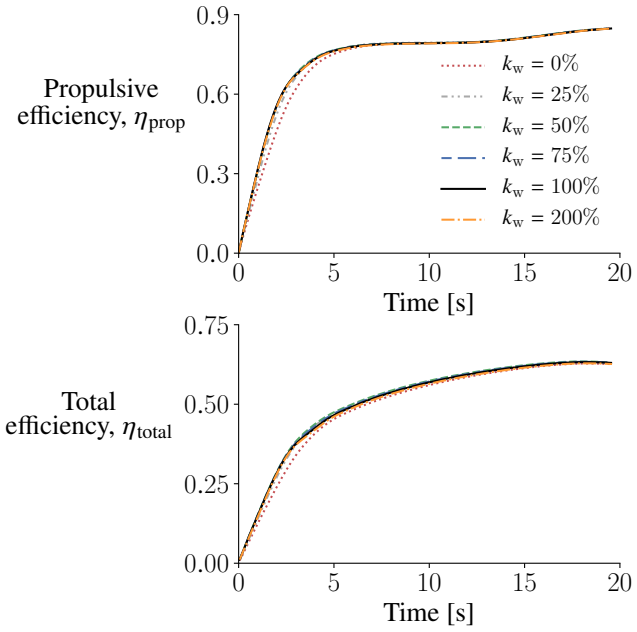

Figure 5.2.4: Propulsive and total efficiency as a function of time for the cases shown in Fig. 5.2.2

control points in Fig. 5.2.5 shows that the design space is relatively flat. The different numbers of control points provide varying levels of control on the design variables (our control variables); a larger number allows more rapid and frequent changes to the control variables. Even with smoother and significantly different control inputs and state variables when the number of control points is low, the differences in energy consumption are small (1% for 5 and 40 control points).

Note that these optimization problems have been converged very tightly and the energy consumption decreases by only $\sim 10^{-5}\%$ or less over the last three orders of convergence of the optimality criterion, and therefore the oscillations are not a result of a lack of convergence. Based on this discussion, we attribute the oscillations to a combination of the design freedom provided by the B-spline parameterization and the optimizer taking advantage of subtle tradeoffs and small benefits in the design space.

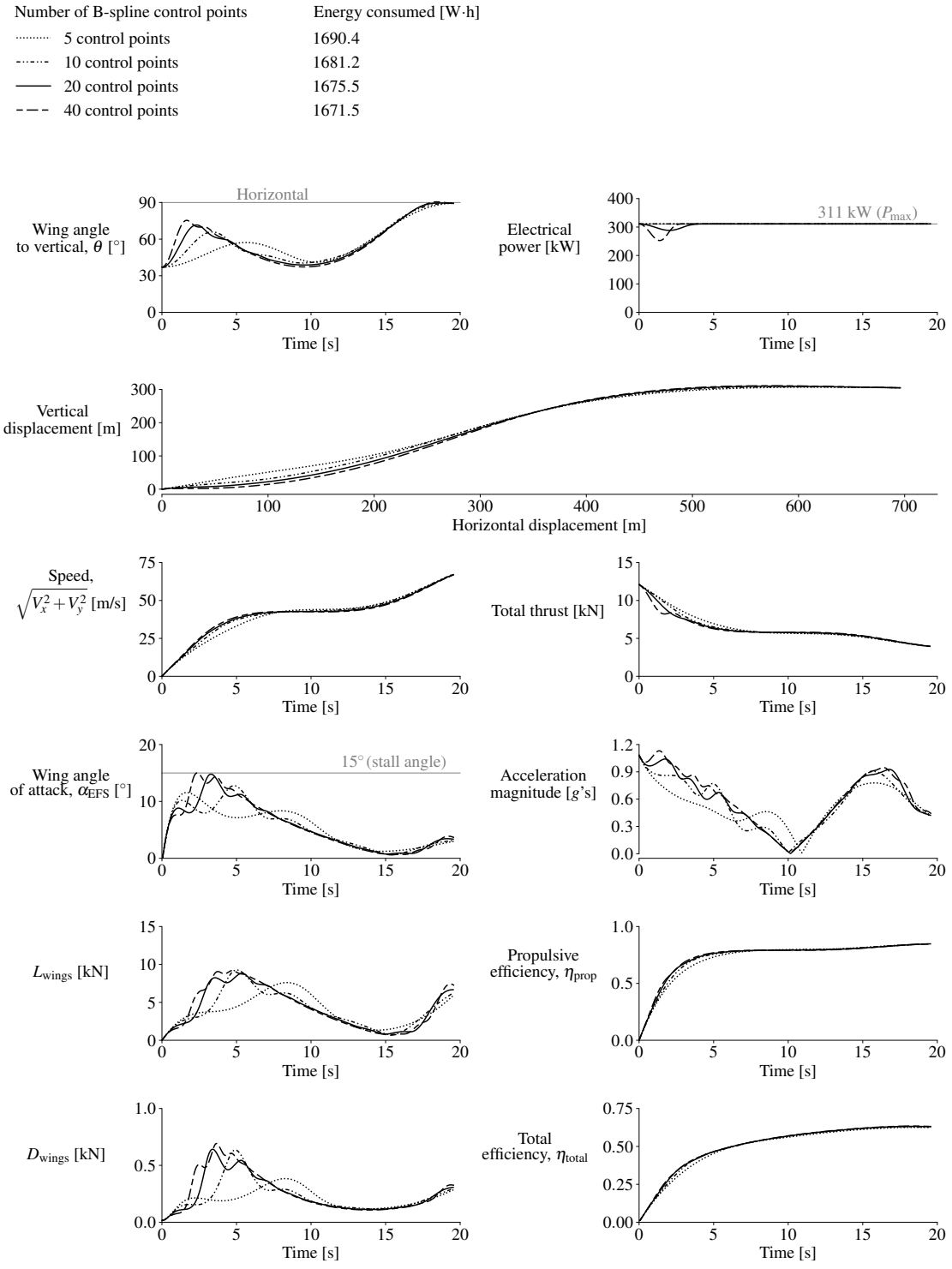

Figure 5.2.5: Optimization results for varying numbers of B-spline control points for the design variables, without stall or acceleration constraints ($k_{\mathrm{w}} = 100\%$; final horizontal displacements = 696 m)

5.2.2 Results With an Acceleration Constraint and a Horizontal-Displacement Requirement

During takeoff, the longitudinal acceleration of commercial airplanes can reach up to $0.5\,g$, without significant discomfort to passengers [99]. Based on this, we add a constraint to limit the magnitude of the accelerations to below $0.3\,g$ for passenger comfort. As discussed in Sec. 5.2.1, the different cases with and without stall constraints and with different k_{w} values have small differences in their final horizontal displacements, and these differences would have to be made up during cruise. For more consistent comparisons, we also add the requirement that the final horizontal displacement must be 900 m. When we solved the optimization problems with the acceleration constraint but without a horizontal-displacement requirement, we found that the final horizontal displacements ranged between 829 m and 869 m. Therefore, we set the horizontal-displacement requirement to 900 m, a value greater than the above horizontal displacements.

Without Stall Constraints

Figure 5.2.6 shows optimization results without stall constraints for the second set of optimization problems, which has the acceleration limit of $0.3\,g$ and the horizontal-displacement requirement of 900 m. The takeoffs are no longer carried out at maximum power, and the wing angle now has a gradual increase instead of a rapid increase and decrease as seen previously in Fig. 5.2.1. With $k_{\mathrm{w}} = 0$, the flow over the wing remains separated for the first 7 s, and for all other k_{w} values except 200%, the wings operate slightly beyond the stall angle of attack for a few seconds. The trajectories show greater gain in altitude during the initial phase compared to the previous set of results without the acceleration constraint. We also no longer see distinct acceleration and climb phases as we did in the previous set of results.

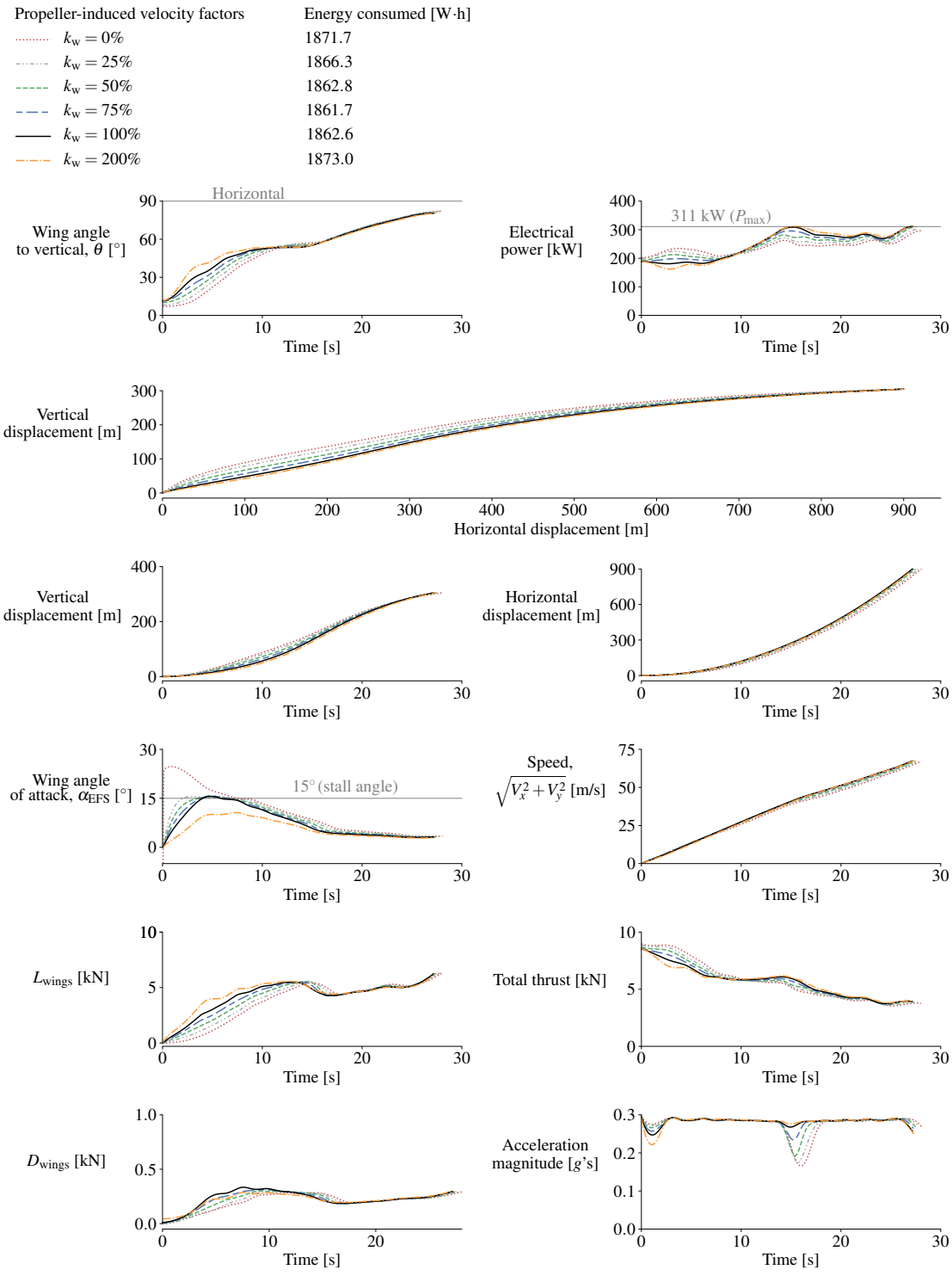

Figure 5.2.6: Results without stall constraints for the optimization problem set that has the acceleration limit of 0.3 g and the horizontal-displacement requirement of 900 m

The optimized trajectories now also have more noticeable differences between them for the different levels of flow augmentation. With lower levels of flow augmentation, the optimized trajectories involve taking off with smaller wing angles to the vertical and gaining more altitude during the initial takeoff phase. However, once again we find that the energy-consumption differences are negligible for the different k_{w} values.

For a direct comparison with energy consumed without an acceleration constraint, energy-consumption values are listed in Table 5.2.1 for optimization cases without the acceleration constraint but with the horizontal-displacement requirement of 900 m. Without the acceleration constraint, the energy consumption is 9% lower on average. Figures 5.2.7 and 5.2.8 plot and compare the results for $k_{\mathrm{w}} = 0$ and $k_{\mathrm{w}} = 100\%$, respectively.

Table 5.2.1: Energy-consumption values for optimizations without acceleration constraints but with the 900 m horizontal-displacement requirement

k_{w}	Energy consumption without stall constraints [W·h]	Energy consumption with stall constraints [W·h]
0%	1694.3	1720.0
25%	1693.8	1707.1
50%	1694.9	1698.1
75%	1697.5	1697.5
100%	1700.2	1700.2
200%	1710.6	1710.6

Figure 5.2.9 shows a comparison of optimization results with different numbers of B-spline control points (5, 10, 20, and 40 control points). With 10, 20, and 40 control points, the same trends are obtained and the energy-consumption differences are within 1%. The energy-consumption difference between the 5 and 40 control-points cases is 3%, which again shows that the design space is relatively flat.

Acceleration constraint	Stall constraints	Energy consumed [W·h]	
No	No	1694.3	($\Delta = -9.6\%$)
No	Yes	1720.0	($\Delta = -8.3\%$)
Yes	No	1871.7	($\Delta = -0.2\%$)
Yes	Yes	1875.0	

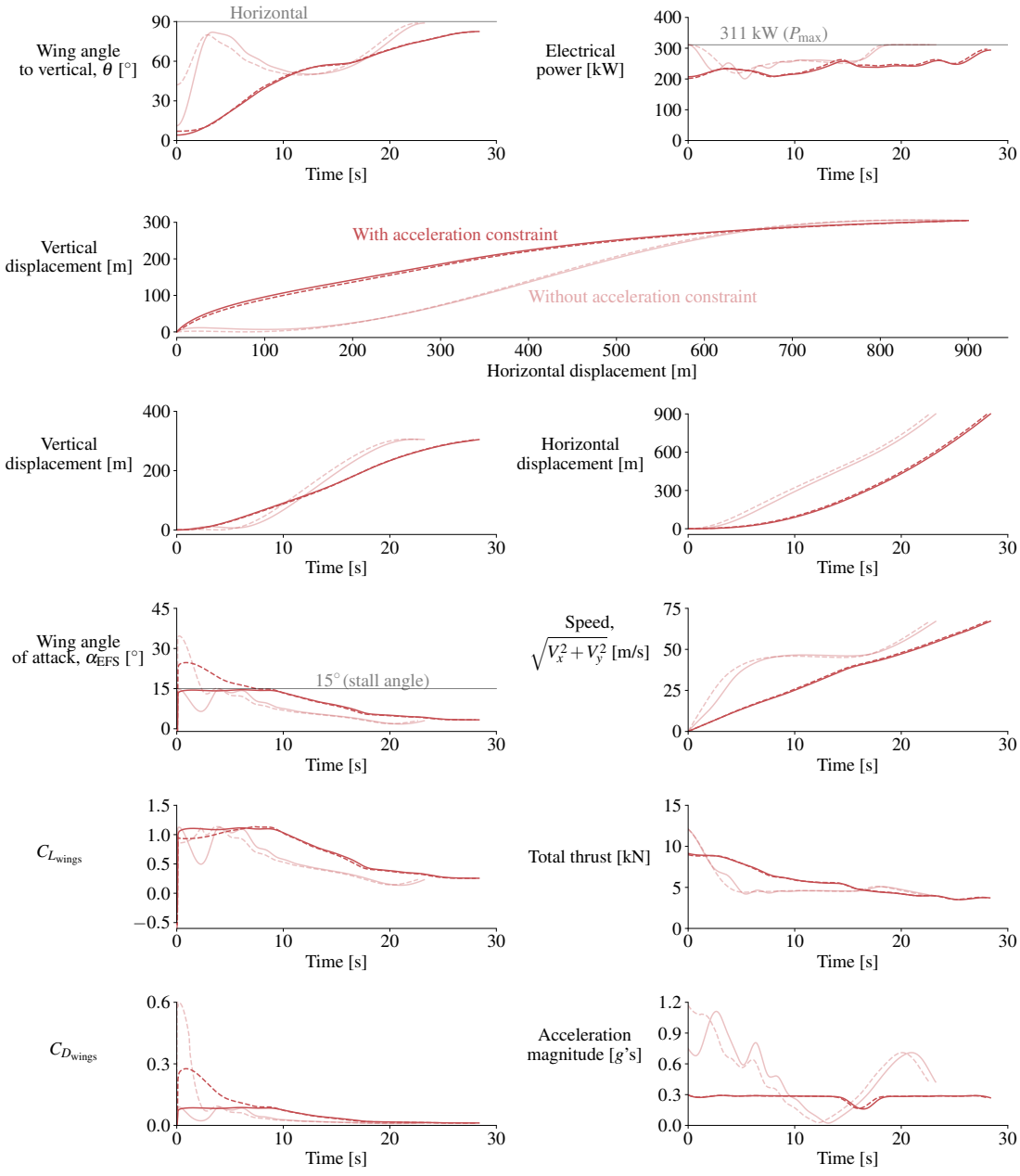

Figure 5.2.7: Results with and without the acceleration constraint compared for $k_w = 0$ (all have the horizontal-displacement requirement of 900 m)

Acceleration constraint	Stall constraints	Energy consumed [W·h]
No	No	1700.2 ($\Delta = -8.7\%$)
No	Yes	1700.2 ($\Delta = -8.7\%$)
Yes	No	1862.6 ($\Delta = -0.0\%$)
Yes	Yes	1863.1

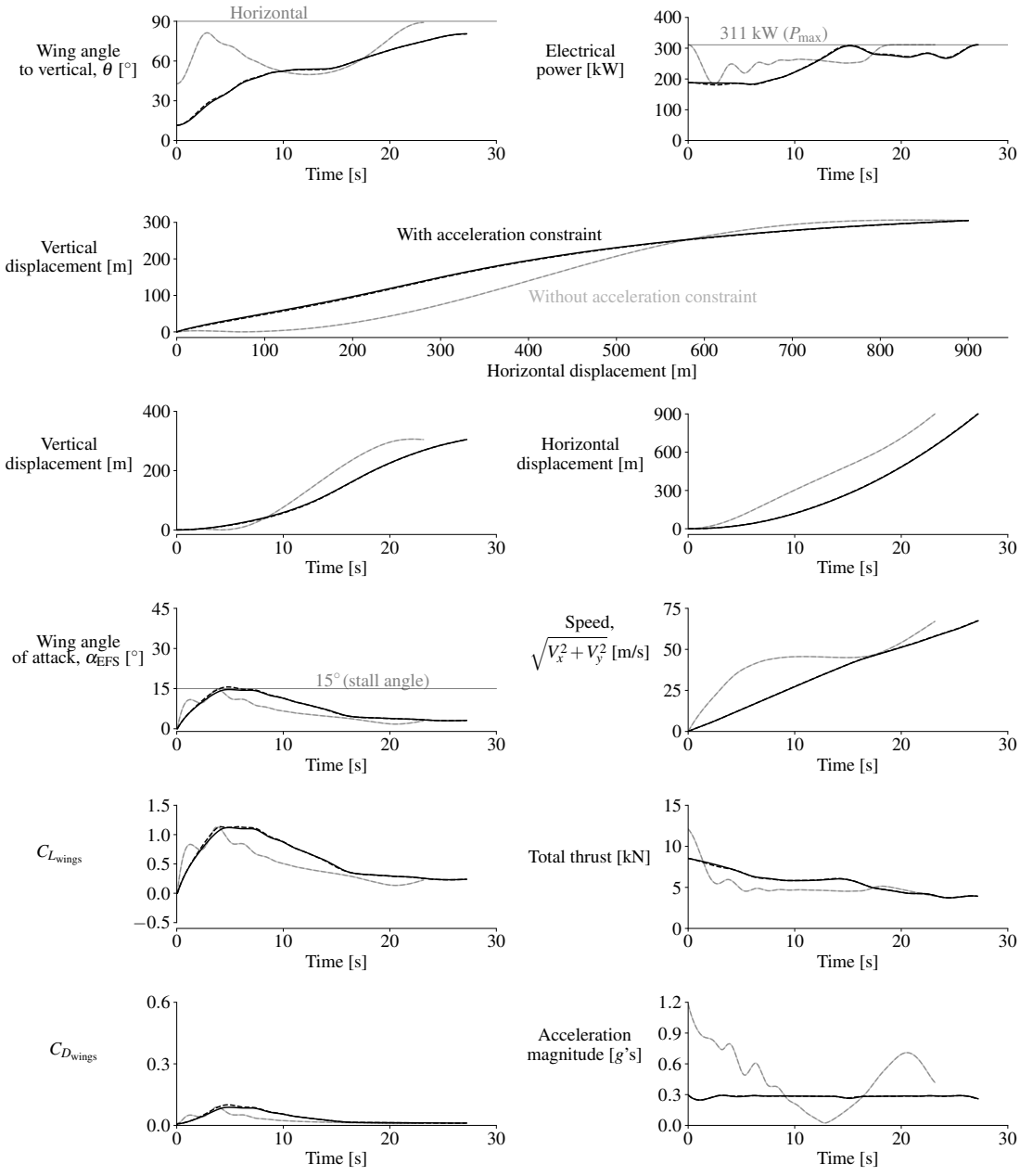

Figure 5.2.8: Results with and without the acceleration constraint compared for $k_{\mathrm{w}} = 100\%$ (all have the horizontal-displacement requirement of 900 m)

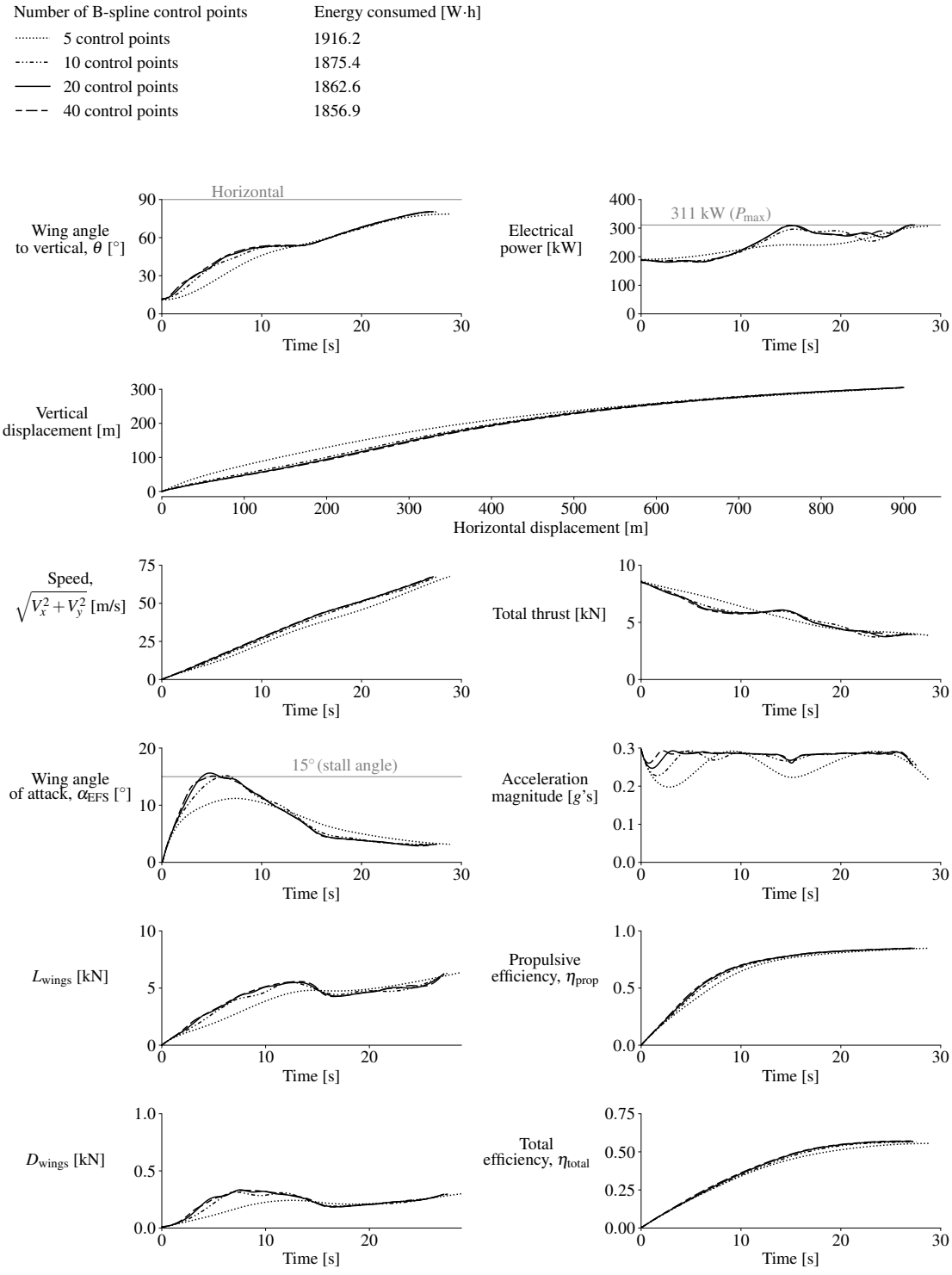

Figure 5.2.9: Optimization results for varying numbers of B-spline control points for the design variables, with the acceleration constraint and horizontal-displacement requirement (no stall constraints; $k_{\mathrm{w}} = 100\%$)

With Stall Constraints

Figure 5.2.10 shows optimization results with stall constraints for the second set of optimization problems, which has the acceleration limit of $0.3\,g$ and the horizontal-displacement requirement of 900 m. Once again, the energy-consumption differences are negligible for the different k_{w} values, and the energy penalty to avoid stalling the wings is negligible as well.

To put the energy-consumption values for the takeoff-to-cruise phase into perspective, we can estimate how much battery mass they translate to. The optimized takeoff-to-cruise energy-consumption values for the cases with acceleration and horizontal-displacement requirements discussed so far range between 1862 and 1875 W·h. With a cell-level specific energy of 200 W·h/kg (roughly the specific-energy value of the cells in today's high-end production electric vehicles), this translates to 9.5 kg of battery. Considering packaging, thermal management, and depth-of-discharge limitations, the installed-battery specific energy at current technology levels is likely to be closer to 100 W·h/kg [11], which translates to a battery weight of approximately 19 kg.

To further put the optimization results into perspective, we compare the energy consumption of the optimized profiles presented so far to a simpler, primarily hand-designed, and somewhat more conventional climb in which the aircraft takes off, climbs at the wing angle for the best rate of climb (θ_{RCmax}), and then accelerates to the required cruise speed. This simpler trajectory has four phases. In the first phase, the aircraft takes off with the wing angle θ increasing from vertical to 35 deg and the power increasing from $70\%P_{\mathrm{max}}$ to $90\%P_{\mathrm{max}}$ over the first 10 s. In the second phase, the aircraft climbs to 250 m at maximum power with the wing angle set at 35 deg, which is θ_{RCmax} for our configuration. In the third phase, the aircraft transitions to

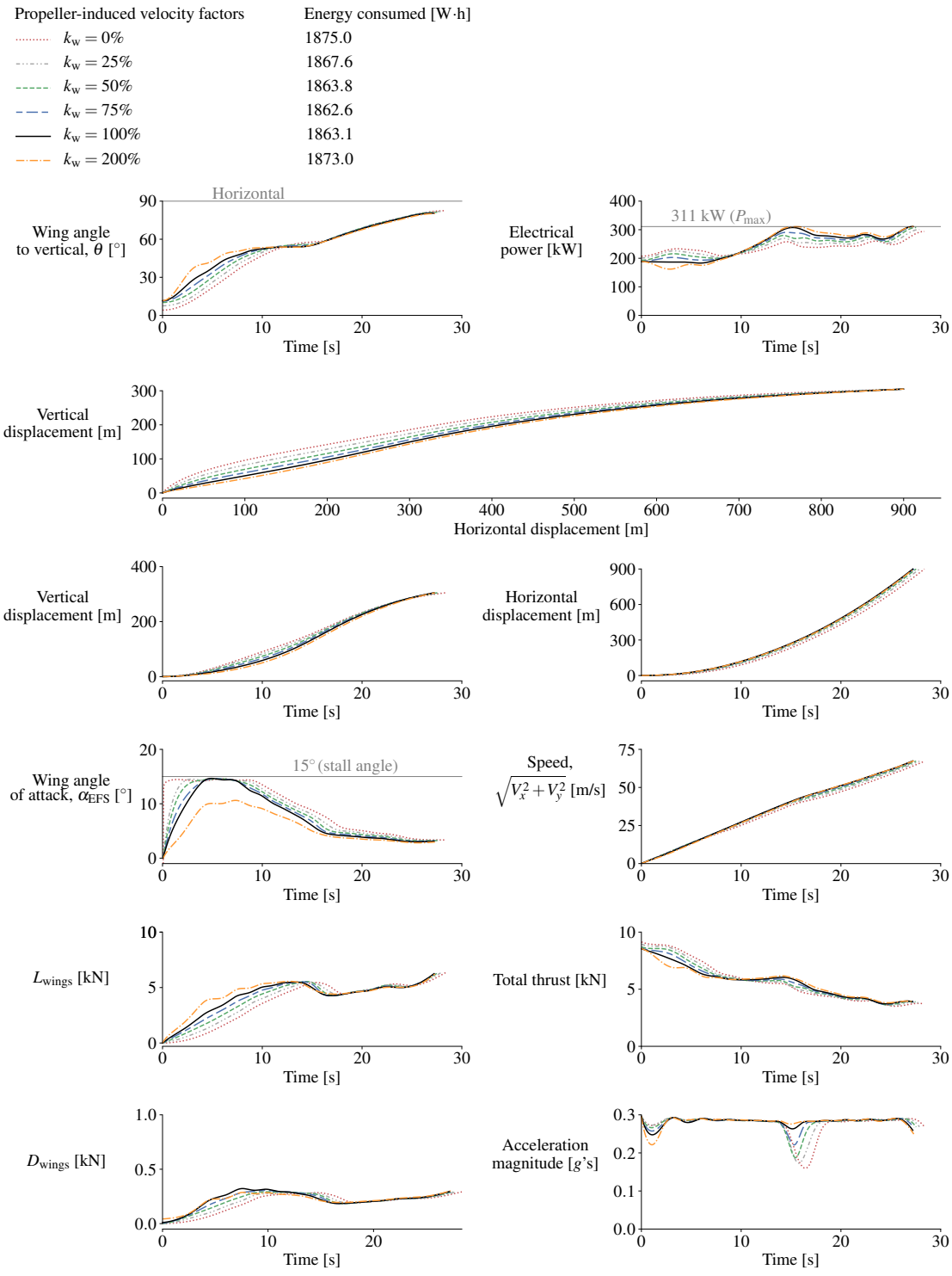

Figure 5.2.10: Results with stall constraints for the optimization problem set that has the acceleration limit of $0.3\,g$ and the horizontal-displacement requirement of 900 m

horizontal flight by increasing θ to 80 deg and reducing the power to $20\%P_{\max}$ over 10 s. Finally, in the fourth phase, the aircraft accelerates to the required cruise speed and satisfies the altitude and horizontal-displacement requirements. This simpler trajectory avoids stalling the wings and the phases have maximum accelerations in the 0.3 to 0.4 g range. On average, this simpler strategy requires 5% more electrical energy than the optimized trajectories (the differences are 5% or 6% depending on the k_{w} value).

There is also the question of whether multiple local minima exist for these optimization problems. We solved the aforementioned optimization problems with over 50 different initial guesses for the wing-angle and electrical-power design variables (including constant, monotonically increasing, monotonically decreasing, and random values for the control points), as well as different initial guesses for the flight-time design variable, and did not find multiple local minima. Although this does not disprove the existence of other minima, it indicates that their existence is unlikely.

5.2.3 Results With Smaller Wings

Since the results discussed so far are for an aircraft with a predetermined total wing planform area, it is also worth investigating what happens to the results when the wing size is different. We redo the optimizations that have the acceleration limit of 0.3 g and the horizontal-displacement requirement of 900 m with smaller wings (80, 60, and 40% of the baseline wing reference area S_{ref} with the span kept constant) to see what happens to the results. Note that we do not change the weight of the aircraft for these optimization cases.

Figures 5.2.11 and 5.2.12 show optimization results with stall constraints for $k_{\mathrm{w}} = 0\%$ and $k_{\mathrm{w}} = 100\%$, respectively. We observe larger angles of attack with smaller wings, and also that it is still possible to avoid stall with significantly smaller wings.

We have omitted plots for results without stall constraints, the main difference being angles of attack up to 25 deg in the first 7 s for $k_w = 0$ as seen in Fig. 5.2.6.

When we compare the electrical energy consumed with the different planform areas, we see that the differences are small. This indicates that when designing the wings of a tilt-wing aircraft for urban mobility, factors such as avoiding flow separation during the takeoff phase and maximizing cruise efficiency should take precedence over considerations such as the energy consumed during the takeoff phase.

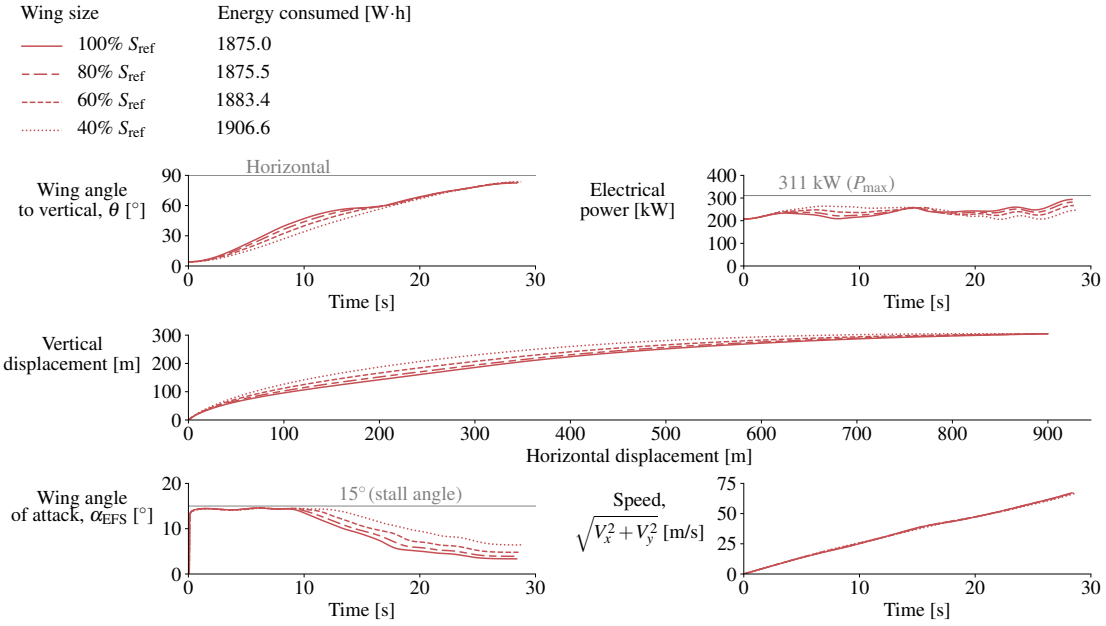

Figure 5.2.11: Results with different wing sizes for the optimization problem that includes the stall constraints, the 0.3 g acceleration limit, and the 900 m horizontal-displacement requirement ($k_w = 0$)

5.2.4 Results With Less Available Power

Next, we also investigate what happens to the optimization results when the maximum power available decreases. We redo the optimizations that have the acceleration limit of 0.3 g and the horizontal-displacement requirement of 900 m, with lower values for the upper bound of the electrical-power control variables (60, 70, and 80% of the baseline upper limit P_{max}). These maximum-power values correspond to

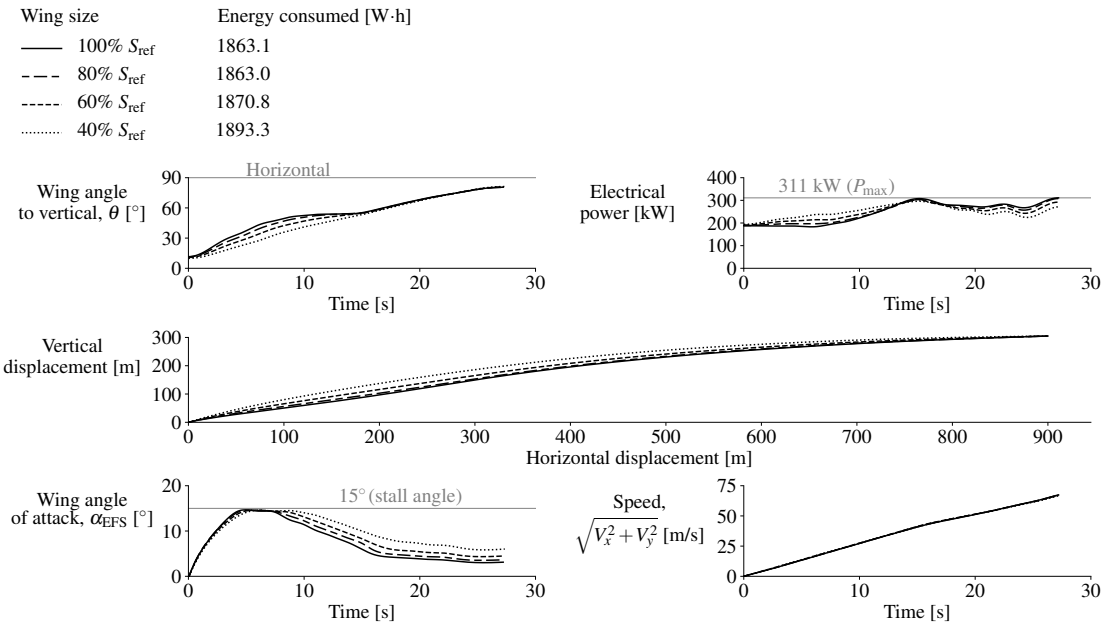

Figure 5.2.12: Results with different wing sizes for the optimization problem that includes the stall constraints, the $0.3\,g$ acceleration limit, and the 900 m horizontal-displacement requirement ($k_{\mathrm{w}} = 100\%$)

thrust-to-weight ratios at hover equal to 1.19, 1.33, and 1.46 (P_{max} corresponds to 1.7). Note that we do not change the weight of the aircraft for these optimization cases.

Figures 5.2.13 and 5.2.14 show optimization results without stall constraints for $k_{\mathrm{w}} = 0\%$ and $k_{\mathrm{w}} = 100\%$, respectively. The takeoffs for the lower-power cases ($60\%\,P_{\mathrm{max}}$ and $70\%\,P_{\mathrm{max}}$) are carried out almost completely at maximum power. For these lower-power cases, we also see purely vertical flight phases in the optimized trajectories, something not seen in the other optimization results presented in this work. These results also show that, up to a certain level due to the acceleration constraint, with more power available, less time and less electrical energy are required to reach the specified cruise altitude and speed. The lowest-power cases consume approximately 30% more electrical energy than the highest-power cases.

With stall constraints, the optimizer indicated that the optimization problems

were infeasible with $k_w \leq 50\%$ for $60\%\, P_{max}$ and with $k_w \leq 25\%$ for $70\%\, P_{max}$. This shows that, with low available power and low levels of flow augmentation, stalling the wings during takeoff can be unavoidable.

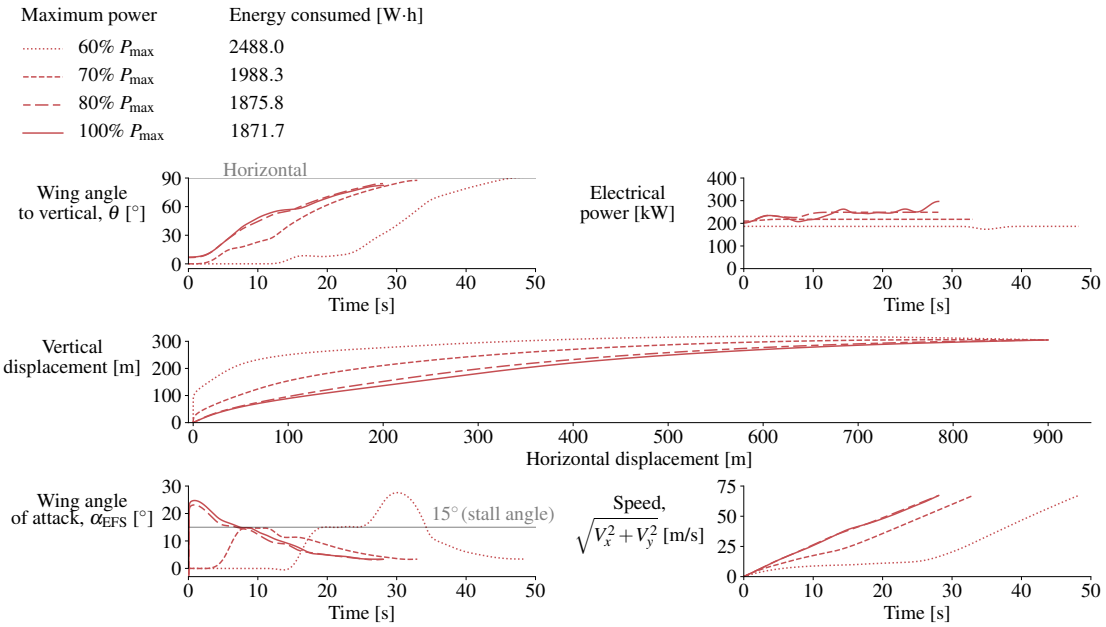

Figure 5.2.13: Results with varying maximum powers for the optimization problem that includes the $0.3\,g$ acceleration limit and the 900 m horizontal-displacement requirement (no stall constraints; $k_w = 0$)

Finally, we revisit the simplifications made in the modeling and discuss what differences may be expected if higher-order models are used in future work. Because of the challenges inherent in accurately predicting stall and poststall behavior with tools such as panel methods and RANS-based CFD [80–85], it is not obvious whether more accurate predictions can be obtained for the wing aerodynamics over a large range of speeds and angles of attack using these types of higher-order methods, even with significant effort and computational cost. However, our results indicate that if such higher-order methods are used for the transition optimization of eVTOL configurations, such as the one studied here, it may be best to limit the wing-angle control variables such that the lift coefficients and angles of attack are restricted to

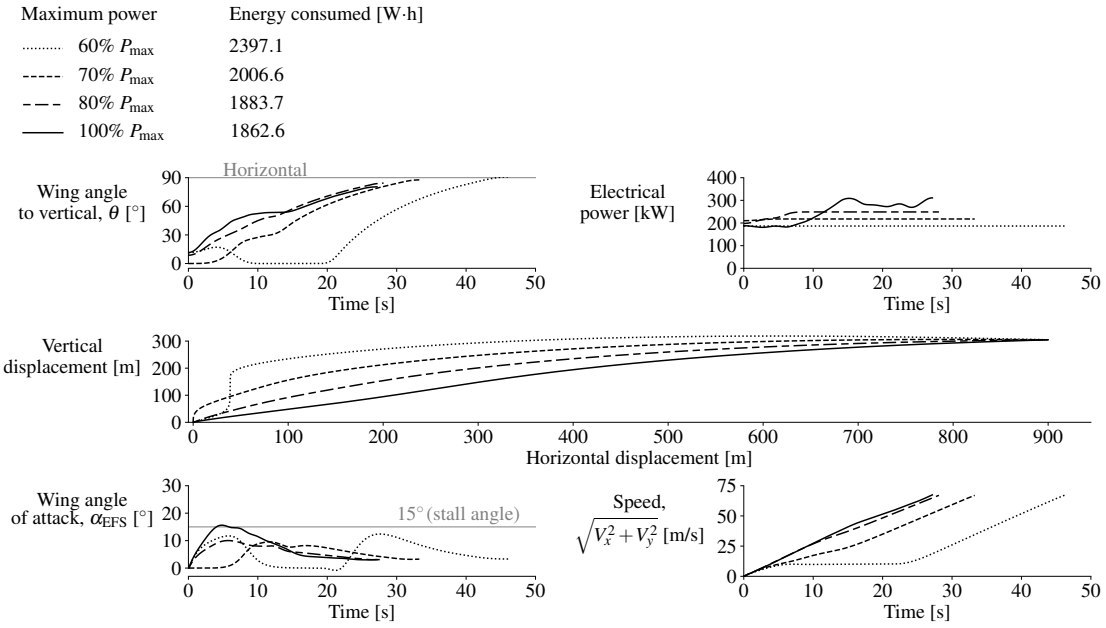

Figure 5.2.14: Results with varying maximum powers for the optimization problem that includes the $0.3\,g$ acceleration limit and the 900 m horizontal-displacement requirement (no stall constraints; $k_w = 100\%$)

prestall values. Since we find that the energy benefits from stalling the wings are negligible for an optimal takeoff, and considering real-world concerns such as safety, stability, and comfort, the effort required to address the accuracy and numerical challenges related to these higher-order methods near and beyond stall does not seem worthwhile for trajectory optimization.

For the propellers, methods such as blade-element methods or free-wake methods [16, 90, 100] can provide more accurate thrust and energy estimates than momentum theory. Connecting blade-element methods with panel methods or CFD tools are approaches that can help provide more accurate flow-augmentation and propeller-wing interaction modeling [5, 14, 17, 20, 21, 54]. However, these approaches can have limitations related to inflow conditions when the propeller incidence angle is not small. Based on our results, improvements in propeller modeling will likely impact the higher-order details of the optimal trajectory, but it seems unlikely that

a significant impact will be made on the general shapes of the optimal flight profiles and the conclusions made on the effects of propeller-wing flow interaction, wing size, and available power on the electrical energy consumption. Further studies are recommended to verify this claim.

Two major assumptions made in this work are that there is no interaction between the forward and rear wings (except for the interaction considered to calculate the effective span efficiencies) and that the wings rotate and behave identically. Reducing these simplifications and considering factors such as downwash, upwash, trim, and stability, the flows experienced by the forward and rear wings will not be identical. Depending on the modeling approach used, higher-order methods and separate control variables for the wings may help provide more accurate simulations. However, we do not expect the main trends seen in our optimization results to change significantly.

5.3 Summary

In this work, to address the lack of literature on the optimal takeoff trajectory for passenger tilt-wing eVTOL aircraft, we constructed a simplified model for a tandem tilt-wing eVTOL aircraft based on the Airbus A^3 Vahana and numerically optimized its takeoff-to-cruise trajectory with the objective of minimizing energy consumption. We used low-order first-principles-based models for the aerodynamics, propulsion, propeller-wing flow-interaction, and flight-mechanics disciplines to capture the primary multidisciplinary trends. We carried out optimizations with and without stall and acceleration constraints, with varying levels of flow augmentation from the propellers.

The optimized trajectories without acceleration constraints involve first transi-

tioning to forward flight and accelerating, followed by climbing at roughly constant speed, and then finally accelerating to the required cruise speed, all performed at or almost at maximum power. With an acceleration limit of $0.3\,g$ for passenger comfort, the transition, climb, and acceleration phases are more gradual, less distinct, and not carried out at maximum power.

The optimized takeoffs involve stalling the wings or flying near the stall angle of attack, both with and without the acceleration limit of $0.3\,g$. However, based on the optimization cases with stall constraints, the energy penalty for avoiding stall is negligible.

With different levels of flow augmentation from the propellers, the optimized trajectories have negligible differences in energy consumption. However, with the acceleration constraint, the optimized trajectories have noticeable differences in shape with the different levels of flow augmentation. With lower levels of flow augmentation, the optimized trajectories involve taking off with smaller wing angles to the vertical and gaining more altitude during the initial takeoff phase.

Based on our models, the optimized takeoff-to-cruise flight with the acceleration constraint, for the air-taxi mission requirements considered (cruise at a speed of 67 m/s and an altitude of 305 m), consumes 1.9 kW·h of electrical energy (19 kg of installed-battery mass based on an installed-battery specific energy of 100 W·h/kg). Without acceleration constraints, the optimized trajectories require 9% less electrical energy. Compared to a simpler, primarily hand-tuned trajectory in which the aircraft takes off, climbs at the wing angle for the best rate of climb, and then accelerates to the required cruise speed, the optimized trajectories with the acceleration constraint require 5% less electrical energy.

We also studied the impact of changing the wing size on the optimization results.

With smaller wings (down to 40% of the baseline reference area), the optimized trajectories involve larger angles of attack, but the flight time and electrical energy consumed do not change substantially. Additionally, even with low levels of flow augmentation, it is still possible to avoid stalling the wings with this wide range of wing sizes.

Similarly, we also studied the impact of decreasing the maximum available power. With low available power, the optimized takeoffs are carried out at or close to maximum power. The time and electrical energy required also increase as the maximum power available decreases. With the two lowest maximum-power levels considered (corresponding to maximum thrust-to-weight ratios of 1.2 and 1.3 at hover), the optimized trajectories include purely vertical flight phases, something not seen in the other optimization results presented here. Additionally, with low available power and low levels of flow augmentation, stalling the wings during takeoff can be unavoidable.

Overall, we conclude that the design space for the takeoff-to-cruise trajectory of the tilt-wing eVTOL aircraft that we study, with the mission specifications used, is relatively flat from an energy-consumption point of view. The induced losses of the propellers dominate the energy consumption, and relatively large changes to the flight profile and the flow-augmentation level, as well as to the baseline wing size and available power, tend to result in relatively small changes to the electrical energy consumed.

Chapter 11 contains a list of the novel contributions, a list of the conclusions, and a list of the recommendations for future work.

Part II

RANS-Based Aerodynamic Shape Optimization of a Wing Considering Propeller-Wing Interaction

CHAPTER 6

Introduction

> ... it is well to distinguish two kinds of influences, one due to variations in velocity, and the other due to variations in direction of the air current.
>
> *L. Prandtl* [37]

As discussed in Chapter 2, when a propeller is placed near a wing, the flow it induces affects the lift of the wing as well as the profile and induced drag of the wing [4, 7, 31–33, 37]. The details of the flow around the wing, and consequently its performance, change with the location and rotation direction of the propeller [4, 7, 31–33, 37].

Considering propeller-wing interaction and accounting for the effects on performance of both the wing and the propeller allow more accurate predictions and improvements of the performance of aircraft with wing-mounted propellers [4–6, 10, 17, 20–22, 24, 32, 33, 51]. There are many approaches of varying complexity and fidelity that have been used to model the interaction between propellers and wings [3–6, 10, 17, 20–22, 24, 32, 33, 49, 51, 101–105]. A popular approach is to connect a vortex-lattice method (VLM) model for the wing to a propeller model that provides induced velocities, such as a blade-element momentum model [4, 6, 20, 21, 24, 101, 105]. This type of approach has limitations related to thickness and viscous effects, and requires correction factors to capture the influence of a propeller's slipstream on

a wing with reasonable accuracy [4, 20, 105]. Another approach that captures these effects more directly is modeling a propeller as an actuator disk in a computational fluid dynamics (CFD) simulation, typically solving the Euler or Reynolds-averaged Navier–Stokes (RANS) equations, by distributing time-averaged propeller forces over a disk using force terms (also referred to as source terms) or boundary conditions [3–5, 10, 17, 49, 102, 106]. This approach allows using steady CFD simulations without modeling the detailed propeller geometry. Another similar approach is to use rotating actuator lines within CFD simulations for unsteady simulations [5]. To capture more detail, an unsteady simulation using RANS CFD with a three-dimensional rotating propeller geometry is an option [3, 5, 10, 103, 107–111]. However, these unsteady approaches result in significantly higher computational cost, which is prohibitive for optimization.

The approach of using an actuator disk with CFD to model propeller-wing interaction has been shown to provide accurate predictions for the time-averaged performance [4, 5, 10, 102]. When computing propeller forces for the actuator disk, using a blade-element method that uses the inflow to the disk from the CFD simulation captures the mutual interaction between the propeller and the wing and can further improve accuracy [10]. Although the flow induced by a propeller is fundamentally unsteady, and unsteady analyses are certainly useful from structures, vibrations, and acoustics points of view, they are found to provide little more on time-averaged aircraft performance than steady approaches, such as using an actuator disk with CFD [4, 5, 10, 102]. Additionally, unsteady phenomena such as the cyclical transitions between laminar and turbulent flow [112], which affect profile drag, are not considered to be something that can be taken advantage of during design optimization [4]. Therefore, the low cost of an actuator-disk approach compared to a fully

unsteady approach makes it a tractable option for RANS-based design studies and optimization.

There are a small number of published studies on optimizing wings accounting for propeller-wing flow interaction. Kroo [32] presented a study to find the optimal lift distributions that minimize the induced losses for a wing with a propeller (in both tractor and pusher configurations). The results show that the optimal lift distribution for a wing with a propeller differs from the elliptical lift distribution that is optimal for an isolated wing. Additionally, significant differences are shown to exist between the optimal lift distributions with inboard-up, outboard-up, and counter-rotating propellers. Kroo [32] also concluded that losses associated with swirl may be recovered with equal increases in efficiency for both tractor and pusher configurations. The limitations of the approach used by Kroo [32] include the low order of the models (a lifting-line approach with an idealized helical propeller wake), neglecting viscous effects, and the optimization of the lift distribution instead of geometric design parameters.

Veldhuis and Heyma [51] presented optimization results for a rectangular wing with a tractor propeller with the objective of minimizing drag subject to a lift constraint using wing-twist design variables. They used a lifting-line approach for the wing and induced-velocity models for the propeller, and they used the Trefftz-plane method and a viscous-drag estimation method to compute the drag. Their results show negligible differences in drag between minimizing only the induced drag and minimizing the sum of the induced and viscous drag (less than 0.1 drag count), which is not surprising because only twist design variables were used. They also optimized a wing based on the Fokker 50 at a cruise condition and predicted induced-drag reductions of 13 drag counts with an inboard-up propeller and 8 drag counts with

an outboard-up propeller relative to an optimized wing with no propeller. Their optimization results show increased twist behind the down-going-blade region and decreased twist behind the up-going-blade region (compared to an optimized wing with no propeller). The limitations of their approach include the low order of the models and the limited design freedom (only twist design variables). Rakshith et al. [104] used a similar low-order approach to carry out chord and twist optimization studies for a wing with a tractor propeller. They concluded that it is beneficial to reduce the chord lengths behind the propeller, and they predicted drag reductions between 2% and 12% for varying flight conditions, constraints, and numbers of design variables, relative to an unoptimized trapezoidal wing.

More recently, Alba et al. [20] constructed a model for coupled propeller-wing interaction and carried out wing optimization with planform and airfoil-shape design variables. They also included weight and performance models for a multidisciplinary design optimization (MDO). They modeled the wing (using a quasi-3-D approach with a VLM model) and the propeller (using XROTOR) in isolation but used a coupling method to account for the mutual interaction. They concluded that adjusting wing twist and camber to align the wing sections with the propeller swirl is beneficial. For an aircraft based on the Tecnam P2012, their optimization results predict fuel-savings of up to 7% relative to the baseline design. The limitations of their approach include the use of low-order models and the limited number of design variables. Epema [105] also presented chord and twist optimization studies for a wing using similar models for the propeller-wing interaction, along with wind tunnel experiments to validate their simulation approaches.

Pedreiro [106] presented an aerodynamic shape optimization study for a wing with a tractor propeller, based on the Embraer EMB-120, using RANS CFD with

an actuator-disk approach and a blade-element model for the propeller loads. Six design variables were used with a design-of-experiments (DOE) approach to optimize the twist and airfoil shapes of the portion of the wing behind the propeller, and a drag reduction of 3 drag counts was obtained for a cruise condition. Unlike the previous studies, the lowest-drag design found by Pedreiro [106] does not have lower twist behind the up-going-blade region and higher twist behind the down-going-blade region. A limitation of the approach used by Pedreiro [106] is that the number of design variables that can be used and the ability to carry out a large number of optimization studies are severely limited because of the poor scaling of DOE approaches with the number of design variables.

To address the aforementioned limitations of the previous work, related to the fidelity of the models and the ability to explore the design space, we developed the capability to perform gradient-based aerodynamic shape optimization using RANS CFD with an actuator-disk approach. We use a modified version of the open-source CFD solver ADflow, which has an adjoint implementation for efficient gradient computation. This allows us to perform multiple aerodynamic shape optimization studies with respect to large numbers of design variables at a manageable computational cost. In this part of the dissertation, we present aerodynamic shape optimization results for a wing with an inboard-mounted tractor propeller and a wing with a tip-mounted tractor propeller. This work is the first published instance of gradient-based aerodynamic shape optimization of a wing considering propeller-wing interaction with RANS CFD, and it is a stepping stone towards a coupled high-fidelity model for mutual propeller-wing interaction suitable for gradient-based optimization of both the propeller and the wing. Additionally, to answer how important it is to optimize the wing while considering the propeller slipstream, we study how much drag re-

duction optimizing a wing in the presence of the propeller slipstream provides over optimizing the wing without considering the propeller slipstream (the final design of the latter is also analyzed with the propeller slipstream). There is a lack of such direct comparisons in the previous literature.

6.1 Background on Actuator-Disk Models in CFD

6.1.1 Basic Principles

Whitfield and Jameson [113] were one of the first to use an actuator-disk approach to model propeller-wing interaction using CFD (i.e., solving finite-volume Euler or Navier–Stokes equations) [49, 113]. Their work was in response to the interest in developing transonic aircraft with advanced propellers during the 1980s. We briefly describe this approach here.

A propeller exerts forces on a fluid as it moves through it. These forces are equal in magnitude and opposite in direction to the lift and drag forces on the propeller blades, and they are experienced directly by the finite volumes located in the propeller region [49]. If the loads on the propeller blades are known, they can be applied in an equal and opposite manner to the cells in the propeller region of a CFD model to effectively simulate a propeller [49]. To further simplify the modeling, the forces can be applied in a time-averaged manner to the entire disk swept by the propeller, for steady simulations. Comparisons with experimental data have shown that this steady approach, called the actuator-disk approach, provides accurate predictions for the time-averaged performance of a wing trailing a propeller [4, 5, 10, 49].

There are two main ways in which an actuator-disk model can be implemented. The first is the force-term (or momentum-source-term) approach, and the second is the boundary-condition approach [114]. For the work presented in this dissertation, we use the force-term approach because it is a more direct approach and is easier

to implement in the flow solver that we use. Additionally, Chetboun et al. [114] found it to be the more robust approach when solving the RANS equations with the multiblock CFD solver NES. In the force-term approach, the necessary forces are applied in the same manner as body forces (i.e., like gravitational or magnetic forces). How body-force terms appear in Euler and Navier–Stokes equations is briefly reviewed here.

The Euler equations can be written as [49]

$$\int_S (\mathbf{F}_x n_x + \mathbf{F}_y n_y + \mathbf{F}_z n_z)\,\mathrm{d}S - \int_V \mathbf{B}\,\mathrm{d}V = 0, \tag{6.1.1}$$

where

$$\mathbf{F}_x = \begin{bmatrix} \rho u \\ \rho u u + p \\ \rho v u \\ \rho w u \\ \rho(E + p/\rho)u \end{bmatrix}, \mathbf{F}_y = \begin{bmatrix} \rho v \\ \rho u v \\ \rho v v + p \\ \rho w v \\ \rho(E + p/\rho)v \end{bmatrix}, \mathbf{F}_z = \begin{bmatrix} \rho w \\ \rho u w \\ \rho v w \\ \rho w w + p \\ \rho(E + p/\rho)w \end{bmatrix},$$

$$\mathbf{B} = \begin{bmatrix} 0 \\ \phi_x \\ \phi_y \\ \phi_z \\ \phi_x u + \phi_y v + \phi_z w \end{bmatrix}, \text{and } E = \frac{p}{\rho(\gamma - 1)} + \frac{u^2 + v^2 + w^2}{2}.$$

Here, $\{u, v, w\}^{\mathrm{T}}$ is the velocity vector, $\{n_x, n_y, n_z\}^{\mathrm{T}}$ is the unit vector normal to the surface S enclosing the control volume V, ρ is the fluid density, p is the pressure, $\{\phi_x, \phi_y, \phi_z\}^{\mathrm{T}}$ is the body-force vector (force per unit volume), and γ is the specific-heat ratio. The first row of this set of equations is the continuity equation, the next three rows are the momentum equations, and the last row is the energy equation. The terms in $\int_V \mathbf{B}\,\mathrm{d}V$ corresponding to the momentum equations are the force

terms representing body forces. In a finite-volume steady-flow solver, time-averaged propeller forces can be applied as these force terms to the cells in the region swept by the propeller. Corresponding terms are also added to the energy equation. For brevity, we used the Euler equations for this explanation instead of RANS equations. However, the same explanation and approach applies to RANS equations. For RANS equations, we would just have more terms in Eq. (6.1.1) to account for viscosity and turbulence, which would not be modified by the force terms.

6.1.2 Comparisons with Experimental Data

Comparisons with experimental data have shown that the actuator-disk approach, which is a steady-flow approach, provides accurate predictions for the time-averaged performance of a wing trailing a propeller, at a small fraction of the computational cost of unsteady CFD approaches [4, 5, 10, 49]. Here, the results of two such recent studies are briefly reviewed to support the claim that actuator-disk approaches are suitable for design studies.

Gomariz-Sancha et al. [10] compared actuator-disk RANS simulation results with full-blade unsteady RANS (URANS) simulation results for a twin-turboprop configuration at a cruise condition (Mach number = 0.5; altitude = 25,000 ft; advance ratio = 2.5; see Fig. 6.1.1a for surface meshes). Their results (Fig. 6.1.1b) show that both approaches predict lift distributions that match within a few percent. Additionally, the pressure distributions corresponding to two wing sections behind the propeller, from these two approaches, are practically indistinguishable (Fig. 6.1.2). They also compared an actuator-disk approach based on forces from a uniform-inflow blade-element model with another actuator-disk approach based on forces from a non-uniform-inflow blade-element model, and concluded that using the non-uniform inflow (that results from propeller inclination and wing-induced velocities) enhances

accuracy.

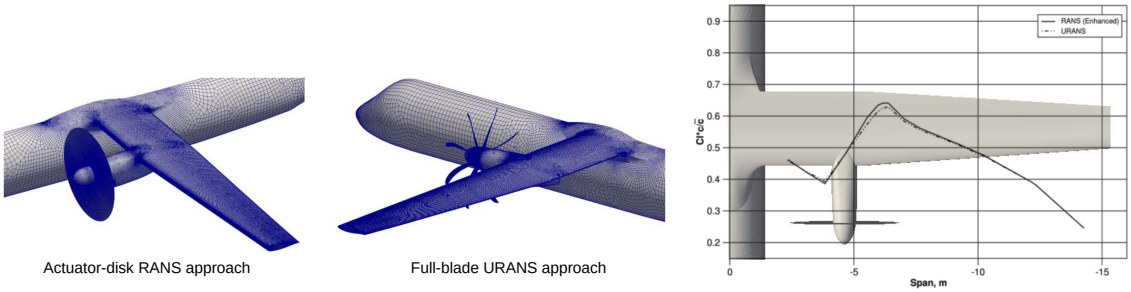

(a) CFD surface meshes

(b) Comparison of lift distributions (advance ratio = 2.5; $\alpha = -2\,\text{deg}$; "RANS (Enhanced)" is the actuator-disk approach; "URANS" is the full-blade approach)

Figure 6.1.1: An actuator-disk approach compared with a full-blade approach (figures from Gomariz-Sancha et al. [10])

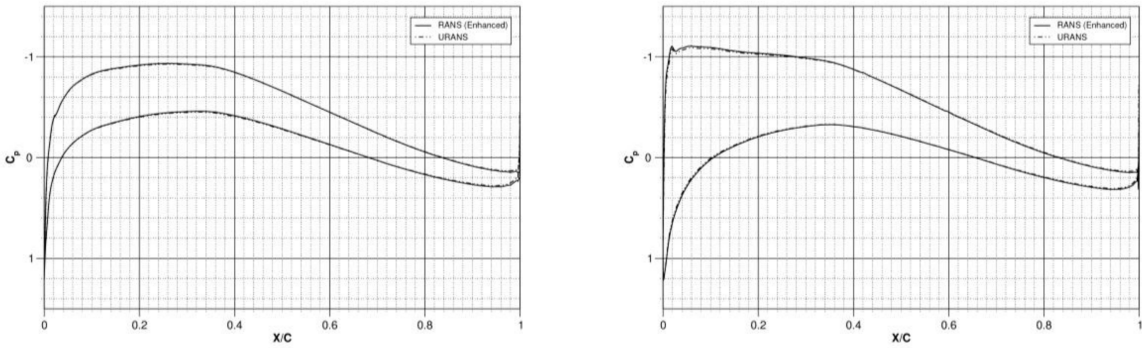

Figure 6.1.2: Pressure coefficients of wing sections, behind the down-going (left) and up-going (right) portions of the propeller, from an actuator-disk simulation compared with results from a full-blade simulation (these correspond to the case in Fig. 6.1.1; figures from Gomariz-Sancha et al. [10])

Gomariz-Sancha et al. [10] also presented comparisons with experimental data (Mach number = 0.5; altitude = 0 ft; advance ratio = 2.5) for a rectangular wing segment representative of the wing portion of the full configuration that the engine is mounted to (see Fig. 6.1.3 for the model). They compared pressure coefficient distributions at a range of sections across the wing and found close agreement between the actuator-disk simulation results and the experimental data (Fig. 6.1.4). The simulation with the actuator-disk model is able to accurately capture the leading-edge

suction peak behind the up-going portion of the propeller and the reduced leading-edge suction behind the down-going portion. There are small pressure coefficient differences near the trailing edges, but they stated that, based on a preliminary investigation, these differences are likely due to differences between the CAD model used for the simulations and the fabricated wind-tunnel model.

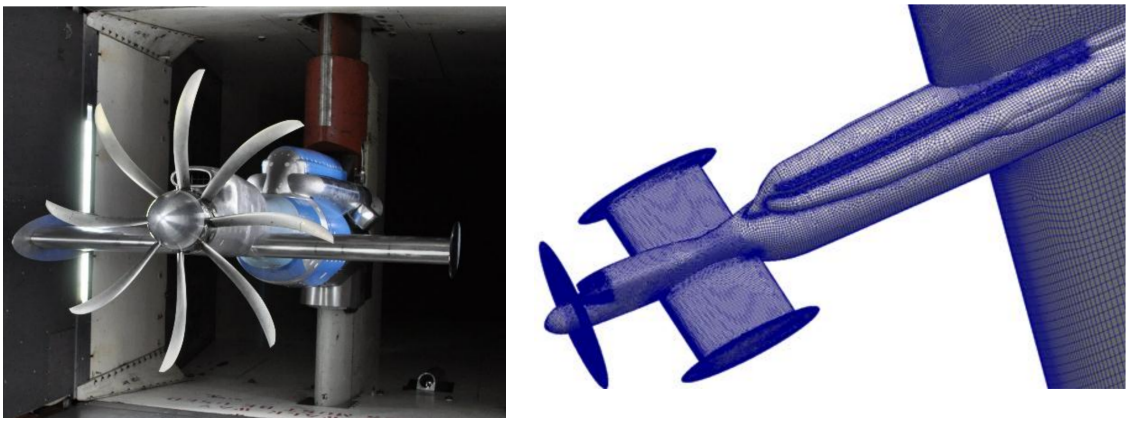

(a) Wind tunnel model (b) Actuator-disk CFD model

Figure 6.1.3: Wind-tunnel models (figures from Gomariz-Sancha et al. [10])

To provide another example of a study that compared actuator-disk CFD results to experimental data, we include results from Stokkermans et al. [5]. Stokkermans et al. [5] presented a careful study in which results from three different types of RANS-based propeller modeling techniques are compared with experimental data for a wing with a tip-mounted propeller. The three RANS-based approaches that they compared are an actuator-disk approach, an actuator-line approach, and a full-blade (sliding mesh for the 3-D rotating propeller) approach.

First, they compared results for an isolated propeller (with nacelle) configuration and found that the actuator approaches compare well with the full-blade approach, and all also agree well with the experimental data (see Fig. 2.1.6 shown previously in Sec. 2.1.2) [5]. The simulation results show slightly less slipstream contraction than

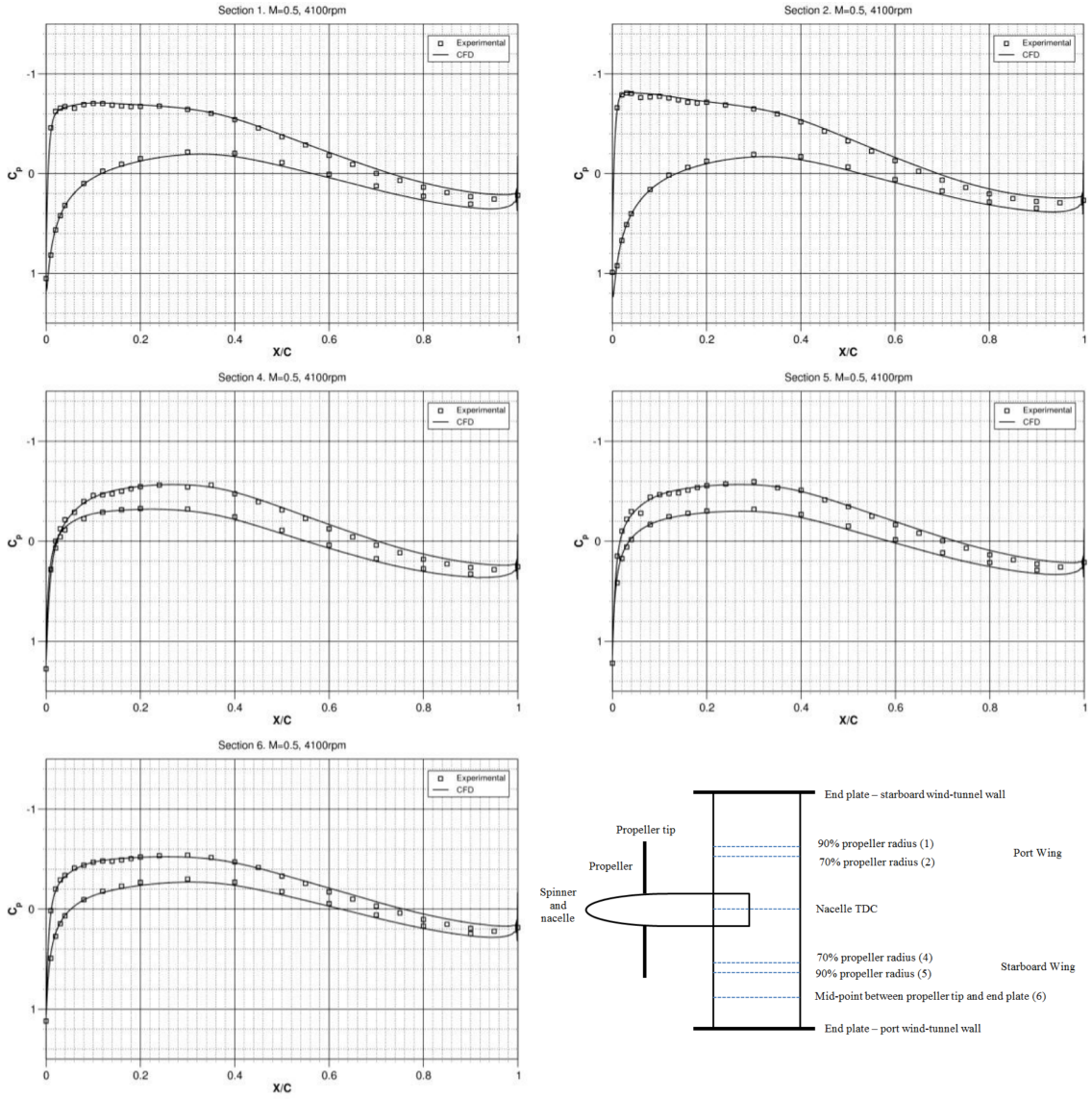

Figure 6.1.4: Pressure coefficient distributions, at a range of sections across a wing, showing close agreement between actuator-disk simulation results and experimental data (advance ratio = 2.5; $\alpha = -2\,\text{deg}$; figures from Gomariz-Sancha et al. [10])

the experimental results and also have some differences in the tangential-velocity trends next to the nacelle surface. They attributed some of the differences to the numerical diffusion in the tip vortex cores of the blades. They also compared the one-equation Spalart–Allmaras turbulence model (with modifications proposed by Dacles-Mariani et al. [115]) and the two-equation $k-\omega$ shear-stress-transport (SST)

turbulence model and found that the numerical diffusion in the slipstream was less with the Spalart–Allmaras model (research by Kim and Rhee [116] on resolving the tip vortex cores of fixed wings also discusses the favorable properties of the Spalart–Allmaras model over $k - \omega$ SST).

For the propeller-wing cases, Stokkermans et al. [5] found that all the RANS-based approaches agree well for the lift and drag distributions (Fig. 6.1.5). Their RANS-based results also match their experimental pressure distributions well (Fig. 6.1.6). The results of their full-blade and actuator-line simulations agree the best. The actuator-disk approach predicts slightly lower pressures on the suction side of the wing airfoils, leading to a small overprediction in the lift coefficient. For a case with a lift coefficient of ~ 0.25, the actuator-disk approach overpredicted lift by 3.9% with practically no difference in drag (relative to the full-blade approach). For their cases, the actuator-line approach is able to reduce computational cost by about 15% relative to the full-blade approach (by removing the need to resolve the 3-D propeller geometry), and the actuator-disk approach is able to reduce computational cost by about 85% (by further removing the time dependency).

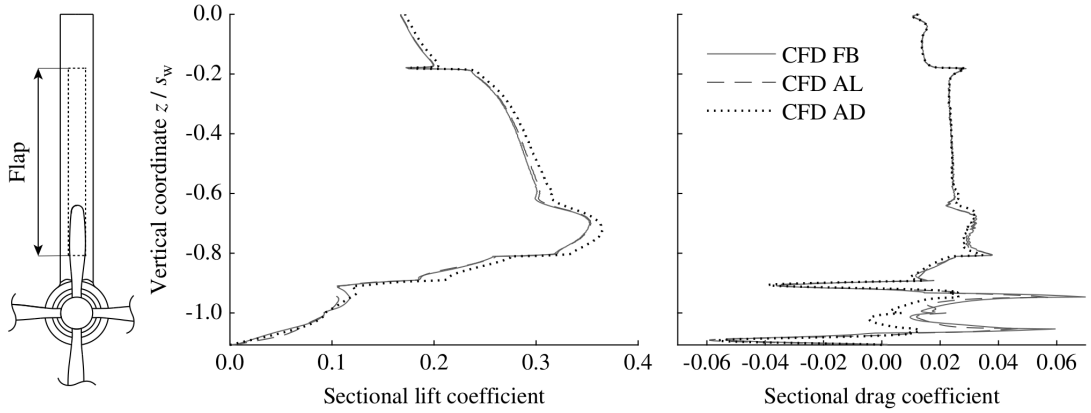

Figure 6.1.5: Lift and drag distributions from three different RANS-based approaches showing good agreement for the performance of a wing with a tip-mounted tractor propeller (advance ratio = 0.8; flap deflection = 10 deg; FB = full blade; AL = actuator line; AD = actuator disk; figures from Stokkermans et al. [5])

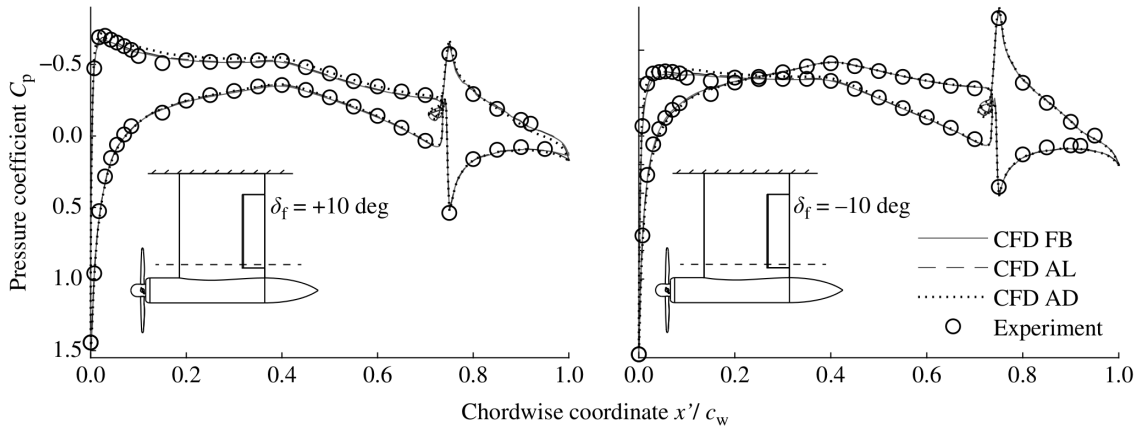

Figure 6.1.6: Pressure coefficient distributions from three different RANS-based approaches compared with experimental data for a wing with a tip-mounted tractor propeller (advance ratio = 0.8; δ_f is the flap deflection; FB = full blade; AL = actuator line; AD = actuator disk; figures from Stokkermans et al. [5])

Overall, from these studies [5, 10], and others [4], we can conclude that, if implemented correctly, actuator-disk CFD approaches provide accurate predictions for the time-averaged performance of a wing trailing a propeller, at a small fraction of the computational cost of unsteady CFD approaches.

CHAPTER 7

Computational Tools

> On ne peut avoir le beurre et l'argent du beurre.
>
> Sagesse ancienne

Optimization with RANS CFD requires a multidisciplinary framework that is computationally efficient because of the high computational cost of the simulations. Additionally, because we use a relatively large number of design variables (~ 200) for this work, gradient-based optimization is necessary to make the problem tractable. With gradient-free methods, the computational cost would be prohibitively large [117, 118]. Therefore, we use the open-source aerodynamics modules of the MDO of Aircraft Configurations with High fidelity (MACH) framework [119].*

7.1 Flow Solver

We use the open-source RANS CFD code ADflow [120, 121] and modify it to use an actuator-disk approach to simulate propeller-wing interaction. The propeller model is described further in Sec. 7.5. ADflow is a second-order finite-volume CFD solver and solves the RANS equations on structured multiblock meshes, and it can also handle overset meshes [122]. For this work, we use the Spalart–Allmaras turbulence model [123] and steady simulations. We do not use a boundary-layer-transition

*`www.github.com/mdolab/MACH-Aero` [Accessed 31 Jul 2020]

model, and therefore, the simulations are fully turbulent.

ADflow uses a discrete adjoint implementation via automatic differentiation to efficiently compute the derivatives of the functions of interest with respect to a large number of design variables [124]. This has enabled several RANS-based optimization studies [125–131].

7.2 Geometry Parameterization

We use pyGeo, MACH's geometry manipulation module, to parameterize and manipulate the wing shape using a free-form deformation (FFD) approach [132]. Using this approach, the surface of the wing is embedded in a grid of control points, and the changes made to the control points are transferred to the embedded surface using a B-spline mapping. When the control points are moved, the embedded shape deforms in a continuous manner, giving the optimizer control over the twist and cross-sectional shapes.

7.3 Mesh Movement

To deform the original volume mesh during optimization to account for the changes to the surface geometry, we use IDWarp, MACH's mesh warping module [133]. IDWarp uses an inverse distance weighting method [134], which helps preserve the quality of the mesh as the surface is deformed.

7.4 Optimizer

We use SNOPT [95], a gradient-based optimizer that uses a sequential quadratic programming algorithm, to solve the optimization problems for this work. SNOPT was developed to handle large-scale nonlinear optimization problems with thousands of constraints and design variables and has been shown to be effective in solving aero-

dynamic shape optimization problems [119, 125–131, 135, 136]. SNOPT is wrapped with the open-source package pyOptSparse [137] for use with the MACH framework. The major optimality and feasibility tolerances for SNOPT are set to $1 \cdot 10^{-5}$ for all the optimization cases in this work, and all the optimization cases finished successfully. To put these tolerances into perspective, for these optimization cases, the objective function changes by less than 0.03% over the last order of convergence of the optimality.

For reference, the optimization cases in Secs. 9.2 and 9.3 require under 24 h to solve on 32 processors[†] (timings ranged from 3 to 22 h depending on whether airfoil-shape design variables were included), and the optimization cases in Secs. 9.5 and 10.2 require under 42 h to solve on 32 processors (timings ranged from 5 to 40 h depending on whether airfoil-shape design variables were included and on the propeller location).

7.5 Propeller Model

We model the propeller using an actuator-disk approach in which forces equal and opposite to time-averaged propeller loads are applied to volume cells in a specified region in the same manner as body forces [49]. To do this, force terms are added to the momentum equations, and the corresponding terms are added to the energy equations, for the specified cells. The propeller loads can be obtained from various sources such as analytical models [138], blade-element methods [10], or CFD simulations of an isolated propeller [5].

We use the following simple models [138] for the distributions of the axial and tangential loading on the propeller. The radial distribution for the axial force is

[†]3.0 GHz Intel Xeon Gold 6154

given by

$$f_x = \tilde{F}\hat{r}^m \left(\frac{a - \hat{r}}{a} \right)^n , \tag{7.5.1}$$

where f_x is the axial force per unit radius, $\tilde{F}$ is a reference value that is adjusted to obtain the required total force, $\hat{r}$ is defined by Eq. (7.5.2), and a, m, and n are parameters that control the shape of the distribution. For example, decreasing n shifts the position of maximum thrust towards the tip, and using a value for a greater than 1.0 results in a finite loading at the tip. The normalized radius $\hat{r}$ is defined as

$$\hat{r} = \frac{r - r_{\text{in}}}{R - r_{\text{in}}}, \tag{7.5.2}$$

where r is the radial distance from the axis of rotation, r_{in} is the inner radius of the propeller (usually the radius at which the blades connect to a hub or spinner), and R is the outer radius of the propeller. The radial distribution for the tangential force is given by

$$f_\theta = f_x \left(\frac{P/D_\varnothing}{\pi(r/R)} \right), \tag{7.5.3}$$

where f_θ is the tangential force per unit radius, and $P/D_\varnothing$ is the propeller pitch-to-diameter ratio.

Since Eqs. (7.5.1) and (7.5.3) provide continuous distributions, we calculate the forces for each cell in the specified region based on their volumes and the distances between their cell-center locations and a specified propeller axis (i.e., r). The axial and tangential forces per unit volume that are used for this are given by $f_x/(2\pi rt)$ and $f_\theta/(2\pi rt)$, where t is the total thickness of the disk of volume cells to which the forces are applied. The reference value $\tilde{F}$, which is not the total force, is set to a value that makes the total axial force applied equal to the desired total force.

CHAPTER 8

Validation Cases

> For one does not have empire over nature except by obeying her.
>
> *F. Bacon* [139]

8.1 Geometry and Specifications

To validate our implementation of the propeller model described in Sec. 7.5, we use test cases from Veldhuis [4]. The configuration, shown in Fig. 8.1.1, is a rectangular NACA 64_2-A015 wing with a tractor propeller mounted near the midspan. The wing is not swept, twisted, or tapered, and the propeller axis lines up with the chord lines of the wing sections. We do not model the nacelle and do not round the leading edge of the wingtip. Our simplified geometry is shown in Fig. 8.2.1a. For the airfoil, we use coordinates from the online UIUC database* and fit them using B-splines. The surface geometry is generated using MACH's pySpline and pyGeo modules.

We compare simulation results with experimental data for 0 and 4 deg angle-of-attack cases tested by Veldhuis [4]. The Reynolds number for these cases is $0.8 \cdot 10^6$, and the dynamic pressure is 1500 Pa [4]. This translates to a flight speed of 49.5 m/s at sea-level conditions (i.e., Mach 0.145). The propeller has an inboard-up rotation, the advance ratio (J) is 0.85, and the thrust coefficient (C_T) is 0.168 [4]. This

*`https://m-selig.ae.illinois.edu/ads/coord/n64015a.dat` [Accessed 01 Mar 2019]

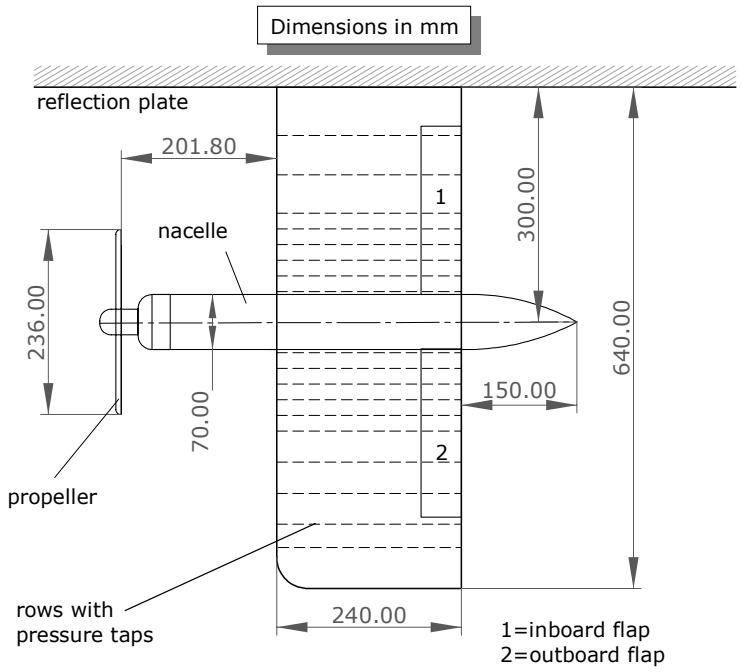

Figure 8.1.1: Geometry of the experimental configuration used for validation (half-wing planform area is $0.15\,\mathrm{m}^2$; aspect ratio is 5.3; also known as the "PROWIM" wing; figure from Veldhuis [4])

translates to a thrust of 38.9 N. Veldhuis [4] mentions that the thrust coefficient is estimated using a bookkeeping approach (measuring forces with and without the propeller on) and using pressure measurements. Here, $J = V_\infty/(\nu D_\varnothing)$, and $C_T = T/(\rho\nu^2 D_\varnothing^4)$, where V_∞ is the freestream speed, ν is the number of rotations per unit time, $D_\varnothing$ is the propeller diameter, ρ is the freestream density, and T is the propeller thrust.

8.2 CFD Volume Meshes

We use three mesh refinement levels for the validation simulations to study how the results change as the mesh is refined. We name these meshes the Level 1 (L1), Level 2 (L2), and Level 3 (L3) meshes, where the L1 mesh is the finest and the L3 mesh is the coarsest.

For the actuator-disk region, we use a structured multiblock cylindrical volume

mesh and apply the forces to a subset of the cells in the middle of this mesh. The outlines of the blocks of this cylindrical volume mesh are shown in Fig. 8.2.1b for the L2 refinement. Forces are applied to the cells in this cylindrical mesh that lie inside the disk shown in Fig. 8.2.1a. The wing has a separate structured multiblock volume mesh, as shown in Fig. 8.2.1b. The wing volume meshes are generated by extruding wing surface meshes using MACH's pyHyp [133] module (Fig. 8.2.1a shows the surface mesh for the L2 refinement). The wing surface meshes are generated using the commercial package ICEM-CFD.

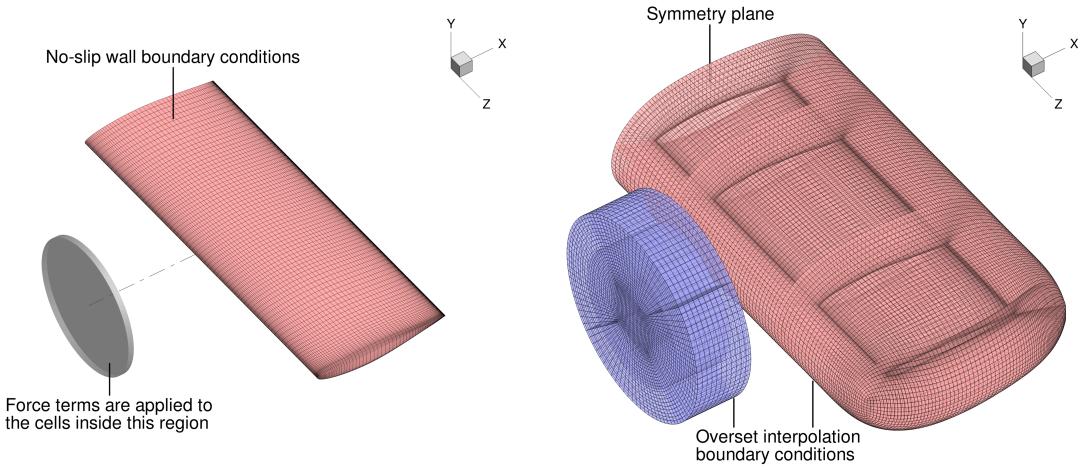

(a) Wing surface mesh (L2 refinement) and the disk used to specify the actuator zone

(b) Wing volume mesh and cylindrical volume mesh (L2 refinement)

Figure 8.2.1: Surfaces and volume meshes

The cylindrical and wing volume meshes are overset with a background mesh (Fig. 8.2.2a). The background mesh consists of a Cartesian volume mesh in the region where the cylindrical and wing meshes are located, and the outer walls of this Cartesian grid are extruded by 45 chord lengths to yield a hemispherical domain. We use far-field boundary conditions for the outer hemispherical surface of this domain and symmetry boundary conditions for the symmetry plane coincident with the root of the wing. The cylindrical volume mesh is larger than the disk inside

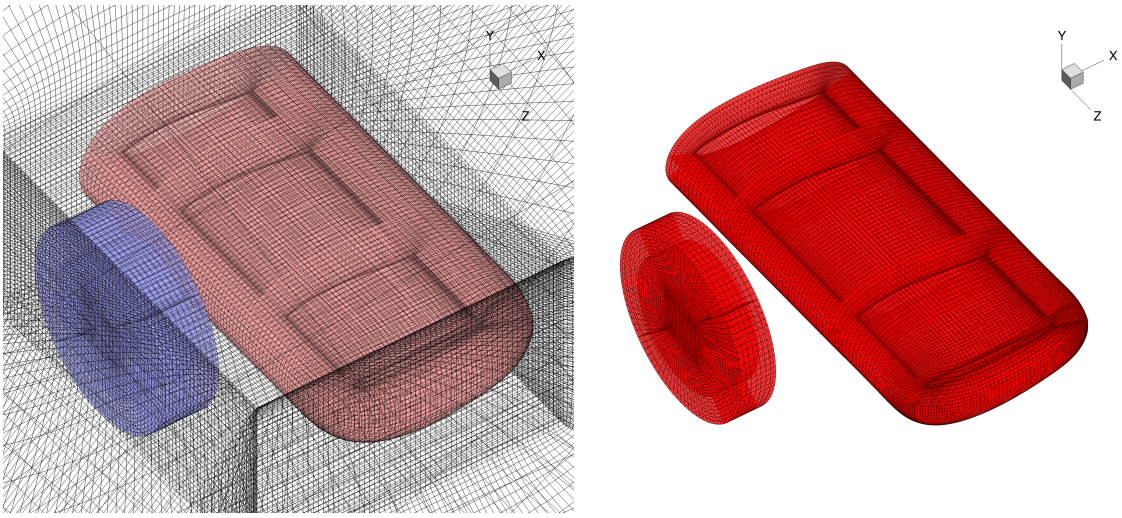

(a) Wing and cylindrical volume meshes overset with a background mesh (L2 refinement)

(b) Regions of the wing and cylindrical volume meshes that are selected as computation cells in the overset mesh (L2 refinement)

Figure 8.2.2: Overset meshes

which the actuator forces are applied (Fig.8.2.1) to allow it to be overset with this background mesh. ADflow uses an implicit hole cutting method for assembling the overset meshes [122, 140]. The computation cells (i.e., the cells used for the CFD solution and not as fringe cells for interpolation) for the cylindrical and wing volume meshes are shown in Fig. 8.2.2b for the L2 refinement.

Figure 8.1.1 shows that the rear face of the disk swept by the propeller is located 0.2 m in front of the leading edge of the wing. In our model, the midplane of the cells that are selected for the actuator disk is located at this distance in front of the wing. The radius of the actuator disk is the propeller radius of 0.12 m, and its thickness is 9.1 mm. A circular disk of cells that is one layer thick is selected for the L2 and L3 meshes, and a circular disk of cells that is two layers thick is selected for the finer L1 mesh, but these disks have the same radius and total thickness.

The wing surface mesh for the L2 refinement is generated by removing every other node of the L1 surface mesh, and the L3 surface mesh is generated by doing the same for the L2 surface mesh. These surface meshes and the grid spacings

of the Cartesian portion of the background meshes are shown in Fig. 8.2.3a. The corresponding cylindrical volume meshes are shown in Fig. 8.2.3b.

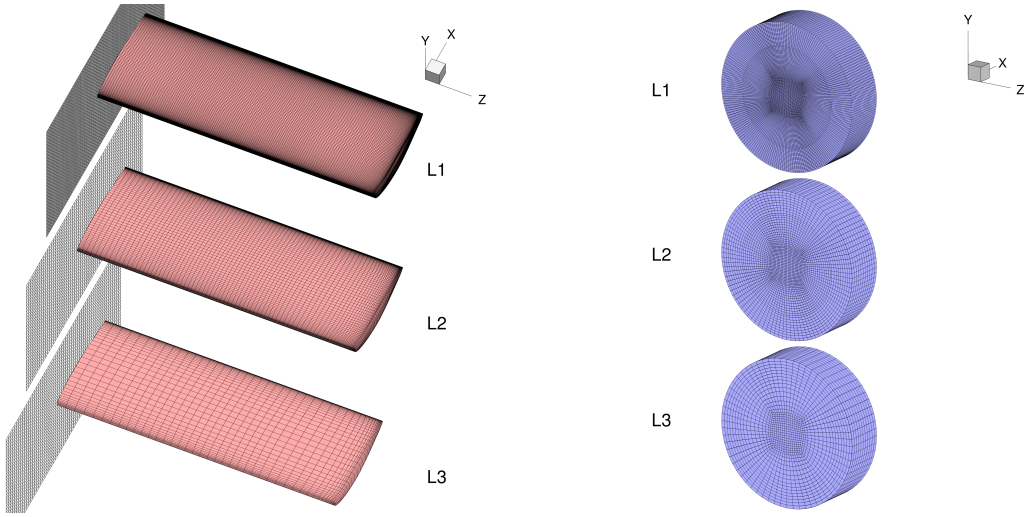

(a) Grid spacings for the L1, L2, and L3 wing surface and Cartesian background meshes

(b) L1, L2, and L3 cylindrical volume meshes

Figure 8.2.3: Comparing L1, L2, and L3 grids

To generate the wing volume meshes, we extrude the wing surface meshes to 0.4 chord lengths around the wing using pyHyp. The L1, L2, and L3 wing volume meshes have 80, 40, and 30 layers of cells extruded around the wing, respectively. The L1, L2, and L3 background meshes have 60, 30, and 15 layers of cells in the far-field extrusion, respectively. The maximum growth ratios, in the off-wall directions, of the wing volume-mesh layers range from 1.1 to 1.3, 1.2 to 1.3, and 1.3 for the L1, L2, and L3 meshes, respectively. The cell thicknesses of the first off-wall layers for the L1, L2, and L3 meshes are set to flat-plate y^+ values of 0.5, 1, and 2, respectively (for the flow conditions of the optimization cases, these would be approximately doubled). The boundary layer resolution does not give a complete picture, and the spanwise discretization of the wing, the radial discretization of the actuator region, and the relative discretizations of the overset interpolation regions are just as important.

To add an additional data point for the mesh refinement plots presented later in

Secs. 8.5 and 9.1.5, we also include results for an intermediate (L1.5) mesh. This mesh is generated with half the number of chordwise wing-surface cells and half the number of layers for the background far-field extrusion as the L1 mesh, but with the rest of the mesh settings, including the spanwise wing-surface discretization, kept the same as those for the L1 mesh. Table 8.2.1 lists the numbers of cells in the four overset meshes, and Table 9.4.1 in Sec. 9.4 lists non-orthogonality and skewness quality metrics for them. Their mean non-orthogonality and skewness values are low, which is favorable for accuracy.

Table 8.2.1: Numbers of cells in the overset meshes

Mesh	Total number of cells	Total number of computation cells, N
L1	10,621,440	10,085,277
L1.5	6,302,080	5,886,188
L2	1,343,520	1,263,010
L3	509,152	472,605

8.3 Propeller Model Inputs

For the adjustable parameters mentioned in Sec. 7.5, we use $a = 1$, $m = 1$, and $n = 0.2$, which gives a loading distribution with the peak near the tip. For the propeller we are modeling, $P/D_{\varnothing}$ ranges from 0.9 to 1.1 for the $r/R = 0.45$ to $r/R = 0.95$ portion of the blades [141]. However, we use $P/D_{\varnothing} = 0.85$ in Eq. (7.5.3) to better match the experimental data plotted in Fig. 8.4.1. Equation (7.5.3), which gives the tangential force distribution as a function of the axial force distribution, is based on the assumptions that the propeller has radially constant pitch and that the forces on the blade are locally perpendicular to the blade chords, which are approximations.

CFD simulations by Stokkermans et al. [5] for this propeller show that the thick root sections of the blades from $r/R = 0.35$ to the root generate negative thrust due

to flow separation. Therefore, for our model, we set $r_{\text{in}} = 0.35R$ and use the axial force distribution from Eq. (7.5.1) between $r = R$ and $r = 0.15R$ (the spinner radius is $0.15R$), which gives negative thrust values between $r = 0.35R$ and $r = 0.15R$. Additionally, for the region between $r = 0.35R$ and $r = 0.15R$, we reduce the axial forces given by Eq. (7.5.1) by multiplying them by a factor of 0.25, as the results of Stokkermans et al. [5] show a change in slope after the axial force becomes zero at approximately $r = 0.35R$. For the spinner portion ($r < 0.15R$), we set the axial forces to zero. The portion of the propeller not generating positive thrust also roughly coincides with the diameter of the nacelle ($r = 0.3R$).

For the tangential forces, we use the distribution from Eq. (7.5.3) only between $r = R$ and $r = 0.35R$, and we set the tangential forces to zero for $r < 0.35R$. The reference value $\tilde{F}$ is set to a value that makes the total axial force applied to the region outside r_{in} equal to the specified thrust. We use the region outside r_{in} because Veldhuis [4] mentioned that the thrust coefficients for the test cases were computed using a bookkeeping approach with pressure measurements, and we consider these thrust coefficients to more likely represent the thrust generated by the propeller region outside the nacelle radius of $r = 0.3R$. The resulting distributions using Eqs. (7.5.1) and (7.5.3) are compared with each other in Fig. 8.3.1. These are also compared with the full-blade unsteady RANS CFD simulation results of Stokkermans et al. [5] for this propeller (isolated configuration) in Fig. 8.3.2. The 3-D geometry of this four-bladed propeller is shown later in Fig. 8.4.2.

8.4 Validation Results

Sectional lift coefficients from ADflow and experimental data for the 0 deg and 4 deg validation cases are compared in Fig. 8.4.1. The results match the experimental

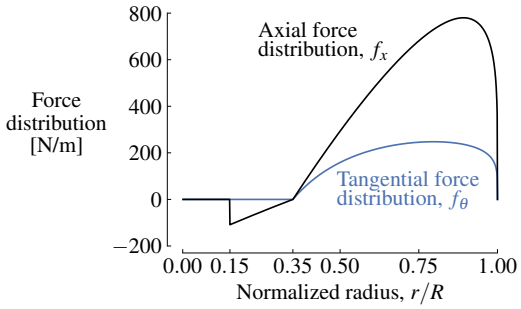

Figure 8.3.1: Distributions of the axial and tangential forces from the propeller-loading model for the validation cases ($J = 0.85$ and $C_T = 0.168$)

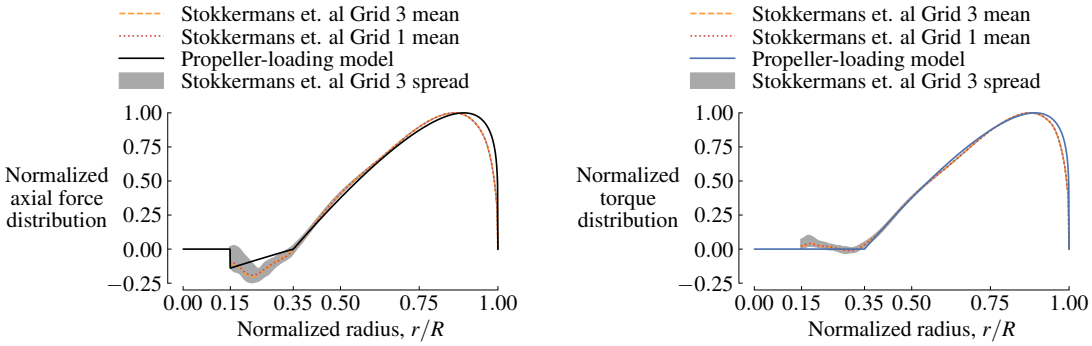

(a) Axial force distribution

(b) Torque distribution

Figure 8.3.2: The propeller-loading model compared with unsteady CFD results from Stokkermans et al. [5] (Grid 3 has $7.4 \cdot 10^6$ cells and Grid 1 has $21.4 \cdot 10^6$ cells)

data well for the 0 deg case and reasonably well with some discrepancies for the 4 deg case.

One discrepancy is the higher lift predicted inboard of the propeller and behind the up-going-blade region for the 4 deg case. A possible physical source of this error is that our axisymmetric propeller model does not capture the non-axisymmetric propeller loading that occurs in reality when there is an angle of attack or wing upwash. When the propeller is at a positive angle of attack, the sections of an up-going blade experience lower effective angles of attack and lower effective speeds than the sections of a down-going blade because of the component of the freestream velocity parallel to the plane of the propeller disk. This results in the up-going

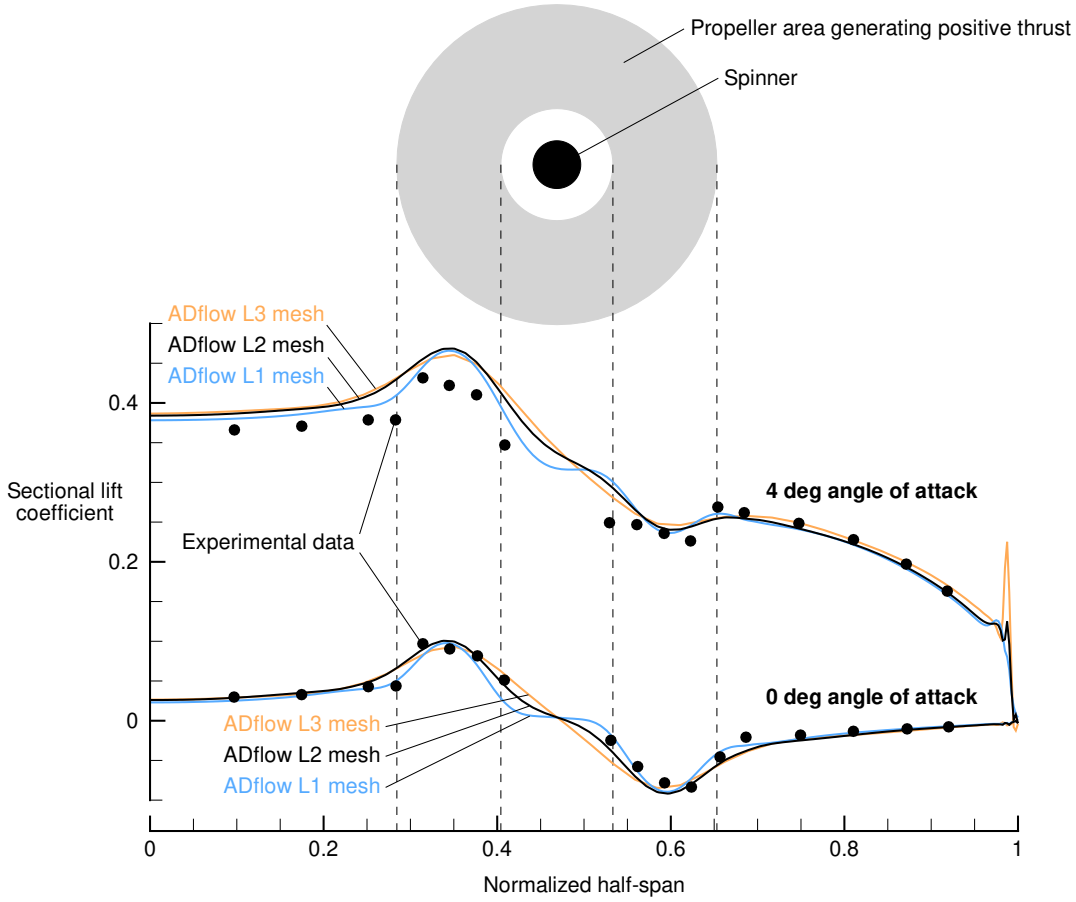

Figure 8.4.1: Sectional lift coefficients from ADflow compared with experimental data from Veldhuis [4]

blade applying lower forces, and consequently lower swirl, to the fluid and the down-going blade applying higher forces, and consequently higher swirl, compared to the axisymmetric forces that result when the propeller is not inclined. Other sources of error include the absence of the nacelle in our simplified geometry.

To visualize the effect of the propeller model on the pressure distributions across the wing, pressure coefficient (C_p) contours and shapes of the distributions at four distinct locations are shown in Fig. 8.4.2 for the 4 deg angle-of-attack case. The C_p curves show a higher suction peak behind the up-going-blade region compared to the sections near the root and the tip of the wing. On the other hand, a leading-edge suction peak is not present behind the down-going-blade region. The C_p distributions

of these two airfoil sections behind the propeller are also compared with experimental data in Fig. 8.4.3. There are offsets, but the shapes match.

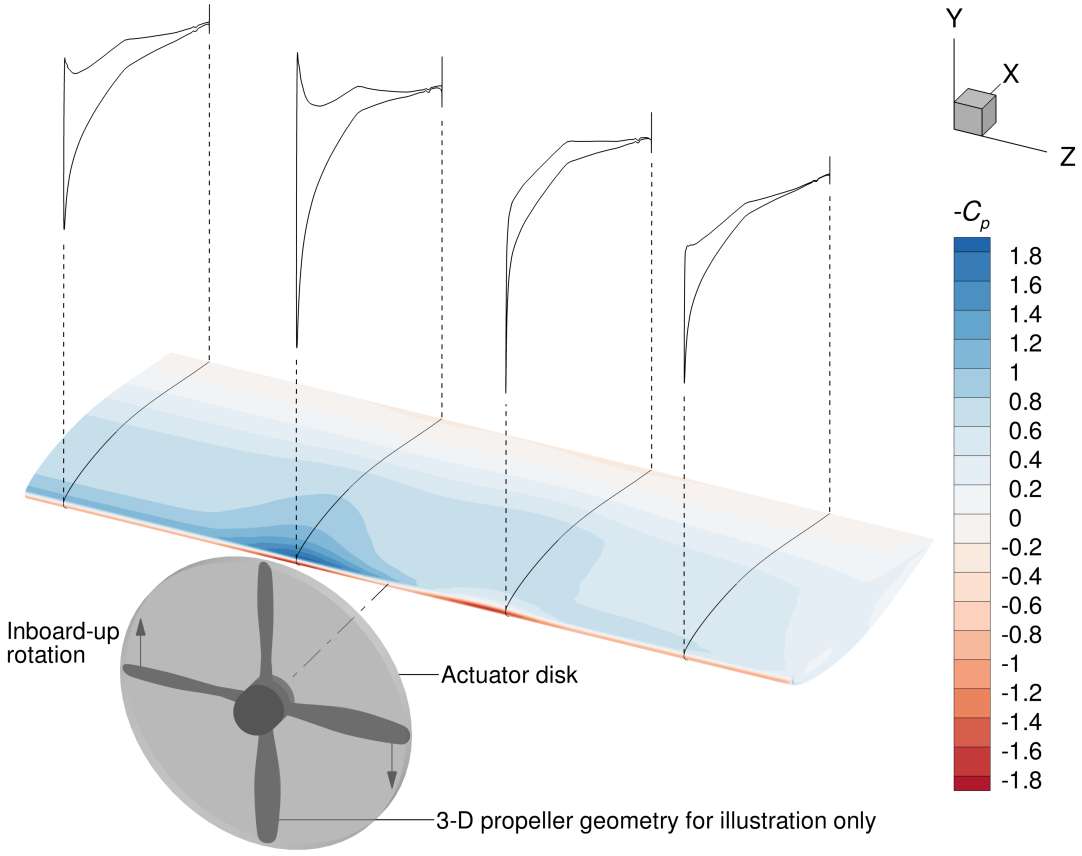

Figure 8.4.2: C_p contours and curves showing the influence of the propeller model on the wing for the 4 deg validation case (L2 mesh; propeller geometry from Sinnige et al. [7])

8.5 Mesh Refinement

Figures 8.5.1 and 8.5.2 plot the lift coefficient (C_L) and drag coefficient (C_D) of the wing for the validation cases and show that, unlike C_D, C_L does not decrease monotonically as the mesh is refined. The CFD solver settings and angle of attack are kept the same for all the meshes within each of these cases. Note that here, and in the rest of this part of the dissertation, these coefficients are only for the wing and are computed by integrating the forces on the wing surface. Because the mesh resolution affects both C_L and C_D, which are not independent, and because all the optimization

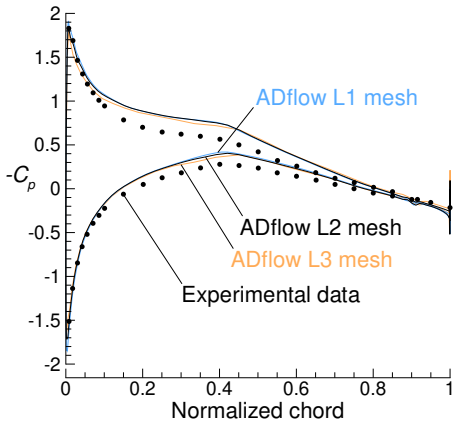

(a) 35% half-span location (behind up-going blade)

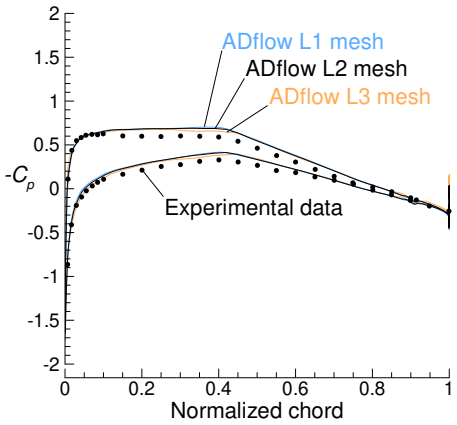

(b) 62% half-span location (behind down-going blade)

Figure 8.4.3: Airfoil C_p distributions from ADflow compared with experimental data from Veldhuis [4] for the 4 deg validation case

cases in this part of the dissertation will constrain C_L to a fixed value, we include another mesh refinement study with a fixed C_L in Sec. 9.1.5 that is more useful for judging these meshes for the optimization cases. We plot the coefficients with respect to $N^{-2/3}$, where N is the number of computation cells, because the inverse of the cube root of the number of cells in a 3-D hexahedral mesh gives a metric for the grid spacing and because ADflow uses a 2$^{\text{nd}}$-order-accurate finite-volume approach for the spatial discretization.

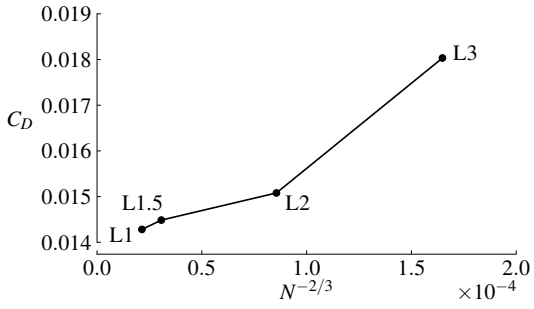

(a) Drag coefficient

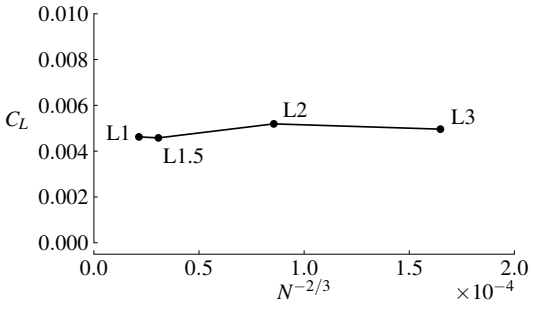

(b) Lift coefficient

Figure 8.5.1: Mesh refinement plots for the 0 deg validation case (N is the number of computation cells)

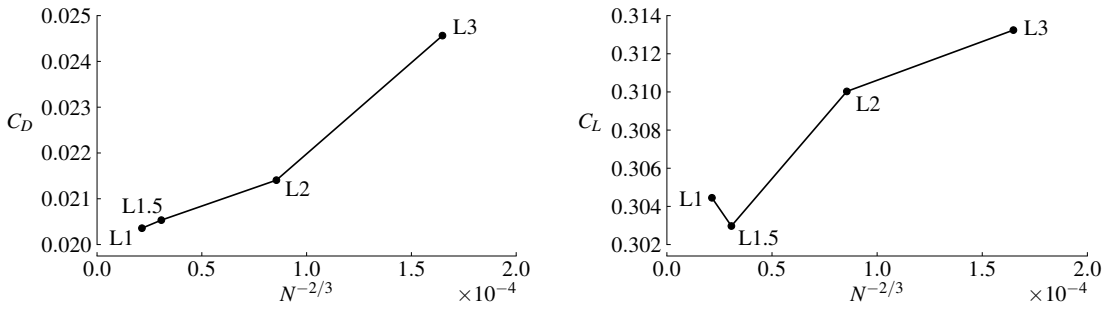

(a) Drag coefficient

(b) Lift coefficient

Figure 8.5.2: Mesh refinement plots for the 4 deg validation case (N is the number of computation cells)

CHAPTER 9

Optimization Problem Formulations and Results for a Wing with an Inboard-Mounted Propeller

> The design of the wing for an efficient integrated propulsion system is affected more by the presence of the propeller than the propeller design is affected by the wing's presence. The wing airfoil shape, twist distribution, and chord must be modified—not to obtain a pressure distribution similar to the clean wing distribution, nor for an efficient power-off span load distribution, but rather to approximate the optimal power-on lift distribution.
>
> *I. Kroo* [32]
> Professor, Stanford University, 1986

9.1 Optimization Problem Descriptions

9.1.1 Geometry and Parameterization

For the optimization cases discussed in this section and in Secs. 9.2 and 9.3, we use the same wing and propeller geometry (0.24 m by 0.64 m half-wing with a 0.24 m diameter propeller) used for the validation cases in Chapter 8. We use the L2 mesh described in Sec. 8.2 and the same propeller model inputs discussed in Sec. 8.3, except for the pitch-to-diameter and total-thrust values, which are modified for the flight conditions described in Sec. 9.1.2. Also, we study both outboard-up and inboard-up propeller rotation cases. We only optimize the wing, and the optimizations begin with the wing untwisted and both the wing and the propeller at an angle of attack

of 0 deg. The actuator disk keeps its angle of attack of 0 deg and does not follow the wing as the wing's inclination changes. We use the L2 mesh because it provides reasonably good resolution at a significantly lower computational cost than the L1 and L1.5 meshes.

The grid of FFD control points that we use to deform and optimize the geometry is shown in Fig. 9.1.1. The positions of these control points are the design variables. The grid has 13 chordwise sections along the span and 8 spanwise sections along the chord. There are 104 control points above the wing and 104 below it (208 in total)*. The control points of each chordwise section can be rigidly rotated together to twist the wing, and all the control points can be moved individually in the vertical direction (y-direction) to change the shapes of the airfoil sections along the wing. The planform area and planform shape of the wing are not optimized in any of the cases presented in this chapter. We place control points closer together over the portions of the wing behind the up-going-blade and down-going-blade regions of the propeller disk for greater control of those portions.

9.1.2 Flight Conditions

The flight conditions that we use for the optimization cases are selected to be representative of a cruise condition for general aviation (GA) and urban air mobility (UAM). We specify a cruise C_L of 0.6 at a Mach number of 0.3 and an altitude of 1500 ft. We also assume that the hypothetical aircraft that the wing belongs to has a cruise lift-to-drag ratio of 10. Based on these numbers, we specify a thrust of 55.0 N for the propeller. Assuming a rotational tip speed of Mach 0.6 (typical for turboprop

*Based on prior experience, the guideline in the MDO Lab is to use roughly $10 \times 2 \times 10$ FFD control points for wing optimization [142]. There is usually little to be gained beyond this approximate resolution. An additional guideline is to have no more than one FFD control point for every four CFD surface-mesh points of a cross-section [130] (e.g., if a wing cross-section has 40 chordwise CFD mesh points on its upper surface, there should not be more than 10 corresponding chordwise FFD control points).

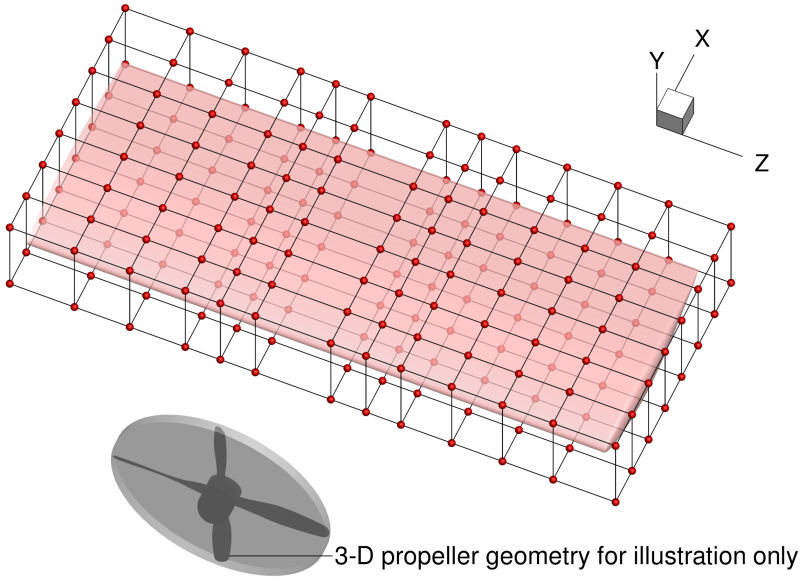

Figure 9.1.1: FFD grid ($8 \times 2 \times 13$ control points) around the wing geometry

aircraft at cruise), the corresponding advance ratio J is 1.6, and the corresponding thrust coefficient C_T is 0.20. This thrust coefficient is on the higher side of the range for typical GA and commuter aircraft at cruise [143–145]. Based on the efficiency charts of typical propellers [41, 143, 144], the pitch angle at $0.75R$ for this advance ratio will likely be around 40 deg. This approximately doubles the propeller pitch-to-diameter ratio used in the validation cases (the pitch angle at $0.75R$ for the validation cases is 24 deg [141]). Therefore, for the optimization cases, we use a $P/D_{\varnothing}$ value of 1.7, which is twice the value used for the validation cases.

9.1.3 Primary Optimization Problem Formulations

We have two primary optimization cases. Table 9.1.1 summarizes the optimization problem formulation for the first optimization case, Case wP+T. In Case wP+T, with the propeller (wP) model included in the simulations during optimization, we optimize the wing twist (T). The twist is controlled by rigidly rotating the FFD control points of each of the 13 chordwise FFD sections located along the span, about their respective quarter-chord points. There are 16 FFD control points, but

only one twist variable, for each chordwise section. We optimize the wing twist using all 13 chordwise FFD sections, including the root section, which means that the twist design variables can also rotate the entire wing and effectively change its angle of attack without changing the angle of attack of the propeller disk. The optimization objective is to minimize C_D, subject to a lift constraint of $C_L = 0.6$. These coefficients are only for the wing and do not include components of the propeller's thrust vector, which remains at an inclination of 0 deg. Additionally, these coefficients do not include any contributions from other components of the hypothetical aircraft that we assume this wing belongs to.

Table 9.1.1: Case wP+T optimization problem formulation

	Function/variable	Description	Quantity
Minimize	C_D	Drag coefficient	
with respect to	$0 \leq \tau \leq 10.0$	Twist of each FFD section [deg]	13
		Total design variables	**13**
subject to	$C_L = 0.6$	Lift constraint	1
		Total constraint functions	**1**

Table 9.1.2 summarizes the optimization problem formulation for the second optimization case, Case wP+T+S. In Case wP+T+S, with the propeller (wP) model included in the simulations during optimization, we optimize the wing twist (T) and the airfoil shapes (S) along the wing. The twist is controlled by rigidly rotating the FFD control points of each section, as described earlier, and the airfoil shapes along the wing are controlled by vertically displacing the individual FFD control points. The optimization objective is again to minimize C_D, subject to a lift constraint of $C_L = 0.6$. We also use thickness constraints to prevent the thickness of the wing from decreasing. We use locations on a uniform 10 by 10 grid over the wing planform to enforce these constraints on. These constraints are used because considerations related to the wing structure or internal components are not considered directly. Ad-

ditionally, we apply constraints on the leading-edge and trailing-edge airfoil-shape design variables to prevent them from moving the leading and trailing edges vertically and from creating shear twist. This ensures that the twist and airfoil-shape design variables are independent, for a well-posed optimization problem, and this is achieved by ensuring that the airfoil-shape design variables only move the FFD control points on the leading and trailing edges equal distances in opposite directions, within each vertical pair. This does not restrict the optimizer's ability to add camber.

Table 9.1.2: Case wP+T+S optimization problem formulation

	Function/variable	Description	Quantity
Minimize	C_D	Drag coefficient	
with respect to	$0 \leq \tau \leq 10.0$	Twist of each FFD section [deg]	13
	$-1.44 \leq \Delta y \leq 1.44$	Vertical displacements of the FFD control points for airfoil-shape control (±40% of the airfoil maximum thickness) [cm]	208
		Total design variables	**221**
subject to	$C_L = 0.6$	Lift constraint	1
	$t_\mathrm{a}/t_\mathrm{a,initial} \geq 1.0$	Constraints to prevent airfoil thicknesses at locations on a uniform 10 by 10 grid from decreasing	100
	$\Delta y_\mathrm{LE,upper} = -\Delta y_\mathrm{LE,lower}$	Constraints to prevent the airfoil-shape design variables from vertically displacing the leading edge	13
	$\Delta y_\mathrm{TE,upper} = -\Delta y_\mathrm{TE,lower}$	Constraints to prevent the airfoil-shape design variables from vertically displacing the trailing edge	13
		Total constraint functions	**127**

9.1.4 Baseline Optimization Cases for Comparison

To quantify the benefit of optimizing the wing while considering propeller effects, we also optimize the wing without propeller effects (i.e., without applying forces to the actuator disk) to obtain baseline cases for comparison. The FFD grid used for these baselines cases is the grid used for the wP cases (Fig. 9.1.1) without the fifth and eighth chordwise FFD sections, counting from the root (the control points at these sections are present for greater control over the region behind the propeller for the wP cases).

The first baseline optimization case, Case T, has the same formulation as Case wP+T, except that it has the aforementioned different number of FFD control points and no

forces applied to the actuator disk. The second baseline optimization case, Case T+S, has the same formulation as Case wP+T+S, except that it has the aforementioned different number of FFD control points and no forces applied to the actuator disk. After optimization, the resulting wings from these baseline cases are analyzed with the propeller forces applied to the actuator disk and with the wing angle of attack adjusted to achieve the specified C_L of 0.6. The wing's angle of attack is adjusted by rotating it using the FFD grid. This gives one-to-one comparisons that allow quantifying the benefit that optimizing a wing with propeller effects considered gives over optimizing the same wing without considering propeller effects.

9.1.5 Mesh Refinement

Because all the optimization cases in this chapter constrain the lift coefficient to 0.6, we include another mesh refinement study here to show how the drag coefficient converges when the lift coefficient is held constant at this value. This differs from the mesh refinement study presented in Sec. 8.5, which is for constant angles of attack and different flow conditions. Figure 9.1.2, which plots C_D for the meshes described in Sec. 8.2 (unoptimized geometry) with the flow settings used for the optimization problems (Sec. 9.1.2), shows linear trends with respect to $N^{-2/3}$, as is expected with our 2^{nd}-order-accurate finite-volume scheme [122, 127, 142, 146]. To achieve the specified C_L, only the wing's angle of attack is adjusted by rotating it using the FFD grid (without twisting it), and the actuator disk keeps its angle of attack of 0 deg and does not follow the wing as the wing's inclination changes. This angle-of-attack adjustment is performed through an optimization (objective: minimize difference to target C_L).

Our experience and earlier research [122, 142, 146] have shown that, with our framework and methods, the mesh refinement results for an optimized geometry

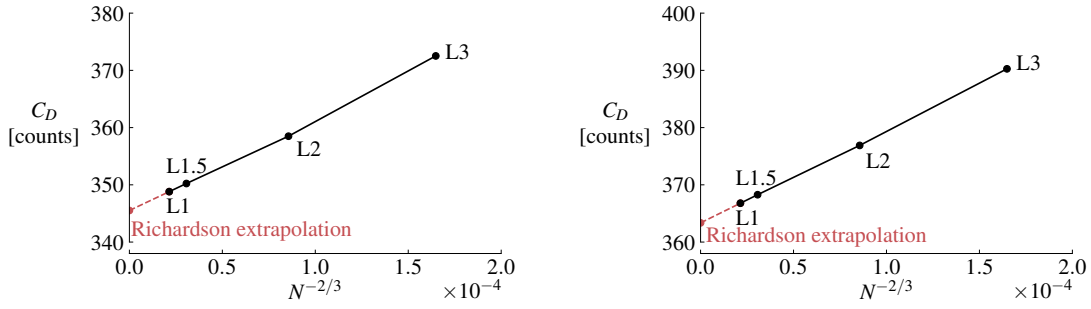

(a) Drag coefficient with inboard-up rotation

(b) Drag coefficient with outboard-up rotation

Figure 9.1.2: Mesh refinement results with the optimization-problem flow conditions for the unoptimized geometry ($C_L = 0.6$ for all)

follow the same trend as the mesh refinement results for the unoptimized geometry, with roughly the same drag offset at each refinement level. Therefore, if we carried out mesh refinement studies for each of the optimized geometries obtained in this work, we would expect to see the same trends shown in Fig. 9.1.2, with roughly the same reduction in drag at each refinement level.

9.2 Optimization Results

The drag coefficients plotted in Fig. 9.2.1 show that, although the drag reductions from changing the propeller rotation direction from outboard-up to inboard-up ($\sim$ 18 counts) and optimizing the wing twist and airfoil shapes ($\sim$ 14 counts) are significant, the drag reductions obtained by optimizing the wing while considering the propeller slipstream, compared to optimizing it without considering the propeller slipstream, are negligible (less than one drag count). As described in Sec. 9.1.4, the wings optimized without considering the propeller (Cases T and T+S) are analyzed with the propeller model and matched to the required lift coefficient after optimization to allow these direct comparisons.

The optimized twist distributions in Fig. 9.2.2 show that, when the propeller model is included in the simulations during optimization (Cases wP+T and wP+T+S),

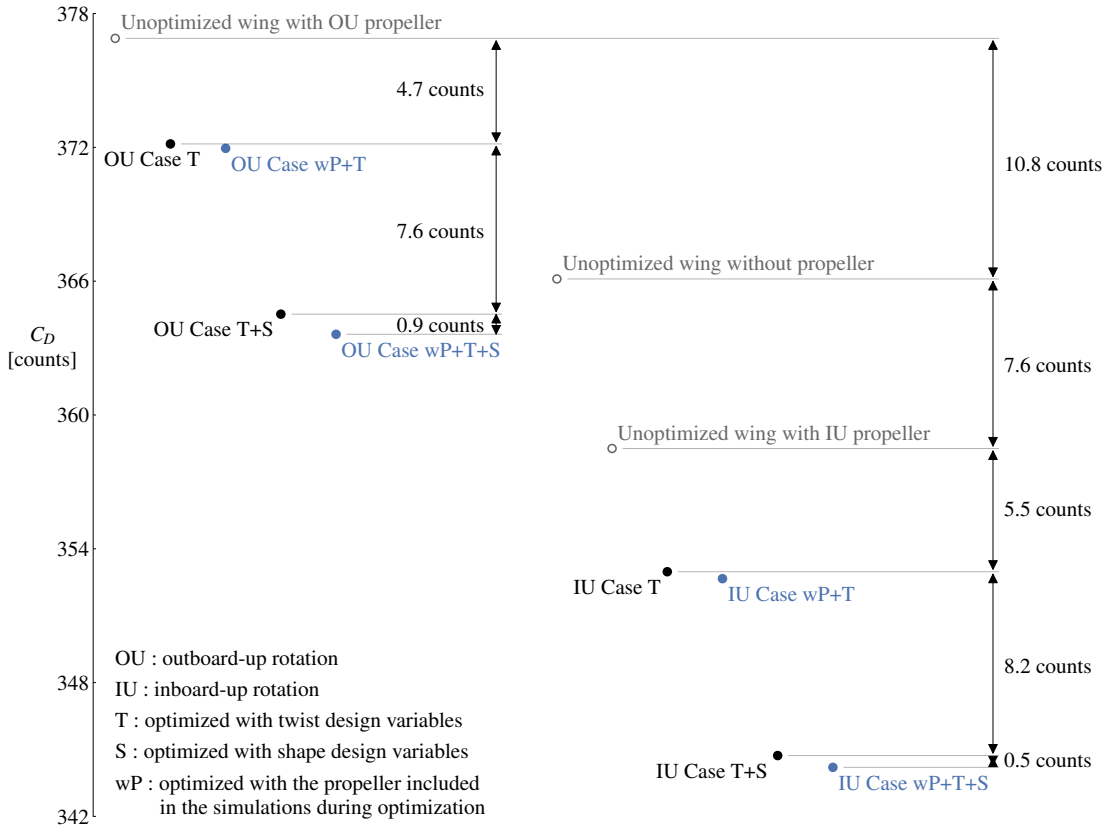

Figure 9.2.1: Reference and optimized drag coefficients ($C_L = 0.6$ for all)

the optimizer decreases the twist angle behind both the up-going-blade and down-going-blade regions. There are also related reductions in lift behind the propeller and increased lift near the root or tip to compensate, as shown by the lift distributions in Fig. 9.2.2.

When airfoil-shape design variables are added, the resulting twist angle of most of the wing is smaller because the optimizer adds camber. There is also significant twisting at the tips, which results in nonplanar wingtips (Figs. 9.2.3 and 9.2.4). Since the optimized wings for both Cases T+S and wP+T+S have similar wingtips, we can safely conclude that this feature is not related to propeller effects. These nonplanar wingtips can be attributed to induced-drag reductions from a reduction in average wing downwash as the shed vorticity is moved away from the wing plane [147]. Similar

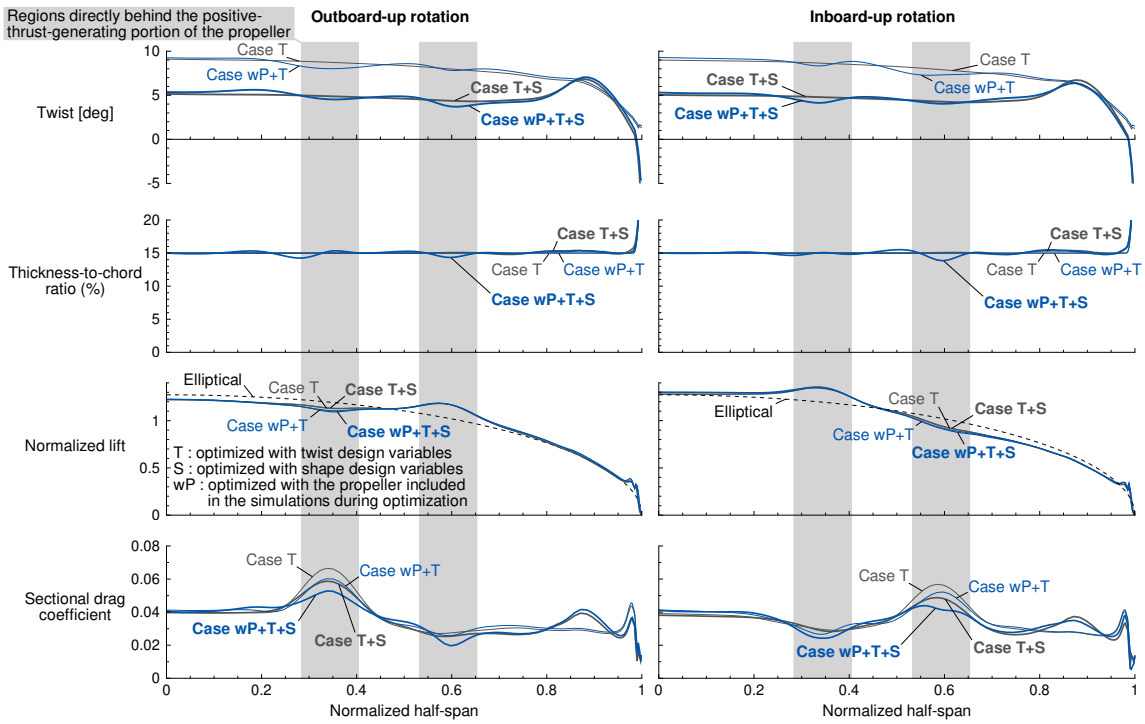

Figure 9.2.2: Optimized twist, thickness, lift, and drag distributions for the primary and baseline optimization cases

nonplanar wingtips from twist optimization were obtained by Bons et al. [129] and Reist et al. [148].

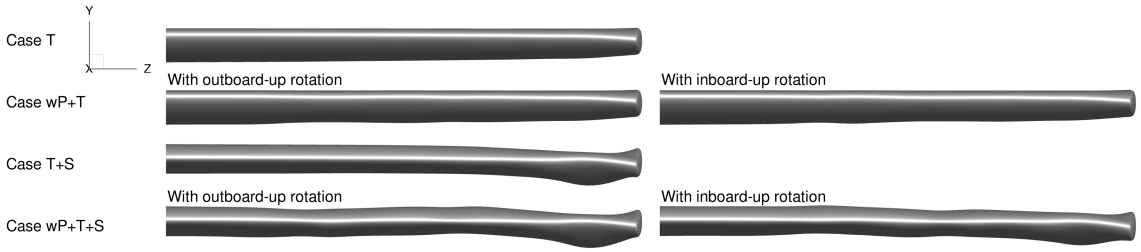

Figure 9.2.3: Front view of the optimized wings

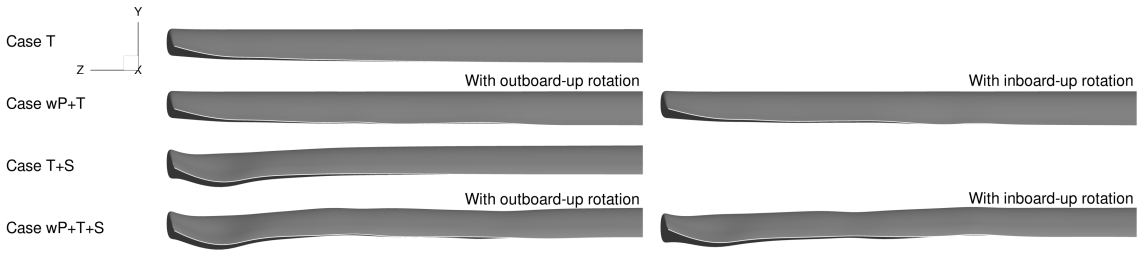

Figure 9.2.4: Rear view of the optimized wings

The lift distributions of the optimized wings are not exactly elliptical (Fig. 9.2.2). From a lifting-line point of view, induced drag depends on the span integral of the product of circulation and downwash. Therefore, for a fixed total lift, it is advantageous to have more lift (i.e., more circulation) where the propeller induces an upwash (i.e., negative downwash) and less lift where the propeller induces a downwash. Another way to view this is to compare it to a stator recovering rotational energy from the flow [32]. However, Kroo [32] points out that, although swirl recovery is also obtained naturally to some extent by an untwisted wing, this does not imply that the naturally resulting lift distribution will be the optimal lift distribution.

Figure 9.2.2 also shows that, for each propeller rotation direction, the resulting lift distributions are almost identical for all the cases. The drag coefficient curves (Fig. 9.2.2) show that, when the propeller model is included in the optimization simulations (Cases wP+T and wP+T+S), the optimizer decreases the drag behind the propeller. However, there are also associated reductions in lift behind the propeller, and the adjustments required to satisfy the lift requirement cause these drag reductions to come with drag penalties near the wing root and tip that reduce the overall benefit. This indicates that, at least for similar configurations and operating conditions, a wing optimized without considering the propeller slipstream can recover swirl practically as effectively as a wing optimized while considering the propeller slipstream.

Figures 9.2.5 and 9.2.6 show that with airfoil-shape design variables the airfoils are cambered, the suction peaks are reduced, and the lift generated by the rear portion of the airfoils is increased. For Case wP+T+S, the optimizer also takes advantage of weaknesses in the thickness constraints to slightly reduce the thickness behind the propeller (Fig. 9.2.2). Visually, there is little difference between the airfoils op-

timized with and without the propeller slipstream. This is because the optimized lift distributions shown in Fig. 9.2.2 do not have large deviations from elliptical and, therefore, the airfoils are not optimized for significantly different sectional lift coefficients between the cases. Propeller-induced velocities, both axial and tangential, at cruise conditions are relatively low in general because of the high freestream speed. This is also the case here and helps explain why the deviations from elliptical are small (for the flight conditions used here, the maximum speed $0.5R$ downstream of the actuator disk is only $\sim$10% higher than the freestream speed).

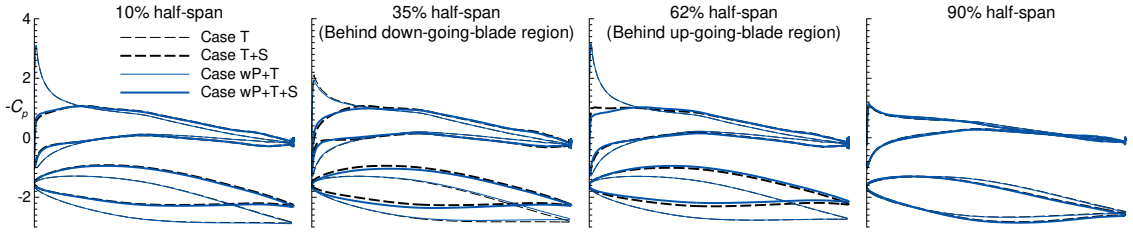

Figure 9.2.5: Optimized airfoil shapes and C_p distributions with outboard-up rotation

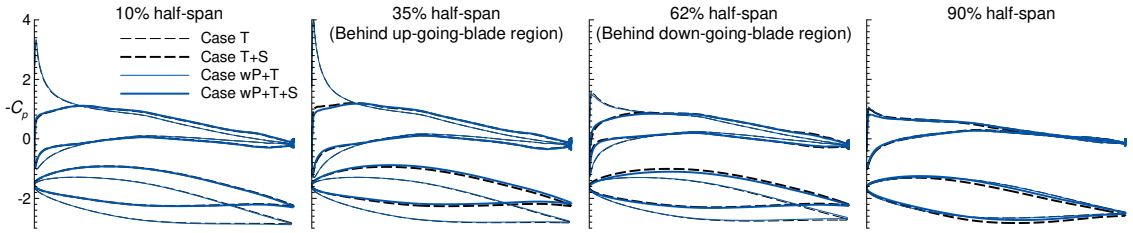

Figure 9.2.6: Optimized airfoil shapes and C_p distributions with inboard-up rotation

The lift distributions of the optimized wings from Cases T and T+S before being analyzed with the propeller model are shown in Fig. 9.2.7 and are elliptical, as expected. Additionally, the breakdown of the sectional drag distributions into pressure and shear components in Fig. 9.2.7 shows that the propeller has a more significant impact on the pressure drag.

Table 9.4.1 in Sec. 9.4 lists non-orthogonality and skewness quality metrics for the meshes of the initial and optimized geometries. The mean non-orthogonality and

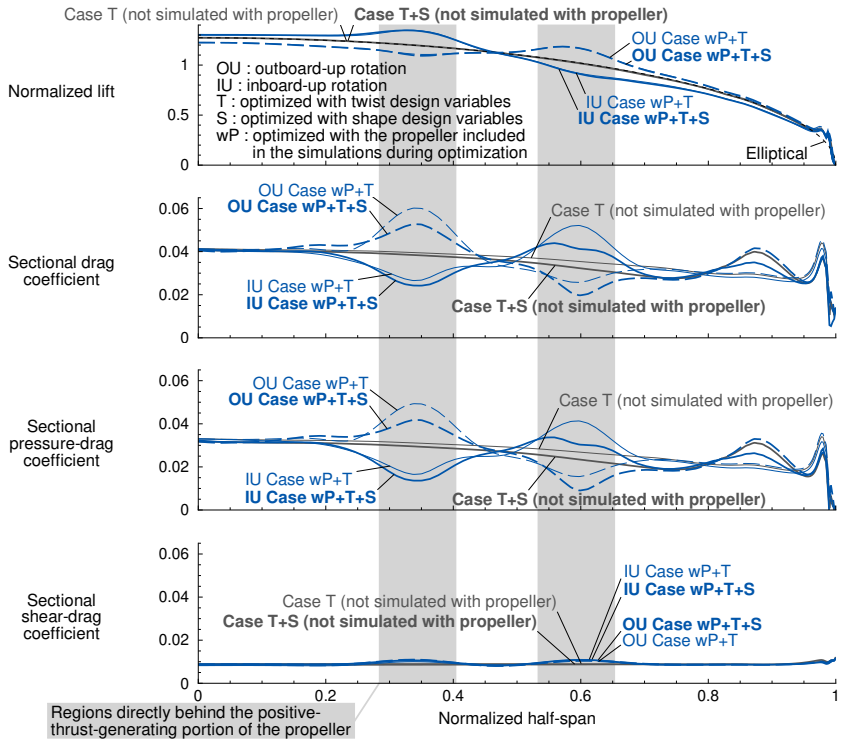

Figure 9.2.7: Lift and drag distributions for the optimized wings from Cases T and T+S, before being analyzed with the propeller model, compared with Cases wP+T and wP+T+S

skewness values of the deformed meshes remain low, which is favorable for accuracy.

9.3 Additional Optimization Cases with Extra Design Freedom

To verify that the small drag benefits of optimizing the wing while considering the propeller slipstream (Sec. 9.2) are not an artifact of overly restrictive thickness constraints or design-variable bounds, we include results for two additional optimization cases that have extra design freedom. These cases, named Cases T+xS and wP+T+xS, do not have thickness constraints, and their airfoil-shape design variables have larger bounds equal to twice those of Cases T+S and wP+T+S (Table 9.1.2). Apart from these differences, Cases T+xS and wP+T+xS have the same optimization problem formulations as Cases T+S and wP+T+S, respectively. These additional cases are not practical design cases because of the lack of thickness constraints in

the absence of structural and packaging considerations.

Again, we find little difference in the final drag when the wing is optimized with or without the presence of the propeller slipstream (Fig. 9.3.1). The optimizer uses the extra design freedom to reduce drag by decreasing the wing thickness, but the differences in the resulting thickness distributions between these two cases are small (Fig. 9.3.2). Also, for each propeller rotation direction, the lift distributions again are almost identical, and they closely match the lift distributions of the primary cases.

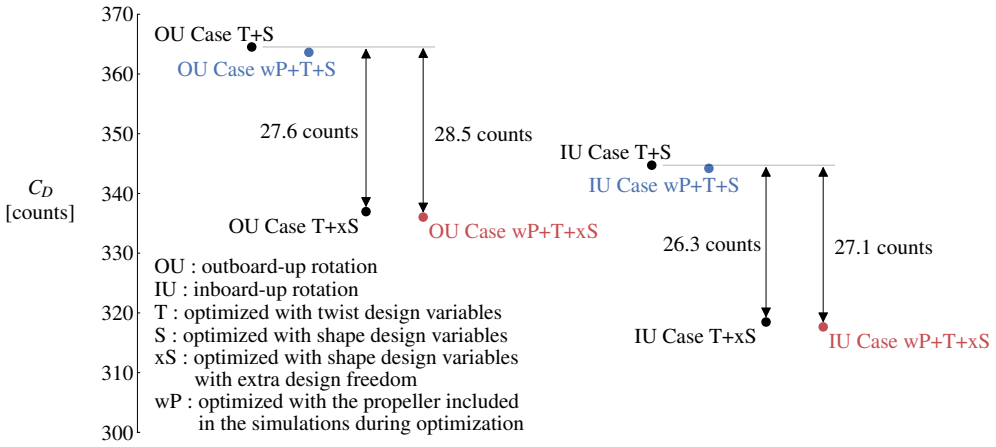

Figure 9.3.1: Optimized drag coefficients for the additional cases that have extra design freedom (Cases T+S and wP+T+S included for comparison; $C_L = 0.6$ for all)

We obtain a different mode of wingtip twisting for these additional cases. Instead of a trailing edge that curves up at the wingtip, the trailing edge curves down (Fig. 9.3.3). This multimodality is similar to the multimodality of winglets in which upward and downward winglets are local optima [129, 149, 150]. Again, because both Cases T+xS and wP+T+xS have this feature, we conclude that this is not related to the propeller.

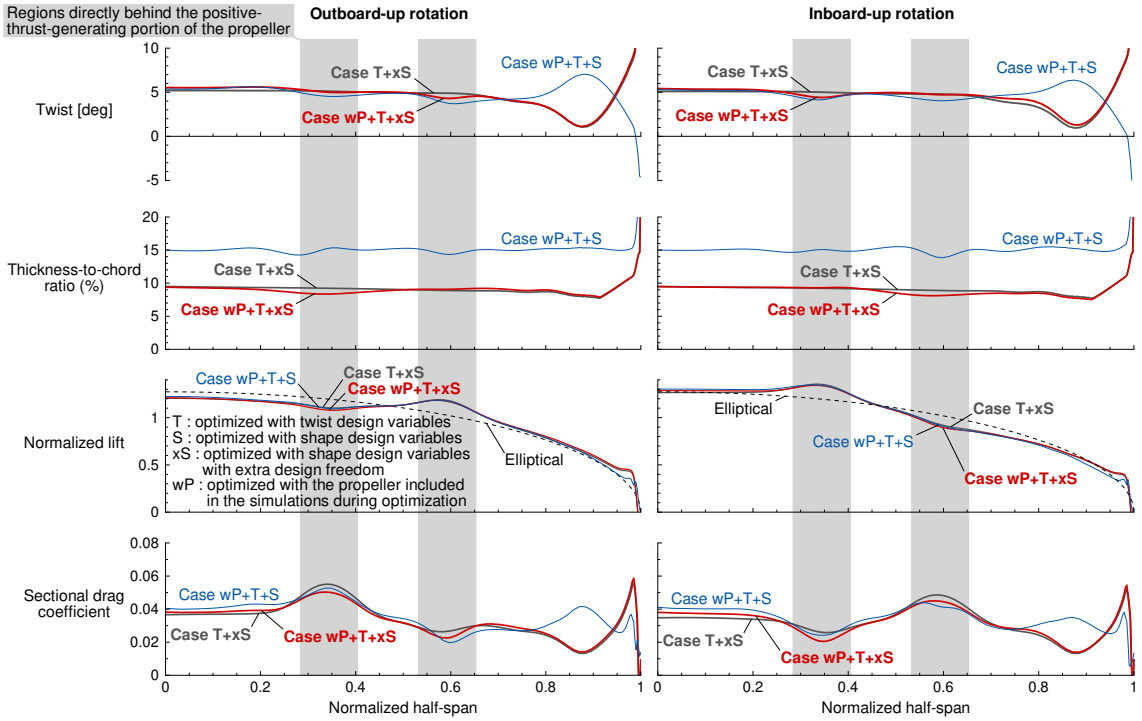

Figure 9.3.2: Optimized twist, thickness-to-chord ratio, lift, and drag distributions for the additional cases (Case wP+T+S included for comparison)

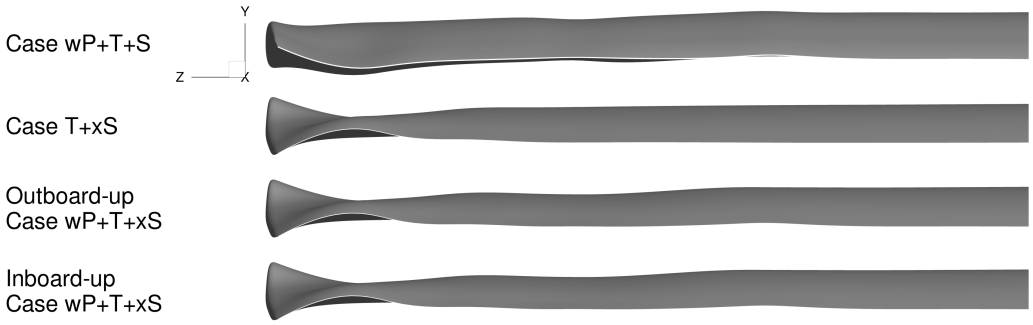

Figure 9.3.3: Rear view of the optimized wings for the cases with additional design freedom, Cases T+xS and wP+T+xS, compared with Case wP+T+S

9.4 Mesh Quality Metrics

Table 9.4.1 lists non-orthogonality and skewness metrics for the meshes of the initial and optimized geometries (see Secs. 8.2, 9.1.3, 9.1.4, and 9.3 for descriptions of the meshes and cases). The non-orthogonality is defined as the angle between the line joining the cell centers of two cells and the normal of their common face. The

skewness is defined as the ratio of the distance between the intersection point of the line joining two cell centers with the plane of their common face and the center of that face to the distance between the cell centers. These metrics are computed using OpenFOAM's† [151] checkMesh utility, and Jasak [152] discusses their significance. Overall, the mean non-orthogonality values of the meshes are low, which is favorable for accuracy, and they increase a small amount as the design freedom increases. The mean skewness values are also low, and Table 9.4.1 shows that the few faces with high non-orthogonality and skewness are in the wing volume mesh.

Table 9.4.1: Quality metrics for the meshes of the initial and optimized geometries

Domain	Case	Non-orthogonality			Skewness	
		Maximum [deg]	Mean [deg]	Number of faces > 70 deg	Maximum	Mean
Complete mesh	Initial L1	44	3	0	2.3	0.02
	Initial L1.5	45	4	0	2.3	0.03
	Initial L2	45	4	0	2.3	0.03
	Initial L3	51	5	0	2.3	0.05
	Case T	66	7	0	2.2	0.04
	Case T+S	75	7	2	2.6	0.04
	Case T+xS	83	9	5	2.2	0.03
	IU Case wP+T	66	7	0	2.2	0.04
	IU Case wP+T+S	73	7	1	2.6	0.03
	IU Case wP+T+xS	83	9	4	2.2	0.03
	OU Case wP+T	66	7	0	2.2	0.04
	OU Case wP+T+S	76	8	2	2.6	0.03
	OU Case wP+T+xS	83	9	19	2.2	0.03
Wing volume mesh	Initial L1	44	4	0	2.3	0.02
	Initial L1.5	45	4	0	2.3	0.03
	Initial L2	45	4	0	2.3	0.04
	Initial L3	51	5	0	2.3	0.08
	Case T	66	8	0	2.2	0.04
	Case T+S	75	10	2	2.6	0.05
	Case T+xS	83	12	5	2.2	0.04
	IU Case wP+T	66	8	0	2.2	0.04
	IU Case wP+T+S	73	9	1	2.6	0.04
	IU Case wP+T+xS	83	11	4	2.2	0.04
	OU Case wP+T	66	8	0	2.2	0.04
	OU Case wP+T+S	76	10	2	2.6	0.04
	OU Case wP+T+xS	83	12	19	2.2	0.04

9.5 Applicability to Larger Wings

The geometry used for Chapter 8 and Sec. 9.3 is a small wing (0.24 m by 0.64 m half-wing) with a proportionately small propeller (0.24 m diameter). However, because of the flight conditions and settings used, we expect our observations and

†`https://www.openfoam.com/releases/openfoam-v1812/` [Accessed 31 Jul 2020]

conclusions to be valid for GA- and commuter-aircraft-sized configurations as well. In this section, we describe what we expect if the configuration used for the previous sections is scaled to a larger size.

The cruise Mach number for the optimization cases presented in the previous sections, $M = 0.3$, falls in the range typical for GA aircraft and UAM targets, and the corresponding Reynolds number of $1.6 \cdot 10^6$ is in the high Reynolds number range [79]. Therefore, for a larger wing with a correspondingly higher Reynolds number and the same Mach number, the flow behavior is not expected to change. A higher Reynolds number will affect the skin-friction component of the drag coefficient [153], but, with fully turbulent flow, changes to the boundary-layer behavior will not be significant.

For the same cruise speed, altitude, lift coefficient, and aircraft lift-to-drag ratio used in this chapter, all of which fall in a reasonable range for GA and commuter aircraft, the cruise thrust with a different-sized wing will be directly proportional to the wing area. With the reasonable assumption that the propeller diameter scales linearly with the wing chord or span (i.e, with the square root of the wing area for a fixed aspect ratio), this means that the cruise disk loading (i.e., the ratio of the thrust to the propeller disk area) does not change as the wing is scaled. Using momentum theory, this observation can be used to obtain insight on how the induced velocities of the propeller are affected as the configuration is scaled.

As follows, the axial induced velocities and their relative distribution can be shown to remain practically the same when the configuration is scaled. The first-principles-based momentum-theory relation for the axial induced velocity of an annular region of a propeller disk is given by [41]

$$V_{\mathrm{i},x} = \sqrt{\frac{V_\infty^2}{4} + \frac{T_{\mathrm{ann}}}{2\rho A_{\mathrm{ann}}}} - \frac{V_\infty}{2}, \tag{9.5.1}$$

where $V_{\mathrm{i},x}$ is the axial induced velocity, V_∞ is the freestream velocity, ρ is the air

density, T_{ann} is the thrust of the annular region, and A_{ann} is the area of the annular region. If the annular region has a mean radius $r = k_1 R$ and a small radial width $\Delta r = k_2 R$ (where k_1 and k_2 are constant fractions that do not change with the disk size), and R is the propeller radius, then $A_{\text{ann}} \simeq 2\pi k_1 k_2 R^2$. This means that A_{ann} can be written as the product of the total disk area A and a constant of proportionality that is independent of the disk size. Additionally, assuming that the normalized shape of the thrust distribution does not change (i.e., when the a, m, and n parameters in Eq. (7.5.1) of the propeller model are kept fixed), T_{ann} can be written as the product of the total thrust T and another constant of proportionality that is independent of the total thrust and disk size. This can be shown using Eq. (7.5.1) by rewriting it as

$$f_x = \frac{k_3 (r/R)^m (1 - r/R)^n T}{R}, \tag{9.5.2}$$

where k_3 is a constant that is independent of the total thrust and disk size ($1/k_3 = \int_0^1 \tilde{r}^m (1-\tilde{r})^n \mathrm{d}\tilde{r}$, and $\tilde{r} = r/R$). Using $A_{\text{ann}} \simeq 2 k_1 k_2 A$, Eq. (9.5.2) gives

$$\frac{T_{\text{ann}}}{A_{\text{ann}}} = \frac{k_3 (r/R)^{m-1} (1 - r/R)^n T}{2A}. \tag{9.5.3}$$

This means that $T_{\text{ann}}/A_{\text{ann}} \propto T/A$ and is also independent of the size of the configuration. Therefore, from Eq. (9.5.1), we can conclude that the axial induced velocities and their relative distribution remain about the same when the configuration is scaled.

We can also obtain insight on the tangential velocity components using a similar approach. Figure 9.5.1 illustrates a disk to which propeller forces are applied and shows a small control volume in the disk.

Using a momentum balance, assuming axisymmetry, neglecting slipstream contraction across the thin disk, and neglecting viscous terms, the rate of change of

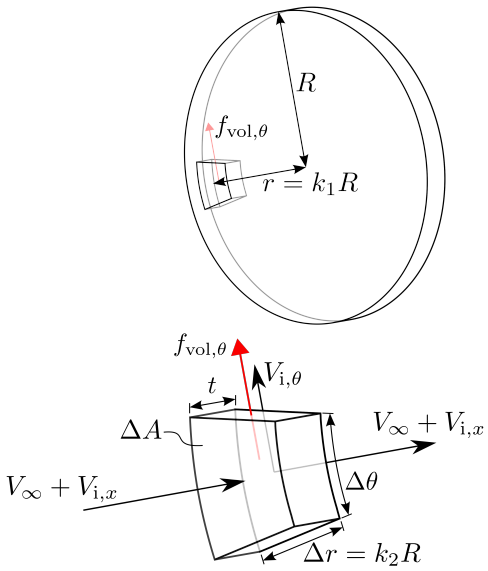

Figure 9.5.1: An element of a disk to which tangential forces are applied

momentum in the tangential direction for the control volume is

$$\rho(V_\infty + V_{\text{i},x})V_{\text{i},\theta}\Delta A = f_{\text{vol},\theta}t\Delta A, \tag{9.5.4}$$

where $V_{\text{i},\theta}$ is the tangential induced velocity, ΔA is the area of the face of the small control volume shown in Fig. 9.5.1, $f_{\text{vol},\theta}$ is the applied tangential force per unit volume, and t is the thickness of the disk. By substituting $f_{\text{vol},\theta} = f_\theta/(2\pi r t)$, Eqs. (7.5.3) and (9.5.2), and $A = \pi R^2$ into its RHS, Eq. (9.5.4) can be rearranged to

$$V_{\text{i},\theta} = \underbrace{\frac{k_3(r/R)^{m-2}(1-r/R)^n}{2\pi}}_{\substack{\text{Only dependent on the normalized} \\ \text{shape of the propeller loading} \\ \text{and the normalized radial position}}} \cdot \frac{(T/A)(P/D_\varnothing)}{\rho(V_\infty + V_{\text{i},x})}. \tag{9.5.5}$$

This simple analytic equation allows estimating swirl velocities and predicting how they change with disk loading, pitch setting, and flight speed. For the same flight and propeller-tip speeds used in this chapter, which fall in the typical range for GA and commuter aircraft at cruise, the advance ratio will not change as the propeller is scaled, and therefore we can also expect the corresponding pitch setting and $P/D_\varnothing$ to

remain about the same. Since we have concluded that, as the configuration is scaled, all the terms in the RHS of Eq. (9.5.5) will remain unchanged, at least approximately, we can also expect the tangential velocities and their relative distribution behind the propeller to remain approximately the same. Furthermore, since the effective local angles of attack seen by the wing depend on the ratio of $V_{\mathrm{i},\theta}$ to $V_\infty + V_{\mathrm{i},x}$, we can also expect these effective angles of attack to remain practically unchanged. This indicates that the observations and conclusions made from the optimization results in the previous sections are also valid for scaled-up configurations with the same flight conditions (i.e., the cruise altitude and Mach number) and the same non-dimensional specifications (i.e., the cruise lift coefficient, aircraft lift-to-drag ratio, and propeller-tip Mach number).

We confirm this hypothesis for a 10X-scaled version (2.4 m by 6.4 m half-wing with a 2.4 m diameter propeller) of the configuration used in the previous sections. This scale is representative of the size of typical twin-propeller GA- and commuter-aircraft wings (Fig. 9.5.2).

We use the T+S and wP+T+S optimization problem formulations (Table 9.1.2) with the bounds of the airfoil-shape design variables and the initial locations of the FFD control points scaled accordingly. The flight conditions and the non-dimensional specifications are kept the same (see Sec. 9.1.2). The propeller thrust coefficient also remains the same ($C_T = 0.20$, $T = 5.5\,\mathrm{kN}$). The wing-surface and cylindrical-actuator-region meshes for these 10X-scaled cases are 10X-scaled versions of the respective L2 meshes described in Sec. 8.2. The wing volume mesh is generated with the thickness of the first off-wall layer set to a flat-plate y^+ value of 1 and with the maximum off-wall growth ratios of the layers ranging primarily between 1.2 and 1.3. The rest of the overset mesh is generated with the same settings as those for the L2

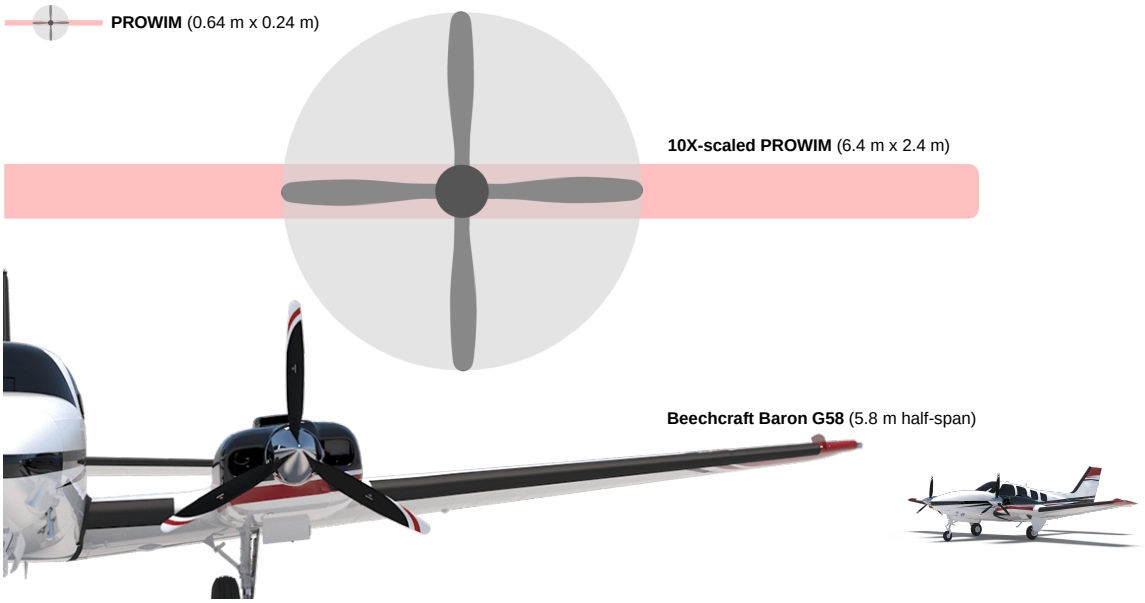

Figure 9.5.2: A comparison of the scales of the PROWIM, 10X-scaled PROWIM, and the Beechcraft Baron G58 wings (G58 images from `https://beechcraft.txtav.com/en/baron-g58` [Accessed: 1 Nov 2020])

mesh described in Sec. 8.2, but with proportionately larger extrusion distances and cell sizes.

Again, the difference in the final C_D when the wing is optimized with or without the presence of the propeller slipstream is less than one drag count. For the inboard-up T+S and wP+T+S cases (10X), the optimized C_D values are 301.7 and 301.1 counts, respectively, and for the outboard-up T+S and wP+T+S cases (10X), the optimized C_D values are 321.4 and 320.6 counts, respectively. The optimized lift distributions are practically identical to the corresponding distributions for the unscaled version, and, as expected because of the higher Reynolds number, the optimized twist and drag coefficient distributions are practically the same as the ones of the unscaled version but with offsets (Fig. 9.5.3).

Figure 9.5.4 shows vertical-velocity contours on a plane just above the wing surface for both the PROWIM and 10X-scaled PROWIM wings (unoptimized wings simu-

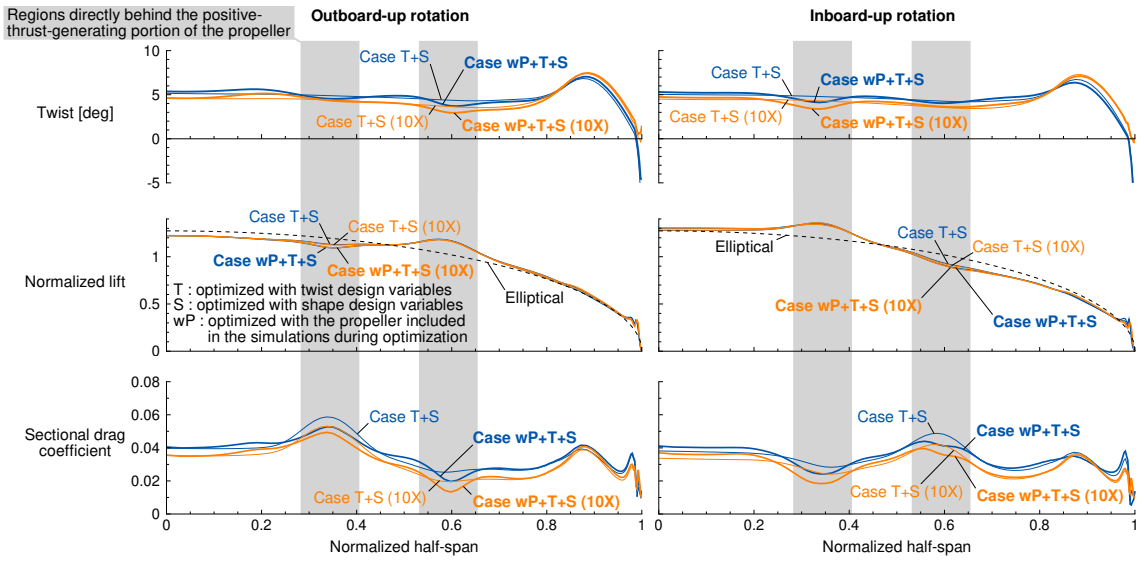

Figure 9.5.3: Optimization results for a 10X-scaled version of the small configuration used in this chapter that support the scaling hypothesis made in Sec. 9.5

lated at 0 deg angle of attack with the flow conditions and propeller-model settings used for the optimization cases).

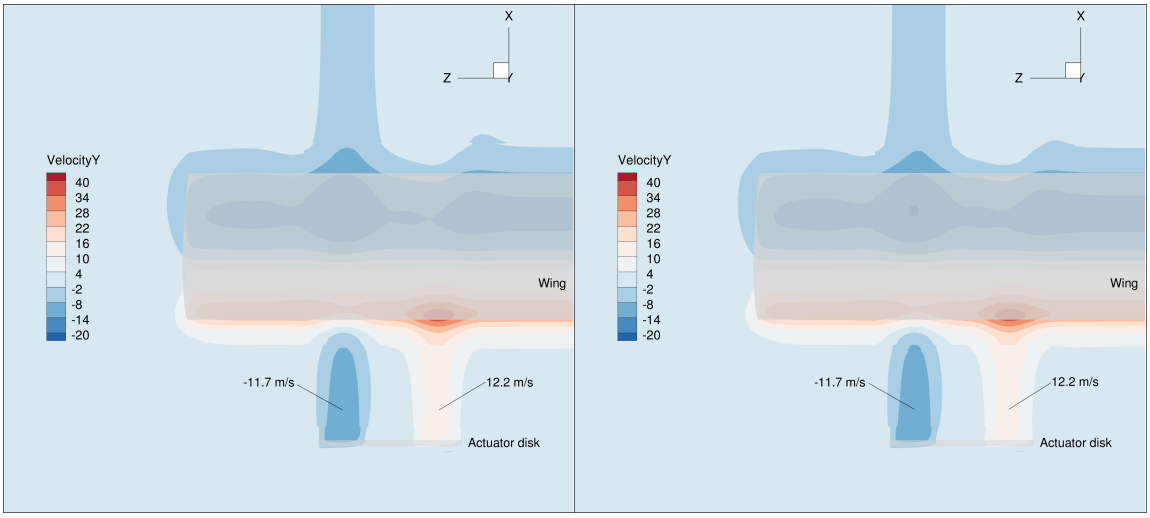

(a) PROWIM wing (0 deg; unoptimized) (b) 10X-scaled PROWIM (0 deg; unoptimized)

Figure 9.5.4: Vertical-velocity contours on a plane just above the wing for the optimization flow conditions (in m/s; bottom view shown; results for the L2 meshes)

The tangential-velocity estimate from Eq. (9.5.5) for $r/R = 0.5$, for both of these cases, is 12.4 m/s, and the values from the CFD simulations at the points shown in Fig. 9.5.4 are -11.7 m/s (behind the down-going-blade region) and 12.2 m/s (behind

the up-going-blade region). For the plane that coincides with the midplane of the wing, the values from the CFD simulations are $-12.4\,\mathrm{m/s}$ and $12.6\,\mathrm{m/s}$ (Fig. 9.5.5). These values give further confidence in the validity of Eq. (9.5.5).

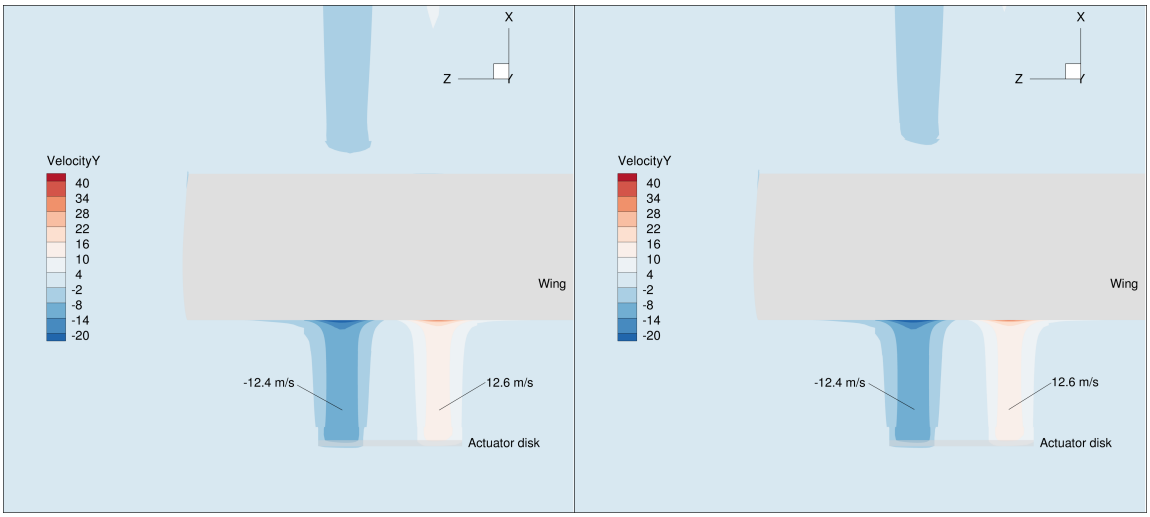

(a) PROWIM wing (0 deg; unoptimized) (b) 10X-scaled PROWIM (0 deg; unoptimized)

Figure 9.5.5: Vertical-velocity contours on the plane coincident with the wing midplane for the optimization flow conditions (in m/s; bottom view shown; results for the L2 meshes)

9.6 Summary

An actuator-disk propeller model was implemented in a CFD solver that has an adjoint implementation, and RANS-based aerodynamic shape optimization studies for a wing with an inboard-mounted tractor propeller were carried out using the open-source aerodynamics modules of the MACH framework. The results of twelve optimization cases that were solved using gradient-based optimization enabled by efficient adjoint gradient computation were presented. To minimize the drag for a cruise condition, the optimizer changed the wing twist, camber, and thickness behind the propeller. The drag reductions from changing the propeller rotation direction from outboard-up to inboard-up ($\sim$ 18 counts) and optimizing the wing twist and airfoil shapes ($\sim$ 14 counts) are significant. However, the additional drag reductions

obtained by optimizing the wing while considering the propeller slipstream, compared to optimizing it without considering the propeller slipstream, are negligible (less than one drag count). The wings optimized without considering the propeller slipstream are able to recover swirl almost as effectively as the ones optimized while considering the propeller slipstream, and the propeller-induced velocities for the cruise condition are not high enough to lead to significant airfoil-shape design changes. These results indicate that for a wing with an inboard-mounted tractor propeller, it is not worthwhile to account for propeller-wing interaction while optimizing the wing twist and airfoil shapes to minimize cruise drag.

Additionally, a simple first-principles-based analytic expression for estimating propeller-induced tangential velocities was derived to predict how the swirl angles behind a propeller change as a propeller-wing configuration is scaled in size. This expression shows that the propeller-induced tangential velocities are directly proportional to the disk loading and to the propeller pitch-to-diameter ratio, and inversely proportional to the fluid density and to the axial velocity. Predictions from this expression were also compared with CFD results to show good agreement.

Chapter 11 contains a list of the novel contributions, a list of the conclusions, and a list of the recommendations for future work.

CHAPTER 10

Optimization Problem Formulations and Results for a Wing with a Tip-Mounted Propeller

> Very serious study, while demanding, always has been a joy. I literally love aerodynamics, mathematics, physics, machinery—all the tools of my trade.
>
> *C. L. "Kelly" Johnson* [154]

As discussed in Chapter 2, both the location and rotation direction of a tractor propeller affect the performance of a trailing wing, and the trends with respect to one of these factors are not independent of the others. The influence on the performance of the wing becomes more interesting (or, in more technical terms, the sensitivities of the performance metrics of the wing to the location and settings of the propeller tend to become larger in magnitude) the closer the propeller is to the wingtip (e.g., see Figs. 2.2.11 and 2.2.12 in Sec. 2.2.4). In this chapter, we investigate whether the conclusions made in Chapter 9 change if the propeller is located at the wingtip.

10.1 Optimization Problem Descriptions

10.1.1 Geometry and Parameterization

For the optimization cases discussed in this chapter, we use the same wing and propeller geometry used previously for Sec. 9.5 (2.4 m by 6.4 m half-wing with a 2.4 m diameter propeller; i.e., a 10X-scaled version of the PROWIM wing shown earlier in Fig. 8.1.1), except with the propeller axis located at the wingtip (i.e., 6.4 m from the

root instead of 3 m from the root). This scale is representative of the size of typical twin-propeller GA- and commuter-aircraft wings. We use the same wing surface mesh and wing volume mesh used for Sec. 9.5, and we also reuse the cylindrical volume mesh used for Sec. 9.5 by translating it in the spanwise direction to align with the wingtip. As mentioned in Sec. 9.5, the wing volume mesh is generated with the thickness of the first off-wall layer set to a flat-plate y^+ value of 1 and with the maximum off-wall growth ratios of the layers ranging primarily between 1.2 and 1.3. Because the location of the cylindrical volume mesh for the actuator region is no longer the same, we generate a new background mesh. This background mesh is generated with the same settings as the background mesh used for Sec. 9.5, which means that the primary difference is a longer (in the spanwise direction) Cartesian-volume-mesh region where the cylindrical and wing volume meshes are located. These meshes are shown in Figs. 10.1.1 and 10.1.2.

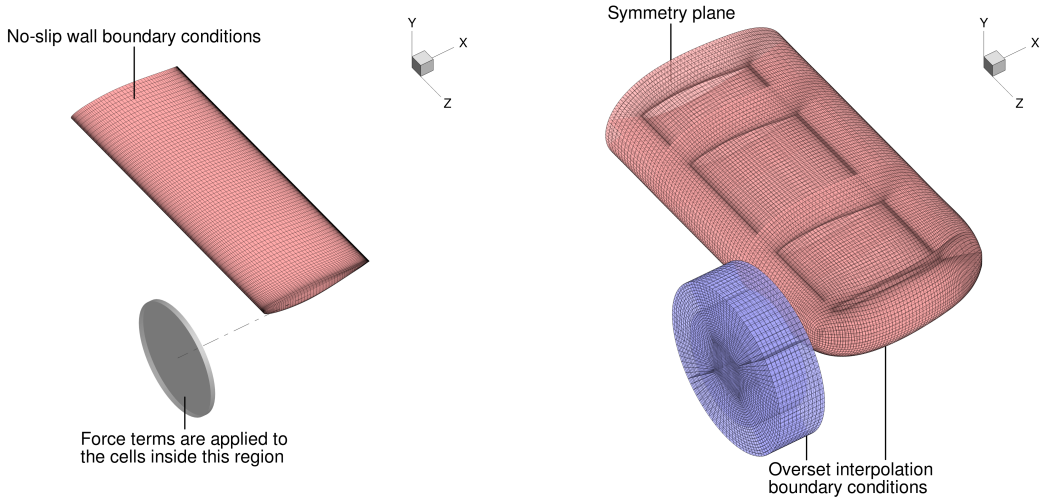

(a) Wing surface mesh and the disk used to specify the actuator zone

(b) Wing volume mesh and cylindrical volume mesh

Figure 10.1.1: Surfaces and volume meshes for the tip-propeller cases

As before, we study both outboard-up and inboard-up propeller rotation cases. We only optimize the wing, and the optimizations begin with the wing untwisted

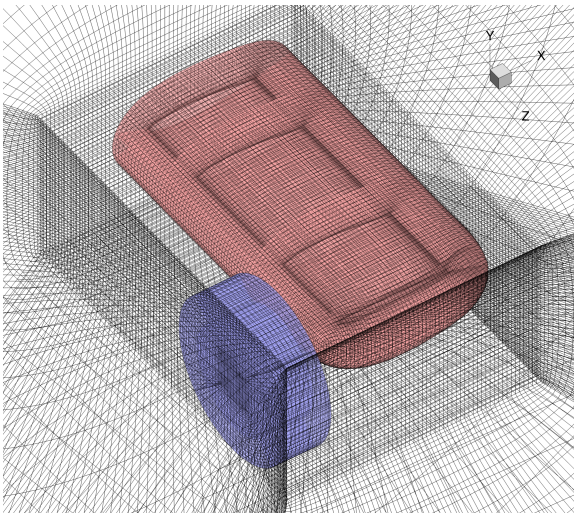

(a) Wing and cylindrical volume meshes overset with a background mesh

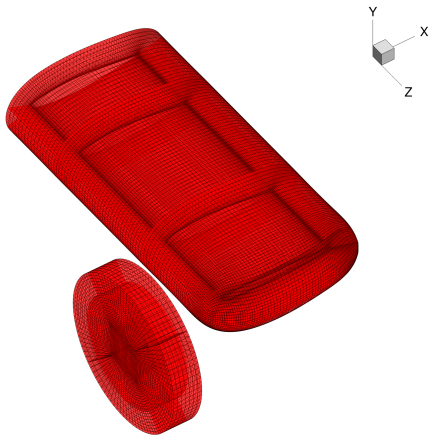

(b) Regions of the wing and cylindrical volume meshes that are selected as computation cells in the overset mesh

Figure 10.1.2: Overset meshes for the tip-propeller cases

and both the wing and the propeller at an angle of attack of 0 deg. The actuator disk keeps its angle of attack of 0 deg and does not follow the wing as the wing's inclination changes.

The grid of FFD control points that we use to deform and optimize the geometry is shown in Fig. 10.1.3. The positions of these control points are the design variables. The grid has 11 chordwise sections along the span and 8 spanwise sections along the chord. There are 88 control points above the wing and 88 below it (176 in total). The control points of each chordwise section can be rigidly rotated together to twist the wing, and all the control points can be moved individually in the vertical direction (y-direction) to change the shapes of the airfoil sections along the wing. The planform area and planform shape of the wing are not optimized in any of the cases presented in this chapter. We place control points closer together over the portion of the wing behind the propeller disk for greater control of this portions.

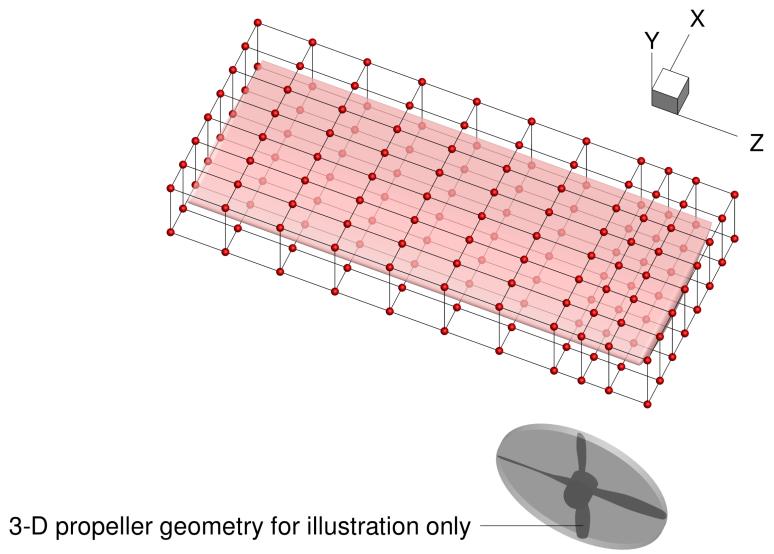

Figure 10.1.3: FFD grid ($8 \times 2 \times 11$ control points) around the wing for the tip-propeller cases

10.1.2 Flight Conditions

The flight conditions that we use for the optimization cases are selected to be representative of a cruise condition for GA and UAM. These are the same as the ones used for Sec. 9.5 and are described in Sec. 9.1.2. We also use the same propeller model inputs used for Sec. 9.5. These flight conditions and propeller parameters are summarized in Tables 10.1.1 and 10.1.2.

Table 10.1.1: Flight conditions and aircraft specifications

C_L	Mach number	Altitude	Assumed aircraft-lift-to-drag ratio	Propeller tip Mach number
0.6	0.3	1,500 ft	10	0.6

Table 10.1.2: Propeller specifications and nondimensional parameters

Advance ratio, $J = V_\infty/(\nu D_\varnothing)$	Thrust coefficient, $C_T = T/(\rho\nu^2 D_\varnothing^4)$	Thrust, T	Pitch-to-diameter ratio, $P/D_\varnothing$
1.6	0.20	5.5 kN	1.7

10.1.3 Primary Optimization Problem Formulations

As before, we have two primary optimization cases. We use the T+S and wP+T+S optimization problem formulations used previously for Sec. 9.2, with the bounds of

the airfoil-shape design variables and the initial locations of the FFD control points modified accordingly. These modified optimization problem formulations for this chapter are summarized in Tables 10.1.3 and 10.1.4.

Table 10.1.3: Case wP+T optimization problem formulation for the tip-propeller cases

	Function/variable	Description	Quantity
Minimize	C_D	Drag coefficient	
with respect to	$0 \leq \tau \leq 10.0$	Twist of each FFD section [deg]	11
		Total design variables	**11**
subject to	$C_L = 0.6$	Lift constraint	1
		Total constraint functions	**1**

Table 10.1.4: Case wP+T+S optimization problem formulation for the tip-propeller cases

	Function/variable	Description	Quantity
Minimize	C_D	Drag coefficient	
with respect to	$0 \leq \tau \leq 10.0$	Twist of each FFD section [deg]	11
	$-14.4 \leq \Delta y \leq 14.4$	Vertical displacements of the FFD control points for airfoil-shape control (±40% of the airfoil maximum thickness) [cm]	176
		Total design variables	**187**
subject to	$C_L = 0.6$	Lift constraint	1
	$t_a/t_{a,\text{initial}} \geq 1.0$	Constraints to prevent airfoil thicknesses at locations on a uniform 10 by 10 grid from decreasing	100
	$\Delta y_{\text{LE,upper}} = -\Delta y_{\text{LE,lower}}$	Constraints to prevent the airfoil-shape design variables from vertically displacing the leading edge	11
	$\Delta y_{\text{TE,upper}} = -\Delta y_{\text{TE,lower}}$	Constraints to prevent the airfoil-shape design variables from vertically displacing the trailing edge	11
		Total constraint functions	**123**

10.1.4 Baseline Optimization Cases for Comparison

To quantify the benefit of optimizing the wing while considering propeller effects, we also optimize the wing without propeller effects (i.e., without applying forces to the actuator disk) to obtain baseline cases for comparison. The FFD grid used for these baselines cases is the same grid used for the wP cases (Fig. 10.1.3).

For this chapter, the first baseline optimization case, Case T, has the same formulation as Case wP+T, except that it has no forces applied to the actuator disk, and the second baseline optimization case, Case T+S, has the same formulation as Case wP+T+S, except that it has no forces applied to the actuator disk. After optimization, the resulting wings from these baseline cases are analyzed with the

propeller forces applied to the actuator disk and with the wing angle of attack adjusted to achieve the specified C_L of 0.6. The wing's angle of attack is adjusted by rotating it using the FFD grid. This gives one-to-one comparisons that allow quantifying the benefit that optimizing a wing with propeller effects considered gives over optimizing the same wing without considering propeller effects.

10.2 Optimization Results

The drag coefficients plotted in Fig. 10.2.1 show that, although the drag reductions from changing the propeller rotation direction from outboard-up to inboard-up ($\sim$ 67 counts) and optimizing the wing twist and airfoil shapes ($\sim$ 12 counts) are significant, the additional drag reductions obtained by optimizing the wing while considering the propeller slipstream, compared to optimizing it without considering the propeller slipstream, are negligible (less than one drag count). This is the same conclusion reached previously in Chapter 9, with the only notable difference being the $\sim$ 3.5X larger change in drag when the rotation direction of the tip propeller is changed.

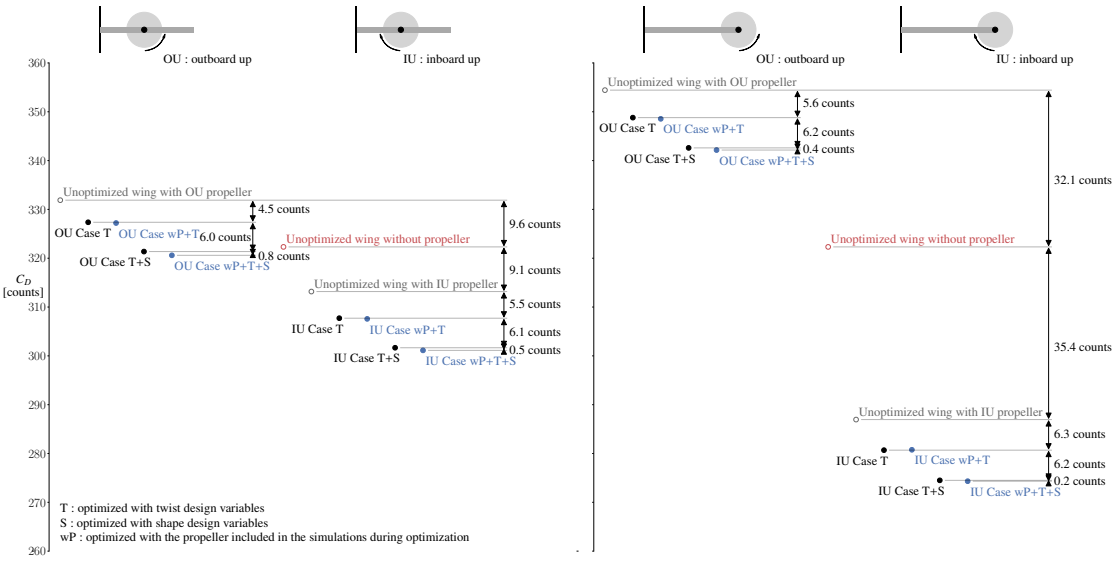

Figure 10.2.1: Reference and optimized drag coefficients for both tip- and inboard-mounted propeller configurations (starting from 10X-scaled versions of the PROWIM wing; $C_L = 0.6$ for all)

The optimized twist distributions in Fig. 10.2.2 show that, when the propeller model is included in the simulations during optimization (Cases wP+T and wP+T+S), the optimizer decreases the twist angle behind the propeller for both the inboard-up and outboard-up cases. There are also small related reductions in lift behind the propeller and increased lift inboard to compensate, as shown by the lift distributions in Fig. 10.2.2. These observations are similar to the ones made in Chapter 9. As mentioned in Chapter 9, the nonplanar wingtips (Figs. 10.2.3 and 10.2.4) can be attributed to induced-drag reductions from a reduction in average wing downwash as the shed vorticity is moved away from the wing plane [147].

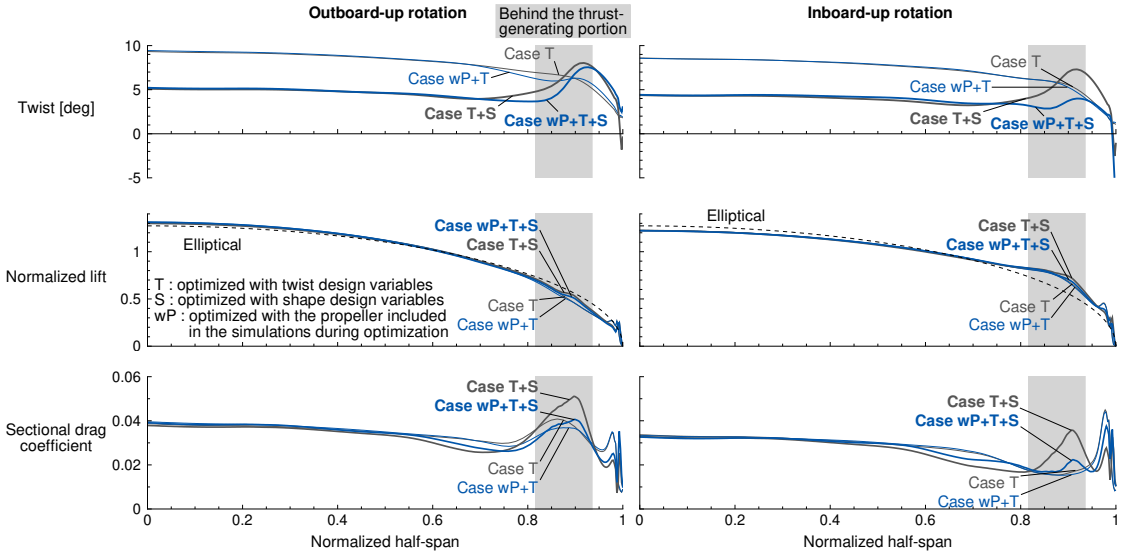

Figure 10.2.2: Optimized twist, lift, and drag distributions for the primary and baseline optimization cases (tip-propeller cases)

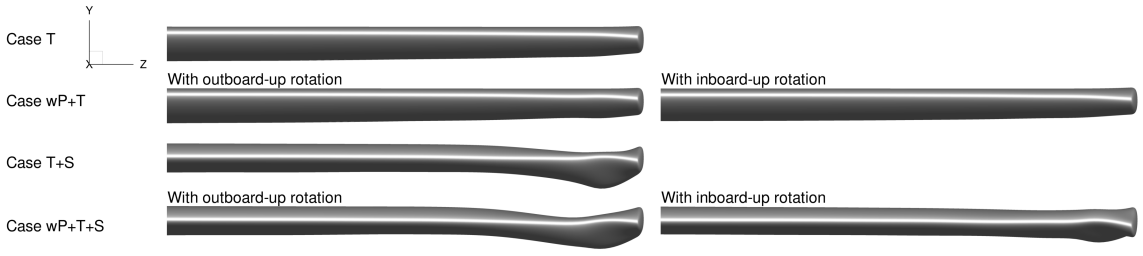

Figure 10.2.3: Front view of the optimized wings (tip-propeller cases)

When the propeller's rotation direction is the opposite of that of the natural flow

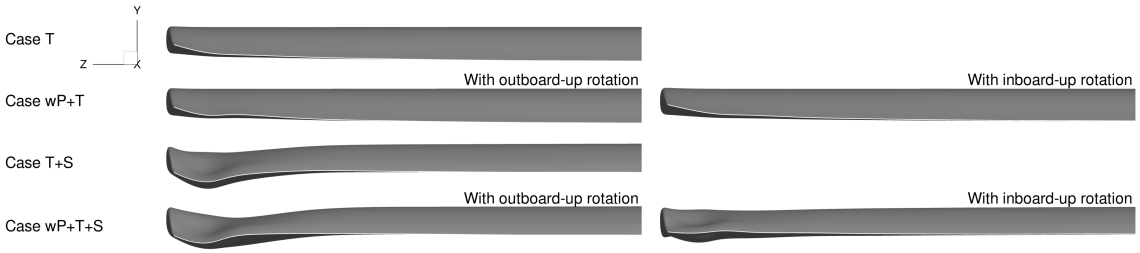

Figure 10.2.4: Rear view of the optimized wings (tip-propeller cases)

around the wingtip (i.e., when the propeller-induced flow counters the wing's lift-induced flow and reduces the downwash on the wing), we obtain a less-distorted optimized wingtip (Figs. 10.2.3 and 10.2.4).

Again, the lift distributions of the optimized wings are not exactly elliptical (Fig. 10.2.2). As discussed previously in Chapter 9, this is because it is advantageous to have more lift (i.e., more circulation) behind the propeller when the propeller induces an upwash (i.e., negative downwash) and less lift behind the propeller when the propeller induces a downwash.

Figure 10.2.2 also shows that, for each propeller rotation direction, the resulting lift distributions do not have large differences. The drag coefficient curves (Fig. 10.2.2) show that, when the propeller model is included in the optimization simulations (Cases wP+T and wP+T+S), the optimizer decreases the drag behind the propeller. However, there are also associated reductions in lift behind the propeller, and the adjustments required to satisfy the lift requirement cause these drag reductions to come with drag penalties inboard that reduce the overall benefit. This again indicates that, at least for similar configurations and operating conditions, a wing optimized without considering the propeller slipstream can recover swirl practically as effectively as a wing optimized while considering the propeller slipstream.

10.3 Summary

RANS-based aerodynamic shape optimization studies for a wing with a tip-mounted tractor propeller were carried out using the open-source aerodynamics modules of the MACH framework, and the results were compared with the optimization results for a wing with an inboard-mounted tractor propeller. The results of twelve optimization cases that were solved using gradient-based optimization enabled by efficient adjoint gradient computation were presented. To minimize the drag for a cruise condition, the optimizer changed the wing twist and camber behind the propeller. The drag reductions from changing the propeller rotation direction from outboard-up to inboard-up ($\sim$ 67 counts) and optimizing the wing twist and airfoil shapes ($\sim$ 12 counts) are significant. However, the additional drag reductions obtained by optimizing the wing while considering the propeller slipstream, compared to optimizing it without considering the propeller slipstream, are negligible (less than one drag count). The wings optimized without considering the propeller slipstream are able to recover swirl almost as effectively as the ones optimized while considering the propeller slipstream. These results indicate that for a wing with a tip-mounted tractor propeller, it is not worthwhile to account for propeller-wing interaction while optimizing the wing twist and airfoil shapes to minimize cruise drag. These conclusions are the same as the conclusions made previously in Chapter 9. The results also show that it is more important to strategically select the propeller location and rotation direction.

Part III

Conclusions, Recommendations, Appendices, and References

CHAPTER 11

Conclusions and Recommendations

11.1 Part I: Tilt-Wing eVTOL Takeoff Trajectory Optimization

For Part I, numerical optimization studies were carried out for the takeoff-to-cruise trajectory of a tandem tilt-wing eVTOL aircraft based on the Airbus A^3 Vahana, with the objective of minimizing energy consumption. Simplified models were used for the aerodynamics, propulsion, propeller-wing interaction, and flight-mechanics disciplines to study the broad design space.

11.1.1 List of Novel Contributions

1. This is the first published takeoff-to-cruise trajectory optimization study for a passenger-scale tilt-wing VTOL aircraft.
2. This work addresses several questions (listed in Sec. 11.1.2) previously unanswered in literature for a passenger-scale tilt-wing VTOL aircraft.
3. This work presents a novel combination of low-order models to simulate the flight and performance of a passenger-scale tandem tilt-wing eVTOL aircraft.
4. The simple, flexible, and novel implementation for trajectory optimization developed and used for this work is publicly available* (this unconventional approach is inspired by wing design optimization).

*https://bitbucket.org/shamsheersc19/tilt_wing_evtol_takeoff

11.1.2 List of Conclusions

The following list summarizes the conclusions from Part I (the questions correspond to the list in Chapter 3).

1. **Question:** What does the optimal takeoff trajectory including transition and climb (to a cruise altitude and speed appropriate for air-taxi operations) look like?

   Answer:

   - To minimize energy consumption, the optimized trajectories without acceleration constraints involve first transitioning to forward flight and accelerating, followed by climbing at roughly constant speed, and then finally accelerating to the required cruise speed, all performed at or almost at maximum power.
   - With an acceleration limit of $0.3\,g$ for passenger comfort, the transition, climb, and acceleration phases are less distinct and are not carried out at maximum power.

2. **Question:** Does the optimal trajectory involve stalling the wings, and, if yes, how much of a benefit does it provide?

   Answer:

   - The optimized takeoffs involve stalling the wings or flying near the stall angle of attack, both with and without the acceleration limit of $0.3\,g$.
   - However, based on the optimization cases with stall constraints, the energy penalty for avoiding stall is negligible.

3. **Question:** How does the augmented flow over the wings due to propellers affect the energy consumption and optimal trajectory?

   Answer:

   - Flow augmentation from the propellers has a negligible effect on the energy consumption of the optimized trajectories.
   - With high levels of flow augmentation, the optimized trajectories do not involve stalling the wings.
   - When the acceleration constraint is added, the optimized trajectories corresponding to different levels of flow augmentation become visibly different. With lower levels of flow augmentation, the optimized trajectories involve taking off with smaller wing angles relative to the vertical and gaining more altitude during the initial takeoff phase. However, the design space for the trajectory is relatively flat and these differences are not important from an energy-consumption point of view.

4. **Question:** How much electrical energy is required?

   Answer:

   - The optimized takeoff-to-cruise flight with the acceleration constraint, for the air-taxi mission requirements used (Uber-specified cruise speed of 67 m/s and altitude of 305 m), requires an estimated 1.9 kW·h of electrical energy (19 kg of installed-battery mass based on an installed-battery specific energy of 100 W·h/kg).
   - Without acceleration constraints, the optimized trajectories require 9% less electrical energy.

- Compared to a simpler, primarily hand-designed trajectory in which the aircraft takes off, climbs at the wing angle for the best rate of climb, and then accelerates to the required cruise speed, the optimized trajectories with the acceleration constraint require 5% less electrical energy.

5. **Question:** How does the wing size affect the optimal trajectory and energy consumption?

   Answer:

   - With smaller wings (down to 40% of the baseline reference area), the optimized trajectories involve larger wing angles of attack, but the flight-time and energy-consumption changes ($< 2\%$) are negligible.
   - Even with low levels of flow augmentation, it is still possible to avoid stalling the wings with this wide range of wing sizes.

6. **Question:** How does the maximum available power affect the optimal trajectory and energy consumption?

   Answer:

   - The time and electrical energy required increase as the maximum available power decreases ($\sim$ 20% increase in energy consumption for the lowest maximum-power level considered, which is 60% of the baseline maximum power).
   - With the two lowest maximum-power levels considered (corresponding to maximum thrust-to-weight ratios of 1.2 and 1.3 at hover), the optimized trajectories include purely vertical flight phases (to gain sufficient altitude while satisfying the horizontal-displacement requirement), something not seen in the other optimization results presented here.

- With low available power and low levels of flow augmentation, stalling the wings during takeoff can be unavoidable.

7. Overall, the design space for the takeoff-to-cruise trajectory of the tilt-wing eVTOL aircraft studied, with the mission specifications used, is relatively flat from an energy-consumption point of view. The induced losses of the propellers dominate the energy consumption, and relatively large changes to the flight profile and the flow-augmentation level, as well as to the baseline wing size and available power, tend to result in relatively small changes to the electrical energy consumed.

11.1.3 Discussion and Recommendations for Future Work

This section contains discussions on some of the methods used, results obtained, and conclusions made in this work, with a focus on recommendations for future work. Some of these statements are speculative in nature.

1. **Different mission and aircraft specifications:** Studying how the results and conclusions presented here change for different mission and aircraft specifications is recommended.

2. **Landing:** Cruise-to-landing trajectory optimization studies are recommended as future work.

3. **Models for stall and poststall behavior:** For this work, a poststall model based on the Tangler–Ostowari model was used, which is suitable for low-order modeling (see Figs. 4.1.2 and 4.1.3). Because the optimization results show that stalling the wings provides negligible energy benefits and can be avoided, a more accurate model for poststall behavior is not required. For future trajectory optimization studies, limiting the wing-angle control variables such that the lift

coefficients and angles of attack are restricted to prestall values is recommended. Therefore, predicting when the wing stalls is important, and higher-order approaches such as detached-eddy simulations may be useful for developing low-cost surrogate models that can be used to more accurately predict stall. Because of the inherent limitations of tools such as panel methods and RANS CFD [80–85], it is unlikely that accurate stall and poststall predictions can be obtained with these models, even with significant effort and computational cost. For mission and aircraft specifications that differ significantly from the ones used in this work, it is recommended that low-order studies like the ones presented here be carried out first to check whether these statements are still applicable.

4. **Models for propeller performance:** For the propellers, methods such as blade-element methods or free-wake methods can provide more accurate thrust and energy estimates than momentum theory. Connecting blade-element methods with panel methods or CFD tools are approaches that can help provide more accurate flow-augmentation and propeller-wing interaction modeling. However, these approaches can still have limitations related to inflow conditions when the propeller incidence angle is not small. Based on the optimization results, improvements in propeller modeling will likely impact the energy-consumption values and the higher-order details of the optimal trajectory, but it seems unlikely that a significant impact will be made on the general shapes of the optimal flight profiles and the conclusions made on the effects of propeller-wing flow interaction, wing size, and available power on the electrical energy consumption. This is because the induced losses of the propellers dominate the energy consumption. Solving the trajectory optimization problems again with different propeller models is recommended as future work to verify this claim.

5. **Other simplifications made:** Two major assumptions made in this work are that there is no interaction between the forward and rear wings (except for the interaction considered to calculate the effective span efficiencies) and that the wings rotate and behave identically. Reducing these simplifications and considering factors such as downwash, upwash, trim, and stability, the flows experienced by the forward and rear wings will not be identical. Depending on the modeling approach used, higher-order methods and separate control variables for the wings may help provide more accurate simulations. However, the main trends are not expected to change significantly because the improved accuracy is likely to only result is higher-order fine-tuning behavior. Further studies are recommended to verify this claim.

6. **Other trajectory optimization approaches:** The NASA OpenMDAO team has used the models presented in this work to solve these trajectory optimization problems using different trajectory optimization approaches (e.g., Gauss–Lobatto collocation) with the open-source tool Dymos [155].[†] Their results match the results presented in this dissertation. Using their publicly-available implementations for studying different trajectory optimization approaches and making recommendations based on the advantages and disadvantages is recommended as future work.

7. **Tilt-wing vs. tilt-rotor configurations:** The low sensitivity of the energy consumption to wing size found in this work indicates that the choice between a tilt-wing design and an offset-tilt-rotor design (i.e., tilt-rotor designs with the rotors offset from the wing to avoid flow-blockage during hover, such as the Hyundai SA-1 concept) does not need to take takeoff energy consumption into

[†] `https://github.com/OpenMDAO/RevHack2020/tree/master/problems/evtol_trajectory` [Accessed:15 Nov 2020]

consideration. Further studies are recommended to confirm this.

11.2 Part II: RANS-Based Aerodynamic Shape Optimization of a Wing Considering Propeller-Wing Interaction

For Part II, an actuator-disk propeller model was implemented in a CFD solver that has an adjoint implementation, and RANS-based aerodynamic shape optimization studies for a wing with a tractor propeller were carried out using the open-source aerodynamics modules of the MACH framework.

11.2.1 List of Novel Contributions

1. This work is the first published instance of gradient-based aerodynamic shape optimization of a wing considering propeller-wing interaction with RANS CFD.

2. The result that the additional drag reductions obtained by optimizing the wing while considering the propeller slipstream, compared to optimizing it without considering the propeller slipstream, are negligible is surprising. This comparison has not been performed previously in literature.

3. A simple first-principles-based analytic expression for estimating propeller-induced tangential velocities is derived as part of this work.

11.2.2 List of Conclusions

The following list summarizes the conclusions from Part II for a wing with a tractor propeller (minimizing drag subject to a lift constraint, by optimizing the wing twist and airfoil shapes, for a GA cruise condition).

1. The additional drag reductions obtained by optimizing the wing while considering the propeller slipstream, compared to optimizing it without considering the propeller slipstream, are negligible (less than one drag count). Therefore, it is

not necessary to model the propeller slipstream during optimization for such a case. However, the final design must be simulated with the propeller slipstream to obtain an accurate prediction of the lift and drag.

2. The wings optimized without considering the propeller slipstream are able to recover swirl almost as effectively as the ones optimized while considering the propeller slipstream, and the propeller-induced velocities for the cruise condition are not high enough to lead to significant airfoil-shape design changes.

3. This is the case for wings with inboard-mounted propellers as well as wings with tip-mounted propellers.

4. Strategically selecting the propeller location and rotation direction is much more important than fine-tuning the wing's twist and airfoil shapes for optimal flow interaction with the propeller slipstream at cruise.

11.2.3 Discussion and Recommendations for Future Work

This section contains discussions on some of the methods used, results obtained, and conclusions made in this work, with a focus on recommendations for future work. Some of these statements are speculative in nature.

1. **Coupled actuator-disk model for non-uniform inflow:** A recommendation for future work is to develop a coupled actuator-disk model that computes its force distributions using the inflow conditions from the CFD simulation (to capture the non-axisymmetric loading that results when a propeller is at an angle of attack or subject to non-uniform inflow) and also implement adjoint-based gradient computation for it for optimization. Such a coupled model will not change the conclusions made in this work, but it will be useful for optimization

studies that include propeller design variables, for investigating pusher configurations, and for simulating large angle-of-attack conditions for UAM operations.

2. **Including climb:** Because of the larger swirl angles expected during climb, investigating how the conclusions made in this work change when a climb phase is included in the optimization problem is recommended. This may be useful for aircraft with missions in which the climb phase has a significant contribution to the total energy consumption.

3. **Optimizing the propeller's spanwise location:** Because there are aerodynamic advantages but aeroelastic disadvantages in moving a wing-mounted propeller to the wingtip, developing the capability to optimize a wing-mounted propeller's spanwise location with dynamic-aeroelasticity considerations is recommended.

4. **Optimizing the propeller's vertical offset:** Because the vertical offset at which the dynamic pressure impinging on a wing is maximum is not the same as the vertical offset at which the wing lift-to-drag ratio is maximum (see Sec. 2.2.2), developing the capability to simultaneously optimize the vertical offsets of wing-mounted propellers and the wing planform area while considering both takeoff requirements and cruise flight is recommended.

5. **Steady vs. unsteady analyses:** The actuator-disk approach is a steady approach that provides good predictions for time-averaged performance (see Secs. 6.1 and 8.4). However, since it is a steady approach, it does not model unsteady effects necessary for acoustics and vibrations-related considerations. Other models must be used for those considerations.

11.3 Overarching Conclusion and Recommendations

For eVTOL aircraft, the design focus should be on sound, simple, and safe aircraft. From a takeoff point of view, the aircraft design should prioritize factors such as mechanical simplicity, noise, and safety because factors such as wing and fuselage drag are not significant during the takeoff-to-cruise phase (the induced losses from the propellers dominate). From a cruise point of view, strategically selecting the locations and rotation directions of wing-mounted propellers should be the primary focus (this will require aeroelastic considerations).

CHAPTER 12

Aside: Low/Mid-Fidelity Aerostructural Optimization of Aircraft Wings with a Simplified Wingbox Model Using OpenAeroStruct

> Sans fausse modestie, je dirai que je me suis efforcé de ne pas manquer d'imagination... Je ne me laisse pas décourager par les difficultés. J'ai la passion de mon travail et je sais, par volonté, écarter tout ce qui pourrait m'en détourner. J'ai une vie simple et heureuse. Tout, autour de moi, concourt et doit concourir à l'œuvre que je me suis fixée.
>
> *M. Dassault* [156]

12.1 Introduction

Due to their low cost, vortex lattice method (VLM) codes and simple finite element method (FEM) models remain popular and useful for preliminary wing design, despite the availability of higher-fidelity tools. Examples of their use in recent literature are the following. Drela [157] used multiple tools including a VLM code and an aircraft design framework with simplified analytical structural models for the development of the D8 configuration, an unconventional transport aircraft configuration. Elham and van Tooren [158] coupled a quasi-3-D aerodynamics model, that combines a VLM code and a 2-D viscous solver, to an FEM code with beam elements. They optimized a wing based on the Airbus A320-200 with respect to

shape, planform, and structural sizing variables [158]. Fujiwara and Nguyen [159] also coupled a quasi-3-D model, combining a VLM code and a 2-D viscous solver, to an FEM code with beam elements calibrated using a NASTRAN wing model for the structure. They focused on trailing-edge morphing and aerodynamic optimization to improve the performance of the Common Research Model (CRM [160]) wing [159].

Unfortunately, these aerostructural design tools are not open-source or easily available to students and researchers. Recently, OpenAeroStruct* (OAS) [34], a low-fidelity tool for aerostructural optimization built using NASA's OpenMDAO† framework [71, 72], was developed to provide students and researchers with an open-source tool for studying coupled-aerostructural design trends. OAS couples a VLM model for the aerodynamics to an FEM spatial beam model for the structures.

Currently, OAS is gaining popularity with both students and researchers [34, 161–164]. However, one limitation of the original OAS is that it models the structures as tubular spars. While this is useful for studying aerostructural coupling and optimization trends, a tubular cross-section is not representative of the wingbox structures commonly found in business, regional, and commercial aircraft.

To remedy this, and because no open-source software is available that couples a VLM code to an FEM code modeling a wingbox structure, we developed and present a modified version‡ of OAS with a wingbox model. To be specific, we modified the FEM analysis in OAS to use the effective properties of a simplified wingbox. To maintain the simplicity and light-weight nature of OAS, we still use six-degree-of-freedom-per-node spatial beam elements. However, we compute the effective cross-sectional properties for the elements using a wingbox model with an airfoil-based cross-section. We think students, instructors, and researchers will find this light-

*`https://github.com/mdolab/OpenAeroStruct`

†`www.openmdao.org`

‡Now available as an option in the main OAS package (`https://github.com/mdolab/OpenAeroStruct`)

weight open-source tool to be useful for aircraft design studies.

12.2 Formulation

Typically, transport aircraft wings are designed with structures called wingboxes. The upper and lower wing skins primarily support the bending loads on the wing, and the two spars primarily support the shear loads. The skins and spars together also provide a closed loop for the torsional shear flow, allowing them to support torsional loads efficiently. This section describes how we model such a structure using beam elements.

As with the original OAS, we use the user-provided VLM mesh for both the VLM and the FEM. The FEM uses the spanwise spacing of the VLM mesh for the beam elements. Figure 12.2.1 illustrates an FEM mesh superimposed on a user-provided VLM mesh. The shaded boxes illustrate the segments of the wingbox structure that are represented by these FEM elements. For the FEM, section properties of these segments, for cross-sections normal to the elements, are required. Please note that in the remainder of the text the term *segment* refers to the wingbox segments illustrated in Fig. 12.2.1 unless modified by another noun.

For each finite element that the wing structure is discretized into, the area moments of inertia about two axes, the torsion constant, and the cross-sectional area are required. We estimate these using user-specified wingbox coordinates, which are coordinates of the portion of the airfoil that the wingbox occupies (e.g., airfoil coordinates of the 15%- to 65%-chord portion of an airfoil). Figure 12.2.2 illustrates how the cross-section of each element is modeled using these coordinates.

The moments of inertia and area contributions of the skins are estimated using parallelograms formed by extruding the lines connecting the coordinates in the el-

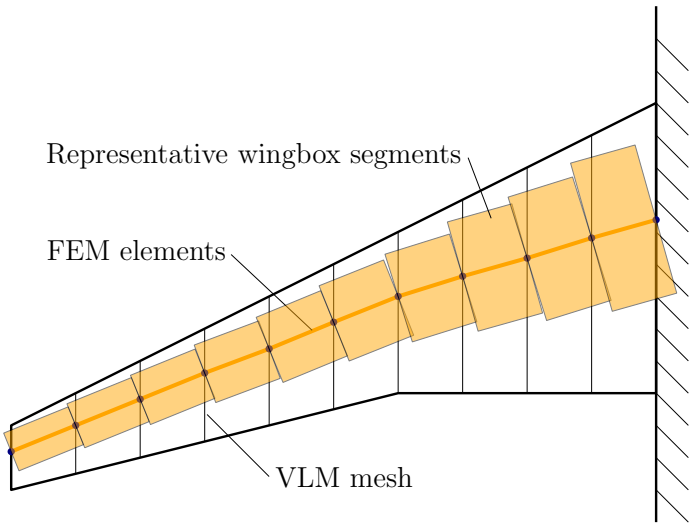

Figure 12.2.1: A planform view of a wing mesh showing the VLM mesh and the FEM mesh with representative wingbox segments

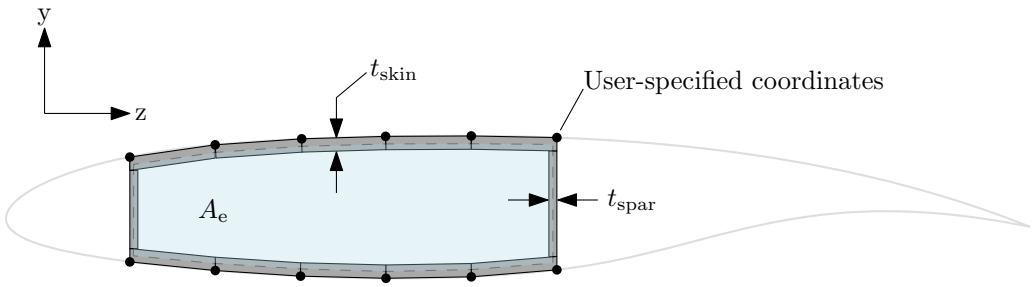

Figure 12.2.2: The wingbox cross-section model is constructed using user-specified airfoil coordinates and the thickness design variables.

ement's local y-direction by the skin thickness. The moments of inertia and area contributions of the spars are estimated using rectangles as shown in Fig. 12.2.2. For each wingbox segment, we use the same skin thickness, t_{skin}, for both the upper and lower skins, and the same spar thickness, t_{spar}, for both the forward and rear spars. Also, we compute the chord length for each segment by taking the mean of the chord lengths at its nodes.

12.2.1 Torsion Constant and Shear Center

For a closed section in which the wall thicknesses are much smaller than the other dimensions, the shear flow can be assumed to be uniform across the wall thickness,

and the torsion constant, J, can be approximated as [165]

$$J = \frac{4A_{\mathrm{e}}^2}{\oint \frac{\mathrm{d}s}{t}}. \tag{12.2.1}$$

Here, A_{e} is the enclosed area of the cross-section defined by the wall midlines, $\mathrm{d}s$ is the length of a differential element along the wall midlines, and t is the corresponding wall thickness.

We compute the enclosed area, A_{e}, for each cross-section by summing the areas of trapezoids that together form the blue shaded region outlined by dashed lines in Fig. 12.2.2. We estimate the $\oint \frac{\mathrm{d}s}{t}$ term in Eq. (12.2.1) by computing the lengths of the dashed line segments shown in Fig. 12.2.2 divided by their corresponding thicknesses.

For transferring loads from the VLM to the FEM, we require the location of the shear center along the chord for each wingbox segment. If the wingbox cross-section has two axes of symmetry, then the shear center coincides with the centroid of the cross-section. However, in general, wingbox cross-sections are not symmetric, and finding the exact shear center of closed asymmetric cross-sections is an involved task [166]. To maintain simplicity, we estimate the location of the shear center along the chord as the average location of the outer edges of the spars, weighted by their areas. While there will be some error associated with this estimate, we expect this to be small, especially for typical wingbox cross-sections which are close to doubly symmetric.

12.2.2 Area Moments of Inertia

In general, the wing being optimized will have a variable twist distribution, and the wingbox sections will have some twist with respect to the local coordinate systems of the FEM elements, as illustrated in Fig. 12.2.3. To account for this, the user-

specified wingbox coordinates are transformed as shown in Fig. 12.2.3. We achieve this by rotating the coordinates by the section's twist angle, and translating them such that the spars are aligned with the local y-axis. This assumes that the wing will be constructed with planar spar segments that are not twisted.

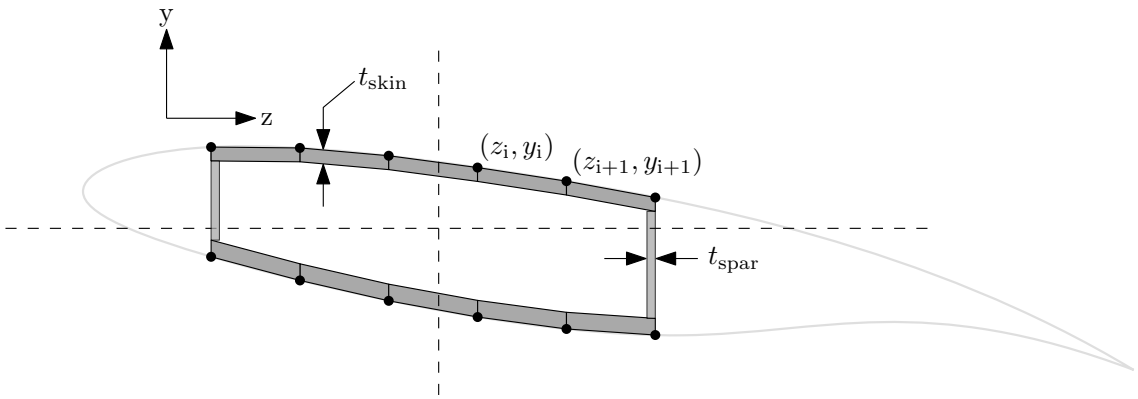

Figure 12.2.3: Twisted wingbox cross-section

The area moment of inertia of each parallelogram on the upper skin about an axis passing through its centroid and parallel to the z-axis, I_{p}, is given by

$$I_{\text{p}} = 2\left(\frac{a^3c^4}{12} + \frac{a^2bc^3}{3} + \frac{ab^2c^2}{2} + \frac{b^3c}{3}\right), \tag{12.2.2}$$

where

$$a = \frac{y_{i+1} - y_i}{z_{i+1} - z_i},\ b = \frac{y_{i+1} - y_i + t_{\text{skin}}}{2},\ \text{and}\ c = z_{i+1} - z_i. \tag{12.2.3}$$

We also compute the area moment of inertia of each parallelogram on the lower skin about their centroids using Eq. (12.2.2). However, the following modified formulas for a and b are required:

$$a_{(\text{lower})} = -\frac{y_{i+1} - y_i}{z_{i+1} - z_i}\ \text{and}\ b_{(\text{lower})} = \frac{-y_{i+1} + y_i + t_{\text{skin}}}{2}. \tag{12.2.4}$$

Here, z_i, y_i, z_{i+1}, and y_{i+1} are consecutive user-specified wingbox coordinates as shown in Fig. 12.2.3. Then we use the parallel-axis theorem to adjust the moments of inertia calculated using the above formulas to moments of inertia about the neutral

axis of the complete cross-section. For the contribution of the spars, we use the standard formulas for rectangular cross-sections.

Computing the area moment of inertia about the neutral axis parallel to the local y-axis is less involved and is carried out using the area moment of inertia formulas for a rectangle. Using the area moment of inertia formulas for a rectangle is also valid here for the parallelograms representing the skins because these parallelograms are simply rectangles sheared in the y-direction.

12.3 Loads

OAS transfers aerodynamic forces computed using the VLM to the FEM structure in a consistent and work-conservative manner [34]. For our modified version, we add additional loads for the weight of the wing structure and the weight of the fuel to these aerodynamic loads. For simplicity, we assume that the weight of the fuel is distributed across the entire wing and that the fraction of the total fuel that each wingbox segment (corresponding to each finite element) holds is equal to the ratio of its enclosed volume to the total enclosed volume of all the wingbox segments. We also assume that the fuel weight for each segment is distributed uniformly across each segment and coincides with the elastic axis. We apply these distributed loads as point loads to the nodes of the elements by computing the work-equivalent nodal forces and moments [167].

In a similar manner, we assume that the loads corresponding to the weight of each wingbox segment (computed using the length, cross-sectional area, and material density) are distributed uniformly along the elastic axis of each segment and apply them to the element nodes by computing the work-equivalent nodal forces and moments.

12.4 Stress Analysis

After OAS converges the aerostructural system, the displacements from the FEM are used to compute von Mises stresses. For each wingbox segment, multiple combinations of stresses need to be taken into consideration. In level flight and positive-g maneuver cases, the upper skin will be subjected to compressive stresses due to bending, and shear stresses due to torsion. The lower skin will be subjected to tensile stresses due to bending, and shear stresses due to torsion. The spars will primarily support shear stresses due to both torsion and shear loads, and some axial stresses due to bending. Figure 12.4.1 shows the stress combinations that we are interested in.

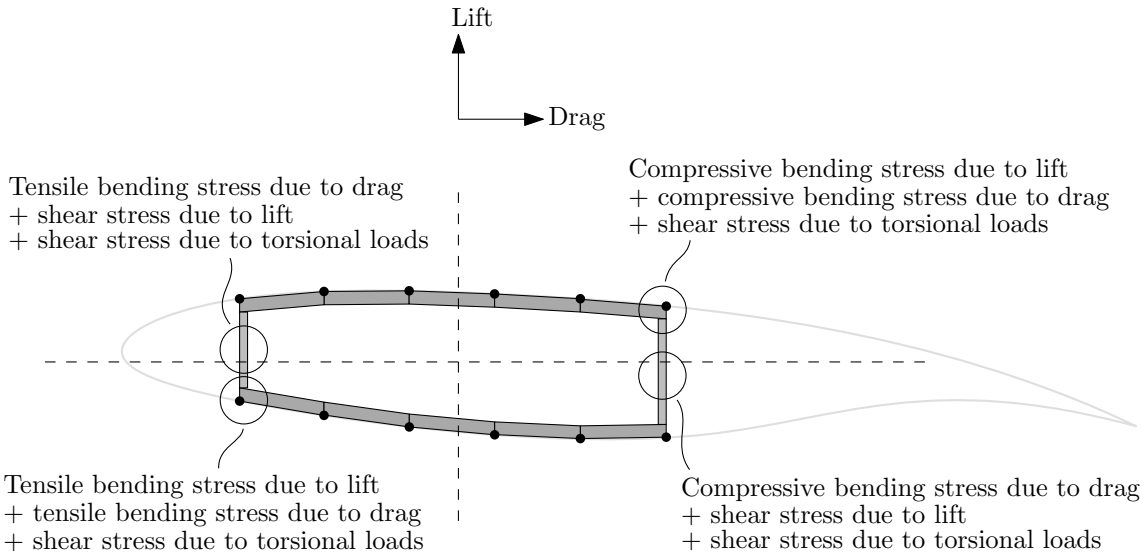

Figure 12.4.1: Stress combinations of interest

To simplify the stress analysis, we focus on the four stress combinations shown in Fig. 12.4.1 to represent the worst loading combinations. To compute the maximum (in magnitude) bending stresses for the upper and lower surfaces, we need the distances of the points that are the farthest away from the neutral axis. Since this requires using a *maximum* function, which is problematic for gradient-based optimiza-

tion, we use the Kreisselmeier–Steinhauser (KS) function [78]. To reduce numerical difficulties we use the alternative formulation described by Lambe et al. [93]. The bending stresses computed using these distances are combined with the maximum bending stresses in the spars (due to loads in the local z-direction) and with the torsional shear stress to obtain a conservative estimate of the maximum von Mises stresses for the combinations corresponding to the corners in Fig. 12.4.1. Since we assume that the spars stay parallel to the local y-axis, computing their distances from the neutral axis is straightforward and does not require using a KS function. For the spars, we combine the maximum transverse shear stresses, the maximum bending stresses (due to loads in the local z-direction), and the torsional shear stress. After the von Mises stresses are computed, we aggregate them using the KS function for a single stress constraint. Note that Fig. 12.4.1 is used for illustrative purposes and, in general, the lift and drag forces will not line up exactly with the element local y- and z-directions.

12.5 Optimization Problem

One of the goals of this work is to compare optimization results from OAS and our wingbox model to results from a framework that uses high-fidelity CFD and FEA. Brooks et al. [2] present optimization results for the aspect-ratio-9 undeflected Common Research Model (uCRM-9) wing, which is an undeflected version of the CRM [160] wing, a transport aircraft wing similar in size to a Boeing 777 wing. They use RANS CFD for the aerodynamics and an FEM model with shell elements for the wing structure [2, 127]. The objective of their optimization problem is to minimize fuel burn by varying airfoil shape and structural sizing variables. For a robust aerodynamic design, they compute their objective function by averaging the

fuel burn for five cruise conditions (Mach numbers ranging from 0.84 to 0.86 and lift coefficients ranging from 0.475 to 0.525). In addition, they have two flight points for buffet constraints. For structural sizing, they use a 2.5 g maneuver flight point, a -1 g maneuver flight point, and a 1 g cruise gust flight point.

Their design variables include angle of attack, tail trim angle, wing twist, airfoil shape variables, and structural sizing variables. They model stiffeners for the wingbox using a smeared stiffness approach [168] and also include buckling constraints. They obtained an optimized wing structural mass of 23,840 kg and an average fuel burn of 94,037 kg.

We try to replicate their optimization problem closely for comparison. Table 12.5.1 lists the specifications and parameters used by Brooks et al. [2] that we also use for this work. We use a wing mesh, based on the uCRM-9 [127], with seven streamwise nodes and 26 spanwise nodes for the semispan (mesh shown in Fig. 12.6.1). Since we do not model a fuselage, the wings extend to the aircraft centerline.

Table 12.5.1: Parameters and specifications [2]

Specification	Value	Notes
Cruise range	7,725 nmi	
Cruise C_L	0.5	Nominal cruise lift coefficient
Cruise Mach no.	0.85	Brooks et al. [2] use five cruise points, three of which are at M 0.85
Cruise altitude	37,000 ft	
Cruise thrust-specific fuel consumption	0.53 lb/lbf h^{-1}	
2.5 g maneuver Mach no.	0.64	
2.5 g maneuver altitude	0 ft	
Aircraft weight without wing structure, payload, and fuel	114,000 kg	
Payload weight	34,000 kg	
Reserve fuel weight	15,000 kg	
Drag counts for nacelles, pylons, and vertical tail	35	
Wing structure material density	2,780 kg/m^3	7000 series aluminum
Wing structure Young's modulus	73.1 GPa	7000 series aluminum
Wing structure Poisson's ratio	0.33	7000 series aluminum
Wing structure yield strength	420 MPa	7000 series aluminum

Table 12.5.2 summarizes our optimization problem. We use a multipoint optimization with a cruise flight point and a 2.5 g maneuver flight point. Minimizing

the fuel burn at cruise is the objective, and we use a single point at the nominal cruise C_L, altitude, and Mach number listed in Table 12.5.1 to compute it. We use the gradient-based optimizer SNOPT [169] to solve the optimization problem with optimality and feasibility tolerances set to $5 \cdot 10^{-6}$ and 10^{-8}, respectively (to put these tolerances into perspective, the objective function changes by less than 10^{-3} % over the last two orders of convergence of the optimality for the cases presented here). The total derivatives for optimization are computed by OpenMDAO using the coupled-adjoint method [71, 72, 119, 170]. The partial derivatives for the various OAS components are computed using a combination of analytic expressions and the complex-step approximation [96].

Table 12.5.2: Optimization problem

	Function/variable	Note	Quantity
minimize	fuel burn	computed using the Breguet range equation	
with respect to	wing twist	B-spline parameterized using 6 control points	6
	thickness-to-chord ratio	B-spline parameterized using 6 control points	6
	spar thickness	B-spline parameterized using 6 control points	6
	skin thickness	B-spline parameterized using 6 control points	6
	angle of attack for the 2.5 g flight point		1
		Total design variables	**25**
subject to	$C_{L,\text{cruise}} = 0.5$	for the cruise flight point	1
	$\text{lift}_{2.5\,\text{g}} = \text{weight}_{2.5\,\text{g}}$	for the 2.5 g maneuver flight point	1
	$\sigma_{\text{von Mises}} \leq \frac{420\,\text{MPa}}{1.5}$	von Mises stresses aggregated using the KS function	1
	fuel volume $\leq$ wingbox volume		1
		Total constraint functions	**4**

For structural sizing, we use a 2.5 g maneuver flight point with the lift constrained to equal the weight. We use B-splines with six control points each to vary the wing twist, streamwise thickness-to-chord ratio, spar thickness, and skin thickness. We use the same thickness distribution for both the upper and lower skins, and the same thickness distribution for both the forward and rear spars. The bounds for the wing twist, thickness-to-chord ratio, and thickness design variables are -15 deg and 15 deg, 0.07 and 0.2, and 0.003 m and 0.1 m, respectively.

Since we do not model the fuselage or tail surfaces, we estimate the unaccounted

coefficient of drag for the fuselage and horizontal tail to be 0.0043. We used turbulent skin friction and form-factor formulas from Raymer [171] and the dimensions of the Boeing 777-200 for this. We further add a coefficient of drag of 0.0035 to this for the vertical tail, nacelles, and pylons (estimate used by Brooks et al. [2]). For the wingbox model used by Brooks et al. [2], at the root, the forward spar is located at the 10% chord location and the rear spar is located at the 60% chord location. At the wingtip, their forward spar is located at the 35% chord location and the rear spar is located at the 60% chord location. For simplicity, we set the forward spar to be at the 10% chord location and the rear spar to be at the 60% chord location for the entire wing. We use airfoil coordinates of the 10% to 60% portion of the NASA SC2-0612 supercritical airfoil for the wingbox cross-section shape. The thickness-to-chord ratio design variables scale these coordinates. Like Brooks et al. [2], for this optimization problem, we compute the weight of the wing structure by multiplying the weight computed from the FEM model by 1.25 to account for the weight of fasteners, overlaps, and other unaccounted components in the wing structure.

12.6 Results

Figure 12.6.1 shows our first set of optimization results. The lift distribution for the 2.5 g maneuver flight point is more triangular than for the cruise flight point. This is expected because moving the lift further inboard for the 2.5 g flight point, which determines the structural sizing, is beneficial for reducing stresses and weight. We also observe a lower twist at the wingtip compared to the midspan and the root. This is expected, as it helps obtain the optimal lift distributions. However, because of the different fidelities, there are differences in the shapes of the distributions in Fig. 12.6.1 and the optimized distributions obtained by Brooks et al. [2, 127]. For

example, the thickness-to-chord ratios obtained by Brooks et al. [2] (for the uCRM-9) first decrease and then increase when moving from the root to the tip.

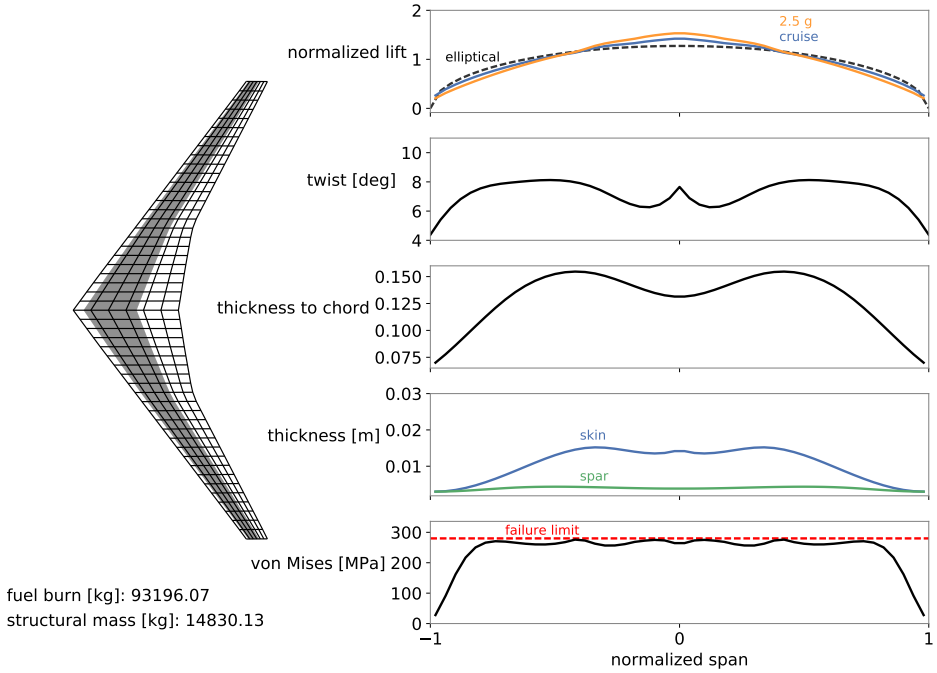

Figure 12.6.1: Optimization results for the case without wave drag (the twist is the jig twist)

The optimized thickness-to-chord ratios are relatively large for this case, between 0.12 and 0.16, in the midsection of each semispan. OAS computes induced drag from the VLM, and parasitic drag using skin friction and form-factor formulas found in Raymer [171]. However, wave drag, which is an important consideration for the design of transonic aircraft, is not included. This explains why we obtain these relatively large thickness-to-chord ratios. The optimized spar thicknesses range between 3 and 5 mm, and the optimized skin thicknesses range between 3 and 16 mm. Brooks et al. [2] obtained spar thicknesses between 5 and 16 mm, skin thicknesses between 3 and 22 mm, and thickness-to-chord ratios between 0.07 and 0.11. Our optimized wing structural mass for this case is 14,830 kg. This is 38% lower than the optimized wing structural mass reported by Brooks et al. [2]. The large differences between

our results can be explained by the larger thickness-to-chord ratios that the lack of wave drag allows.

Next, we add a wave-drag computation to OAS. We use the following relations [172] for the drag based on the Korn equation:

$$M_{\text{crit}} = \frac{\kappa}{\cos\Lambda} - \frac{t/c}{\cos^2\Lambda} - \frac{C_L}{10\cos^3\Lambda} - \left(\frac{0.1}{80}\right)^{1/3} \tag{12.6.1}$$

and

$$C_{D,\text{wave}} = 20(M - M_{\text{crit}})^4. \tag{12.6.2}$$

Here, M is the flight Mach number, M_{crit} is the critical Mach number, κ is an airfoil technology factor (set to 0.95 for NASA supercritical airfoils), t/c is the streamwise thickness-to-chord ratio, C_L is the wing coefficient of lift, and Λ is the sweep angle. We compute $\cos\Lambda$ by averaging the cosines of the quarter-chord sweep angles for each spanwise segment of the VLM mesh, weighted by their areas. Similarly, we compute the average thickness-to-chord ratio, t/c, by averaging the thickness-to-chord ratios corresponding to each spanwise segment, weighted by their areas.

Figure 12.6.2 shows our optimization results including the wave-drag computation. We notice similar results for the lift and twist distributions as the previous case.

However, now we obtain a thinner wing (thickness-to-chord ratios between 0.07 and 0.12) with thicker spars (between 3 and 10 mm) and thicker skins (between 3 and 25 mm). As shown in Fig 12.6.3, these thickness ranges are closer to the ranges obtained by Brooks et al. [2] (spar thicknesses between 5 and 16 mm, and skin thicknesses between 3 and 22 mm). This also translates to a larger wing mass than before of 21,468 kg, which is 10% less than the wing mass of 23,840 kg obtained by Brooks et al. [2]. Note that these wing mass values are the masses computed from the wingbox structural models (combined total for both semispans) and do not

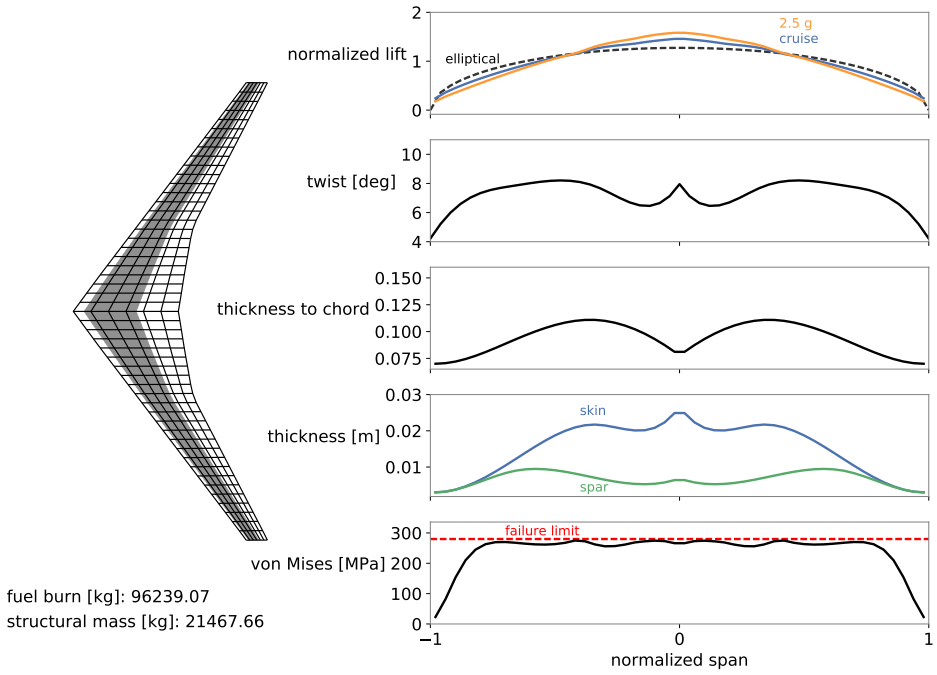

Figure 12.6.2: Optimization results for the case with wave-drag estimates (the twist is the jig twist)

include the 1.25 factor mentioned earlier. Since Brooks et al. [2] also considered buckling constraints and modeled ribs, which we do not, our lower wing mass is not surprising. These numbers are also comparable to the mass of 22,988 kg obtained by Klimmek [173] for the CRM using a doublet lattice method (DLM) code and a detailed FEM model.

Because we use a rough wave-drag estimation method, our thickness-to-chord-ratio range matches that of Brooks et al. [2], but the spanwise trend does not match (Fig. 12.6.4). The RANS CFD solver used by Brooks et al. [2] can capture the physics of shocks much more accurately.

Our optimized fuel burn value is 96,239 kg, which is 2% greater than the fuel burn value of 94,037 kg obtained by Brooks et al. [2]. Table 12.6.1 summarizes the optimized fuel burn and structural mass values.

Figure 12.6.5 shows how the optimized fuel burn and wingbox mass change as the

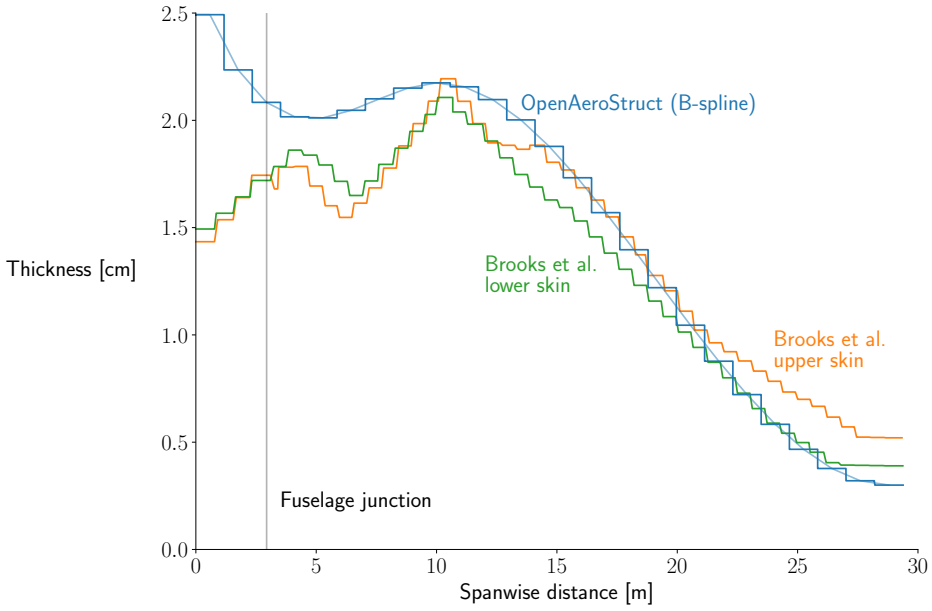

Figure 12.6.3: Optimized skin thickness comparison with results from Brooks et al. [2]. The trends are different near the root because of differences in boundary conditions (Brooks et al. [2] applied displacement constraints at the fuselage junction, which we do not).

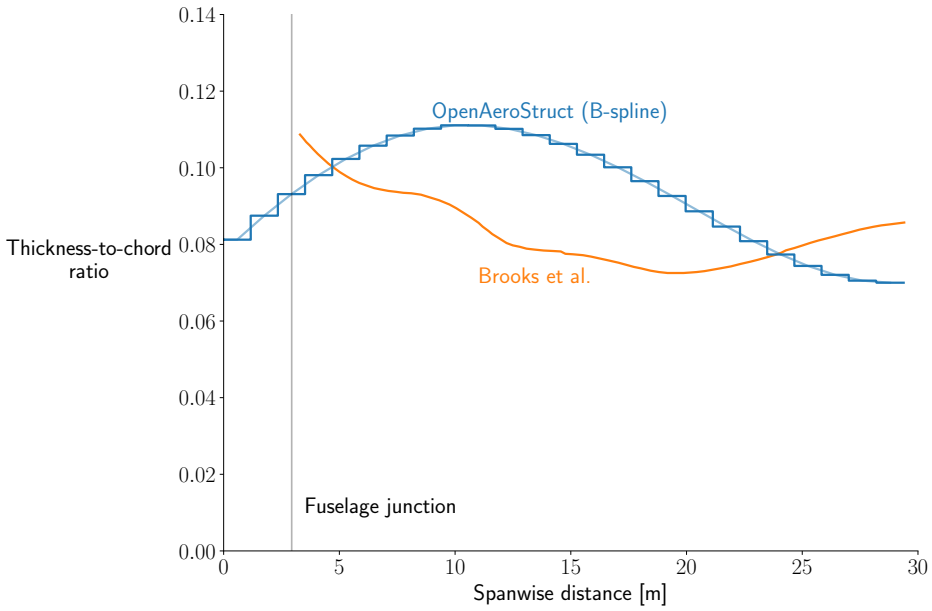

Figure 12.6.4: Optimized thickness-to-chord ratio comparison with results from Brooks et al. [2]. The spanwise trends do not match because the RANS CFD solver used by Brooks et al. [2] can capture the physics of shocks much more accurately.

Table 12.6.1: Optimized fuel burn and wing structural mass values (percentage differences relative to Brooks et al. [2] are shown in parentheses)

	OAS + wingbox		Brooks et al. [2]
	without wave drag	with wave drag	
Wing structural mass [kg]	14,830.13 (−38.8%)	21,467.66 (−10.0%)	23,840
Fuel burn [kg]	93,196.07 (−0.9%)	96,239.07 (+2.3%)	94,037

OAS mesh is refined, along with timings on a laptop (2.70 GHz Intel i7-7500U). This shows that optimizing a wing, with a reasonably fine mesh, requires on the order of a few hours with OAS and the wingbox model on a personal computer.

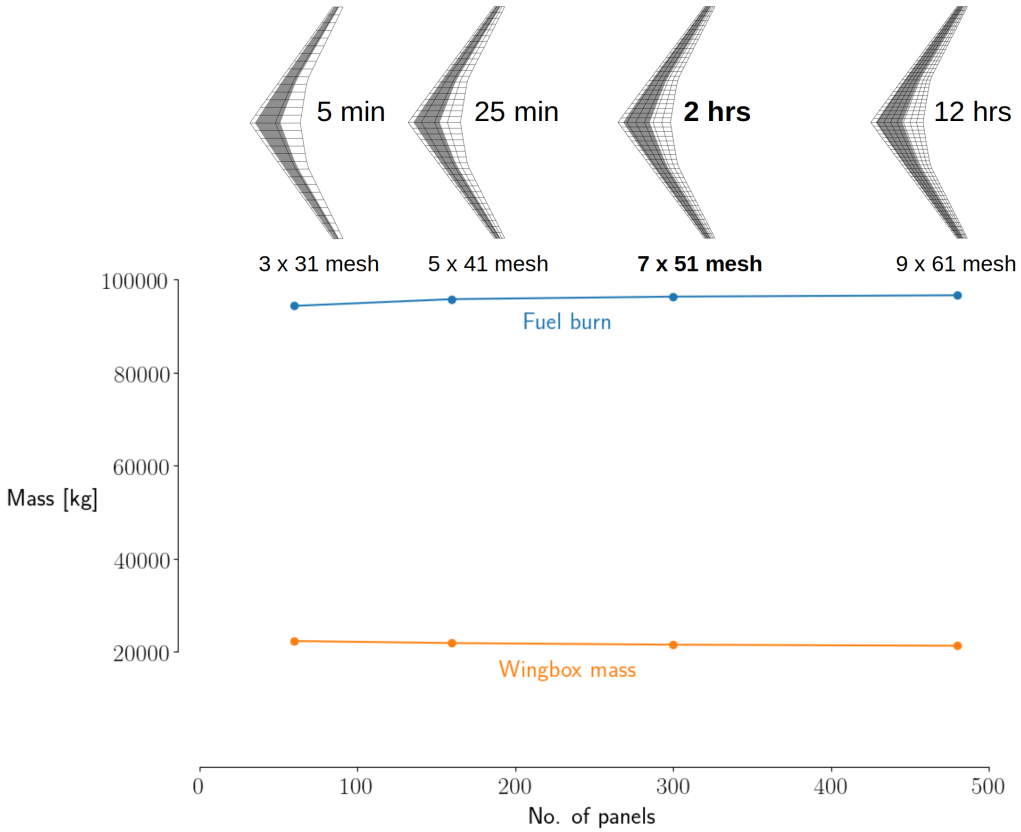

Figure 12.6.5: Mesh refinement study showing how the optimization results change as the mesh is refined (these cases have the wave-drag computation)

12.7 Results for Additional Cases with Planform Design Variables

In this section, we present two additional optimization cases that show what happens when span, sweep, and chord design variables are added to the optimization

problem. The first of these additional cases has span and sweep design variables, and the second has chord design variables in addition to span and sweep. Their optimization problem formulation is summarized in Table 12.7.1. The initial design used as the starting point for these cases is an unswept version of the uCRM-9 geometry. Apart from the design variables, bounds, and mesh (unswept uCRM-9 mesh with seven streamwise nodes and 36 spanwise nodes for the semispan), we maintain the same settings and specifications described in Sec. 12.5. These additional cases also use the wave-drag computation described in Sec. 12.6.

Table 12.7.1: Optimization problem formulation for the two additional cases with planform design variables

	Function/variable	Note	Quantity
minimize	fuel burn	computed using the Breguet range equation	
with respect to	wing twist	B-spline parameterized using 5 control points	5
	thickness-to-chord ratio	B-spline parameterized using 5 control points	5
	spar thickness	B-spline parameterized using 5 control points	5
	skin thickness	B-spline parameterized using 5 control points	5
	wing span		1
	wing sweep		1
	angle of attack for the 2.5 g flight point		1
		Total design variables	**23**
	wing chord	B-spline parametrized using 7 control points	7
		Total design variables	**30**
subject to	$C_{L,\text{cruise}} = 0.5$	for the cruise flight point	1
	$\text{lift}_{2.5\,\text{g}} = \text{weight}_{2.5\,\text{g}}$	for the 2.5 g maneuver flight point	1
	$\sigma_{\text{von Mises}} \leq \frac{420\,\text{MPa}}{1.5}$	von Mises stresses aggregated using the KS function	1
	fuel volume $\leq$ wingbox volume		1
	wing planform area $\geq 414\,\text{m}^2$	$414\,\text{m}^2$ is the planform area of our uCRM-9 mesh	1
		Total constraint functions	**5**

Since we are now changing the planform shape in the absence of takeoff and landing constraints, we use a planform area constraint to prevent the planform area from decreasing to a value less than the baseline planform area ($414\,\text{m}^2$ for our uCRM-9 mesh). The bounds for the wing span are 10 m and 100 m, and the bounds for the wing sweep are -60 deg and 60 deg. We reduce the bounds for the twist design variables to -8 deg and 8 deg because we haven't implemented stall constraints in OAS yet, and during initial testing we obtained results with large twist angles that would likely stall the wing in reality. The bounds for the chord design variables

(measured streamwise) are 0.25 m and 15 m. The rest of the bounds are the same as before.

Figure 12.7.1 shows the results for the case without chord design variables, and Fig. 12.7.2 shows the results for the case with chord design variables. The optimizer increases the span and the wing area in both the cases (initially 58.9 m and 414 m^2). With chord design variables, the optimizer converges to an unconventional planform shape. This shape is similar to the shapes obtained by Wakayama and Kroo [174].

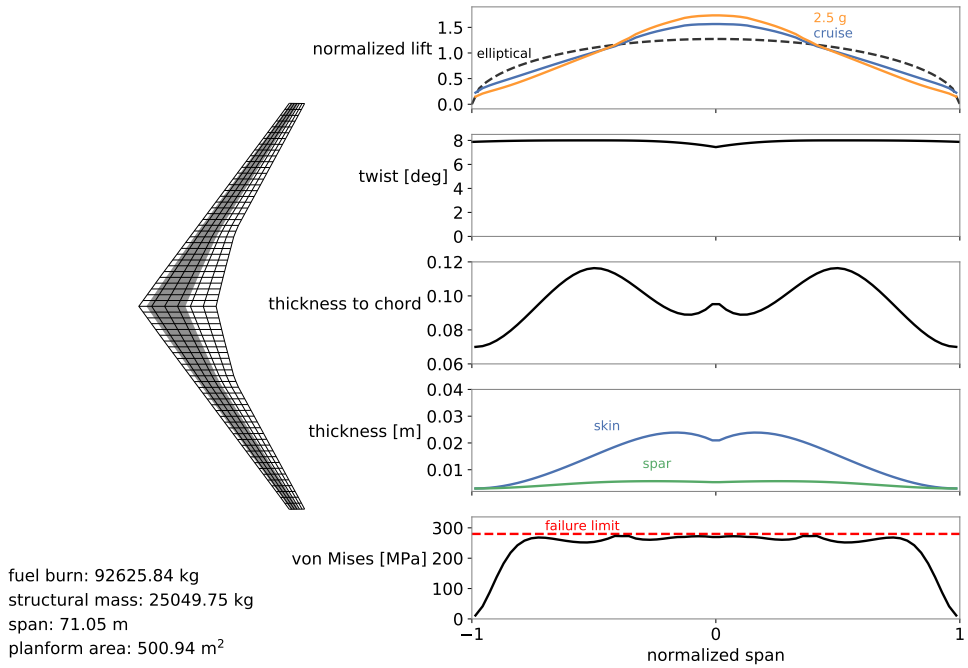

Figure 12.7.1: Optimization results for the additional case with span and sweep design variables but without chord design variables (the twist is the jig twist)

For both these cases, the twist design variables are at their upper bounds. We recommend future work to implement stall constraints or a quasi-3-D approach [82, 158, 159] in OAS. Videos visualizing the optimization histories of these two cases are available online[§¶].

[§]Video for the case without chord design variables: `https://youtu.be/8mkQfYYaK64`
[¶]Video for the case with chord design variables: `https://youtu.be/6cF6TBiUyr4`

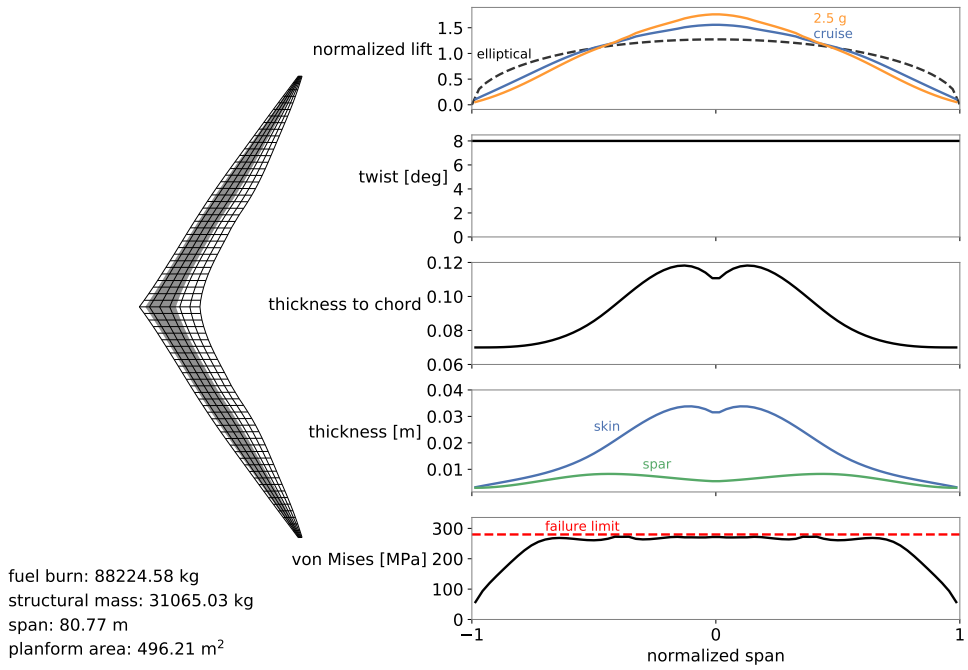

Figure 12.7.2: Optimization results for the additional case with span, sweep, and chord design variables (the twist is the jig twist)

12.8 Summary

We developed a simplified wingbox model and implemented it for use with OpenAeroStruct. This model is now available as an option in the main OpenAeroStruct package, which is open-source and publicly available[‖]. We optimized a wing based on the CRM wing and compared the results to results from Brooks et al. [2], who used high-fidelity models. Our optimized wing mass value is 10% lower and our optimized fuel burn value is 2% higher than their results. As expected, because of the differences in the fidelities of our models, there are differences in the trends and details of the optimized twist, thickness-to-chord ratio, and structural thickness distributions. In contrast to the 48 h on 1000 processors required by Brooks et al. [2], OpenAeroStruct requires on the order of minutes to hours on a personal computer. Additionally, we included optimization results for cases with planform design vari-

[‖] `https://github.com/mdolab/OpenAeroStruct`

ables. With chord design variables, we obtained an unconventional planform shape. We think students and researchers studying aircraft design will find this tool to be useful**. a

**Further optimization studies using OpenAeroStruct and this wingbox model have been carried out by Jasa et al. [35] and Hendricks et al. [36].

APPENDICES

APPENDIX A

Momentum Theory for Propellers with Non-Axial Inflow

A.1 Momentum Theory Derivation with Non-Axial Inflow

Consider the large control volume (dotted lines) shown in Fig. A.1.1. An actuator disk inside this control volume creates a pressure jump ΔP in the x-direction (normal to the disk) and accelerates the flow.

We make the usual assumptions that are also made for the axial-flow version of momentum theory [41] (incompressible, inviscid, uniform loading, no rotation imparted, a well-defined slipstream separating the flow through the disk and the flow outside, equal static pressure far upstream and downstream, and flow properties only change in the direction of the pressure jump). In reality, the loading and flow will not be azimuthally uniform, which adds additional sources of error to the predictions from this simplified approach.

For continuity, the mass fluxes through the three planes labeled 1 to 3 in Fig. A.1.1 must be equal, and therefore

$$\rho A_1 \mathbf{V}_\infty \cdot \mathbf{n_1} = \rho A_2 (\mathbf{V}_\infty + \mathbf{V_2}) \cdot \mathbf{n_2} = \rho A_3 (\mathbf{V}_\infty + \mathbf{V_3}) \cdot \mathbf{n_3}. \tag{A.1.1}$$

Here, ρ is the air density, A_1 is the streamtube cross-sectional area far upstream, A_2 is the actuator area, A_3 is the streamtube cross-sectional area far downstream, $\mathbf{V}_\infty$

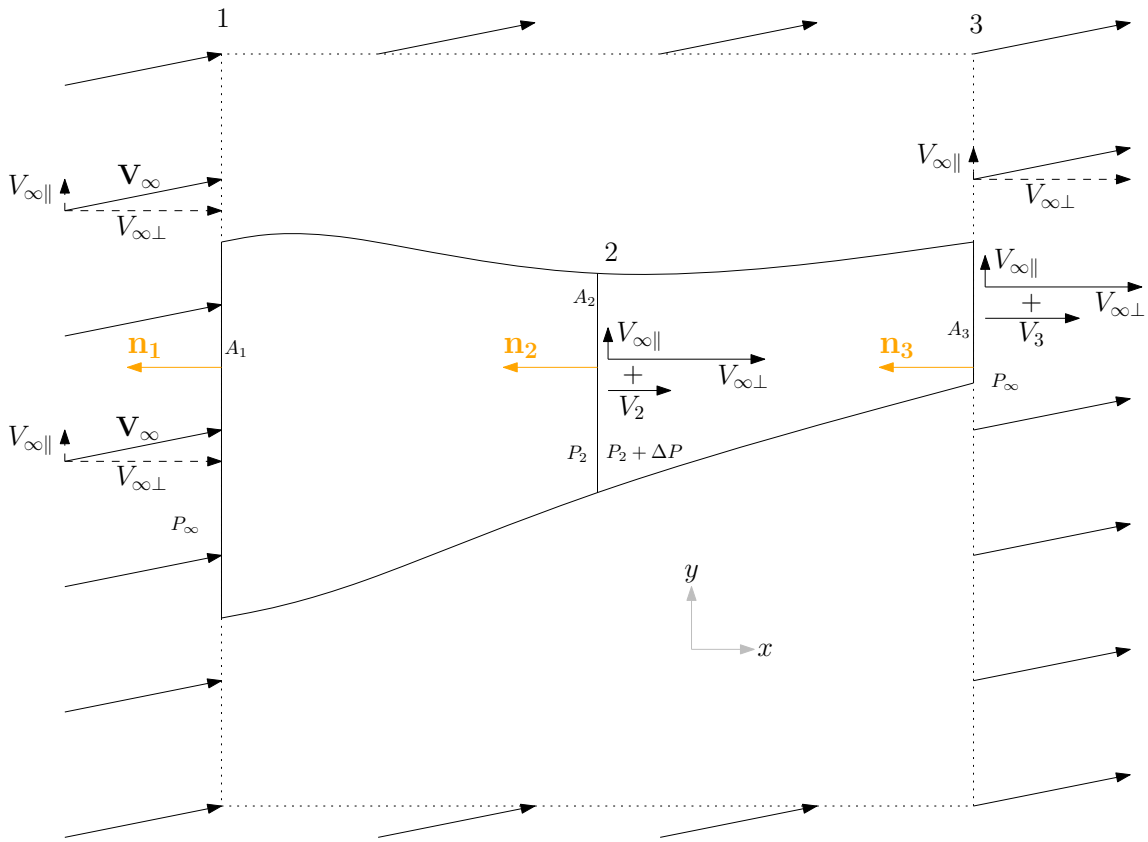

Figure A.1.1: Control volume for the momentum theory derivation with non-axial inflow

is the freestream velocity vector, $\mathbf{V_2}$ is the induced velocity vector at the disk, $\mathbf{V_3}$ is the induced velocity vector far downstream, and $\mathbf{n_1}$, $\mathbf{n_2}$, and $\mathbf{n_3}$ are unit vectors normal to planes 1, 2, and 3. This simplifies to

$$\rho A_1 V_{\infty\perp} = \rho A_2 (V_{\infty\perp} + V_2) = \rho A_3 (V_{\infty\perp} + V_3). \tag{A.1.2}$$

For momentum conservation, the difference between the momentum fluxes through the inlet and outlet of the streamtube must equal the force applied by the actuator disk. We also make the usual assumption that the control volume is large and the control surfaces are far removed from the actuator disk. This also means that the momentum flux through the bottom control surface is the same as the momentum flux through the top control surface, and therefore they do not involve a change in

momentum. Therefore, the thrust vector is

$$\mathbf{T} = \rho A_1(\mathbf{V}_\infty)(\mathbf{V}_\infty \cdot \mathbf{n_1}) - \rho A_3(\mathbf{V}_\infty + \mathbf{V_3})((\mathbf{V}_\infty + \mathbf{V_3}) \cdot \mathbf{n_3}). \tag{A.1.3}$$

This can be decomposed in the x-direction,

$$T = A_2\Delta P = -\rho A_1 {V_{\infty\perp}}^2 + \rho A_3(V_{\infty\perp} + V_3)^2, \tag{A.1.4}$$

and in the y-direction,

$$0 = -\rho A_1 V_{\infty\parallel} V_{\infty\perp} + \rho A_3 V_{\infty\parallel}(V_{\infty\perp} + V_3). \tag{A.1.5}$$

Since $\rho A_1 V_{\infty\perp} = \rho A_3(V_{\infty\perp} + V_3)$, from Eq. (A.1.2), Eq. (A.1.5) reduces to $V_{\infty\parallel} = V_{\infty\parallel}$ and is satisfied.

Next, using Bernoulli's equation in front of the disk, we can write

$$\frac{1}{2}\rho(V_{\infty\perp}^2 + V_{\infty\parallel}^2) + P_\infty = \frac{1}{2}\rho((V_{\infty\perp} + V_2)^2 + V_{\infty\parallel}^2) + P_2. \tag{A.1.6}$$

Since the flow is assumed to be incompressible, this simplifies to

$$\frac{1}{2}\rho V_{\infty\perp}^2 + P_\infty = \frac{1}{2}\rho(V_{\infty\perp} + V_2)^2 + P_2. \tag{A.1.7}$$

Similarly, behind the disk we have

$$\frac{1}{2}\rho((V_{\infty\perp} + V_2)^2 + V_{\infty\parallel}^2) + P_2 + \Delta P = \frac{1}{2}\rho((V_{\infty\perp} + V_3)^2 + V_{\infty\parallel}^2) + P_\infty. \tag{A.1.8}$$

Again, since the flow is assumed to be incompressible, this simplifies to

$$\frac{1}{2}\rho(V_{\infty\perp} + V_2)^2 + P_2 + \Delta P = \frac{1}{2}\rho(V_{\infty\perp} + V_3)^2 + P_\infty. \tag{A.1.9}$$

Subtracting Eq. (A.1.7) from Eq. (A.1.9) gives

$$\Delta P = \rho(V_{\infty\perp} + \frac{1}{2}V_3)V_3. \tag{A.1.10}$$

Equations (A.1.2), (A.1.4), and (A.1.10) are the same as the equations for the axial-flow version, but with $V_{\infty\perp}$ instead of V_∞.

Using Eq. (A.1.2), Eq. (A.1.4) can be rewritten as

$$T = A_2\Delta P = -\rho A_2(V_{\infty\perp} + V_2)V_{\infty\perp} + \rho A_2(V_{\infty\perp} + V_2)(V_{\infty\perp} + V_3), \tag{A.1.11}$$

which further expands to

$$\Delta P = \rho(-V_{\infty\perp}^2 - V_2V_{\infty\perp} + V_{\infty\perp}^2 + V_2V_{\infty\perp} + V_{\infty\perp}V_3 + V_2V_3). \tag{A.1.12}$$

Equating this to Eq. (A.1.10) gives

$$V_2 = \frac{1}{2}V_3. \tag{A.1.13}$$

Substituting this in Eq. (A.1.11) and rearranging gives

$$T = 2\rho A_2(V_{\infty\perp} + V_2)V_2. \tag{A.1.14}$$

Finally, solving this quadratic equation for V_2 gives

$$V_2 = \left(-\frac{V_{\infty\perp}}{2} + \sqrt{\frac{V_{\infty\perp}^2}{4} + \frac{T}{2\rho A_2}}\right), \tag{A.1.15}$$

and the power supplied to the disk can be written as

$$P = \mathbf{T}\cdot(\mathbf{V}_\infty + \mathbf{V_2}) = T(V_{\infty\perp} + V_2) = T\left(\frac{V_{\infty\perp}}{2} + \sqrt{\frac{V_{\infty\perp}^2}{4} + \frac{T}{2\rho A_2}}\right). \tag{A.1.16}$$

Equations (A.1.15) and (A.1.16) are the same as the equations for the axial-flow version, but with $V_{\infty\perp}$ instead of V_∞.

A.2 Comparing Momentum Theory Predictions With and Without Glauert's Modification

Figure A.2.1 compares predictions from momentum theory with and without Glauert's modification, for the specifications used in Part I. These plots show that

the thrust estimates are not significantly different for incidence angles (the angle of attack of the propeller axis) between 0 deg and 60 deg. The differences are large when the freestream speed is high and the incidence angle is large (> 60 deg), which is a combination that is typical for helicopters but not for tilt-wing aircraft. For the combinations of incidence angle, speed, and power that we are interested in (0 deg to 60 deg, 1 to 67 m/s, and 100 to 311 kW), Glauert's modified momentum theory predicts slightly higher (0 to 10%) thrust values.

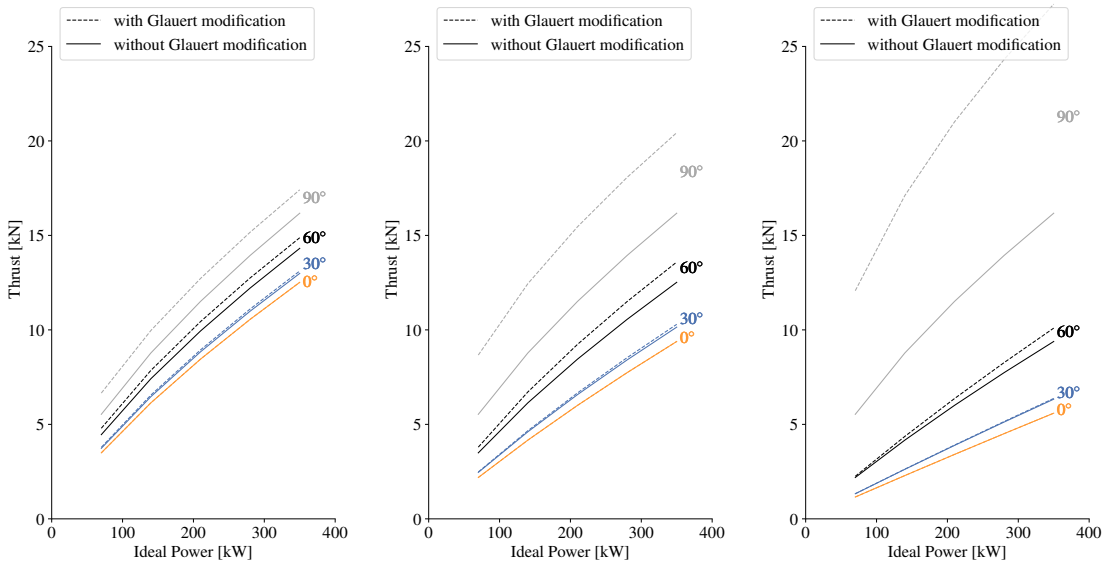

(a) $V_\infty = 15$m/s (b) $V_\infty = 30$m/s (c) $V_\infty = 60$m/s

Figure A.2.1: Comparisons of thrust predictions as a function of ideal power from momentum theory, with and without Glauert's modification, for varying freestream velocities and incidence angles

McCormick [41] describes the approach of using Glauert's modified momentum theory, along with the blade-element-analysis-based profile-power estimate that is typically used for rotors in forward flight, to model the performance of a tilting propeller, and he also includes a comparison with experimental data showing good agreement.

REFERENCES

[1] Tangler, J. L., and Ostowari, C., "Horizontal axis wind turbine post stall airfoil characteristics synthesization," Conference paper presented at the DOE/NASA Wind Turbine Technology Workshop, May 1984. In Collected Papers on Wind Turbine Technology, NASA-CR-195432, May 1995.

[2] Brooks, T. R., Kenway, G. K. W., and Martins, J. R. R. A., "Undeflected Common Research Model (uCRM): An aerostructural model for the study of high aspect ratio transport aircraft wings," *18th AIAA/ISSMO Multidisciplinary Analysis and Optimization Conference*, Denver, CO, 2017. doi:10.2514/6.2017-4456.

[3] Stokkermans, T., Veldhuis, L., Soemarwoto, B., Fukari, R., and Eglin, P., "Breakdown of aerodynamic interactions for the lateral rotors on a compound helicopter," *Aerospace Science and Technology*, Vol. 101, 2020. doi:10.1016/j.ast.2020.105845.

[4] Veldhuis, L. L. M., "Propeller wing aerodynamic interference," Ph.D. thesis, Delft University of Technology, 2005.

[5] Stokkermans, T. C. A., van Arnhem, N., Sinnige, T., and Veldhuis, L. L. M., "Validation and comparison of RANS propeller modeling methods for tip-mounted applications," *AIAA Journal*, Vol. 57, No. 2, 2019, pp. 566–580. doi:10.2514/1.J057398.

[6] Witkowski, D. P., Lee, A. K. H., and Sullivan, J. P., "Aerodynamic interaction between propellers and wings," *Journal of Aircraft*, Vol. 26, No. 9, 1989, pp. 829–836. doi:10.2514/3.45848.

[7] Sinnige, T., van Arnhem, N., Stokkermans, T. C. A., Eitelberg, G., and Veldhuis, L. L. M., "Wingtip-mounted propellers: Aerodynamic analysis of interaction effects and comparison with conventional layout," *Journal of Aircraft*, Vol. 56, No. 1, 2019, pp. 295–312. doi:10.2514/1.C034978.

[8] Chinwicharnam, K., and Thipyopas, C., "Comparison of wing–propeller interaction in tractor and pusher configuration," *International Journal of Micro Air Vehicles*, Vol. 8, No. 1, 2016, pp. 3–20. doi:10.1177/1756829316638206.

[9] Ostowari, C., and Naik, D., "Post-stall wind tunnel data for NACA 44XX series airfoil sections," Subcontract Report SERI/STR-217-2559, Solar Energy Research Institute, January 1985.

[10] Gomariz-Sancha, A., Maina, M., and Peace, A. J., "Analysis of propeller-airframe interaction effects through a combined numerical simulation and wind-tunnel testing approach," *53rd AIAA Aerospace Sciences Meeting*, AIAA, 2015. doi:10.2514/6.2015-1026.

[11] Johnson, W., Silva, C., and Solis, E., "Concept vehicles for VTOL air taxi operations," *Proceedings of the AHS technical conference on Aeromechanics Design for Transformative Vertical Flight*, 2018.

[12] Moore, M. D., and Fredericks, B., "Misconceptions of electric aircraft and their emerging aviation markets," *52nd Aerospace Sciences Meeting*, AIAA, 2014. doi:10.2514/6.2014-0535.

[13] Duffy, M. J., Wakayama, S. R., Hupp, R., Lacy, R., and Stauffer, M., "A study in reducing the cost of vertical flight with electric propulsion," *17th AIAA Aviation Technology, Integration, and Operations Conference*, AIAA, 2017. doi:10.2514/6.2017-3442.

[14] Stoll, A. M., Bevirt, J., Moore, M. D., Fredericks, W. J., and Borer, N. K., "Drag reduction through distributed electric propulsion," *14th AIAA Aviation Technology, Integration, and Operations Conference*, AIAA, 2014. doi:10.2514/6.2014-2851.

[15] Stoll, A. M., Bevirt, J., Pei, P. P., and Stilson, E. V., "Conceptual design of the Joby S2 electric VTOL PAV," *14th AIAA Aviation Technology, Integration, and Operations Conference*, AIAA, 2014. doi:10.2514/6.2014-2407.

[16] Patterson, M. D., and German, B., "Conceptual design of electric aircraft with distributed propellers: Multidisciplinary analysis needs and aerodynamic modeling development," *52nd Aerospace Sciences Meeting*, AIAA, 2014. doi:10.2514/6.2014-0534.

[17] Deere, K. A., Viken, S. A., Carter, M. B., Viken, J. K., Derlaga, J. M., and Stoll, A. M., "Comparison of high-fidelity computational tools for wing design of a distributed electric propulsion aircraft," *35th AIAA Applied Aerodynamics Conference*, AIAA, 2017. doi:10.2514/6.2017-3925.

[18] Fredericks, W. J., McSwain, R. G., Beaton, B. F., Klassman, D. W., and Theodore, C. R., "Greased lightning (GL-10) flight testing campaign," Technical Memorandum NASA-TM-2017-219643, NASA, July 2017.

[19] Antcliff, K. R., and Capristan, F. M., "Conceptual design of the parallel electric-gas architecture with synergistic utilization scheme (PEGASUS) concept," *18th AIAA/ISSMO Multidisciplinary Analysis and Optimization Conference*, 2017. doi:10.2514/6.2017-4001.

[20] Alba, C., Elham, A., German, B. J., and Veldhuis, L. L. M., "A surrogate-based multidisciplinary design optimization framework modeling wing-propeller interaction," *Aerospace Science and Technology*, Vol. 78, 2018, pp. 721–733. doi:10.1016/j.ast.2018.05.002.

[21] Hwang, J. T., and Ning, A., "Large-scale multidisciplinary optimization of an electric aircraft for on-demand mobility," *2018 AIAA/ASCE/AHS/ASC Structures, Structural Dynamics, and Materials Conference*, Kissimmee, FL, 2018. doi:10.2514/6.2018-1384, AIAA-2018-1384.

[22] Droandi, G., Syal, M., and Bower, G., "Tiltwing multi-rotor aerodynamic modeling in hover, transition and cruise flight conditions," *AHS International Forum 74*, 2018. Paper 74-2018-1267.

[23] Brelje, B., and Martins, J. R. R. A., "Electric, hybrid, and turboelectric fixed-wing aircraft: A review of concepts, models, and design approaches," *Progress in Aerospace Sciences*, Vol. 104, 2019, pp. 1–19. doi:10.1016/j.paerosci.2018.06.004.

[24] Moore, K. R., and Ning, A., "Takeoff and performance trade-offs of retrofit distributed electric propulsion for urban transport," *Journal of Aircraft*, Vol. 56, No. 5, 2019, pp. 1880–1892. doi:10.2514/1.C035321.

[25] de Vries, R., Brown, M., and Vos, R., "Preliminary sizing method for hybrid-electric distributed-propulsion aircraft," *Journal of Aircraft*, Vol. 56, No. 6, 2019, pp. 2172–2188. doi:10.2514/1.C035388.

[26] Chauhan, S. S., and Martins, J. R. R. A., "Tilt-wing eVTOL takeoff trajectory optimization," *Journal of Aircraft*, Vol. 57, No. 1, 2020, pp. 93–112. doi:10.2514/1.C035476.

[27] Hoogreef, M., de Vries, R., Sinnige, T., and Vos, R., "Synthesis of aero-propulsive interaction studies applied to conceptual hybrid-electric aircraft design," *AIAA Scitech 2020 Forum*, 2020. doi:10.2514/6.2020-0503.

[28] Pacini, B., Droandi, G., and Syal, M., "Parametric aeroacoustic analysis of two fans in hover flight condition," *VFS Aeromechanics for Advanced Vertical Flight Technical Meeting*, 2020.

[29] Kuhn, R. E., and Draper, J. W., "An investigation of a wing-propeller configuration employing large-chord plain flaps and large-diameter propellers for low-speed flight and vertical take-off," Technical Note NACA-TN-3307, NACA, January 1954.

[30] Kuhn, R. E., and Draper, J. W., "Investigation of the aerodynamic characteristics of a model wing-propeller combination and of the wing and propeller separately at angles of attack up to 90°," Technical Report NACA-TR-1263, NASA, January 1956.

[31] Snyder, M. H., Jr., and Zumwalt, G. W., "Effects of wingtip-mounted propellers on wing lift and induced drag," *Journal of Aircraft*, Vol. 6, No. 5, 1969, pp. 392–397. doi:10.2514/3.44076.

[32] Kroo, I., "Propeller-wing integration for minimum induced loss," *Journal of Aircraft*, Vol. 23, No. 7, 1986, pp. 561–565. doi:10.2514/3.45344.

[33] Miranda, L. R., and Brennan, J. E., "Aerodynamic effects of wingtip-mounted propellers and turbines," *4th Applied Aerodynamics Conference*, AIAA, 1986. doi:10.2514/6.1986-1802.

[34] Jasa, J. P., Hwang, J. T., and Martins, J. R. R. A., "Open-source coupled aerostructural optimization using Python," *Structural and Multidisciplinary Optimization*, Vol. 57, No. 4, 2018, pp. 1815–1827. doi:10.1007/s00158-018-1912-8.

[35] Jasa, J. P., Chauhan, S. S., Gray, J. S., and Martins, J. R. R. A., "How certain physical considerations impact aerostructural wing optimization," *AIAA/ISSMO Multidisciplinary Analysis and Optimization Conference*, Dallas, TX, 2019. doi:10.2514/6.2019-3242.

[36] Hendricks, E. S., Falck, R. D., Gray, J. S., Aretskin-Hariton, E. D., Ingraham, D. J., CHapman, J. W., Schnulo, S. L., Chin, J. C., Jasa, J. P., and Bergeson, J. D., "Multidisciplinary optimization of a turboelectric tiltwing urban air mobility aircraft," *AIAA/ISSMO Multidisciplinary Analysis and Optimization Conference*, Dallas, TX, 2019.

[37] Prandtl, L., "Mutual influence of wings and propeller," Technical Note NACA-TN-74, NACA, December 1921. An English translation of an extract from the First Report of the Gottingen Aerodynamic Laboratory, Chapter 4, Section 6, pp. 112–118.

[38] Pegg, R. J., "Summary of flight-test results of the VZ-2 tilt-wing aircraft," Technical Note NASA-TN-D-989, NASA, February 1962.

[39] Anonymous, "Development of the U.S. Army VZ-2 (Boeing-Vertol 76) research aircraft," Technical Report R-219, The Boeing Company, August 1963.

[40] Konrad, J. W., "Flight and operational suitability testing of the XC-142, V/STOL assault transport," *AIAA Flight Test, Simulation and Support Conference*, AIAA, 1967. doi:10.2514/6.1967-261.

[41] McCormick, B. W., *Aerodynamics of V/STOL Flight*, 1st ed., Academic Press, 1967.

[42] Kelley, H. L., Reeder, J. P., and Champine, R. A., "Summary of a flight-test evaluation of the CL-84 tilt-wing V/STOL aircraft," Technical Memorandum NASA-TM-X-1914, NASA, March 1970.

[43] Nichols, J., "The Hiller X-18 experimental aircraft - lessons learned," *AIAA/AHS/ASEE Aircraft Design, Systems and Operations Conference*, AIAA, 1990. doi:10.2514/6.1990-3203.

[44] Phillips, F. C., "The Canadair CL-84 experimental aircraft - lessons learned," *AIAA/AHS/ASEE Aircraft Design, Systems and Operations Conference*, AIAA, 1990. doi:10.2514/6.1990-3205.

[45] Chana, W. F., and Sullivan, T. M., "The tilt wing configuration for high speed VSTOL aircraft," *19th Congress of the International Council of the Aeronautical Sciences*, ICAS/AIAA, 1994.

[46] Leishman, J. G., *Principles of Helicopter Aerodynamics*, 1st ed., The Press Syndicate of the University of Cambridge, 2000.

[47] McKinney, M. O., Kirby, R. H., and Newsom, W. A., "Aerodynamic factors to be considered in the design of tiltwing V/STOL airplanes," *Annals of the New York Academy of Sciences*, Vol. 107, No. 1, 1963, pp. 221–248. doi:10.1111/j.1749-6632.1963.tb13279.x.

[48] Fay, C. B., "A cursory analysis of the VTOL tilt-wing performance and control problems," *Annals of the New York Academy of Sciences*, Vol. 107, No. 1, 1963, pp. 102–146. doi:10.1111/j.1749-6632.1963.tb13275.x.

[49] Whitfield, D. L., and Jameson, A., "Euler equation simulation of propeller-wing interaction in transonic flow," *Journal of Aircraft*, Vol. 21, No. 11, 1984, pp. 835–839. doi:10.2514/3.45052.

[50] Fratello, G., Favier, D., and Maresca, C., "Experimental and numerical study of the propeller/fixed wing interaction," *Journal of Aircraft*, Vol. 28, No. 6, 1991, pp. 365–373. doi:10.2514/3.46036.

[51] Veldhuis, L. L. M., and Heyma, P. M., "Aerodynamic optimisation of wings in multi-engined tractor propeller arrangements," *Aircraft Design*, Vol. 3, No. 3, 2000, pp. 129–149. doi:10.1016/s1369-8869(00)00010-0.

[52] Carlton, J. S., *Marine Propellers and Propulsion*, 4th ed., Butterworth-Heinemann, 2018.

[53] Smith, H. R., "Engineering models of aircraft propellers at incidence," Ph.D. thesis, University of Glasgow, 2015.

[54] Stone, R. H., "Aerodynamic modeling of the wing-propeller interaction for a tail-sitter unmanned air vehicle," *Journal of Aircraft*, Vol. 45, No. 1, 2008, pp. 198–210. doi:10.2514/1.15705.

[55] Kubo, D., and Suzuki, S., "Tail-sitter vertical takeoff and landing unmanned aerial vehicle: Transitional flight analysis," *Journal of Aircraft*, Vol. 45, No. 1, 2008, pp. 292–297. doi:10.2514/1.30122.

[56] Selig, M. S., "Real-time flight simulation of highly maneuverable unmanned aerial vehicles," *Journal of Aircraft*, Vol. 51, No. 6, 2014, pp. 1705–1725. doi:10.2514/1.c032370.

[57] Verling, S., Stastny, T., Battig, G., Alexis, K., and Siegwart, R., "Model-based transition optimization for a VTOL tailsitter," *2017 IEEE International Conference on Robotics and Automation (ICRA)*, IEEE, 2017. doi:10.1109/icra.2017.7989454.

[58] Singh, P., and Friedmann, P. P., "A computational fluid dynamics-based viscous vortex particle method for coaxial rotor interaction calculations in hover," *Journal of the American Helicopter Society*, Vol. 63, No. 4, 2018. doi:10.4050/JAHS.63.042002.

[59] Selig, M., "Modeling full-envelope aerodynamics of small UAVs in realtime," *AIAA Atmospheric Flight Mechanics Conference*, AIAA, 2010. doi:10.2514/6.2010-7635.

[60] Hargraves, C. R., "An analytical study of the longitudinal dynamics of a tilt-wing VTOL," Technical Report 561, U.S. Army Transportation Research Command, June 1961.

[61] Chambers, J. R., and Grafton, S. B., "Calculation of the dynamic longitudinal stability of a tilt-wing V/STOL aircraft and correlation with model flight tests," Technical Note NASA-TN-D-4344, NASA, February 1968.

[62] Holsten, J., Ostermann, T., and Moormann, D., "Design and wind tunnel tests of a tiltwing UAV," *CEAS Aeronautical Journal*, Vol. 2, No. 1, 2011, pp. 69–79. doi:10.1007/s13272-011-0026-4.

[63] Cetinsoy, E., Dikyar, S., Hancer, C., Oner, K., Sirimoglu, E., Unel, M., and Aksit, M., "Design and construction of a novel quad tilt-wing UAV," *Mechatronics*, Vol. 22, No. 6, 2012, pp. 723–745. doi:10.1016/j.mechatronics.2012.03.003.

[64] Sato, M., and Muraoka, K., "Flight controller design and demonstration of quad-tilt-wing unmanned aerial vehicle," *Journal of Guidance, Control, and Dynamics*, Vol. 38, No. 6, 2015, pp. 1071–1082. doi:10.2514/1.G000263.

[65] Hartmann, P., Meyer, C., and Moormann, D., "Unified velocity control and flight state transition of unmanned tilt-wing aircraft," *Journal of Guidance, Control, and Dynamics*, Vol. 40, No. 6, 2017, pp. 1348–1359. doi:10.2514/1.G002168.

[66] Stone, R. H., and Clarke, G., "Optimization of transition maneuvers for a tail-sitter unmanned air vehicle," *Australian Aerospace International Congress, Paper 105*, 2001.

[67] Stone, R. H., Anderson, P., Hutchison, C., Tsai, A., Gibbens, P., and Wong, K. C., "Flight testing of the T-wing tail-sitter unmanned air vehicle," *Journal of Aircraft*, Vol. 45, No. 2, 2008, pp. 673–685. doi:10.2514/1.32750.

[68] Maqsood, A., and Go, T. H., "Optimization of transition maneuvers through aerodynamic vectoring," *Aerospace Science and Technology*, Vol. 23, No. 1, 2012, pp. 363–371. doi:10.1016/j.ast.2011.09.004.

[69] Oosedo, A., Abiko, S., Konno, A., and Uchiyama, M., "Optimal transition from hovering to level-flight of a quadrotor tail-sitter UAV," *Autonomous Robots*, Vol. 41, No. 5, 2017, pp. 1143–1159. doi:10.1007/s10514-016-9599-4.

[70] Pradeep, P., and Wei, P., "Energy optimal speed profile for arrival of tandem tilt-wing eVTOL aircraft with RTA constraint," *Proceedings of IEEE/CSAA Guidance, Navigation and Control Conference (GNCC), Xiamen, China*, 2018.

[71] Gray, J. S., Hwang, J. T., Martins, J. R. R. A., Moore, K. T., and Naylor, B. A., "OpenMDAO: An open-source framework for multidisciplinary design, analysis, and optimization," *Structural and Multidisciplinary Optimization*, Vol. 59, No. 4, 2019, pp. 1075–1104. doi:10.1007/s00158-019-02211-z.

[72] Hwang, J. T., and Martins, J. R. R. A., "A computational architecture for coupling heterogeneous numerical models and computing coupled derivatives," *ACM Transactions on Mathematical Software*, Vol. 44, No. 4, 2018, p. Article 37. doi:10.1145/3182393.

[73] Viterna, L. A., and Corrigan, R. D., "Fixed pitch rotor performance of large horizontal axis wind turbines," *Large Horizontal-Axis Wind Turbines (NASA-CP-2230)*, NASA Conference Publication, 1982, pp. 69–86.

[74] Critzos, C. C., Heyson, H. H., and Robert W. Boswinkle, J., "Aerodynamic characteristics of NACA 0012 airfoil section at angles of attack from 0 degrees to 180 degrees," Technical Note NACA-TN-3361, NACA, January 1955.

[75] Abbott, I. H., and Von Doenhoff, A. E., *Theory of wing sections, including a summary of airfoil data*, Dover Publications, New York, 1959.

[76] Prandtl, L., "Induced drag of multiplanes," Technical Note NACA-TN-182, NACA, February 1924.

[77] McLaughlin, M. D., "Calculations, and comparison with an ideal minimum, of trimmed drag for conventional and canard configurations having various levels of static stability," Technical Note NASA-TN-D-8391, NASA, May 1977.

[78] Kreisselmeier, G., and Steinhauser, R., "Systematic control design by optimizing a vector performance index," *International Federation of Active Controls Symposium on Computer-Aided Design of Control Systems, Zurich, Switzerland*, 1979. doi:10.1016/S1474-6670(17)65584-8.

[79] Winslow, J., Otsuka, H., Govindarajan, B., and Chopra, I., "Basic understanding of airfoil characteristics at low Reynolds numbers ($10^4 - 10^5$)," *Journal of Aircraft*, Vol. 55, No. 3, 2018, pp. 1050–1061. doi:10.2514/1.c034415.

[80] van Dam, C. P., Kam, J. C. V., and Paris, J. K., "Design-oriented high-lift methodology for general aviation and civil transport aircraft," *Journal of Aircraft*, Vol. 38, No. 6, 2001, pp. 1076–1084. doi:10.2514/2.2875.

[81] Rumsey, C. L., Allison, D. O., Biedron, R. T., Buning, P. G., Gainer, T. G., Morrison, J. H., Rivers, S. M., Mysko, S. J., and Witkowski, D. P., "CFD sensitivity analysis of a modern civil transport near buffet-onset conditions," Tech. Rep. TM-2001-211263, NASA, 2001.

[82] van Dam, C. P., "The aerodynamic design of multi-element high-lift systems for transport airplanes," *Progress in Aerospace Sciences*, Vol. 38, No. 2, 2002, pp. 101–144. doi:10.1016/s0376-0421(02)00002-7.

[83] Mukherjee, R., and Gopalarathnam, A., "Poststall prediction of multiple-lifting-surface configurations using a decambering approach," *Journal of Aircraft*, Vol. 43, No. 3, 2006, pp. 660–668. doi:10.2514/1.15149.

[84] Petrilli, J. L., Paul, R. C., Gopalarathnam, A., and Frink, N. T., "A CFD database for airfoils and wings at post-stall angles of attack," *31st AIAA Applied Aerodynamics Conference*, AIAA, 2013. doi:10.2514/6.2013-2916.

[85] Parenteau, M., Sermeus, K., and Laurendeau, E., "VLM coupled with 2.5D RANS sectional data for high-lift design," *2018 AIAA Aerospace Sciences Meeting*, AIAA, 2018. doi:10.2514/6.2018-1049.

[86] Glauert, H., "A general theory of the autogyro," Reports and Memoranda 1111, Aeronautical Research Committee, 1926.

[87] de Young, J., "Propeller at high incidence," *Journal of Aircraft*, Vol. 2, No. 3, 1965, pp. 241–250. doi:10.2514/3.43646.

[88] Patterson, M. D., "Conceptual design of high-lift propeller systems for small electric aircraft," Ph.D. thesis, Georgia Institute of Technology, 2016. URL `http://hdl.handle.net/1853/55569`.

[89] Patterson, M. D., Derlaga, J. M., and Borer, N. K., "High-lift propeller system configuration selection for NASA's SCEPTOR distributed electric propulsion flight demonstrator," *16th AIAA Aviation Technology, Integration, and Operations Conference*, AIAA, 2016. doi:10.2514/6.2016-3922.

[90] Cole, J. A., Maughmer, M. D., Kinzel, M., and Bramesfeld, G., "Higher-order free-wake method for propeller–wing systems," *Journal of Aircraft*, Vol. 56, No. 1, 2019, pp. 150–165. doi:10.2514/1.c034720.

[91] Chauhan, S. S., and Martins, J. R. R. A., "RANS-based aerodynamic shape optimization of a wing considering propeller-wing interaction," *AIAA SciTech Forum*, AIAA, Orlando, FL, 2020. doi:10.2514/6.2020-1764.

[92] Poon, N. M. K., and Martins, J. R. R. A., "An adaptive approach to constraint aggregation using adjoint sensitivity analysis," *Structural and Multidisciplinary Optimization*, Vol. 34, No. 1, 2007, pp. 61–73. doi:10.1007/s00158-006-0061-7.

[93] Lambe, A. B., Martins, J. R. R. A., and Kennedy, G. J., "An evaluation of constraint aggregation strategies for wing box mass minimization," *Structural and Multidisciplinary Optimization*, Vol. 55, No. 1, 2017, pp. 257–277. doi:10.1007/s00158-016-1495-1.

[94] Chauhan, S. S., and Martins, J. R. R. A., "Low-fidelity aerostructural optimization of aircraft wings with a simplified wingbox model using OpenAeroStruct," *Proceedings of the 6th International Conference on Engineering Optimization, EngOpt 2018*, Springer, Lisbon, Portugal, 2018, pp. 418–431. doi:10.1007/978-3-319-97773-7_38.

[95] Gill, P. E., Murray, W., and Saunders, M. A., "SNOPT: An SQP algorithm for large-scale constrained optimization," *SIAM Review*, Vol. 47, No. 1, 2005, pp. 99–131. doi:10.1137/S0036144504446096.

[96] Martins, J. R. R. A., Sturdza, P., and Alonso, J. J., "The complex-step derivative approximation," *ACM Transactions on Mathematical Software*, Vol. 29, No. 3, 2003, pp. 245–262. doi:10.1145/838250.838251.

[97] Hargraves, C. R., and Paris, S. W., "Direct trajectory optimization using nonlinear programming and collocation," *Journal of Guidance, Control, and Dynamics*, Vol. 10, No. 4, 1987, pp. 338–342. doi:10.2514/3.20223.

[98] Hendricks, E. S., Falck, R. D., and Gray, J. S., "Simultaneous propulsion system and trajectory optimization," *18th AIAA/ISSMO Multidisciplinary Analysis and Optimization Conference*, Denver, CO, 2017. doi:10.2514/6.2017-4435, AIAA-2017-4435.

[99] Gebhard, J. W., "Acceleration and comfort in public ground transportation," Transportation Programs Report TPR 002, The Johns Hopkins University, 1970.

[100] Bramesfeld, G., and Maughmer, M. D., "Relaxed-wake vortex-lattice method using distributed vorticity elements," *Journal of Aircraft*, Vol. 45, No. 2, 2008, pp. 560–568. doi:10.2514/1.31665.

[101] Ardito Marretta, R. M., Davi, G., Milazzo, A., and Lombardi, G., "Wing pitching and loading with propeller interference," *Journal of Aircraft*, Vol. 36, No. 2, 1999, pp. 468–471. doi:10.2514/2.2455.

[102] Moens, F., and Gardarein, P., "Numerical simulation of the propeller/wing interactions for transport aircraft," *19th AIAA Applied Aerodynamics Conference*, 2001. doi:10.2514/6.2001-2404.

[103] Roosenboom, E. W. M., Stürmer, A., and Schröder, A., "Advanced experimental and numerical validation and analysis of propeller slipstream flows," *Journal of Aircraft*, Vol. 47, No. 1, 2010, pp. 284–291. doi:10.2514/1.45961.

[104] Rakshith, B. R., Deshpande, S. M., Narasimha, R., and Praveen, C., "Optimal low-drag wing planforms for tractor-configuration propeller-driven aircraft," *Journal of Aircraft*, Vol. 52, No. 6, 2015, pp. 1791–1801. doi:10.2514/1.C032997.

[105] Epema, K., "Wing optimisation for tractor propeller configurations," Master's thesis, Delft University of Technology, 2017.

[106] Pedreiro, L. N., "Estudo e otimização de uma asa sob efeito de hélice na configuração tractor para redução de arrasto," Master's thesis, Universidade Federal de Minas Gerais, 2017.

[107] van Arnhem, N., Sinnige, T., Stokkermans, T. C., Eitelberg, G., and Veldhuis, L. L., "Aerodynamic interaction effects of tip-mounted propellers installed on the horizontal tailplane," *2018 AIAA Aerospace Sciences Meeting*, AIAA, 2018. doi:10.2514/6.2018-2052.

[108] van Arnhem, N., Vos, R., and Veldhuis, L. L., "Aerodynamic loads on an aft-mounted propeller induced by the wing wake," *AIAA Scitech 2019 Forum*, 2019. doi:10.2514/6.2019-1093.

[109] van Arnhem, N., de Vries, R., Vos, R., and Veldhuis, L. L., "Aerodynamic performance of an aircraft equipped with horizontal tail mounted propellers," *AIAA Aviation 2019 Forum*, AIAA, 2019. doi:10.2514/6.2019-3036.

[110] Sharpe, P., and Agarwal, R. K., "Conceptual and numerical analysis of active wingtip vortex cancellation in propeller-driven electric aircraft," *AIAA Scitech 2019 Forum*, AIAA, 2019. doi:10.2514/6.2019-1091.

[111] Sharpe, P., and Agarwal, R. K., "Numerical analysis of propeller-wing interaction in aircraft with distributed electric propulsion," *AIAA Aviation 2019 Forum*, AIAA, 2019. doi:10.2514/6.2019-3691.

[112] Miley, S. J., Howard, R. M., and Holmes, B. J., "Wing laminar boundary layer in the presence of a propeller slipstream," *Journal of Aircraft*, Vol. 25, No. 7, 1988, pp. 606–611. doi:10.2514/3.45630.

[113] Whitfield, D., and Jameson, A., "Three-dimensional Euler equation simulation of propeller-wing interaction in transonic flow," *21st Aerospace Sciences Meeting*, AIAA, 1983. doi:10.2514/6.1983-236.

[114] Chetboun, J., Rubin, T., and Seror, S., "Complete RANS simulation of a propelled generic UAV with the blade element model," *54th Israel Annual Conference on Aerospace Sciences*, 2014. URL `https://www.researchgate.net/publication/290035878_Complete_RANS_simulation_of_a_propelled_generic_UAV_with_the_blade_element_model`.

[115] Dacles-Mariani, J., Zilliac, G. G., Chow, J. S., and Bradshaw, P., "Numerical/experimental study of a wingtip vortex in the near field," *AIAA Journal*, Vol. 33, No. 9, 1995, pp. 1561–1568. doi:10.2514/3.12826.

[116] Kim, S.-E., and Rhee, S. H., "Efficient engineering prediction of turbulent wing tip vortex flows," *Computer Modeling in Engineering & Sciences*, Vol. 62, No. 3, 2010, pp. 291–310. doi:10.3970/cmes.2010.062.291.

[117] Lyu, Z., Xu, Z., and Martins, J. R. R. A., "Benchmarking optimization algorithms for wing aerodynamic design optimization," *Proceedings of the 8th International Conference on Computational Fluid Dynamics*, Chengdu, Sichuan, China, 2014. ICCFD8-2014-0203.

[118] Yu, Y., Lyu, Z., Xu, Z., and Martins, J. R. R. A., "On the influence of optimization algorithm and starting design on wing aerodynamic shape optimization," *Aerospace Science and Technology*, Vol. 75, 2018, pp. 183–199. doi:10.1016/j.ast.2018.01.016.

[119] Kenway, G. K. W., Kennedy, G. J., and Martins, J. R. R. A., "Scalable parallel approach for high-fidelity steady-state aeroelastic analysis and derivative computations," *AIAA Journal*, Vol. 52, No. 5, 2014, pp. 935–951. doi:10.2514/1.J052255.

[120] Yildirim, A., Kenway, G. K. W., Mader, C. A., and Martins, J. R. R. A., "A Jacobian-free approximate Newton–Krylov startup strategy for RANS simulations," *Journal of Computational Physics*, Vol. 397, 2019, p. 108741. doi:10.1016/j.jcp.2019.06.018.

[121] Mader, C. A., Kenway, G. K. W., Yildirim, A., and Martins, J. R. R. A., "ADflow—an open-source computational fluid dynamics solver for aerodynamic and multidisciplinary optimization," *Journal of Aerospace Information Systems*, 2020. doi:10.2514/1.I010796.

[122] Kenway, G. K. W., Secco, N., Martins, J. R. R. A., Mishra, A., and Duraisamy, K., "An efficient parallel overset method for aerodynamic shape optimization," *Proceedings of the 58th AIAA/ASCE/AHS/ASC Structures, Structural Dynamics, and Materials Conference, AIAA SciTech Forum*, Grapevine, TX, 2017. doi:10.2514/6.2017-0357.

[123] Spalart, P., and Allmaras, S., "A one-equation turbulence model for aerodynamic flows," *30th Aerospace Sciences Meeting and Exhibit*, 1992. doi:10.2514/6.1992-439.

[124] Kenway, G. K. W., Mader, C. A., He, P., and Martins, J. R. R. A., "Effective adjoint approaches for computational fluid dynamics," *Progress in Aerospace Sciences*, Vol. 110, 2019, p. 100542. doi:10.1016/j.paerosci.2019.05.002.

[125] Lyu, Z., and Martins, J. R. R. A., "Aerodynamic design optimization studies of a blended-wing-body aircraft," *Journal of Aircraft*, Vol. 51, No. 5, 2014, pp. 1604–1617. doi:10.2514/1.C032491.

[126] Kenway, G. K. W., and Martins, J. R. R. A., "Buffet onset constraint formulation for aerodynamic shape optimization," *AIAA Journal*, Vol. 55, No. 6, 2017, pp. 1930–1947. doi:10.2514/1.J055172.

[127] Brooks, T. R., Kenway, G. K. W., and Martins, J. R. R. A., "Benchmark aerostructural models for the study of transonic aircraft wings," *AIAA Journal*, Vol. 56, No. 7, 2018, pp. 2840–2855. doi:10.2514/1.J056603.

[128] Secco, N. R., and Martins, J. R. R. A., "RANS-based aerodynamic shape optimization of a strut-braced wing with overset meshes," *Journal of Aircraft*, Vol. 56, No. 1, 2019, pp. 217–227. doi:10.2514/1.C034934.

[129] Bons, N. P., He, X., Mader, C. A., and Martins, J. R. R. A., "Multimodality in aerodynamic wing design optimization," *AIAA Journal*, Vol. 57, No. 3, 2019, pp. 1004–1018. doi:10.2514/1.J057294.

[130] Madsen, M. H. A., Zahle, F., Sørensen, N. N., and Martins, J. R. R. A., "Multipoint high-fidelity CFD-based aerodynamic shape optimization of a 10 MW wind turbine," *Wind Energy Science*, Vol. 4, 2019, pp. 163–192. doi:10.5194/wes-4-163-2019.

[131] Mangano, M., and Martins, J. R. R. A., "Multipoint aerodynamic shape optimization for subsonic and supersonic regimes," *Journal of Aircraft*, 2020. doi:10.2514/1.C035826.

[132] Kenway, G. K., Kennedy, G. J., and Martins, J. R. R. A., "A CAD-free approach to high-fidelity aerostructural optimization," *Proceedings of the 13th AIAA/ISSMO Multidisciplinary Analysis Optimization Conference*, Fort Worth, TX, 2010. doi:10.2514/6.2010-9231.

[133] Secco, N. R., Kenway, G. K. W., He, P., Mader, C. A., and Martins, J. R. R. A., "Efficient mesh generation and deformation for aerodynamic shape optimization," *AIAA Journal*, 2020. (Submitted).

[134] Luke, E., Collins, E., and Blades, E., "A fast mesh deformation method using explicit interpolation," *Journal of Computational Physics*, Vol. 231, No. 2, 2012, pp. 586–601. doi:10.1016/j.jcp.2011.09.021.

[135] He, P., Mader, C. A., Martins, J. R. R. A., and Maki, K. J., "An aerodynamic design optimization framework using a discrete adjoint approach with OpenFOAM," *Computers & Fluids*, Vol. 168, 2018, pp. 285–303. doi:10.1016/j.compfluid.2018.04.012.

[136] He, P., Mader, C. A., Martins, J. R. R. A., and Maki, K. J., "DAFoam: An open-source adjoint framework for multidisciplinary design optimization with OpenFOAM," *AIAA Journal*, Vol. 58, No. 3, 2020. doi:10.2514/1.J058853.

[137] Perez, R. E., Jansen, P. W., and Martins, J. R. R. A., "pyOpt: A Python-based object-oriented framework for nonlinear constrained optimization," *Structural and Multidisciplinary Optimization*, Vol. 45, No. 1, 2012, pp. 101–118. doi:10.1007/s00158-011-0666-3.

[138] Hoekstra, M., "A RANS-based analysis tool for ducted propeller systems in open water condition," *International Shipbuilding Progress 53*, Vol. 53, 2006, pp. 205–227.

[139] Bacon, F., Jardine, L., and Silverthorne, M., *The New Organon*, Cambridge University Press, 2000.

[140] Lee, Y., and Baeder, J., "Implicit hole cutting-a new approach to overset grid connectivity," *16th AIAA Computational Fluid Dynamics Conference*, 2003, p. 4128. doi:10.2514/6.2003-4128.

[141] Sinnige, T., de Vries, R., Corte, B. D., Avallone, F., Ragni, D., Eitelberg, G., and Veldhuis, L. L. M., "Unsteady pylon loading caused by propeller-slipstream impingement for tip-mounted propellers," *Journal of Aircraft*, Vol. 55, No. 4, 2018, pp. 1605–1618. doi:10.2514/1.C034696.

[142] Lyu, Z., Kenway, G. K. W., and Martins, J. R. R. A., "Aerodynamic shape optimization investigations of the Common Research Model wing benchmark," *AIAA Journal*, Vol. 53, No. 4, 2015, pp. 968–985. doi:10.2514/1.J053318.

[143] Biermann, D., and Hartman, E. P., "Full-scale tests of 4- and 6-blade, single- and dual-rotating propellers," Special Report NACA-SR-157, NACA, August 1940.

[144] Anonymous, "Generalized method of propeller performance estimation," Technical Report PDB 6101 Revision A, Hamilton Standard, June 1963.

[145] Raymer, D. P., *Aircraft Design: A Conceptual Approach*, 5$^{\text{th}}$ ed., AIAA, 2012.

[146] Secco, N. R., Jasa, J. P., Kenway, G. K. W., and Martins, J. R. R. A., "Component-based geometry manipulation for aerodynamic shape optimization with overset meshes," *AIAA Journal*, Vol. 56, No. 9, 2018, pp. 3667–3679. doi:10.2514/1.J056550.

[147] Kroo, I. M., "Drag due to lift: Concepts for prediction and reduction," *Annual Review of Fluid Mechanics*, Vol. 33, 2000, pp. 587–617. doi:10.1146/annurev.fluid.33.1.587.

[148] Reist, T. A., Koo, D., Zingg, D. W., Bochud, P., Castonguay, P., and Leblond, D., "Cross validation of aerodynamic shape optimization methodologies for aircraft wing-body optimization," *AIAA Journal*, 2020. doi:10.2514/1.J059091.

[149] Koo, D., and Zingg, D. W., "Investigation into aerodynamic shape optimization of planar and nonplanar wings," *AIAA Journal*, Vol. 56, 2018, pp. 250–263. doi:10.2514/1.j055978.

[150] Khosravi, S., and Zingg, D. W., "Aerostructural perspective on winglets," *Journal of Aircraft*, Vol. 54, No. 3, 2017, pp. 1121–1138. doi:10.2514/1.C033914.

[151] Weller, H. G., Tabor, G., Jasak, H., and Fureby, C., "A tensorial approach to computational continuum mechanics using object-oriented techniques," *Computers in Physics*, Vol. 12, No. 6, 1998, pp. 620–631. doi:10.1063/1.168744.

[152] Jasak, H., "Error analysis and estimation for finite volume method with applications to fluid flow," Ph.D. thesis, Imperial College of Science, Technology and Medicine, 1996.

[153] Schlichting, H., and Gersten, K., *Boundary-Layer Theory*, 7$^{\text{th}}$ ed., McGraw Hill, 1979.

[154] Johnson, C. L., and Smith, M., *Kelly: More than my share of it all*, Smithsonian Books, 1985.

[155] Falck, R. D., and Gray, J. S., "Optimal control within the context of multidisciplinary design, analysis, and optimization," *AIAA Scitech 2019 Forum*, 2019. doi:10.2514/6.2019-0976.

[156] Dassault, M., *Le Talisman*, Éditions J'ai Lu, 1970.

[157] Drela, M., "Development of the D8 transport configuration," *29th AIAA Applied Aerodynamics Conference*, American Institute of Aeronautics and Astronautics, 2011. doi:10.2514/6.2011-3970.

[158] Elham, A., and van Tooren, M. J. L., "Coupled adjoint aerostructural wing optimization using quasi-three-dimensional aerodynamic analysis," *Structural and Multidisciplinary Optimization*, Vol. 54, No. 4, 2016, pp. 889–906. doi:10.1007/s00158-016-1447-9.

[159] Fujiwara, G. E., and Nguyen, N. T., "Aeroestructural design optimization of a subsonic wing with continuous morphing trailing edge," *35th AIAA Applied Aerodynamics Conference*, American Institute of Aeronautics and Astronautics, 2017. doi:10.2514/6.2017-4218.

[160] Vassberg, J. C., DeHaan, M. A., Rivers, S. M., and Wahls, R. A., "Development of a Common Research Model for applied CFD validation studies," 2008. doi:10.2514/6.2008-6919.

[161] Peherstorfer, B., Beran, P. S., and Willcox, K. E., "Multifidelity Monte Carlo estimation for large-scale uncertainty propagation," *2018 AIAA Non-Deterministic Approaches Conference*, American Institute of Aeronautics and Astronautics, 2018. doi:10.2514/6.2018-1660.

[162] Tracey, B. D., and Wolpert, D., "Upgrading from Gaussian processes to Student's-t processes," *2018 AIAA Non-Deterministic Approaches Conference*, American Institute of Aeronautics and Astronautics, 2018. doi:10.2514/6.2018-1659.

[163] Chaudhuri, A., Jasa, J., Martins, J. R. R. A., and Willcox, K., "Multifidelity optimization under uncertainty for a tailless aircraft," *2018 AIAA/ASCE/AHS/ASC Structures, Structural Dynamics, and Materials Conference; AIAA SciTech Forum*, Orlando, FL, 2018. doi:10.2514/6.2018-1658.

[164] Chauhan, S. S., Hwang, J. T., and Martins, J. R. R. A., "An automated selection algorithm for nonlinear solvers in MDO," *Structural and Multidisciplinary Optimization*, Vol. 58, No. 2, 2018, pp. 349–377. doi:10.1007/s00158-018-2004-5.

[165] Beer, F. P., E. Russell Johnston, J., DeWolf, J. T., and Mazurek, D. F., *Mechanics of Materials, 7th Edition*, McGraw-Hill Education, 2014.

[166] Grant, C., "Shear centre of thin-walled sections," *The Journal of Strain Analysis for Engineering Design*, Vol. 27, No. 3, 1992, pp. 151–155. doi:10.1243/03093247v273151.

[167] Chandrupatla, T. R., and Belegundu, A. D., *Introduction to Finite Elements in Engineering*, 4^{th} ed., Pearson Education, 2012.

[168] Kennedy, G. J., Kenway, G. K. W., and Martins, J. R. R. A., "High aspect ratio wing design: Optimal aerostructural tradeoffs for the next generation of materials," *Proceedings of the AIAA Science and Technology Forum and Exposition (SciTech)*, National Harbor, MD, 2014. doi:10.2514/6.2014-0596.

[169] Gill, P. E., Murray, W., and Saunders, M. A., "SNOPT: An SQP algorithm for large-scale constrained optimization," *SIAM Journal of Optimization*, Vol. 12, No. 4, 2002, pp. 979–1006. doi:10.1137/S1052623499350013.

[170] Martins, J. R. R. A., and Hwang, J. T., "Review and unification of methods for computing derivatives of multidisciplinary computational models," *AIAA Journal*, Vol. 51, No. 11, 2013, pp. 2582–2599. doi:10.2514/1.J052184.

[171] Raymer, D. P., *Aircraft Design: A Conceptual Approach*, 4^{th} ed., AIAA, 2006.

[172] Malone, B., and Mason, W., "Multidisciplinary optimization in aircraft design using analytic technology models," *Journal of Aircraft*, Vol. 32, No. 2, 1995, pp. 431–438. doi:10.2514/3.46734.

[173] Klimmek, T., "Parametric set-up of a structural model for FERMAT configuration aeroelastic and loads analysis," *Journal of Aeroelasticity and Structural Dynamics*, Vol. 3, No. 2, 2014, pp. 31–49. doi:10.3293/asdj.2014.27.

[174] Wakayama, S., and Kroo, I., "Subsonic wing planform design using multidisciplinary optimization," *Journal of Aircraft*, Vol. 32, No. 4, 1995, pp. 746–753.